



**HAL**  
open science

# Numerical modeling of an aeronautical injector : from the internal flow to the dispersed spray

Alberto Remigi

► **To cite this version:**

Alberto Remigi. Numerical modeling of an aeronautical injector : from the internal flow to the dispersed spray. Fluid mechanics [physics.class-ph]. Normandie Université, 2021. English. NNT : 2021NORMR012 . tel-03231663

**HAL Id: tel-03231663**

**<https://theses.hal.science/tel-03231663v1>**

Submitted on 21 May 2021

**HAL** is a multi-disciplinary open access archive for the deposit and dissemination of scientific research documents, whether they are published or not. The documents may come from teaching and research institutions in France or abroad, or from public or private research centers.

L'archive ouverte pluridisciplinaire **HAL**, est destinée au dépôt et à la diffusion de documents scientifiques de niveau recherche, publiés ou non, émanant des établissements d'enseignement et de recherche français ou étrangers, des laboratoires publics ou privés.

---

# Numerical modeling of an aeronautical injector: from the internal flow to the dispersed spray

---

Thesis submitted for the degree of Doctor of Philosophy of the University of Rouen

Normandie

Alberto Remigi

remigia@coria.fr

Jury:

François-Xavier Demoulin	CORIA, University of Rouen Normandie	Directeur de thèse
Marc Massot	CMAP, École Polytechnique	Co-Directeur de thèse
Benjamin Duret	CORIA, University of Rouen Normandie	Co-Encadrant
Stéphane Vincent	MSME, Université Gustave Eiffel	Rapporteur
Pierre Boivin	M2P2, Centrale Marseille	Rapporteur
Federico Piscaglia	DAER, Politecnico di Milano	Examineur
Nicolas Grenier	Limsi, Université Paris Saclay	Examineur
Petar Tomov	Ingénieur, Safran Aircraft Engines	Invité

CORIA UMR 6614 - University of Rouen Normandie

University avenue, B.P. 12

76801 Saint-Etienne du Rouvray - France



PhD, University of Rouen and CORIA - France

This research was done under the supervision of François-Xavier Demoulin, Benjamin Duret, Marc Massot and Petar Tomov with the financial support of SAFRAN Aircraft Engines (SAE) within a total of 3 years, from 2018 to 2021.

Edition date *May 10, 2021*

*Ai miei genitori, che hanno sempre creduto in me*

*A Marion, che mi ha dato forza quando non ne avevo*



# Acknowledgements

After a long trip like this I need to make the proper acknowledgements to everyone. First of all I need to thank F.X Demoulin. He managed to regulate and to contrast my stubbornness and my will to go always in new directions. He taught me a lot of things for my life, and this is the most important thing. It is because of this I want to thank him from the deep of my heart, and tell him he made me a better person. I want to thank Marc Massot for the opportunity he gave me at Polytechnique and for his help. Every second he dedicated to me was precious. Thanks to Benjamin and his precious help in re-reading this thesis and for all the time he was available (also during the week end) to answer to my questions. Thank you to Julien Réveillon for the discussion and the help in the difficult moments.

In *SAFRAN Aircraft Engines* I was like in a family. Everyone was kind with me and very helpful. For this reason I need to thank Petar and Hugo for being my light during this path. They were always available and let me say it: they were always like friends, very patient friends (mainly when I was not speaking french). I hope to work with them again because they are wonderful colleagues and people. Special mention for Antoine: always a true friend. He made my life a lot easier in Paris. Part of this work it is also thank to him who helped me in all my down moments (I still need to make him my risotto). I thank also all IHESF département. Among others: Gilles, David, Loic, Théodore, Kevin, Laetitia among others.

CORIA and my group in Rouen was a big part of my PhD. First of all I need to thank Aqeel for listening to me always, for his precious help and all the discussions. Later I want to say a big thank you to my true ARCHER friends with whom I shared a lot of ideas and happy moments and that I will never forget: Victor and Anirudh. I can't forget neither Niccolò and Lorenzo. We shared very interesting discussion about science and a lot of Italian moments. You are wonderful people. I will not forget who was my true help all along the end of the PhD: Cleante, Diego and Sabina. You are all so special. Thank you. A special mention for Sabina. She was always ready to listen to me when I was in need. I missed our discussion during COVID months.

Thank you to my Polytechnique friends. In particular to Pierre and Quentin. How many crazy adventures and shared moments. They are some of the smartest and funniest people I ever met in my life. They are also people with whom is very easy to work with and perfect team players.

Thank you to Roxane and Louis. They are a wonderful couple, and also beautiful friends. I loved all the moments we passed together: in Rio, Udine and Paris of course. In addition to it they are people with whom I have exchanged a lot of ideas about science. Part of this PhD comes from our exchanges.

People think PhDs have not a social life outside work. Well, people are wrong. Each of us has friends that mean family. I need to say thank you to my friends in Italy (and outside Italy): Emanuele, Alessio, Matteo, Veronica, Marco, Nicolò, Daniele, Edoardo, Marta, Alberto. They are my family. I can't forget Stefano: since our days in Karlsruhe we have a special connection. He is always ready to listen to me, to share and to use the right words. He is a true friend.

Thank you. A special thank to Omri and Emilio. We shared a lot, they are people I can always trust and that gives me always good vibes. Part of this PhD is has been done because they have always been there for me. They deserve only the best. Thank you to Adrien, to our running days, to our parties and to our exchange. You are a true friend. Thank you to whom made my life in Paris less heavy: Martina, Dario and Julia. I loved exchanging with you and you were there in tough time, so thank you.

Thank you to my team. Thank you to Sonia. I cannot imagine all this trip without you. Thank you for the days, for the nights, for our infinite exchange for everything. You are awesome. Thank you to Josefina. For your smile, for your right words, for your bonheur. You deserve only the best. Thank you to Stefano. My copain de soirée before and de Neuilly after. Thank for the fun, for the run, for the days out. Thank you for your counsel and for letting me understand what does it mean arrive in late.

Thank you to Ruben. I cannot explain in words what bounded us together during these years. It is something you cannot explain. I can only say thank you for the moments passed together, for the days and nights in *Rat city*, for the crazy ideas, for the emotions. He is the most trust-worth person I ever met in my life and the most dedicated. He deserves only the best. "*Confondere i miei co'suoi sospir*" is said in "L'elisir d'amore", thus I dedicate this thesis to Marion, to her interest in what I was doing and to her unconditional love. For her patience, for my early morning alarms, for her will to take care of me also when she was tired. She deserves all the best.

"*L'amor che move il sole e l'altre stelle*" said Dante. I finish my acknowledgements section with my parents. They have always been there, supporting me, suffering with me. I know how hard it is to have a son away from home when he is the only son, or maybe it is better I don't know. It is because of this that I want to dedicate everything in my thesis to them. It is proof of my unconditional love, and a little thing I can do to thank them. They deserve this and more.

# Abstract

The more stringent regulation about aeronautical engines emission posed by ICAO requires always more predictive design tools. The droplets diameter distribution produced during the atomization process is a key parameter in order to predict the pollutant emission released during the combustion process. Thus the study of the atomization phenomenon with its multi-scale nature is a relevant and an important challenge.

For this reason the objective of this work are: first to review the existent models in the literature to understand their key features in order to define a classification that gives guidelines on the modeling choices; second to apply industrial oriented approaches on an aeronautical configuration, in order to propose an improvement of the available design tools.

A systematic classification of the models is done with respect to the length-scale considered to represent the interface characteristics. From this point of view, it is possible to distinguish two kinds of approaches: the separated phases representation and the mixed phases representation. The diffuse interface approaches belongs on the second category together with many other approaches, compressible and incompressible, that share the same characteristic: they considers a mixture that contains both phases.

An air-assisted liquid sheet configuration has been built to test different models in order to define a metric of comparison. Two different models using the sharp interface approach (*ARCHER* and *InterFoam*), two models using the diffuse interface approach (*CEDRE* and *ELSA*) and an hybrid model (*ICMelsa*) have been considered on this test case. A comparison on two parts, based on statistical quantities, has been proposed. A first part called "*classical study*", compare the first order statistics showing that all approaches lead to very similar results, as soon as certain level of mesh resolution is achieved. At the contrary the second order statics present noticeable differences. These results motivate a second part called "*phase analysis*" to study the link between the small scale representation of the interface and the second-order statics. In particular, the phase marker variance and the associated segregation level are found to be sensible indicators of the interface description. A 1D signal analysis shows that they can be used to detect any departure from the separated phases representation. Then the importance of the phase indicator variance is demonstrated on other second-order statistics: Reynolds stress components and turbulent liquid flux. Thus, second-order statistics are partly described with direct mixed phases representations and require complementary model to be fully recovered. A first attempt, based on a linear approach, is proposed to model the level of segregation of mixed phases representation. It is based on the filtering of a fully segregated signal at a given scale.

In a second part of this thesis, an industrial test case (a pressure swirling injector) proposed by *SAFRAN Aircraft Engines* is studied. Three industrial oriented models, among those studied in the first part, have been applied to simulate this injector flow (*InterFoam*, *ELSA*, *ICMelsa*). Their present numerical approaches are able to work with complex geometries, with a computational effort representative of the industrial current standards. The results of the three models (liquid film thickness, breakup length and Sauter Mean Diameter) have been

compared with respect to the available experimental data. Eventually, a proposal to improve the *ICMelsa* model multi-scale have been successfully tested on the liquid sheet configuration and implemented to further improve the results of the *SAFRAN Aircraft Engines* industrial case. These results have shown that we are very close to predict the characteristics of a spray produced by a real aeronautical injection system.

*Keywords:* multiphase, atomization, multi-scale, turbulence, interface, sharp interface, diffuse interface, mixed phases , separated phases .

# Resumé

La réglementation plus stricte sur les émissions des moteurs aéronautiques posée par l'OACI nécessite des outils de conception toujours plus prédictifs. La distribution des diamètres des gouttelettes produites pendant le processus de combustion est un paramètre clé pour prédire les émissions de polluants libérées pendant le processus de combustion. L'étude du phénomène d'atomisation avec son caractère multi-échelles est donc un défi pertinent et important.

Pour cette raison, les objectifs de cette étude sont: tout d'abord de passer en revue les modèles existants dans la littérature, pour comprendre leurs caractéristiques clés, afin de définir une classification qui donne des lignes directrices sur les choix de modélisation; deuxièmement, d'appliquer des approches plus compatibles avec les problématiques industrielles du secteur sur une configuration aéronautique, afin de proposer une amélioration des outils de conception disponibles. Une classification systématique des modèles est effectuée par rapport à l'échelle de longueur considérée pour représenter les caractéristiques de l'interface. De ce point de vue, il est possible de distinguer deux types d'approches: la représentation des phases séparées et la représentation des phases mixtes. Les approches diffuse interface appartiennent à la seconde catégorie avec de nombreuses autres approches, compressibles et incompressibles, qui partagent la même caractéristique: elles considèrent un mélange qui contient les deux phases. Une configuration de nappe de liquide assistée par air a été conçue pour tester différents modèles afin de définir une mesure de comparaison. Deux représentations différentes de l'approche sharp interface (*ARCHER* et *InterFoam*), deux représentations de l'approche diffuse interface (*CEDRE* et *ELSA*) et un modèle hybride (*ICMelsa*) ont été considérés dans cette étude. Une comparaison en deux parties basée sur des quantités statistiques a été proposée. Une première partie appelée "étude classique", compare les statistiques du premier ordre montrant que toutes les approches conduisent à des résultats très similaires dès qu'un certain niveau de résolution de maillage est atteint. Au contraire, les secondes statistiques présentent des différences notables. Ces résultats motivent une deuxième partie appelée «analyse de phase» pour étudier le lien entre la représentation à petite échelle de l'interface et la statique du second ordre. En particulier, la variance du marqueur de phase et le niveau de ségrégation associé se révèlent être des indicateurs sensibles de la description de l'interface. Une analyse de signal 1D montre qu'ils peuvent être utilisés pour détecter tout écart par rapport à la représentation des phases séparées, puis l'importance de la variance de l'indicateur de phase est démontrée sur d'autres statistiques de second ordre: les composantes de contrainte de Reynolds et le flux de liquide turbulent. Ainsi, les statistiques du second ordre sont partiellement décrites avec des représentations directes de phases mixtes et nécessitent un modèle complémentaire pour être entièrement récupérées. Une première tentative, basée sur une approche linéaire, est proposée pour modéliser le niveau de ségrégation de la représentation des phases mixtes, construit en filtrant un signal totalement ségrégué à une échelle donnée.

Dans une seconde partie de cette thèse, un cas de test industriel (un injecteur à pression tourbillonnante) proposé par *SAFRAN Aircraft Engines* est étudié. Trois modèles à vocation



industrielle, parmi ceux étudiés dans la première partie, ont été appliqués pour simuler ce flux d'injecteur (*InterFoam*, *ELSA*, *ICMelsa*). Leurs approches numériques actuelles sont capables de travailler avec des géométries complexes, avec un effort de calcul représentatif des normes industrielles actuelles. Les résultats des trois modèles (épaisseur du film liquide, longueur de rupture et Sauter Mean Diameter) ont été comparés par rapport aux données expérimentales disponibles. Enfin, une proposition d'amélioration du modèle multi-échelles *ICMelsa* a été testée avec succès sur la configuration de la nappe liquide et mise en œuvre pour améliorer encore les résultats du cas industriel des moteurs aéronautiques Safran. Ces résultats ont montré que nous sommes très proches de prédire les caractéristiques d'un spray produit par un véritable système d'injection aéronautique.

*Mots clés:* multiphase, atomisation, multi-échelle, turbulence, interface, interface diffuse, phases mixtes, phases séparées.

# Sommario

Le normative più rigorose sulle emissioni dei motori aeronautici poste dall'ICAO, richiedono strumenti di progettazione sempre più predittivi. La distribuzione dei diametri delle droplets prodotte durante il processo di atomizzazione è un parametro chiave per predire l'emissione di inquinanti rilasciati durante il processo di combustione. Lo studio del fenomeno di atomizzazione con la sua natura multi scala diventa una sfida rilevante.

Per questo motivo, gli obiettivi di questo lavoro sono: in primo luogo una revisione dei modelli esistenti in letteratura per comprenderne le caratteristiche chiave al fine di definire una classificazione che dia delle linee guida sulle scelte di modellistica; in secondo luogo applicare approcci orientati all'industria ad una configurazione aeronautica, al fine di proporre un miglioramento degli strumenti di progettazione disponibili al giorno d'oggi. Nella prima parte del PhD proponiamo una classificazione sistematica dei modelli rispetto alla scala di lunghezza considerata per rappresentare l'interfaccia. Da questo punto di vista, è possibile distinguere due tipi di approccio: una rappresentazione a fasi separate e una rappresentazione delle fasi miste. Gli approcci a interfaccia diffusa appartengono alla seconda categoria insieme a molti altri approcci (che ricorrano ad un approccio comprimibile o incomprimibile) che condividono la stessa caratteristica: considerano una miscela che contiene entrambe le fasi. È stata realizzata una configurazione *air-assisted liquid sheet* per testare diversi modelli al fine di definire una metrica di confronto. In questo caso per i test sono stati considerati due diversi modelli che utilizzano l'approccio *sharp interface* (*ARCHER* e *InterFoam*), due modelli che utilizzano l'approccio a interfaccia diffusa (*CEDRE* e *ELSA*) e un modello ibrido (*ICMelsa*). È stato proposto un confronto su due parti, basato su statistiche di diversa natura. Una prima parte chiamata "studio classico", confronta le statistiche del primo ordine, le quali mostrano che tutti gli approcci portano a risultati molto simili non appena viene raggiunto un certo livello di risoluzione della mesh. Al contrario, le statistiche di secondo ordine presentano notevoli differenze. Questi risultati motivano una seconda parte dello studio, chiamata "analisi di fase" sviluppata per studiare il legame tra le piccole scale dell'interfaccia e le statiche di secondo ordine. In particolare, la varianza del marker di fase e il livello di segregazione associato si trovano ad essere indicatori sensibili alla descrizione dell'interfaccia. Un'analisi di un segnale 1D mostra che questi due indicatori possono essere utilizzati per rilevare qualsiasi deviazione dalla rappresentazione a fasi separate. Successivamente l'importanza della varianza del marker di fase è dimostrata su altre statistiche di secondo ordine: componenti del tensore degli sforzi di Reynolds e flusso liquido turbolento. Pertanto, le statistiche di secondo ordine che sono descritte con una rappresentazione a fasi miste richiedono un modello complementare per essere completamente recuperate. Un primo tentativo, basato su un approccio lineare, è proposto per modellare il livello di segregazione della rappresentazione a fasi miste. Si basa sul filtraggio di un segnale completamente separato su una data scala.

In una seconda parte della tesi viene studiato un caso industriale (un iniettore di tipo swirling) proposto dall'azienda *SAFRAN Aircraft Engines*. Per simulare il flusso prodotto da questo iniettore sono stati applicati tre modelli (con un approccio industriale) tra quelli studiati nella

prima parte (*InterFoam* , *ELSA* , *ICMelsa* ). Tali approcci numerici sono in grado di lavorare con geometrie complesse, con un costo computazionale rappresentativo degli standard industriali attuali. I risultati dei tre modelli (spessore del film liquido, lunghezza di rottura del film e Sauter Mean Diameter) sono posti a confronto con i dati sperimentali disponibili. Una proposta per migliorare il modello multiscala *ICMelsa* è stata testata con successo sulla configurazione della prima parte del PhD, e implementata per migliorare ulteriormente i risultati del caso industriale di *SAFRAN Aircraft Engines* . Questi risultati hanno dimostrato che siamo molto vicini a prevedere le caratteristiche di uno spray prodotto da un sistema di iniezione aeronautica realistico.

*Parole chiave:* multifase, atomizzazione, multi-scala, turbolenza, interfaccia, sharp interface, interfaccia diffusa, fasi miste, fasi separate.

# Table of Contents

	Page
<b>1 Introduction</b> .....	<b>1</b>
1.1 Atomizers in the Aeronautical world	4
1.2 Atomization problem for pressure-swirl atomizers	5
1.3 Modeling the atomization problem	8
1.4 Outline of the thesis	9
<b>2 Numerical models</b> .....	<b>11</b>
2.1 Introduction	12
2.1.1 Numerical models and numerical methods .....	12
2.1.2 Typical model length-scales .....	12
2.2 Models classified by the length-scale analysis (LSA)	13
2.2.1 Flow description .....	13
2.2.2 Interface length-scales .....	14
2.2.3 Droplet length-scales .....	20
2.2.4 Flow dynamic instability length-scales .....	21
2.2.5 ELSA .....	25
2.2.6 Multi-scale modeling .....	28
2.2.7 ICM-ELSA .....	29
2.3 Map of the models	31
<b>3 Numerical models comparison: the air-assisted liquid sheet test case</b>	<b>35</b>
3.1 Modeling the interface	36
3.1.1 ARCHER .....	36
3.1.2 CEDRE .....	38
3.1.3 InterFoam .....	40
3.2 Physical model of sub-grid interface	43
3.2.1 ELSAFoam .....	43
3.2.2 ICMelsa Foam .....	44
3.3 Configuration	46
3.3.1 Bibliography about the air assisted liquid sheets .....	46
3.3.2 Building a benchmark configuration .....	47
3.3.3 Geometry and description of various meshes .....	48

<b>3.4</b>	<b>Metric of comparison</b>	<b>49</b>
<b>3.5</b>	<b>Statistical convergence</b>	<b>50</b>
<b>3.6</b>	<b>Region of validity of the results</b>	<b>52</b>
<b>3.7</b>	<b>Classical analysis</b>	<b>54</b>
3.7.1	Phenomenological observation	55
3.7.2	Averaged liquid volume fraction	60
3.7.3	Averaged velocities	62
3.7.4	Turbulent Kinetic Energy (TKE) and Reynolds stress components	64
<b>3.8</b>	<b>Conclusion</b>	<b>70</b>
<b>4</b>	<b>Phase analysis</b>	<b>71</b>
<b>4.1</b>	<b>The statistical tools</b>	<b>71</b>
<b>4.2</b>	<b>Analysis on 1D signal</b>	<b>72</b>
4.2.1	Fully segregated flow field	73
4.2.2	Not segregated flow field, diffuse interface	75
4.2.3	Probability of presence	77
<b>4.3</b>	<b>The phase marker variance</b>	<b>80</b>
4.3.1	Results	81
4.3.2	Conclusion about the phase marker variance analysis	89
<b>4.4</b>	<b>1D model</b>	<b>89</b>
<b>4.5</b>	<b>Conclusion and perspectives</b>	<b>91</b>
<b>5</b>	<b>Silvercrest</b>	<b>95</b>
<b>5.1</b>	<b>The pressure-swirl atomizer</b>	<b>96</b>
<b>5.2</b>	<b>Performance and Physical phenomena of a Pressure-Swirl atomizer</b>	<b>96</b>
5.2.1	Inside the swirling chamber	97
5.2.2	Outside the swirling chamber	103
<b>5.3</b>	<b>Silvercrest engine</b>	<b>106</b>
5.3.1	Experimental Campaign	107
<b>5.4</b>	<b>The numerical process</b>	<b>114</b>
5.4.1	Solving strategy	116
5.4.2	Meshing process	117
5.4.3	Simulation with interface capturing model	122
5.4.4	Simulation with ELSA model	131
5.4.5	Simulation with <i>ICMelsa</i> model	136
<b>5.5</b>	<b>Conclusion</b>	<b>143</b>
<b>6</b>	<b>Conclusion and perspectives</b>	<b>147</b>
<b>6.1</b>	<b>Conclusion</b>	<b>147</b>
<b>6.2</b>	<b>Perspectives</b>	<b>149</b>

---

<b>Appendices</b> .....	<b>167</b>
<b>A Computation of Gaussian curvature through an analytical method</b>	<b>169</b>
<b>A.1 Introduction</b>	<b>169</b>
<b>A.2 Theoretical framework</b>	<b>169</b>
<b>A.3 Validation</b>	<b>170</b>
A.3.1 Sphere .....	170
A.3.2 Ellipsis .....	172
<b>B <math>IRQ_{\Sigma}</math> parametric study</b> .....	<b>173</b>
<b>C Weak ergodicity</b> .....	<b>177</b>
<b>D Other phase analysis results</b> .....	<b>181</b>
<b>D.1 Turbulent liquid flux</b>	<b>181</b>



# List of Tables



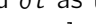
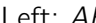

Table	Page
2.1 Table with the resume of the map of the models referred to fig. 2.9. Are represented some examples of models relative to the classification discussed along the chapter. . . . .	33
3.1 Dimensions and physical properties of the configuration. . . . .	48
3.2 Mesh statistics of the simulations. . . . .	49
3.3 Average time and convergence results for the database of simulations we have built	52
4.1 Percentage of the total time for which the signal is in one of the three states. . .	80
5.1 Properties of the Fuel and air used during the experimental campaign. . . . .	107
5.2 Different condition tested during the experimental campaign with the different performance indexes. . . . .	111
5.3 Sauter Mean Diameter ( $D_{32}$ ) data at different flow rate inlet conditions $\dot{m}_L$ . The tests are made at the same condition of the table 5.1. . . . .	112
5.4 Characteristics of the meshes A, B, C . . . . .	119
5.5 characteristics of the mesh D . . . . .	120
5.6 Boundary condition assigned at the different boundary patch. . . . .	121



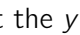

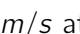
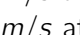





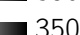














# List of Figures




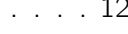
Figure	Page
1.1 Scheme of a jet engine, courtesy of <i>SAFRAN Aircraft Engines</i> . ① the fan, ② low pressure compressor stages, ③ high pressure compressor stages, ④ combustion chamber, ⑤ high pressure turbine stages, ⑥ low pressure turbine stages, ⑦ outlet. . . . .	1
1.2 Simplified scheme of the <i>Sam 146</i> engine's fuel system, courtesy of <i>SAFRAN Aircraft Engines</i> . ① Fuel pumps. The first one volumetric, the second one gear pump, ② heat exchanger, ③ filter, ④ FMU, ⑤ actuators actuated by servo-valves, ⑥ lines to the injectors. . . . .	3
1.3 Example of two different injection technologies in aeronautical engines. On the left an air-assisted injector, on the right an aero-mechanic injector With the courtesy of <i>SAFRAN Aircraft Engines</i> . . . . .	4
1.4 On the left:conceptual scheme of a TAPS atomizer took from [SB13]. On the right:Scheme of a PERM atomizer took from [And+15]. . . . .	5
1.5 Graphical representation of the progression of the different atomization phases with respect to the injection pressure. [LM88] . . . . .	7
1.6 Shadowgraph of the progression of the different atomization phases with respect to the injection pressure. For a graphical representation refer to fig. 1.5. [LM88] . . . . .	8
1.7 Review of the possible <i>multi-phase</i> flow modeling approach it is possible to find in literature. Review done in [MJD17] . . . . .	9
2.1 Shadowgraph of the atomization process encountered with the <i>Silvercrest</i> injector studied in chapter 5. The typical reference length-scales are reported. $\lambda_1$ is the injector length-scale, $\lambda_2$ is the flow dynamic instability length-scale, $\lambda_3$ is the droplets length-scale. On the bottom part of the subdivision of the atomization domain is showed, following [LM88]. . . . .	12
2.2 The thickness of the liquid-vapour interface versus the reduced liquid temperature as predicted from molecular dynamics simulation showed in [XSC11]. . . . .	14
2.3 Figure represents schematically the part of the flow that is resolved, here all scales greater than the physical interface thickness. The different length-scales refer to fig. 2.1. . . . .	15
2.4 Graphical explanation of the separated phases modeling approach. On the left an instantaneous of a simulation of an air-assisted liquid sheet, using the separated phases approach, on the right the plot of the phase marker function $\alpha$ across the interface. . . . .	17
2.5 Graphical explanation the mixed phases modeling approach. On the left an instantaneous of a simulation of an air-assisted liquid sheet, using the diffuse interface approach, on the right the plot of the phase marker $\alpha$ across the interface.	18

2.6	The figure represent schematically the part of the flow that is resolved, here all scales greater than the droplet dimension. The different length-scales refer to fig. 2.1. . . . . .	20
2.7	The figure represent schematically the part of the flow that is resolved, here all scales greater than the flow dynamic instability length-scale. The different length-scales refer to fig. 2.1. . . . . .	21
2.8	Given the computational grid, on the left the interface reconstruction provides a certain $\Sigma_{min}$ , on the right the real interface $\Sigma$ . The difference of area is $\Sigma'$ . . .	30
2.9	Map of the modeling possibilities for the atomization problem. The 2 dimensional modeling space couples the modeling length scales chosen and the type of interface modeling chosen. $\square$ represents the compressible flow models and the $\circ$ the incompressible flow ones. In table 2.1 the reference to the different point represented in the modeling space. . . . . .	33
3.1	Flow chart of the step for the solution of the incompressible multiphase system issued by an interface compression model inside the <i>InterFoam</i> solver. . . . . .	43
3.2	Flow chart of the step for the solution of the incompressible multiphase system issued by the ELSA model inside the <i>ElsaFoam</i> solver. . . . . .	44
3.3	Flow chart of the step for the solution of the incompressible multiphase system issued by the ICM model inside the <i>ICMElsaFoam</i> solver. . . . . .	45
3.4	Instabilities that brings to the film disintegration in an air assisted liquid sheet configuration [CHS02]. . . . . .	47
3.5	Geometry of the configuration. . . . . .	48
3.6	Evolution of the parameter $\epsilon$ for the <i>ARCHER</i> simulation. . . . . .	51
3.7	<i>IRQ<sub>k</sub></i> PDF analysis at time $t = 12 ms$ (bottom), in two regions identified by the red dashed rectangles drawn on the plan $y^* = 0$ showing liquid volume fraction $\alpha_l$ (top). . . . . .	53
3.8	Istantaneous picture of the flapping liquid sheet. On the left CEDRE(HR) simulation. The colorscale goes from low levels of $\alpha_l$ (blue) to high levels (red). On the right <i>ARCHER</i> simulation. The iso-contour represents the 0 iso-value of the <i>level-set distance function</i> . . . . . .	55
3.9	Transient evolution of the plane $y^* = 0$ of liquid volume fraction near the injector, $\alpha_l = 0$  1. Left: <i>ARCHER</i> , right: CEDRE. We define $t_0$ as the starting time and $\delta t$ as the progression time step. The window showed is in the range $x^* = [0, 5.5]$ . . . . . .	56
3.10	Transient evolution of the plane $y^* = 0$ liquid volume fraction near the injector, $\alpha_l = 0$  1. Left: <i>ARCHER</i> , right: <i>InterFoam</i> . We define $t_0$ as the starting time and $\delta t$ as the progression time step. The window showed is in the range $x^* = [0, 5.5]$ . . . . . .	57
3.11	Transient evolution of the plane $y^* = 0$ liquid volume fraction near the injector, $\alpha_l = 0$  1. Left: <i>ARCHER</i> , right: <i>ELSA</i> . We define $t_0$ as the starting time and $\delta t$ as the time step. The window showed is in the range $x^* = [0, 5.5]$ . . . . . .	58
3.12	Transient evolution of the plane $y^* = 0$ of liquid volume fraction near the injector, $\alpha_l = 0$  1. Left: <i>ARCHER</i> , right: <i>ICMelsa</i> . We define $t_0$ as the starting time and $\delta t$ as the time step. The window showed is in the range $x^* = [0, 5.5]$ . . . . . .	58
3.13	Transient evolution of the plane $y^* = 0$ of liquid volume fraction near the injector, $\alpha_l = 0$  1. Left: <i>InterFoam</i> , center: <i>ICMelsa</i> , right: <i>ELSA</i> . We define $t_0$ as the starting time and $\delta t$ as the time step. The window showed is in the range $x^* = [0, 5.5]$ . . . . . .	59


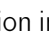


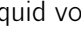







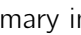
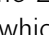
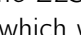
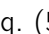
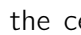



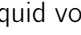


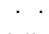
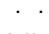



3.14	Averaged liquid volume fraction isolines ${}^t\bar{\alpha}_l = 0.1$  1 at the $y^* = 0$ plane. Dashed lines located at $x^* \in \{1, 2, 3\}$ .	60
3.15	Averaged liquid volume fraction isolines ${}^t\bar{\alpha}_l = 0.1$  1 at the $y^* = 0$ plane. Dashed lines located at $x^* \in \{1, 2, 3\}$ .	60
3.16	Averaged liquid volume fraction $\bar{\alpha}_l$ along streamwise axis. — ARCHER , ----- CEDRE (HR), ---- CEDRE (MR), ..... InterFoam , ..... ELSA , ----- ICMelsa .	61
3.17	Averaged liquid volume fraction $\bar{\alpha}_l$ along fig. 3.14 and fig. 3.15 dashed lines. — ARCHER , ----- CEDRE (HR), ---- CEDRE (MR), ..... InterFoam , ..... ELSA ----- ICMelsa . Reader must take care to the fact that the $\bar{\alpha}_l$ range is different for the three slices.	62
3.18	Averaged axial velocity ${}^t\bar{v}_x = 0$  70 m/s at the $y^* = 0$ plane.	63
3.19	Averaged axial velocity ${}^t\bar{v}_x = 0$  70 m/s at the $y^* = 0$ plane.	63
3.20	Averaged axial velocity $\bar{v}_x$ along fig. 3.14 and fig. 3.15 dashed lines. — ARCHER , ----- CEDRE (HR), ---- CEDRE (MR), ..... InterFoam , ..... ELSA , ----- ICMelsa .	63
3.21	Averaged transversal velocity ${}^t\bar{v}_z = -3$  3 m/s at the $y^* = 0$ plane.	64
3.22	Averaged transversal velocity ${}^t\bar{v}_z = -3$  3 m/s at the $y^* = 0$ plane.	64
3.23	Averaged transversal velocity $\bar{v}_z$ along Figure fig. 3.14 and fig. 3.15 dashed lines. — ARCHER , ----- CEDRE (HR), ---- CEDRE (MR), ..... InterFoam , ..... ELSA , ----- ICMelsa .	64
3.24	Turbulent Kinetic Energy (TKE) $1/2\overline{v'_i v'_i} = 0$  380 $m^2/s^2$ at the $y^* = 0$ plane.	65
3.25	Turbulent Kinetic Energy (TKE) $1/2\overline{v'_i v'_i} = 0$  380 $m^2/s^2$ at the $y^* = 0$ plane.	65
3.26	Turbulent Kinetic Energy (TKE) $(1/2)\overline{v'_i v'_i}$ along Figure fig. 3.14 and fig. 3.15 dashed lines. — ARCHER , ----- CEDRE (HR), ---- CEDRE (MR), ..... InterFoam , ..... ELSA , ----- ICMelsa .	65
3.27	Reynolds stress tensor component ${}^t\overline{v'_x v'_x} = 0$  350 $m^2/s^2$ at the $y^* = 0$ plane.	67
3.28	Reynolds stress tensor component ${}^t\overline{v'_x v'_x} = 0$  350 $m^2/s^2$ at the $y^* = 0$ plane.	67
3.29	Reynolds stress tensor component $\overline{v'_x v'_x}$ along fig. 3.14 and fig. 3.15 dashed lines. — ARCHER , ----- CEDRE (HR), ---- CEDRE (MR), ..... InterFoam , ..... ELSA , ----- ICMelsa .	67
3.30	Reynolds stress tensor component ${}^t\overline{v'_z v'_z} = 0$  350 $m^2/s^2$ at the $y^* = 0$ plane.	68
3.31	Reynolds stress tensor component ${}^t\overline{v'_z v'_z} = 0$  350 $m^2/s^2$ at the $y^* = 0$ plane.	68
3.32	Reynolds stress tensor component $\overline{v'_z v'_z}$ along fig. 3.14 and fig. 3.15 dashed lines. — ARCHER , ----- CEDRE (HR), ---- CEDRE (MR), ..... InterFoam , ..... ELSA , ----- ICMelsa .	68
3.33	Reynolds stress tensor component ${}^t\overline{v'_z v'_x} = -150$  150 $m^2/s^2$ at the $y^* = 0$ plane.	69
3.34	Reynolds stress tensor component ${}^t\overline{v'_z v'_x} = -150$  150 $m^2/s^2$ at the $y^* = 0$ plane.	69
3.35	Reynolds stress tensor component $\overline{v'_z v'_x}$ along fig. 3.14 and fig. 3.15 dashed lines. — ARCHER , ----- CEDRE (HR), ---- CEDRE (MR), ..... InterFoam , ..... ELSA , ----- ICMelsa .	69
4.1	Localisation of the point ( + ) used to extract the 1D signal of the phase marker $\alpha$ . Here, the phase marker field is extracted from the level-set distance function.	72

4.2	Signal of the level-set distance function sign at a probe placed at $(L_x/6, L_y/2, L_z/2)$ in the domain. The interval taken is from 8[ms] to 11[ms]. . . . .	73
4.3	PDF ( $f(\alpha)$ ) of the level-set distance function Heaviside function $\mathcal{H}(\phi)$ at a probe placed at $(L_x/6, L_y/2, L_z/2)$ in the domain. The time range extends from 3.8 to 30[ms]. Bins interval is of $\Delta\alpha_{bins} = 0.02$ , and hence $n.bins = 50$ . . . . .	74
4.4	CDF ( $\mathcal{C}(\alpha)$ ) of the level-set distance function Heaviside function $\mathcal{H}(\phi)$ at a probe placed at $(L_x/6, L_y/2, L_z/2)$ in the domain. The time range extends from 3.8 to 30[ms]. Bins interval is of $\Delta\alpha_{bins} = 0.02$ , and hence $n.bins = 50$ . . . . .	74
4.5	Signal of the liquid volume fraction at a probe placed at $(L_x/6, L_y/2, L_z/2)$ in the domain. The time interval is taken from 8[ms] to 11[ms]. . . . .	76
4.6	PDF ( $f(\alpha)$ ) of the liquid volume fraction at a probe placed at $(L_x/6, L_y/2, L_z/2)$ in the domain. The time interval is taken from 3.8 to 30[ms]. Bins interval is of $\Delta\alpha_{bins} = 0.02$ . . . . .	76
4.7	CDF ( $\mathcal{C}(\alpha)$ ) of the liquid volume fraction at a probe placed at $(L_x/6, L_y/2, L_z/2)$ in the computational domain. The time interval is taken from 3.8 to 30[ms]. The transitory has been considered in the range $[0[ms], 3.8[ms]]$ . On the background a zoom of the probability density function $f(\alpha)$ is reported. Bins interval is of $\Delta\alpha_{bins} = 0.02$ . . . . .	77
4.8	Liquid time interval PDF ( $f(\Delta t)$ ) on the left and CDF ( $\mathcal{C}(\Delta t)$ ) on the right for a segregated signal similar to fig. 4.2. . . . .	78
4.9	Gas time interval PDF ( $f(\Delta t)$ ) on the left and CDF on the right for a segregated signal similar to fig. 4.2. . . . .	79
4.10	Liquid time interval PDF ( $f(\Delta t)$ ) on the left and CDF ( $\mathcal{C}(\Delta t)$ ) on the right for a not segregated signal similar to fig. 4.5. . . . .	79
4.11	Gas time interval PDF ( $f(\Delta t)$ ) on the left and CDF ( $\mathcal{C}(\Delta t)$ ) on the right for a not segregated signal similar to fig. 4.5. . . . .	79
4.12	Liquid volume fraction variance $\overline{\alpha'_l \alpha'_l} = 0$  0.250 at the $y^* = 0$ plane. . . . .	82
4.13	Liquid volume fraction variance $\overline{\alpha'_l \alpha'_l} = 0$  0.250 at the $y^* = 0$ plane. . . . .	82
4.14	Liquid volume fraction variance $\overline{\alpha'_l \alpha'_l}$ along Figure fig. 3.14 and fig. 3.15 dashed lines. — ARCHER, - - - - CEDRE (HR), - . - . CEDRE (MR), - . . . interFoam, - . . . ELSA, - - - - ICMelsa . . . . .	82
4.15	Phase marker variance for the ARCHER code using $\alpha_{VOF}$ . 0  0.250 at plane $y^* = 0$ . On the left the representation of the variance field, on the right the representation of the variance computed in the segregated way. . . . .	83
4.16	Phase marker variance for the ARCHER code using $\alpha_{LS}$ . 0  0.250 at the $y^* = 0$ plane. On the left the representation of the variance field, on the right the representation of the variance computed in the segregated way. . . . .	83
4.17	Phase marker variance computed using the $\alpha_{VOF}$ along slices at $x^* = 1, 2, 3$ . — $\overline{\alpha_{VOF}}(1 - \overline{\alpha_{VOF}})$ , - - - - $\overline{\alpha'_{VOF} \alpha'_{VOF}}$ , - . . . residual difference. . . . .	84
4.18	Phase marker computed using the $\alpha_{LS}$ along slices at $x^* = 1, 2, 3$ . — $\overline{\alpha_{LS}}(1 - \overline{\alpha_{LS}})$ , - - - - $\overline{\alpha'_{LS} \alpha'_{LS}}$ , - . . . residual difference. . . . .	84
4.19	Liquid volume fraction variance for the <i>InterFoam</i> model. 0  0.250 at plane $y^* = 0$ . On the left the representation of the variance field, on the right the representation of the variance computed in the segregated way. . . . .	85
4.20	Liquid volume fraction variance for the <i>interFoam</i> model along slices at $x^* = 1, 2, 3$ . — $\overline{\alpha_l}(1 - \overline{\alpha_l})$ , - - - - $\overline{\alpha'_l \alpha'_l}$ , - . . . residual difference. . . . .	85
4.21	Liquid volume fraction variance for the <i>ICMelsa</i> model. 0  0.250 at plane $y^* = 0$ . On the left the representation of the variance field, on the right the representation of the variance computed in the segregated way. . . . .	86

4.22	Liquid volume fraction variance for the <i>ICMelsa</i> model along slices at $x^* = 1, 2, 3$ . — $\overline{\alpha}_l(1 - \overline{\alpha}_l)$ , ..... $\overline{\alpha}'_l\alpha'_l$ , ..... residual difference. . . . .	86
4.23	Liquid volume fraction variance for the <i>ELSA</i> model. 0  0.250 at plane $y^* = 0$ . On the left the representation of the variance field, on the right the representation of the variance computed in the segregated way. . . . .	87
4.24	Liquid volume fraction variance for the <i>ELSA</i> model along slices at $x^* = 1, 2, 3$ . — $\overline{\alpha}_l(1 - \overline{\alpha}_l)$ , ..... $\overline{\alpha}'_l\alpha'_l$ , ..... residual difference. . . . .	87
4.25	Liquid volume fraction variance for the <i>CEDRE</i> model with the HR mesh. 0  0.250 at plane $y^* = 0$ . On the left the representation of the variance field, on the right the representation of the variance computed in the segregated way. . . . .	88
4.26	Liquid volume fraction variance for the <i>CEDRE</i> model along slices at $x^* = 1, 2, 3$ with the HR mesh. — $\overline{\alpha}_l(1 - \overline{\alpha}_l)$ , ..... $\overline{\alpha}'_l\alpha'_l$ , ..... residual difference. . . . .	88
4.27	The convoluted signal using the kernel represented in eq. (4.24) of the level-set distance function signal in fig. 4.2 at a probe placed at $(L_x/6, L_y/2, L_z/2)$ in the domain. On the left: interval taken is from 8[ms] to 11[ms]. On the right: zoom on one transition. . . . .	90
4.28	Results of the segregation ( $S$ ) of the convoluted phase marker with respect to the linear model for different $\lambda$ . ..... Completely segregated signal, — Ideal linear model, • convoluted signal values. . . . .	91
4.29	Snapshot of the sign level-set distance function for the <i>ARCHER</i> simulation. The red cross + indicates the point in which the 1D signal has been extracted for the analysis proposed in this chapter, the blue crosses + represent the location of the probes for the future analysis. . . . .	93
5.1	Important quantities characterizing the flow field outside the pressure-swirl atomizer from [LM88]. . . . .	96
5.2	Schematic representation of the simplex swirl atomizer ([RL85]). $D_p$ represents the diameter of a single circular inlet port, $L_p$ represents the length of the inlet port, $L_s$ represents the width of the swirling chamber sky, $D_s$ represents the diameter of the swirling chamber sky, $d_0$ represents the diameter of the outlet orifice, $l_0$ represents the length of the outlet orifice throat, $2\theta$ represents the double of the cone angle created by the discharged liquid sheet. . . . .	98
5.3	Shadowgraphy of a jet with the rim disintegration mode ([ARA11]). . . . .	103
5.4	Shadowgraphy of a jet with the wave disintegration mode ([Dum05]). . . . .	104
5.5	Shadowgraphy of a jet with the perforated hole disintegration mode ([MD01]). . . . .	104
5.6	picture of the <i>Silvercrest</i> engine. . . . .	106
5.7	<i>Silvercrest</i> 's front view of the combustion chamber with the highlight on the injectors and on the spark plugs. . . . .	107
5.8	Slice of the <i>Silvercrest</i> injector with reference names. With $l_1$ we denote the diameter of the inlet, with $d_0$ the diameter of the throat of the swirling chamber, with $t$ the liquid film thickness. . . . .	108
5.9	Slice of the <i>Silvercrest</i> C42 injector. In is possible to observe the primary injector covered by the injector cap. . . . .	109
5.10	Representation of the variation of the Sauter mean diameter ( $D_{32}$ ) with respect to to the mass flow rate ( $\dot{m}_L$ ) for the <i>Silvercrest</i> engine's atomizer with the fuel properties reported in table 5.1. The detection point is placed at 20[mm]. . . . .	112

5.11	Critical condition graph for the aircraft's engine during the admissible flight path, defined by analysing the aerodynamic performance, the engine performances, the structure performances and the load factor. . . . .	113
5.12	On the left: illustration of the Kelvin-Helmoltz instability and spiral mode happening in the swirling injection by [BCH98]. On the right: Shadowgraphy of the <i>Silvercrest</i> at the re-light point. . . . .	114
5.13	Flow chart of the plan of the numerical study. . . . .	116
5.14	Clip of the entire C42 duplex injector of the <i>Silvercrest</i> engine produced by <i>SAFRAN Aircraft Engines</i> . . . . .	117
5.15	Slice of the geometry at the level of the primary injector entrance. It is possible to observe the crown that brings to the inlet of the injector. The arrows indicates the direction of the flow of JP5 fuel. . . . .	117
5.16	Slice of the <i>Silvercrest</i> 's primary injector's domain at the level of the inlet. . . . .	118
5.17	Zoom of the outlet patch of the injector. A clear improvement is observed in the C configuration. . . . .	119
5.18	z-normal slice of the mesh D. On the left representation of the connection among the primary injector and the outside environment. On the right representation of the throat and final part of the primary injector. . . . .	120
5.19	Side view of the computational domain, marked with numbers to define the different boundary patch. ② : inlet, ① : air, ① : wall near the outlet and injector wall. For the boundary condition associated evaluate the table 5.6. . . . .	121
5.20	Top view of the computational domain, marked with number to define the different boundary patch. On the left: top view of the primary injector. ② : inlet, ① : wall of the primary injector. On the right: top view of the external domain simulating the external environment. ① : air, ① : wall near the outlet of the injector. . . . .	121
5.21	Snapshot of the eddy viscosity $\nu_t$ in the computational domain. $\nu_t = 0[m^2/S]$  $1.1 \cdot 10^{-5}[m^2/s]$ . . . . .	122
5.22	Contour plot of the iso-surface defined by liquid volume fraction $\alpha_l = 0.3$ of the <i>Silvercrest</i> primary injector. Startup phase on the mesh C. On the bottom left we can see the shadow of the liquid volume fraction . . . . .	124
5.23	Contour plot of the iso-surface defined by liquid volume fraction $\alpha_l = 0.3$ of the <i>Silvercrest</i> primary injector. Startup phase on the mesh C. On the bottom left we can see the shadow of the liquid volume fraction . . . . .	124
5.24	Maximum pressure at the patch ② , with mesh C. . . . .	124
5.25	On the left: Contour plot of the iso-surface defined by liquid volume fraction $\alpha_l = 0.3$ of the <i>Silvercrest</i> primary injector. On the right: Contour plot of the iso-surface defined by liquid volume fraction $\alpha_l = 0.8$ of the <i>Silvercrest</i> primary injector. . . . .	125
5.26	On the left: Volume rendering of the liquid volume fraction field at $t = 14.5[ms]$ , $\alpha_l = 0$  1. The arrows point to the two main instabilities features. On the right: snapshot of the shadowgraphy of the <i>Silvercrest</i> injector at the re-light point . . . . .	126
5.27	On the left: side view of the time averaged liquid volume fraction , ${}^t\bar{\alpha}_l = 0$  1. On the right: view of the time averaged liquid volume fraction at the injector exit plane ${}^t\bar{\alpha}_l = 0$  1. ----- Line A, ----- line B. . . . .	127
5.28	Plot of the time averaged liquid volume fraction ${}^t\bar{\alpha}_l$ along the two lines defined in fig. 5.27. — line A, — line B, ----- the empirical value. Distance are adimensionalized by the diameter of the injector $D$ . . . . .	127





5.29	On the left: snapshot of the shadowgraphy of the <i>Silvercrest</i> injector at the re-light point. On the right: Contour plot of the liquid volume fraction iso-surface defined by $\alpha_l = 0.3$ of the <i>Silvercrest</i> simulation. . . . .	129
5.30	On the left: snapshot of the shadowgraphy of the <i>Silvercrest</i> injector at the re-light point. On the right: volume rendering plot of the <i>Silvercrest</i> . Liquid volume fraction field. $\alpha_l = 0$  1. . . . .	129
5.31	On the left: rendering of the <i>InterFoam</i> liquid volume fraction field, and in dashed blue  the location in which we collect the $D_{32}$ values. $\alpha_l = 0$  1. On the right: plot of the $D_{32}$ value post processed following the formulation proposed in eq. (5.48). In  the experimental value at $y^* \approx 33$ . . . . .	131
5.32	Volume rendering of the liquid volume fraction field at $t = 14.5[ms]$ , $\alpha_l = 0$  1.	133
5.33	On the left: side view of the time averaged liquid volume fraction , $\overline{\alpha_l} = 0$  1. On the right: view of the time averaged liquid volume fraction at the outlet $\overline{\alpha_l} = 0$  1 and lines of where the liquid film thickness is evaluated. The averaging time is $\Delta t_{avg} = 2[ms]$ starting from $t_0 = 12[ms]$ .  Line A,  line B. . . . .	134
5.34	Plot of the time averaged liquid volume fraction $\overline{\alpha_l}$ for the two lines defined on fig. 5.27.  line A,  line B,  the empirical value Length scale are adimensionalized by the diameter of the injector $D$ . . . . .	134
5.35	On the left: snapshot of the shadowgraphy of the <i>Silvercrest</i> injector at the re-light point. On the right: Contour plot of the $\alpha_l = 0.3$ of the <i>Silvercrest</i> primary injector. . . . .	135
5.36	On the left: snapshot of the shadowgraphy of the <i>Silvercrest</i> injector at the re-light point. On the right: volume rendering plot of the liquid volume fraction field of the <i>Silvercrest</i> primary injector. $\alpha_l = 0$  1. . . . .	135
5.37	On the left: rendering of the <i>ELSA</i> liquid volume fraction field, and in dashed blue  the location in which we collect the $D_{32}$ values. $\alpha_l = 0$  1. On the right: On the right: plot of the $D_{32}$ value post processed following the formulation proposed in eq. (5.50). In  the experimental value at $y^* \approx 33$ . . . . .	136
5.38	On the left: slice of the domain presented in chapter 3, liquid volume fraction field. $\alpha_l = 0$  1. On the center: Field of $C_\alpha$ before the modification proposed. $C_\alpha = 0$  1. On the right: Field of $C_\alpha$ after the modification proposed. $C_\alpha = 0$  1. . . . .	138
5.39	On the left: slice of the minimum interface area computed as the magnitude of the gradient of the liquid volume fraction ([Pal21]). On the right: slice of the minimum interface area computed as defined in [Che10]. $\Sigma_{min} = 0[1/m]$  $7 \cdot 10^3[1/m]$ . . . . .	138
5.40	Volume rendering of the liquid volume fraction field at $t = 14.5[ms]$ , $\alpha_l = 0$  1.	139
5.41	On the left: side view of the time averaged liquid volume fraction , $\overline{\alpha_l} = 0$  1. On the right: view of the time averaged liquid volume fraction at the outlet $\overline{\alpha_l} = 0$  1 and lines where the liquid film thickness is evaluated.  Line A,  line B. . . . .	140
5.42	Plot of the time averaged liquid volume fraction $\overline{\alpha_l}$ along lines defined in fig. 5.27.  line A,  line B,  the empirical value. The length are adimensionalized by the diameter of the injector $D$ . . . . .	140
5.43	On the left: snapshot of the shadowgraphy of the <i>Silvercrest</i> injector at the re-light point. On the right: Contour plot of the liquid volume fraction field $\alpha_l = 0.3$ of the <i>Silvercrest</i> primary injector. . . . .	141



5.44	On the left: snapshot of the shadowgraphy of the <i>Silvercrest</i> injector at the re-light point. On the right: volume rendering plot of the liquid volume fraction field $\alpha_l$ . . . . .	141
5.45	On the left: rendering of the <i>ICMelsa</i> liquid volume fraction field, and in dashed blue $\alpha_l = 0$ the location in which we collect the $D_{32}$ values. $\alpha_l = 1$ . On the right: plot of the $D_{32}$ value post processed following the formulation proposed in eq. (5.50). In $y^* \approx 33$ . . . . .	143
5.46	Plot of the time averaged liquid volume fraction $\overline{\alpha_l}$ for the different models presented in the chapter. . . . .	145
5.47	Volume rendering of the liquid volume fraction field. . . . .	145
5.48	Plot of the $D_{32}$ value post processed following the formulation proposed in eq. (5.50) and eq. (5.49). . . . .	145
A.1	Domain of computation for the test of the curvature algorithm on a sphere. On the left the 0 iso-surface of the level-set function, on the right a slice of the field with the shadow of the level-set distance function 0 iso-surface. . . . .	171
A.2	Relative error trend for the two Gaussian curvature on the surface of the sphere ( — $H$ , — $G$ ). The $L1$ relative error has been computed with the formulation in eq. (A.14) and eq. (A.13). . . . .	171
A.3	Slice of the domain for the ellipsis test case with distance function iso-contour and shaded 0 iso-surface. . . . .	172
A.4	Relative error changing for the two Gaussian curvature on the surface of the ellipsis ( — $H$ , — $G$ ). The $L1$ relative error has been computed with the formulation in eq. (A.14) and eq. (A.13). . . . .	172
B.1	On the left: liquid volume fraction surface plot of a snapshot of the box configuration defined along the thesis. $\alpha_l = 0$ to $1$ . On the right: $IRQ_\Sigma$ surface plot, on the clipped field of liquid volume fraction $\alpha_l \in [0.1, 1]$ . . . . .	174
B.2	The $C_\alpha$ field with varying $IRQ$ limit $IRQ_{\Sigma,lim}$ . In black $C_\alpha = 1$ , in white $C_\alpha = 0$ . On the left: $IRQ_{\Sigma,lim} = 0.5$ . On the right: $IRQ_{\Sigma,lim} = 0.55$ . For the $\alpha_l$ field, refer to fig. B.1a. . . . .	174
B.3	The $C_\alpha$ field with varying $IRQ$ limit $IRQ_{\Sigma,lim}$ . In black $C_\alpha = 1$ , in white $C_\alpha = 0$ . On the left: $IRQ_{\Sigma,lim} = 0.65$ . On the right: $IRQ_{\Sigma,lim} = 0.75$ . For the $\alpha_l$ field, refer to fig. B.1a. . . . .	175
C.1	Moving average $\overline{\alpha_l}$ taking as a phase marker the level-set distance function. $t$ is the dimension of the averaging window starting from $t_0 = 3.8[ms]$ . . . . .	177
C.2	Autocorrelation function for the time interval $[3.8[ms], 30[ms]]$ with $t_0 = 3.8[ms]$ . . . . .	178
C.3	Autocorrelation function for the time window A. Time interval $[10[ms], 20[ms]]$ , $t_0 = 10[ms]$ . . . . .	178
C.4	Autocorrelation function for the time window B. Time interval $[20[ms], 30[ms]]$ , $t_0 = 20[ms]$ . . . . .	179
D.1	Liquid volume fraction contour with over imposed the liquid volume fraction dispersion. In red the scaled $\overline{\alpha_l}$ and in green the scaled $\overline{\alpha_l}$ . . . . .	181
D.2	$z^*$ component of the turbulent liquid flux $\overline{v'_z \alpha'_l} = -1.5$ to $1.5[m/s]$ at the $y^* = 0$ plane. . . . .	182
D.3	$z^*$ component of the turbulent liquid flux $\overline{v'_z \alpha'_l} = -1.5[m/s]$ to $1.5[m/s]$ at the $y^* = 0$ plane. . . . .	182

---

D.4	$z^*$ component of the turbulent liquid flux $\overline{v'_z \alpha'_l}$ along $x^* = 1, 2, 3$ . — ARCHER, ..... CEDRE (HR), ..... CEDRE (MR), ..... <i>InterFoam</i> , ..... <i>ELSA</i> , ..... <i>ICMelsa</i> . . . . .	183
D.5	Streamwise turbulent liquid flux $\overline{v'_x \alpha'_l} = -2$  $2[m/s]$ at the $y^* = 0$ plane. . . . .	183
D.6	Streamwise turbulent liquid flux $\overline{v'_x \alpha'_l} = -2$  $2[m/s]$ at the $y^* = 0$ plane. . . . .	183
D.7	Streamwise turbulent liquid flux $\overline{v'_x \alpha'_l}$ along fig. 3.14 and fig. 3.15 dashed lines. — ARCHER, ..... CEDRE (HR), ..... CEDRE (MR), ..... <i>InterFoam</i> , ..... <i>ELSA</i> , ..... <i>ICMelsa</i> . . . . .	184



# List of Symbols

$D_{ab}$	Mean or averaged $ab$ diameter
$C_\alpha$	Sharpening constant
$C_D$	Discharge coefficient
$CFL$	CFL number
$\bar{\cdot}_{ _{\text{test}}}$	Conditional average operator with condition test
$\rho$	Density
$\epsilon_f$	Dissipation due to the filtered field
$\nu_t$	Eddy Viscosity
$\langle \cdot \rangle$	Ensemble averaging
$\Sigma_{eq}$	Equilibrium surface area density
$\tau_{eq}$	Equilibrium time-scale
$We^*$	Equilibrium Weber number
$\Delta$	LES filter width
$E_f$	Filtered energy
$FN$	Flow number
$\dot{m}_L$	Liquid mass flow rate
$\Sigma'$	Sub-grid interface area density
$G$	Gauss curvature
$\mathbb{I}$	Identity matrix
$\Sigma$	Interface area density
$e$	Internal energy
$IRQ$	Interface resolution quality
$K_V$	Velocity coefficient
$\lambda$	length-scale

---

$H$	Mean curvature
$\Sigma_{min}$	Minimum interface area density
$M$	Momentum ratio
$Oh$	Ohnesorge number
$\alpha$	Phase marker
$p$	Pressure
$k_1, k_2$	Principal curvatures
$P_r$	Rate of production of residual kinetic energy
$Re$	Reynolds number
$k_r$	Residual kinetic energy
$Sc_t$	Turbulent Schmidt number
$S$	Segregation factor
$\tau^R$	Sub-grid stress tensor
$\mathbf{U}_r$	Sharpening velocity of the <i>InterFoam</i> model
$\mathbf{S}$	Shear stress
$\sigma$	Surface tension
$C_S$	Smagorinsky constant
$Sw$	Swirling number
$\overline{\cdot}$	Time averaging
$\lambda_g$	Taylor length-scale
$E$	Total energy
$k$	Turbulent kinetic energy
$\mathbf{R}_{\alpha_l}$	Turbulent liquid flux
$y^+$	Distance in wall units
$\mathbf{v}$	Velocity
$\mu$	Dynamic viscosity
$\nu$	Kinematic viscosity
$\mathbf{D}$	Viscous tensor
$\alpha_l$	Liquid volume fraction
$We$	Weber number
$\overline{\cdot}^w$	Weighted averaging operator
$\overline{\cdot}^x$	Space averaging

# Acronyms

**ACARE** Advisory Council for Aeronautics Research in Europe. 1

**B-N** Baer-Nunziato. 8, 20, 39

**CDF** Cumulative Density Function. xxii, 73, 74, 77–79

**CIT** Controlled Interface Thickness. 15, 18, 19, 31, 35, 36, 40, 43, 44

**CLSVOF** Coupled Level Set/Volume of Fluid. 19, 28, 35, 36, 54, 60, 76, 83–85, 114, 131, 148

**DNS** Direct Numerical Simulation. 25, 29, 30, 36, 44, 114, 147, 169

**EOS** equation of state. 14–18, 25

**FADEC** Full Authority Digital Engine Control. 2

**FCT** Flux-Corrected Transport. 42

**FIT** Free Interface Thickness. 15, 18, 20, 25, 29, 31, 35, 36, 38, 40, 43, 44

**FMU** Fuel Melting Units. 2

**GFM** Ghost Fluid Method. 19, 38

**IC** interface capturing. 18, 115, 116, 122, 131, 132

**ICAO** International Civil Aviation Organization. 4, 5, 147

**IFSD** In-Flight Shut-Down. 112

**K-H** Kelvin-Helmoltz. 105, 113, 125, 132

**LES** Large Eddies Simulation. 22, 24, 26–30, 35, 43, 44, 49, 114, 122, 125, 132, 147

**LSA** Length-Scale Analysis. 13

**MGCG** MultiGrid preconditioned Conjugate Gradient. 37

**MULES** Multidimensional Universal Limiter for Explicit Solution. 42, 44, 122, 132

**N-S** Navier-Stokes . 11, 22, 36, 39, 40, 43, 122, 132

**NDF** Number Density Function. 21

**PDA** Phase Doppler Analysis. 108, 109

**PDF** Probability Density Function. xxii, 52, 54, 73–80, 89–91, 148

**PISO** Pressure-Implicit with Splitting of Operators. 40, 42, 44, 122, 123, 132

**PLIC** piecewise linear interface calculation. 19, 35–37, 72

**RANS** Reynolds-Averaged Navier-Stokes. 22, 26, 132, 147

**RHS** Right Hand Side. 20, 23, 43, 44

**SGS** Sub-Grid Scale. 29, 30

- SLIC** simple line interface calculation. 19, 72
- SMD** Sauter Mean Diameter. 106, 109, 129–131, 136, 142, 144, 149, 150
- TAPS** Twin Annular Premixing Swirler. 5
- TKE** Turbulent Kinetic Energy. 27, 54, 64, 65, 70, 71, 148
- TVD** Total Variation Diminishing. 42, 123
- VOF** volume of fluid. 18, 19, 28, 36, 37, 41
- WBE** Williams-Boltzman Equation. 21, 147
- WENO** Weighted Non-Oscillatory Scheme. 36

# Chap. 1 | Introduction

"Education isn't something you can finish."

I.Asimov

Aviation changed the world in the early 1900s and brought the development of different technologies in order to make it possible. To produce the lift to make an airplane fly it is necessary to produce a relative movement between the body and the fluid in which it is immersed ([And05]). This concept was already studied by the scientist and philanthropist *Leonardo da Vinci* with his studies on the *ornithopters* ([Hag12]). In the *codex* he sketched a flying machine in which the flapping of the wings would create at the same time propulsion and lift. Since the first flight of *Wright's brothers* in 1905, such a relative movement has been created by generating thrust through engines. Aeronautical engines have had a huge evolution through aviation's history. Starting from the earliest propeller mechanically actuated, passing through piston engines, after the Second World War the technology allowed to develop jet engines that became standard for modern airplanes. With the growth of the air traffic, nowadays the goal of most of the aeronautical engines' manufacturers is to reduce the pollution through improvements in the efficiency of the different part of the engine (Advisory Council for Aeronautics Research in Europe (ACARE) 2050 objectives set a reduction of 75% in production of  $CO_2$  and of 90% of  $NO_x$ ).

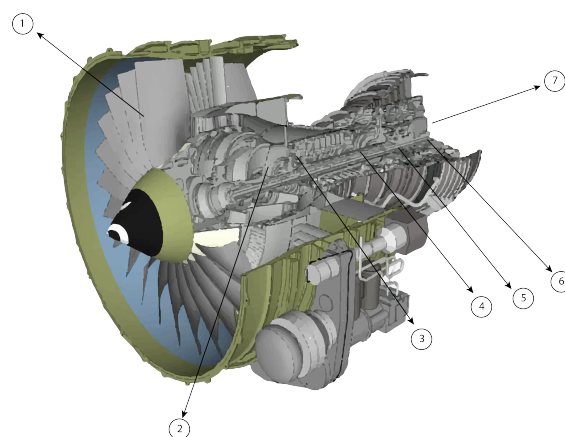


Figure 1.1 – Scheme of a jet engine, courtesy of *SAFRAN Aircraft Engines* . ① the fan, ② low pressure compressor stages, ③ high pressure compressor stages, ④ combustion chamber, ⑤ high pressure turbine stages, ⑥ low pressure turbine stages, ⑦ outlet.



Given a jet engine, we can commonly divide it in 3 major macro parts (see fig. 1.1):

- the fan ( ① ) and the compressor group: low pressure stage ( ② ) and high pressure stage ( ③ );
- the combustion chamber ( ④ );
- the turbine group: high pressure stage ( ⑤ ) and low pressure stage ( ⑥ ). The outlet ( ⑦ ).

The part of the engine mostly involved in the production of pollutants is the combustion chamber. Designing and optimizing the fuel system and combustion chamber means optimizing the combustion process and hence:

- **reduce pollutants:** a homogeneous cloud of droplets allows a more efficient combustion, burning homogeneously the atomized fuel. A complete review of pollutants produced by the aircraft engine can be found in [FHL71];
- **fuel savings:** increase in the atomization efficiency brings to fuel savings, as far as the fuel injected is all used to create the enthalpy step. Hence increasing the atomization efficiency and the fuel savings means also to reduce the  $CO_2$  production.

Depending on the model of the engine, the structure of the fuel system can be different, but it is common to identify the parts reported in the scheme of the fig. 1.2. The main parts are:

- **Pumps ( ① )** : in each fuel system of a civil aircraft it is possible to identify a *supply pump*, centrifugal type, installed generally with a *principal pump*, of volumetric type.
- **Heat exchangers ( ② )** : they pre-heat the fuel e.g thanks to the heat released by the oil on the return lines.
- **Filters ( ③ )** : There are many on the fuel system line and helps to clean it from impurity (like metal residuals coming from the natural use of the different part on the line).
- **Fuel Meltering Units (FMU)( ④ )** : the main tasks of this part are to assure the right amount of fuel following the electric command of the Full Authority Digital Engine Control (FADEC) and manage all the safety tasks on the fuel line.
- **Actuators ( ⑤ )** : they are needed to change the orientation of some stage of the compressor and they are actuated by the fuel of the HP line are, usually, linear actuators.
- **Injectors ( ⑥ )** : responsible for the atomization of the fuel inside the combustion chamber.

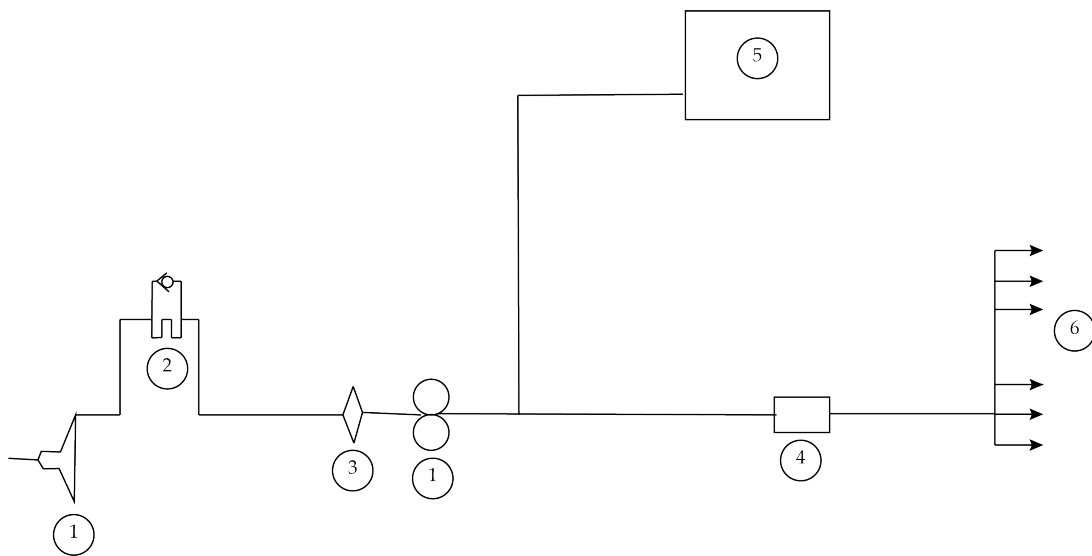


Figure 1.2 – Simplified scheme of the *Sam 146* engine's fuel system, courtesy of *SAFRAN Aircraft Engines* . ① Fuel pumps. The first one volumetric, the second one gear pump, ② heat exchanger, ③ filter, ④ FMU, ⑤ actuators actuated by servo-valves, ⑥ lines to the injectors.

In the conception of a fuel system, it is important to take into account different parameters and as a consequence different studies are conducted:

- Thermal study of the whole engine: sizing of the different heat exchangers and different tests in extreme conditions, depending on the typical flight condition.
- Study of the flow passing through the high pressure (HP) and low pressure (LP) lines.
- Fuel pressure and flow rate computations.

In order to make the engine work properly, it is important to have a strong design synergy between the combustion chamber and the Injector.

The key parameters for the design of the combustor are:

- The performances: in this class we consider the efficiency of the combustion and the exit plane temperature.
- The thermo-structural management: the lifetime of the product and vibrations analysis;
- The operability: the ignition, the ground, the start and the restart in-flight, the extinction limits (due to water or bird strike) and the stability in case of off-design condition.
- Pollutant's production: as already mentioned, International Civil Aviation Organization (ICAO) regulations are very strict nowadays in  $NO_x$ ,  $CO_2$  and soot productions.

For all of these points, the design of the injector is concerned. In particular an interaction about the design volume and the dilution zone spray characteristics is required. The injector must satisfy the spray characteristics dictated by the combustor's design.

So far, in most of the cases, injectors have been designed taking into account slight modifications of the previous configurations and trying to adapt them to the particular engine requests. New performances were verified through experimental campaigns. In the next section, we'll give a brief overview of the most used type of injectors inside the aeronautical world.

## 1.1 Atomizers in the Aeronautical world



Figure 1.3 – Example of two different injection technologies in aeronautical engines. On the left an air-assisted injector, on the right an aero-mechanic injector. With the courtesy of *SAFRAN Aircraft Engines*.

In aeronautical applications, different types of injectors have been deployed during history. It is possible to identify two main categories of configuration. Categories are split taking into account if there is an additional air flux that helps the atomization with jet entrainment. In

fig. 1.3 left, it is possible to find the atomizer used by the *SAFRAN Aircraft Engines* engine. Here the atomizer is of *air-assisted* type. Before the outlet, the air is mixed with the fuel to produce, through friction, instabilities that helps in the atomization process. On the right, atomization is performed through conversion of pressure in kinetic energy. These are called *pressure atomizers* and in that case there is not pre-mixing with the air.

The needs to reduce the  $NO_x$  imposed by the ICAO ([Ica]), brought to the development of new combustion chambers and new types of injectors. The actual field of research is the improvement of the fuel/air mixing in order to perform a better combustion. As said in [And+16], The Injector exploited in the GE-Twin Annular Premixing Swirler (TAPS) combustor ([Mon03]), which currently represents the only lean burn combustion system employed on a certified aircraft engine (GEnX family), is particularly relevant. This is the typical *multi-point injector*. There is a pilot pressure atomizer surrounded by two co-rotating swirling injectors (fig. 1.4).

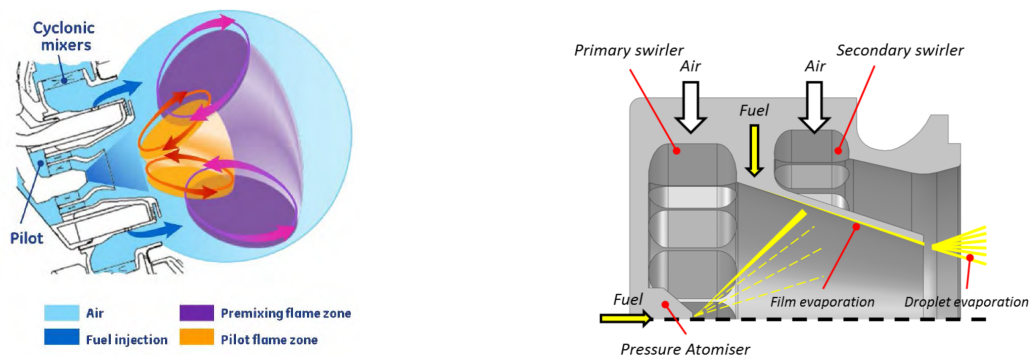


Figure 1.4 – On the left: conceptual scheme of a TAPS atomizer took from [SB13]. On the right: Scheme of a PERM atomizer took from [And+15].

A fuel film grows up in the inner part of the lip. As the film reaches the end of the lip, it goes through the primary atomization through the action of the gas flow. The two co-rotating swirled flows generated by the double swirler help the mixing. At low-pressure condition, a second hollow cone pressure atomizer (pilot) is activated.

These two technologies are regarded as the technologies of the future for aeronautical engines, in which a design process that joins together the design of the injectors and of the combustion chamber is every day more necessary.

Nowadays most used atomizers in middle-low engines sector are still pressure-swirl atomizers. The fluid feeds a swirling chamber it starts to rotate and is delivered through the outlet to the combustion chamber as a conical liquid sheet. Given that this technology is currently the most commonly used, it is interesting to detail the physics of atomization process and to study more in-depth the physics behind it.

## 1.2 Atomization problem for pressure-swirl atomizers

During the years, dimensionless parameters helped to classify the atomization problem. Here is a brief review of the most used parameters for the pressure-swirl atomizers.

**Reynolds number** The Reynolds number is a dimensionless parameter that represents the ratio between the inertial forces and the viscous forces. Given  $v$  a characteristic velocity,  $l$  a characteristic length scale,  $\nu$  kinematic viscosity of the fluid, it is possible to define the

Reynolds number as:

$$Re = \frac{\mathbf{v}l}{\nu} \quad (1.1)$$

It is possible to define different flow regime starting from a laminar flow to a turbulent flow thanks to the Reynolds number. As it is possible to see in the definition of this parameter, different choices are possible for the velocity  $\mathbf{v}$ , characteristic length scale  $l$ , and, in case of the multi-phase problem, also for the kinematic viscosity  $\nu$ . An example of Reynolds number computed for swirling injectors is the *Walzel Reynolds number* defined as [Wal93]:

$$Re_w = \frac{\sqrt{2\rho_l\Delta P}d_0}{\mu_l} \quad (1.2)$$

Where  $d_0$  is the diameter of the exit orifice,  $\rho_l$  is the liquid density,  $\mu_l$  is the dynamic viscosity and  $\Delta P$  is the pressure drop. Other choices have been to compute the Reynolds numbers:

- a. at the inlet of the injector.
- b. of the film thickness at the end of the swirling chamber.

Through the present thesis, when a Reynolds number will be used, it will be properly defined.

**Weber number** The Weber number is defined as the ratio between the inertial force and the surface area force. Given the phase density  $\rho$ , the characteristic speed  $\mathbf{v}$ , the characteristic length-scale  $l$  and the surface tension  $\sigma$ , it is possible to define:

$$We = \frac{\rho\mathbf{v}^2l}{\sigma} \quad (1.3)$$

Thanks to the Weber number, it is possible to define different breakup mechanisms and behaviour of the liquid interface. Like the Reynolds number  $Re$ , different formulations of the Weber number  $We$  are possible. One example is the gas Weber number. The gas Weber number is defined, as said in [Jed+18], as the ratio between the disrupting gas forces and the consolidating surface tension forces of the liquid film, and hence:

$$We = \frac{\rho_g\mathbf{v}_l^2l}{\sigma} \quad (1.4)$$

A critical Weber number  $We_{gc} = 27$  (studied in [Sen+99]) determines whether long-wave or short-wave growth dominates the process. Long waves prevail when  $We < We_{gc}$  and short waves in the opposite case.

**Ohnesorge number** The Ohnesorge number ([MR11]) relates the viscous, inertial, and surface tension forces. Starting from the definitions of Reynolds and Weber number it is possible to write:

$$Oh = \frac{\sqrt{We_l}}{Re_l} = \frac{\mu_l}{\sqrt{\rho_l\sigma}l} \quad (1.5)$$

Where  $\mu$  is the dynamic viscosity,  $\rho$  is the density,  $l$  is a characteristic length-scale and  $\sigma$  is the surface tension.

**Swirl number** The swirl number is defined as the ratio between the axial transport of the angular momentum and the product to the axial transport of momentum. Different definitions can be found in literature, where the swirl number takes into account secondary effects like the Reynolds stresses. Here we will consider the definition (refer to [Fal13]):

$$S_w = \frac{\int_A \rho u_\theta (\mathbf{v} \cdot \mathbf{n}) r dA}{R \int_A \rho (\mathbf{v} \cdot \mathbf{n})^2 dA} \quad (1.6)$$

Where  $\mathbf{n}$  is normal to the surface,  $u_\theta$  is the tangential velocity in polar coordinate,  $A$  is the area of a surface taken inside the domain and  $R$  is the radius of the slice considered.

The physics of the atomization problems have been studied through the years. Different experiments, relying on the different adimensional numbers just cited. In this sense an interesting review can be found in [LM88], where the different breakup phases of the conical sheet are studied with respect to increasing pressure. In particular Lefebvre defined clearly the different phase that the flow passes when discharged from the orifice (fig. 1.5, fig. 1.6). A first stage where the liquid dribbles from the orifice. Increasing the pressure, we have the typical phase where the coherent liquid structures take the shape of a distorted pencil. Later we notice what is called the onion stage and the tulip phase, where the pressure approaches to the value where the atomization is finally fine and fully developed. The same study has been performed in [RN01], where the study is extended, taking into account different Ohnesorge numbers.

Once the injection pressure is sufficient to sustain the cone raising from the swirling chamber, the structure of the liquid sheet is constant. Classically the liquid has been divided into three different zones. Near the nozzle outlet, coherent structures of liquid are separated from the gas phase and this region is commonly called separated phase zone. In a transition zone instabilities decompose the elongated structures in ligaments of liquid and downstream, they end up in a polydisperse spray [Rem+19]. As it is possible to observe, we go through a strong multi-scale problem, where in each zone, the features of the flow studied are different. In the separated phase zone, the focus is mainly on the liquid film thickness and the cone angle and air core entering inside the swirling chamber ([Tay50],[SL86],[NP00],[MASB10],[Mal+18],[Siv+15] and more). In the transition zone, the focus is on the mechanism of transition and on the instability raising ([RN01],[DH62],[Siv+15]). In the dispersed region, the focus is on the droplet distribution ([LE92],[SHT16]). It is possible to observe, how for each zone, the length-scale involved are strongly different. This creates different challenges from the experimental point of view ([Bac00],[Bac94]) that we can try to overcome with numerical studies.

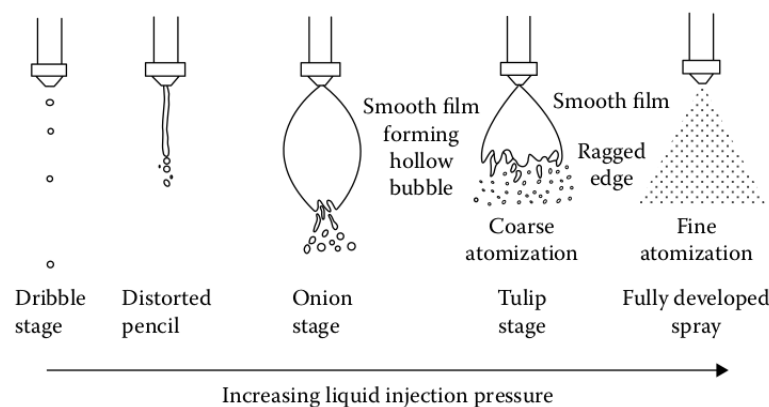


Figure 1.5 – Graphical representation of the progression of the different atomization phases with respect to the injection pressure. [LM88]

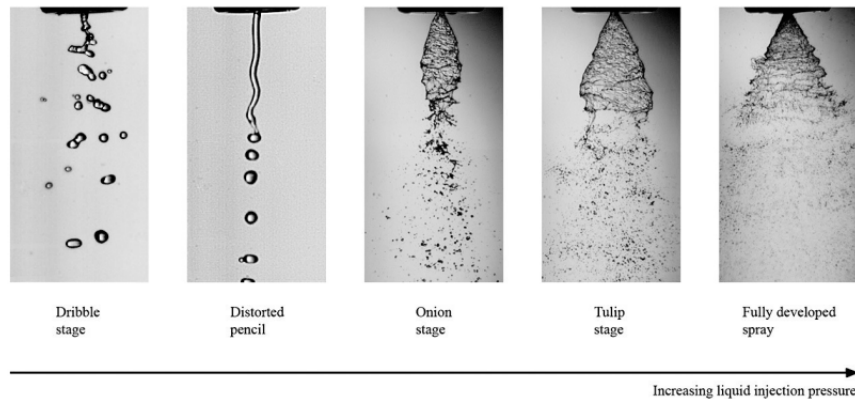


Figure 1.6 – Shadowgraph of the progression of the different atomization phases with respect to the injection pressure. For a graphical representation refer to fig. 1.5. [LM88]

### 1.3 Modeling the atomization problem

All along the last years different physical models have been developed to try to represent such a complex problem as the atomization phenomenon. It poses different deals, of which the most important is the multi-scale characterization. The researcher has to choose which effects to model in the problem and which effect to represent with the equations. Even if some innovative works are underway ([Cor20], [DB21]), it is still not possible to represent all the scales.

The first hypothesis posed is the continuum hypothesis, where the interface should be modeled, as far as the physical scale is too small to be directly resolved (for examples of length-scales related to the interface, refer to [XSC11]). It is possible to find in literature reviews about different interface modeling techniques ([MJD17],[AMW98],[SP18]). The classification given in [MJD17] (fig. 1.7) is based on the structure of the equations representing the fluid system (two-fluid, one-fluid, following the notation given in [TSZ11]). Successively the review treats the classification by the interface modeling approach, distinguishing among *diffuse interface* approach and the *sharp interface* methods.

In [AMW98] after an historical introduction of the way of considering the diffuse interface in history, focused on one component and two component fluid interface modeling.

In [SP18] the review is focused more on what Mirjalili would call the *two-fluid models* ([MJD17]). This family of models have as a common starting point the Baer-Nunziato (B-N) model, introduced in [BN86], and are mostly based on the compressible flow formalism. In fact, the numerical method to solve the equations postulated in the models come from the compressible flow formalism ([LeV92]). From all these works and from literature it is possible to distinguish two families of models concerning the interface ([DB20]):

- Sharp interface model: the interface is a discontinuity among the properties of the two phases. There are models that consider it directly as a discontinuity and other models that try to obtain it by sharpening a thickened interface.
- Diffuse interface model: the interface is an extended portion of space where the properties change gradually among the two phases.

Other works in literature are more focused on higher length-scale modeling. Examples of other modeling length scales models are the classical kinetic approach ([Ess+17]), where, in

the disperse zone, the droplets are modelled as separated bodies, or turbulence modeling, where part of the flow dynamic is relegated to the model ([Ani11]).

Other papers are dedicated to these topics ([Che+11],[PMO15],[Vin+18]), They focus on higher length scales modeling, such as turbulence modeling aspects.

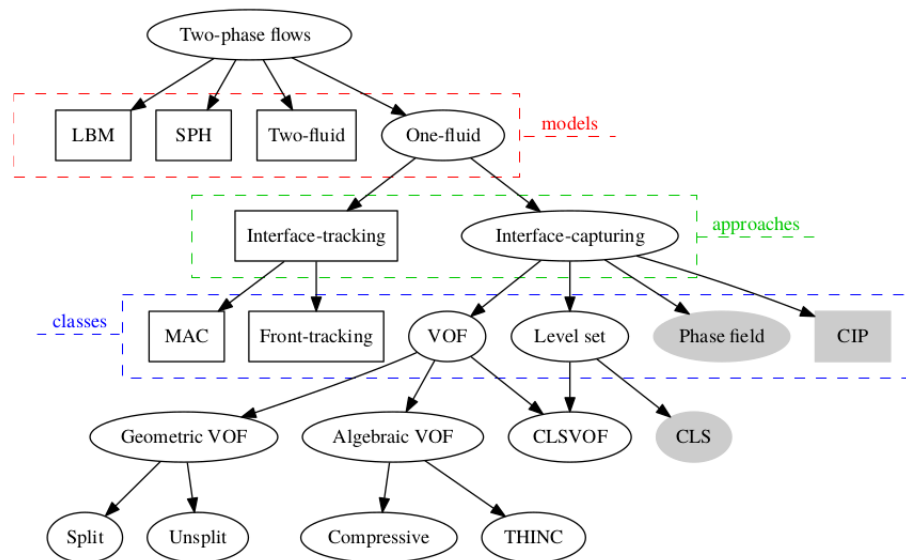


Figure 1.7 – Review of the possible *multi-phase* flow modeling approach it is possible to find in literature. Review done in [MJD17]

## 1.4 Outline of the thesis

In this chapter we gave a general introduction to the atomization problem. We gave the context of the aeronautical engine's atomization and a general overview of the experimental and numerical studies it is possible to find in the literature.

The present work is structured in the following way:

- **CHAPTER 2: NUMERICAL MODELS:** an improved numerical models classification, based on modeling length-scale is introduced. A wide review is presented and we will give two extended examples of models: *ELSA* and *ICMelsa*.
- **CHAPTER 3: NUMERICAL MODELS COMPARISON: THE AIR-ASSISTED LIQUID SHEET TEST CASE:** after having introduced the different physical models in *chapter 2*, we chose three numerical models representative of the interface modeling techniques and two representatives of the flow dynamic instability modeling approaches. A simple new testing configuration has been designed and proposed: an air assisted liquid sheet atomizer. The configuration has been optimized to be representative of an aeronautical configuration. The analysis of the results is divided in two different parts: a "classical analysis" part and a "phase analysis" part. In the classical analysis will go through classical statistics analysed in *single-phase* turbulence related works.
- **CHAPTER 4: PHASE ANALYSIS:** in the phase analysis we highlight the importance of the phase marker variance and we add some statistical tools to study it. After having analysed the phase marker variance on the domain of the different simulation performed, we propose a one-dimensional model to represent the departure of the non segregated variance from the segregated one.



- **CHAPTER 5: SILVERCREST:** The primary injector of the atomizer installed on the *Silvercrest* engine is treated and studied starting on the conclusion of the models tested in chapter 2. First an analytical study of the swirling injectors is presented. The experimental setup and experience are introduced, before treating the numerical procedure. In this chapter it is possible to find a new way to extract the Sauter Mean Diameter from the simulations and a contribution to improve the accuracy in the surface area density approximation for the *ICMelsa* model.
- **CHAPTER 6: CONCLUSION**

#### Conferences and Summer Schools

- ICMF 2019, *Rio de Janeiro, 2019*.
- CISM Summer School 2019, *Udine, 2019*.
- ILASS 2019, *Paris, 2019*.

#### Contributions

- Remigi A., Di Battista R., Demoulin F.X, Duret B., Massot M., Ménard T., Deneuille H. (2019) Exploring different approaches for the simulation of multi-scale atomization process. 10th International Conference of Multiphase Flow, May 2019, Rio de Janeiro, Brazil.
- Cordesse P., Remigi A., Duret B., Murrone A., Ménard T., Demoulin F. X., Massot M. (2020). Validation strategy of reduced-order two-fluid flow models based on a hierarchy of direct numerical simulations. *Flow, Turbulence and Combustion*, 1-31.

## Chap. 2 | Numerical models

The atomization phenomenon has been widely studied during the last decades. It is possible to find the first analytical studies about immiscible flows in literature as soon as the 19th century ([Pla73]). Nowadays, regardless of the fact that a lot of models have been introduced, it is possible to find wide reviews on the modeling techniques used for a generic *multi-phase* flow ([SP18], [MJD17]) but also for the specific case of the atomization [Ess+18].

The atomization phenomenon can be defined as a fluid system composed of two immiscible phases, one gaseous and one liquid. Concerning the physical process, regardless of the atomization technique, it is not always possible to identify a carrying phase and a carried phase. The flow field has been classically divided in three different regions ([LM88]). A first region where it is possible to identify coherent liquid structures (*separated phase zone*), a zone where it is possible to identify a polydisperse spray (*disperse phase zone*) and a transition zone between the two, where it is possible to identify the breakup of the coherent liquid structures. Mathematically speaking, is hard to address the challenge of the modeling, due to the multi-scale nature of the physical process itself. Due to the complexity of the phenomena, of the choice of the representation and of the associated numerical methods, it is not clear yet which is the most suitable model for each application. The complete and the direct description is mostly based at the lowest level on the Navier-Stokes (N-S) system, extended to liquid gas flows with an interface. It is possible to remark that does not exist a well established and unified model able to address the three zones cited above, at least for industrial related configuration cases.

In this chapter, the objective is to review the numerical models and methods present in literature, highlighting the different modeling length-scales used within each approach. In this way it is possible to understand, for each model, the different representation of the atomization process. In the first part of the chapter we will go into the different modeling techniques for the liquid-gas interface, reviewing the principal numerical methods to deal with the models proposed.

In the second part of the chapter we will focus on the classical *multi-phase* approach and reduced order models.

In the final part of the chapter we will introduce the *ELSA* formalism and a multi-scale model (*ICMelsa*) that aims to address the whole atomization process.

## 2.1 Introduction

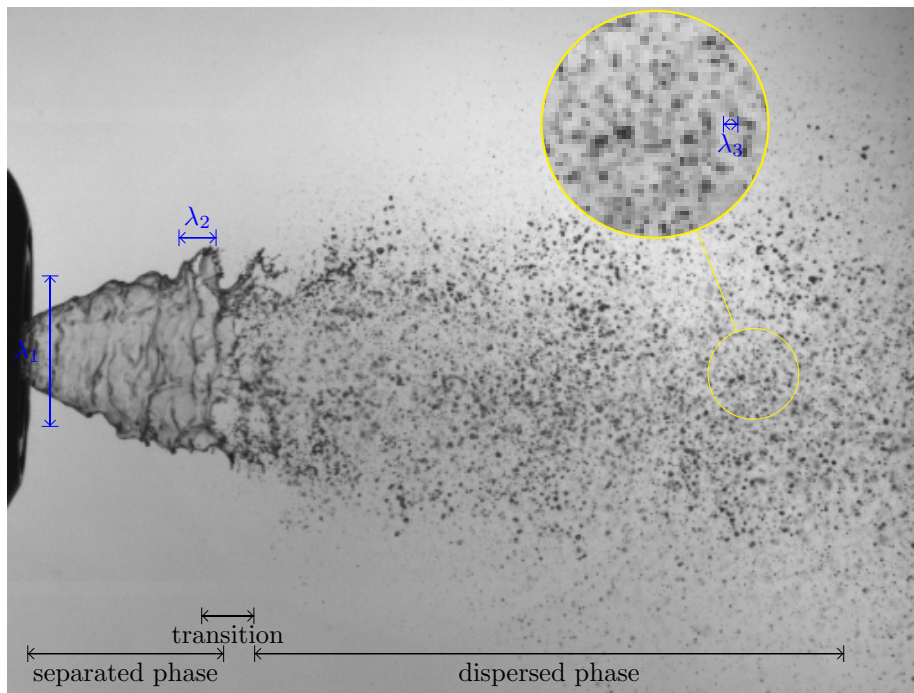


Figure 2.1 – Shadowgraph of the atomization process encountered with the *Silvercrest* injector studied in chapter 5. The typical reference length-scales are reported.  $\lambda_1$  is the injector length-scale,  $\lambda_2$  is the flow dynamic instability length-scale,  $\lambda_3$  is the droplets length-scale. On the bottom part of the subdivision of the atomization domain is shown, following [LM88].

### 2.1.1 Numerical models and numerical methods

In this section we clarify the terminology used in this work to differentiate among numerical models and numerical methods. The numerical modeling refers to the description of a physical model through appropriate equations, together with the numerical method suitable to solve the problem. In this case, to build a model, we will refer to the physical laws and mathematical tools. With the term numerical methods we refer to the numerical approach used to solve the equations postulated in the physical model. An example of a strategy to build a numerical model can be found in [Cor+20a]. Here the least-action principle is used to derive a hierarchy of *multi-phase* models. As we will see in the following section, there are cases in which numerical models are built and tuned considering, for example, the discretization of the equations. In the next sections we will try to clarify the difference between models and methods, even if in some cases they are extremely bounded together ([Cor20]).

### 2.1.2 Typical model length-scales

The atomization can be characterized by a wide range of length-scales. Taking as an example an atomized flow of aeronautical interest (typically we have  $Re_l \sim 10^4 - 10^5$  -  $We_l \sim 10 - 10^2$  where the  $Re_l$  and  $We_l$  are defined at the outlet of the injector, considering the liquid film sheet thickness as length-scale), then it is possible to define at least 4 typical length-scales (fig. 2.1):

- **Injector length-scale** ( $\lambda_1$ ): typical injectors for aeronautical purpose deal with length-scales between  $10^{-2}[m]$  and  $10^{-3}[m]$ .

- **Instability length-scale** ( $\lambda_2$ ):  $10^{-4}[m]$ .
- **Dimension of the different droplets** ( $\lambda_3$ ):  $10^{-5}[m]$ .
- **Interface** ( $\lambda_I$ ):  $10^{-8}[m]$ ;

When we approach the problem in order to propose the numerical model, we have to deal with a set of morphology of the interface among liquid and gas that ranges from the well separated phases, near the outlet of the injector, up to the polydisperse spray. In this process, as it is possible to see in fig. 2.1 the flow passes through a transition zone, where the morphology of the interface can be complex ([Ish75]). In each of these zones we can identify different typical length-scales. When we decide to adopt a numerical model we choose a *cutting/modelling length-scale*. Every physical phenomenon (related either to the dynamic of the interface, either to the dynamic of the flow itself) happening below this cutting length-scale is relegated to the physical model, everything that is above is represented by the equations describing the fluid system. Nowadays the connection between the modelling length-scale and the part of atomization process is still a matter of study. New models are being conceived in order to describe the whole process ([Cor+20a],[Ess+18]), but a unified, comprehensive model has not been established yet.

## 2.2 Models classified by the length-scale analysis (LSA)

In this section, we propose a possible classification of the different approaches that are used to describe liquid-gas flows. We have in mind the application to atomization but we expect this classification to be applicable more generally to any liquid-gas flow. The point of view developed is based on the length-scale at which we would like to resolve the flow, this is why we will call it Length-Scale Analysis (LSA). The first part is dedicated to the equations representative of such flow and the second one to the related numerical method.

### 2.2.1 Flow description

We base our analysis on continuum, at the possible exception of the interface. As reported in [Ish75] and [TSZ11] the establishment of any conservation law or governing equation in fluid mechanics is based on the continuum hypothesis. The fluids that we are going to treat are composed of molecules and atoms. Considering a box of size  $l$ , for small  $l$ , the fluctuations of the density  $\rho$  (mass of the molecules with respect to the occupied volume) would be relevant, and the discrete property of matter would appear. As the length  $l$  becomes bigger and bigger, the density function becomes smoother. For dilute gases we can say that we can apply the *continuum hypothesis* for length-scales  $l$  such as:  $l \gg l_{fp}$ , where  $l_{fp}$  is the *mean free path* length-scale that represents the distance among two molecules. As far as fluid mechanics is concerned, the typical LSA is taken larger than the inter-molecular distance between molecules. The main reason to consider LSA bigger than the molecular scale is the present impossibility to describe large system with a lower level of refinement. In addition, the physical representation of fluids at this scale requires molecular simulation that are based on very different physical description. Such simulations have been performed to access to very fine details of the interface characteristics, but they are restricted to very small portion of liquid-gas surface in simplified geometry. For instance in [Yan+14] a “1-D” droplet with a radius of  $r = 10[nm] = 10^{-2}[\mu m]$  is considered. Such sub-micron droplets are in general too small and with a vaporisation time scale too short to be captured in engine’s simulations. At this scale, the interface can be considered at the zone of transition between the gas and the liquid phase with a non zero length-scale. In this zone, in average the respective concentration of the gas and liquid varies continuously from pure liquid to pure gas. Typically, the thickness of this transition, thus the interface thickness, is, in this case, of the order of few nanometers

[nm]. Figure 2.2 from [XSC11] shows the liquid-gas interface thickness for different species as the function of the temperature to critical temperature ratio.

Thus in most of the cases any numerical simulation of liquid-gas flow at the range of atomization system dedicated to gas-turbine engine will not be able to simulate continuously the actual physical phase transition, since the typical mesh resolution, characterized by a length-scale  $\lambda$ , is greater than the physical interface thickness. It follows that the mesh resolution, and hence the level of details we are observing, is much bigger than the molecular inter-distance allowing continuous description of fluids on both sides of the interface. Therefore, to represent the physical interface transition between phases two models exist: on the one hand, the interface can be represented as an infinitely thin interface or on the other hand it can be artificially thickened to be described as a smooth transition at the level of the resolution retained. This leads to two different formalisms, respectively a separated phases approach with jump conditions at the interface and a mixed phases approach with adapted equation of state (EOS) to describe the mixture of the thickened zone of transition. This will be matter of discussion in the next section.

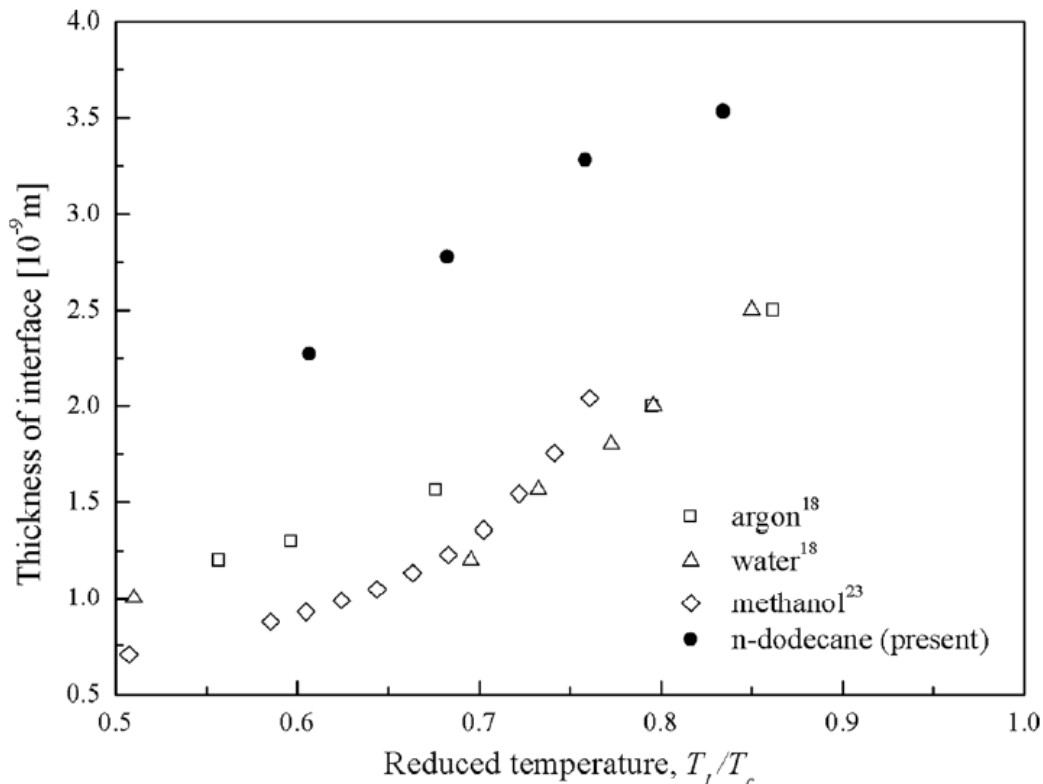


Figure 2.2 – The thickness of the liquid-vapour interface versus the reduced liquid temperature as predicted from molecular dynamics simulation showed in [XSC11].

### 2.2.2 Interface length-scales

The main difference among the *multi-phase* flows and the *single-phase* flows is the presence of the interface. In the previous section we remarked how the liquid-gas interface can not be solved directly, hence we would need a model to deal with it. One model proposition is to consider the interface as a infinitely thin region which separates two different fluids. Writing the transport equations for each of the fluid, they are supplemented with Rankine-Hugoniot's like

jump relations, to treat the jump of the properties across the interface. This is the so-called separated phases approach. There is not yet general and definitive terminology adopted by all communities. Accordingly, the meaning of *single-fluid*, *single-flow*, *multi-fluid*, *multi-phase* flow, among other, has to be understood in the context of the scientific community for which the specific article has been written. This has been a difficulty all along this work and we have tried our best to define such terms properly.

Another approach is to consider the interface as a thickened zone. The system is composed of a single fluid mixture with highly variable density and viscosity. Furthermore, it is supplemented with an adapted EOS to cover the thickened interface of transition. This is the so-called mixed phases approach. Along the thesis the terms Free Interface Thickness (FIT) and Controlled Interface Thickness (CIT) will be used. They will be used to describe two different kinds of mixed phases interface methods. The CIT term would describe the sharp transition of properties in case of mixed phases, where the thickness of the interface has a controlled thickness, while FIT term a gradual transition on an extended zone, where the interface of the mixed phases approach is left free to evolve. For general interface shape description we will use the terms *diffuse interface* and *sharp interface*, where *diffuse interface* term will describe the gradual transition of properties and *sharp interface* a net transition of the properties. It is important to remark that the two terms will not be used to define a model, but to describe the shape properties of the particular interface method used. An example it is the *InterFoam* model. It will be addressed as *sharp interface*, owing to the class of mixed phases models using a CIT method. In the next paragraph we will detail the different models formalism.

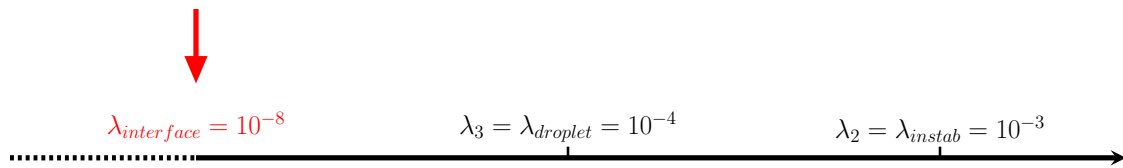


Figure 2.3 – Figure represents schematically the part of the flow that is resolved, here all scales greater than the physical interface thickness. The different length-scales refer to fig. 2.1.

### Separated phases approach

Given the *multi-phase* flow system, from the local description of [Ish75], it is possible to write the transport equations of the flow system. Given  $\mathbf{v}$  the velocity,  $\rho$  the density and  $p$  the pressure, we have on both sides of the interface the mass conservation equation:

$$\frac{\partial \rho}{\partial t} + \nabla \cdot (\rho \mathbf{v}) = 0 \quad (2.1)$$

The momentum conservation equation:

$$\frac{\partial \rho \mathbf{v}}{\partial t} + \nabla \cdot (\rho \mathbf{v} \otimes \mathbf{v} + p \mathbb{I}) = \nabla \cdot \mathbf{D} \quad (2.2)$$

The energy conservation equation:

$$\frac{\partial \rho E}{\partial t} + \nabla \cdot [(\rho E + p) \mathbf{v}] = \nabla \cdot (\mathbf{D} \cdot \mathbf{v} - q) + \dot{q} \quad (2.3)$$

Where  $E$  is the total energy defined starting from the velocity  $\mathbf{v}$  and the internal energy  $e$  as:

$$E = \frac{1}{2} \mathbf{v}^2 + e \quad (2.4)$$

With  $\mathbf{D}$  we define the *viscous tensor*  $\mathbf{D} = [\mu(\nabla\mathbf{v} + \nabla^T\mathbf{v})]$ , with the *Fourier Heat Flux* defined as  $q = k\nabla T$ ,  $\dot{q}$  energy source per unit volume and  $\mathbf{I}$  the identity matrix.

The interface is modelled as infinitely thin. As already explained in the previous section, the physical interface actually has a thickness itself, but its length-scale is lower than the length-scale chosen for the modeling purpose. This approach leads to a discontinuity of fluid and flow properties, leading to undetermined space and time derivatives at the surface. A set of jump relations must be supplemented to deal with the interface, in order to recover the continuity of the first order derivative and close the system of equations. We can analyse the equations in the neighborhood of the discontinuity identifying with  $k = +, -$  the approaching from one phase or the other to the interface itself. Considering  $\mathbf{n}_k$  to be the outward normal vector with respect to the side  $k$  of a surface defined as  $\mathcal{S}(\mathbf{x}, t) = 0$ , with  $\mathbf{x} \in \mathbb{R}^3$ ,  $t \in \mathbb{R}$  that separates the two phases, the jump conditions, can be written as:

$$\sum_{k=-,+} \int (f(\phi_k) - f_I) \cdot \mathbf{n}_k dS = 0 \quad (2.5)$$

Where  $f(\phi_k)$  are the fluxes of each of the two phases, associated with the variable  $\phi$  and  $f_I$  are the fluxes associated with the interface. Hence for the system of conservative equation, it is possible to write:

$$\sum_{k=-,+} [\rho_k(\mathbf{v}_k - \mathbf{v}_I)] \cdot \mathbf{n}_k = 0 \quad (2.6)$$

$$\sum_{k=-,+} [\rho_k \mathbf{v}_k \otimes (\mathbf{v}_k - \mathbf{v}_I) + \rho_k \mathbf{I} - \mathbf{D}_k] \cdot \mathbf{n}_k = 2\sigma H \quad (2.7)$$

$$\sum_{k=-,+} [\rho_k E_k(\mathbf{v}_k - \mathbf{v}_I) + \rho_k \mathbf{I} \cdot \mathbf{v}_k - \mathbf{D}_k \cdot \mathbf{v}_k + q_k] \cdot \mathbf{n}_k = 2\sigma H \mathbf{v}_I \cdot \mathbf{n}_k \quad (2.8)$$

where:

- $\mathbf{v}_-, \mathbf{v}_+, \rho_-, \rho_+, \rho_-, \rho_+, E_-, E_+$  are the flow variable in the neighborhood of the interface approaching from one phase or the other phase.
- The normal interface velocity  $\mathbf{v}_I$  is defined as the surface displacement velocity.
- $\sigma$  is the surface tension.
- $H$  is the local curvature of the interface with respect to the approaching side  $k = +$ .
- $\mathbf{I}$  is the identity matrix.

In this case two different thermodynamics with two EOS are defined for the two phase flow. They are made compatible, thorough the discontinuity, thanks to *Rankine-Hugoniot* like jump relations. The proper derivation of the jump relations can be found in [KIS86], [Kat86] or in [Ish75].

We want to highlight how in this case that the interface is modeled as a discontinuity (fig. 2.4), there is only one phase at a given position and time, and no mixture is present. This is the most important difference with the mixed phases approach presented hereafter.

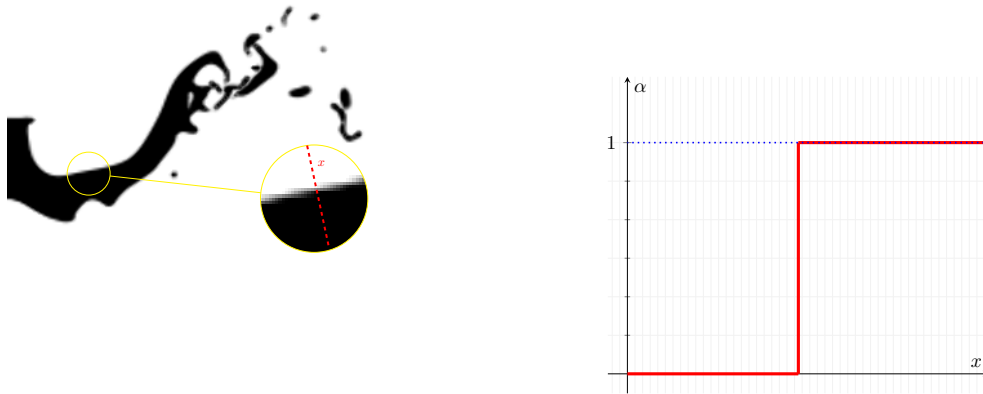


Figure 2.4 – Graphical explanation of the separated phases modeling approach. On the left an instantaneous of a simulation of an air-assisted liquid sheet, using the separated phases approach, on the right the plot of the phase marker function  $\alpha$  across the interface.

### Mixed phases approach

In the mixed phases formalism, the system is considered composed of one fluid with highly variable density and viscosity ([MJD17]). This approach considers the interface as a transition zone with a certain thickness, where the properties changes gradually. There a thickened interface would be defined, in which both phases coexist.

As it has been done before, it is possible to write the mass transport, momentum transport and energy transport equations:

$$\frac{\partial \rho}{\partial t} + \nabla \cdot (\mathbf{v}\rho) = 0 \quad (2.9)$$

$$\frac{\partial \rho \mathbf{v}}{\partial t} + \nabla \cdot (\rho \mathbf{v} \otimes \mathbf{v} + p\mathbb{I}) = \nabla \cdot \mathbf{D} \quad (2.10)$$

$$\frac{\partial \rho E}{\partial t} + \nabla \cdot (\rho E + p)\mathbf{v} = \nabla \cdot (\mathbf{D} \cdot \mathbf{v} - q) + \dot{q} \quad (2.11)$$

The difference with the separated phases approach is that, in each position of the flow domain, it is possible to define a mixture of  $\hat{p}$  phases, and no discontinuity of properties is present (fig. 2.5).

In order to treat the mixture zone, it is necessary to supplement the conservation laws with an EOS able to describe the thermodynamics in the thickened interface. In the context of compressible flow, it is possible to find mainly two modeling approaches:

- A continuous EOS is defined, that takes into account the phase changes (e.g [Waa94]).
- Two different EOSs are defined and coupled among them. An example can be found in [Cor20], in which the thermodynamic properties of the two fluid are coupled through a mixture entropy.

The thickened interface approach has been formalized mostly in the context of compressible formalism under the name of *diffuse interface* approach. However, other incompressible approaches used this concept without stating they belong to the *diffuse interface* formalism. In the context of the incompressible flow it is possible, also, to define different EOS such as



for the density:

$$\begin{cases} \rho_l = \text{constant} \\ \rho_g = \text{constant} \\ \rho = \alpha_l \rho_l + \alpha_g \rho_g \end{cases} \quad (2.12)$$

Where  $\rho_l$  and  $\rho_g$  are respectively the density of liquid and gas, while  $\alpha_l$  and  $\alpha_g$  are respectively the volume fraction of liquid and gas. This particular EOS, allows to extend the mixed phases formalism to the incompressible flow. Mixed phases formalism is illustrated on fig. 2.5. With respect to the fig. 2.4 the thickened interface seems do be a place where the phase have been diffused, thus the name of *diffuse interface* has been used to describe this kind of approach, even if we will see in the next section are possible mixed phases models that try to recover *sharp interface* profile and proper names will be defines (FIT and CIT approach).

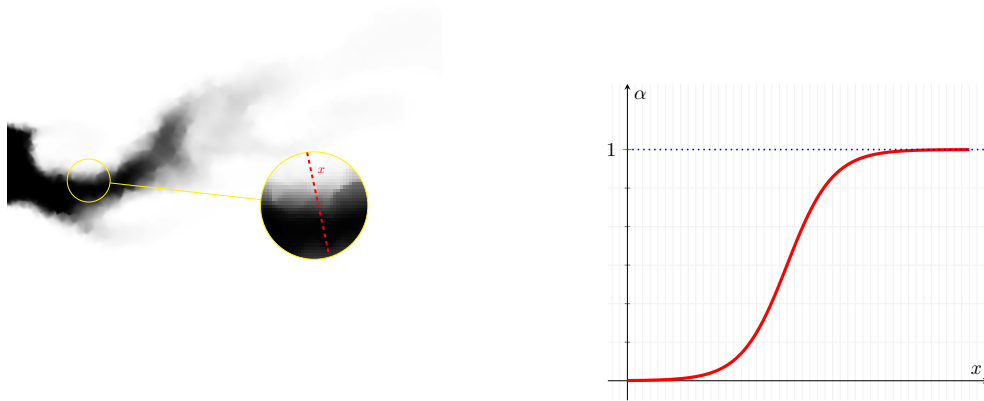


Figure 2.5 – Graphical explanation the mixed phases modeling approach. On the left an instantaneous of a simulation of an air-assisted liquid sheet, using the diffuse interface approach, on the right the plot of the phase marker  $\alpha$  across the interface.

### Numerical methods

It is possible to find in literature different numerical methods to solve the previously described sets of the equation. Concerning the separated phases formalism, we can identify the *interface tracking* method, where the interface is identified by points that moves and evolves in a *Lagrangian* way. One of the most famous method is described in [Try+01]. The second approach is represented by the interface capturing (IC) methods. The discontinuity is represented by a function, for which an unsteady transport equation is postulated. Mostly it is possible to identify two functions used in the literature:

- *Volume of fluid (VOF)*: derived in [HN81], it is still widely in use. A phase marker ( $\alpha$ ), that in case of incompressible formulation represents the volume occupied by one of the fluids (and hence it is called liquid volume fraction  $\alpha_l$ ), is advected using a first-order advection equation:

$$\frac{\partial \alpha_l}{\partial t} + \nabla \cdot (\mathbf{v} \alpha_l) = 0 \quad (2.13)$$

The liquid volume fraction  $\alpha_l$  ranges between:  $\alpha_l \in [0, 1]$ . This method guarantees the conservation of the liquid volume fraction mass. In the context of separated phases approach, it is necessary to apply the jump conditions on an actual discontinuity located at the interface, this holds in particular for the liquid volume flux. In general the

VOF method requires the reconstruction of the interface. One possibility is to use the geometric VOF techniques. This methods contains also a way to reconstruct the interface. The simplest one are the simple line interface calculation (SLIC) [NW76] that try to fit the interface with a 1st order function, keeping the interface parallel to one of the coordinate of the numerical domain. More accurate methods try to fit the interface with a piece-wise linear function (are representative the piecewise linear interface calculation (PLIC) methods reported in [Li95],[SGD18] among other works).

- *Level-set*: introduced in [OS88], the interface is defined implicitly by a distance function  $\phi$ , where the iso-values 0 ( $\phi = 0$ ) represents the interface boundary between the two fluids that is advected by an unsteady transport equation:

$$\frac{\partial \phi}{\partial t} + \mathbf{v} \cdot \nabla \phi = 0 \quad (2.14)$$

Resolving eq. (2.14), the level-set distance function does not preserve the distance feature of the field  $\phi$ . Thus a re-distancing algorithm must be deployed in order to return to a mathematically valid distance function ( $|\nabla \phi| = 1$ ). Some examples can be found in [SF99], [SSO94],[Kim98]. The advantage of the level-set method is that it allows to reconstruct in a more precise way the geometric evolution of the interface, while the main disadvantage is that it is not mass conservative. The interested readers are addressed to the review [SS03].

In the recent years these two interface capturing methods have been joined together in order to take the advantage of both methods, and hence the mass conservation property of VOF and the accuracy in capturing the dynamic of the interface for the level-set method. The hybrid level-set / VOF , called Coupled Level Set/Volume of Fluid (CLSVOF), has been introduced in [SP00] and later improved in [MTB07]. In addition a particular approach have been used to strictly apply the jump conditions (eq. (2.6)-eq. (2.8)): the Ghost Fluid Method (GFM), introduced in [Fed+99], [DSG17].

For what it concerns the mixed phases models, it is possible to find in literature different kinds of approach to solve the equations and treat the interface. One possible approach it is possible to find in [Rus02] and implemented in *OpenFoam* finite volume library, it is based on advecting the phase marker ( $\alpha$ ) as in the VOF method and try to sustain the *sharp interface* shape of the separated phases models through an empirical tuned sharpening term on the right hand side of the transport equation for the liquid volume fraction .

$$\frac{\partial \alpha_I}{\partial t} + \nabla \cdot (\mathbf{v} \alpha_I) = -\nabla \cdot [C_\alpha \mathbf{U}_r \alpha_I (1 - \alpha_I)] \quad (2.15)$$

Where  $\mathbf{U}_r$  is an empirical velocity used to modulate the compression, defined as:

$$\mathbf{U}_r = |\mathbf{v}| \cdot \mathbf{n} \quad (2.16)$$

where  $\mathbf{n}$  is the normal to the liquid-gas interface directed toward it,  $C_\alpha$  is a parameter that in literature is always set to 1 (for an example where the value is varied, see [WW13]). This method is called *InterFoam* ([Wel]).

We called this approach of considering the interface mixed zone and try to regulate the thickness through a source term in the phase marker advection equation mixed phases CIT models. This approach has been used in another family of models, called phase-field models. The main idea, as described in [BCB03], is to introduce a *phase field* that is constant in the two phases but varies gradually at the interface. The thickness of the interface will remain constant. The evolution of the *phase-field* is described by the *Cahn-Hilliard* equation ([CH58],

[Cah59]). Given  $\phi$ , the *phase-field* variable,  $M(\phi)$ , a mobility variable,  $\eta$  the chemical potential, it is possible to write:

$$\frac{\partial \phi}{\partial t} + \mathbf{v} \cdot \nabla \phi = \nabla \cdot (M(\phi) \nabla \eta) \quad (2.17)$$

The Right Hand Side (RHS) term of the eq. (2.17) can vary with respect to the physical problem addressed (e.g [MIM19]). For the interested reader to the *Cahn-Hilliard* model and *phase field* it is possible to read a review in [Ell89].

In addition it exists a family of methods that derives from the compressible *single-phase* formalism, able to describe shock wave discontinuities. This kind of methods are referred in the text as FIT approach in the context of mixed phases formalism. One of them is the averaged approach ([Dre83]), in which a macroscopic method is used, averaging the conservation equations. In this case, following the averaging procedure described in [Ish75] many unclosed terms would be created. In literature there are many closure propositions ([SA99],[Dre83]). In some cases, the mixture phase formalism is enriched by considering different separated state variables in liquid and gas phases, instead of single state variables. The conservation equations are postulated and later each of them is supplemented with mass, momentum and energy exchange ([LL59]). All the models based on this approach derives from the first implementation for *multi-phase* flow proposed in [BN86] as mentioned in [SP18]. The B-N system is also called *seven equations model*. It is a first-order non-linear non-conservative system of equations representing the transport equations in an enriched description of the flow: one equation for the conservation of mass for each phase, one equation of conservation of momentum for each phase, one equation for the conservation of energy for each phase and a seventh equation to describe the evolution of the phase marker  $\alpha$  in order to identify the interface. Further transport equations can be added to model further physical effects. One extension can be found in [SA99], where an interfacial pressure and velocity are added and needs to be closed. Starting from the 7 equation model, with the instantaneous relaxation of the pressure and velocity it is possible to find the 5-equation model ([Kap+01]) and by instantaneously relaxing the temperature it is also possible to find the compressible Navier-Stokes equations (4-equation model). A complete review about the hierarchy of these approaches based on the irreversible relaxation terms can be found in [Dru17] and [Cor20].

### 2.2.3 Droplet length-scales

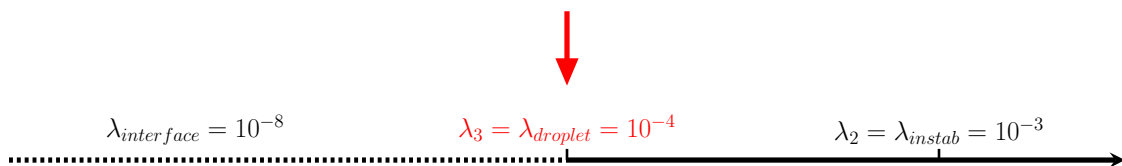


Figure 2.6 – The figure represent schematically the part of the flow that is resolved, here all scales greater than the droplet dimension. The different length-scales refer to fig. 2.1.

The modeling length-scale in this case is chosen to be larger than the droplet sizes. This level of description is suitable to describe the poly-disperse spray resulting of the atomization process, even if recent developments (e.g [Ess+18]) have opened the possibility to extend this approach to the separated-phase part of the atomization process.

In the case of poly-disperse spray, the modeling of the interface is not enough. It is assumed that the spray is composed by a set of discrete droplets. Accordingly a carrier phase and a discrete phase can be identified : the gas and the droplets themselves that are supposed to

behave like isolated elements. Thus a size distribution effect is more adapt. This approach is inspired by the Kinetic theory of gases.

### Kinetic approach

An equation to model the evolution of a cloud of droplets, which is described by a Number Density Function (NDF) has been widely used. This equation is also called Williams-Boltzman Equation (WBE) and has been postulated for the first time in the case of spray in [Wil58]. The variables in this equation describe the evolution of the statistical quantities that characterize the population of droplets such as the diameter, the velocity or the temperature. In order to deal with industrial problems, and hence to try to reduce the phase space, different modelling strategies have been developed during the most recent years. When the dimension of this space is not too large the WBE can be solved directly (e.g the Vlasov equation in [Gra+07]). One of the most used approaches is the stochastic Lagrangian approach which is based on Monte-Carlo simulations. In this case the particles are represented by samples that are tracked using a Lagrangian description. The shortcomings are that a huge number of stochastic particles is required for statistical convergence. An approach that has been developed a lot during last decades is to derive an Eulerian moment model from the WBE. A differential system of a finite set of moments of the NDF has been developed requiring some assumption on the variables of the phase space or on the mathematical form of the distribution to be closed ([FLM08], [Kah+12], [Ess+18]).

#### 2.2.4 Flow dynamic instability length-scales

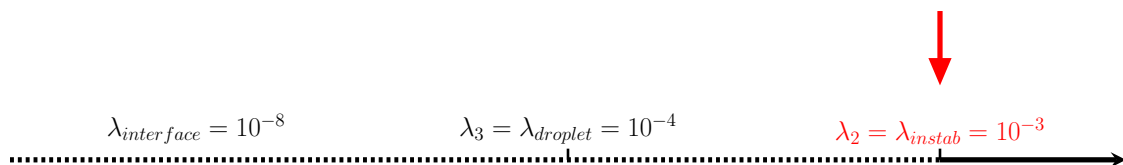


Figure 2.7 – The figure represent schematically the part of the flow that is resolved, here all scales greater than the flow dynamic instability length-scale. The different length-scales refer to fig. 2.1.

Even in *one-fluid* flow the multi-scale nature of the dynamic can be important as soon as turbulent flows are concerned. The instabilities and the following hierarchy of length-scales in case of turbulence (integral length-scale, Taylor length-scale and Kolmogorov length-scale as referred in [FK95]) are also present in liquid-gas flows. With respect to the previous description of the interface representation this leads to an ever more complex problem. In addition those length-scales related phenomena, occurring in *one-fluid* flows, happen also on both side of the interface and even interact with it. There is not yet a clear theory to help us to describe the liquid-gas flow with turbulence. There are clearly cases where it is possible to identify a scale separation between turbulent scales and interface length scales, but this not the case in general. For the scope of this PhD, like in many works in the present literature, turbulence description and modeling is treated separately from the description of the interface. Here, for sake of clarity, we refer to the flow dynamic instability length-scales and set it on top of the droplet length-scale, even if we are aware that the reality is more complex. The modelling of the dynamic of the flow it is known as *turbulence modelling* and it is based on classical textbooks like [Pop00] or [FK95]. In the following sections, starting from the turbulence modelling, we are giving a detailed example of one of the most used approaches developed in the recent years.

### Turbulence modeling in spray and atomization problem

Disserting about dynamic of the flow we are referring to *turbulence* phenomena. The highly non linear phenomena dictated by turbulence have been firstly visualized by Reynolds ([Rey83]) and later studied by Richardson whom introduced the idea of energy cascade in his seminal work ([Ric07]). The theory has been further developed mathematically by the Russian mathematician A.N Kolmogorov who, under the strong hypothesis of HIT (Homogeneous Isotropic Turbulence) with the K41 model, defined the first closed theory of turbulence ([Kol41b],[Kol41a]). Among other results it leads to an *Energy spectra* with the  $-5/3$  scaling law for the inertial range ([Vee+93],[SV94]) and the definition of the smallest length-scale, the so-called *Kolmogorov length-scale*. Thanks to this model it is possible to define typical *eddies* length-scales related with the phenomena of the energy cascade.

Practically, it is in general impossible to solve all the scales of a flow at large Reynolds number. Accordingly, a length-scale is retained, from which only all larger length-scales are resolved. In this case, a filter is applied to the quantities describing the flow. In this way a part of the dynamic is not resolved and requires a physical model, while the rest is directly resolved in term of filtered quantities. This approach is called Large Eddies Simulation (LES) since only the large eddies are resolved. Given that, the flow is turbulent, it is not fully predictable and only its statics can be predicted. The most important statistic is the mean. For instance, the mean can be obtained by averaging any flow quantity in time. It is even possible to average the set of equations describing the flow to define a new set of equations for the mean values, in the approach called Reynolds-Averaged Navier-Stokes (RANS). The non linearity of the N-S equations induce the presence of unclosed terms.

If only a filter is applied at a given length-scale, we obtain a set of equations for the filtered values that describe the LES approach. These equations contain also unclosed terms.

**Space filter** A space filter is applied to the system of equation describing the fluid domain. The filtering operation is described using spatial convolution filter  $G$  with a characteristic length-scale  $\Delta$ . Therefore, given a generic quantity  $\phi(x, y, z, t)$ , where  $(x, y, z)$  are the three Cartesian coordinates of the domain and  $t$  is the time, it is possible to write:

$$\bar{\phi}(x, y, z, t) = \iiint_{-\infty}^{+\infty} G_{\Delta}(x - x', y - y', z - z', t) \phi(x', y', z') dx' dy' dz' \quad (2.18)$$

Where  $\bar{\phi}(x, y, z, t)$  is the filtered variable. It is possible to distinguish among the so-called *implicit filters*, also referred as *grid is the filter approach* ([Ani11]), where the filter is the cell of the computational grid, and the so-called *explicit filters*, where the approach is to use a specific kernel. In this thesis we will use the implicit filtering approach. For a full discussion about implicit and explicit filtering we suggest [Pop00], [Sag06] and among the others [Che10], [Ani11],[KG21]. Applying the filter to the *single-phase* incompressible ( $\rho = \text{const.}$ ,  $\mu = \text{const.}$ ) momentum conservation equation, it is possible to write the filtered equation:

$$\frac{\partial \bar{\rho}}{\partial t} \bar{\mathbf{v}} + \nabla \cdot \bar{\rho} \bar{\mathbf{v}} \otimes \bar{\mathbf{v}} = -\nabla \bar{p} + \mu \nabla^2 \bar{\mathbf{v}} - \nabla \cdot \boldsymbol{\tau}^R \quad (2.19)$$

In this case the equation requires to be closed with the modeling of the residual stress tensor term  $\boldsymbol{\tau}^R$ . The residual stress tensor physically couples the small and big scales of turbulence. Even if it is possible to see a similarity among the form of the RANS equation and the space filtered equation, it is important to underline that the nature of the Reynolds stress tensor (term that takes into account the turbulent momentum velocity fluctuations in the Reynolds averaging procedure of the N-S equations) is different from the nature of the residual stress tensor. The main difference stays on the fact that the residual stress tensor is a fluctuating

quantity, and hence time dependent  $\boldsymbol{\tau}^R(t, \mathbf{x})$ . Multiple effort has been used to try to interpret this term. The best known decomposition was first done by Leonard in [Leo75]. It is possible to split the residual stress tensor  $\boldsymbol{\tau}^R$  in the following parts:

$$\boldsymbol{\tau}^R = \overline{\mathbf{v} \otimes \mathbf{v}} - \bar{\mathbf{v}} \otimes \bar{\mathbf{v}} = \mathbf{L} + \mathbf{C} + \mathbf{R} \quad (2.20)$$

The different terms are representative of the following physical effects:

- **L**: called *Leonard* stress tensor, it is representative of the interaction among the resolved scales.
- **C**: called *Cross* stress tensor, it is representative of the interaction among the not resolved and resolved scales.
- **R**: called *SGS Reynolds* stress tensor it is representative of the interaction among the not resolved scales.

As mentioned previously, the residual stress tensor represents the interaction term inside the momentum conservation equation among the small and big scales of the turbulence. One of the most important issue (as highlighted in [Pop00]) is the energy transfer between the filtered and residual motions. We can define the averaged kinetic-energy field as:

$$\bar{E} = \frac{1}{2} \overline{\mathbf{v} \cdot \mathbf{v}} \quad (2.21)$$

This energy can be decomposed in:

$$\bar{E} = E_f + k_r \quad (2.22)$$

where the filtered energy  $E_f$  is defined  $E_f = \frac{1}{2} \bar{\mathbf{v}} \cdot \bar{\mathbf{v}}$  and hence it is possible to define the residual kinetic energy as:

$$k_r = \frac{1}{2} \overline{\mathbf{v} \cdot \mathbf{v}} - \frac{1}{2} \bar{\mathbf{v}} \cdot \bar{\mathbf{v}} = \frac{1}{2} \tau_{ii}^R \quad (2.23)$$

To better understand how energy is distributed in the system it is possible to write the conservation equation for the filtered energy  $E_f$  by pre-multiplying the eq. (2.19) by the filtered speed  $\bar{\mathbf{v}}$ . The resulting equation can be written as:

$$\frac{\partial E_f}{\partial t} + \bar{\mathbf{v}} \cdot \nabla E_f - \nabla \bar{\mathbf{v}} \left( 2\nu \bar{S} - \boldsymbol{\tau}^R - \frac{\bar{p}}{\rho} \cdot \mathbb{I} \right) = -\epsilon_f - P_r \quad (2.24)$$

where:

$$\epsilon_f = 2\nu \bar{S}_{ij} \bar{S}_{ij} \quad (2.25)$$

$$P_r = -\tau_{ij}^R \bar{S}_{ij} \quad (2.26)$$

with:

$$S_{ij} = \frac{1}{2} \left( \frac{\partial u_i}{\partial x_j} + \frac{\partial u_j}{\partial x_i} \right) \quad (2.27)$$

On the left hand side of the equation we can identify the transport, while on the RHS we have the source and sink term.  $\epsilon_f$  is the dissipation due to the filtered field. The term  $P_r$  is the rate of production of residual kinetic energy and appears both in the transport equation of the filtered (as a sink term) and residual energy (as a source term). Hence we can identify it as the rate transfer of energy from the filtered motions to the residual motions. In order to close the equation it is necessary a model for the residual stress tensor  $\boldsymbol{\tau}^R$ . We consider at that level an implicit filtering technique, in which we consider a filter dimension ( $\Delta$ ) of the width of the cells composing the computational mesh. The simplest model is a linear

eddy-viscosity model introduced by *Smagorinsky* in [Sma63]. The residual stress tensor is modelled as:

$$\tau_{ij}^R = -2\nu_r \bar{S}_{ij} \quad (2.28)$$

$\nu_r$  is the eddy viscosity and it is taken proportional to the average stress tensor. It is modelled as:

$$\nu_r = (C_S \Delta)^2 \bar{\mathbf{S}} \quad (2.29)$$

Eventually it is possible to compute the transfer rate as:

$$P_r = 2\nu_r \bar{\mathbf{S}}^2 \quad (2.30)$$

The advantage of using the *Smagorinsky* stress model relies on its simplicity and on the fact that it does not require additional computational effort. The main disadvantages are that it is not possible to represent the backscatter ( $P_r$  is always positive) and the constant identified as  $(C_S \Delta)$  must be damped in some way near the wall. For an in-depth analysis about the other possible modelling alternatives (WALE [Nic99], Bardina [BFR80] and Germano [Ger+91] among the others) and the issue related we suggest the reading of the LES chapter in [Pop00]. However, since these models have been developed for *single-phase* flows, they have to be validated for turbulent liquid-gas flow applications. There is not yet a confirmation that this more advanced models are suitable for liquid-gas flows. Other than this it is possible to find recent studies in which different models have been tested in order to better understand the effect they have on the decomposition ([Vin+18]). This will be discussed in the next section.

**Multi-phase flow case** Pioneering work in the direction of modeling the flow dynamic of *multi-phase* flow problems have been done in [VB99], [BB+01], [Dem+07] among others, but hereafter the focus is on the LES modeling and filter approach. Following the LES approach recalled in the previous section, we filter the incompressible mixed phases conservation equations, supplemented by the transport equation for the phase marker. We highlight how we add to the mixed phases interface modeling, a flow dynamic modeling approach. We'll use the formalism introduced for instance in [Pug18] and [Che10]. Applying eq. (2.18), some filtered quantities, with respect to the *single-phase* case, appear. The filtered mixing velocity  $\bar{\mathbf{v}}$  the filtered mixing pressure  $\bar{p}$  and the filtered liquid volume fraction  $\bar{\alpha}_l$  induces further unclosed terms. The space filtering procedure of the transport equations leads to the mass transport equation:

$$\frac{\partial \bar{p}}{\partial t} + \nabla \cdot [\bar{\rho} \bar{\mathbf{v}}] = 0 \quad (2.31)$$

The momentum transport equation:

$$\frac{\partial (\bar{p} \bar{\mathbf{v}} + \tau_{\rho \mathbf{v}})}{\partial t} + \nabla \cdot (\bar{p} \bar{\mathbf{v}} \otimes \bar{\mathbf{v}} + \tau_{\rho \mathbf{v} \mathbf{v}}) = -\nabla \bar{p} + \bar{\mu} \nabla \cdot (\nabla \bar{\mathbf{v}} + \tau_S) - \bar{\rho} \mathbf{g} - \tau_\sigma \quad (2.32)$$

In addition, by using as an interface model the liquid volume fraction  $\alpha_l$  transport equation has to be filtered:

$$\frac{\partial \bar{\alpha}_l}{\partial t} + \nabla \cdot (\bar{\mathbf{v}} \bar{\alpha}_l + \mathbf{R}_{\alpha_l}) = 0 \quad (2.33)$$

Where the different non-closed terms can be identified with:

$$\begin{cases} \mathbf{R}_{\alpha_l} = \bar{\mathbf{v}} \bar{\alpha}_l - \bar{\mathbf{v}} \bar{\alpha}_l \\ \tau_{\rho \mathbf{v}} = \bar{\rho} \bar{\mathbf{v}} - \bar{\rho} \bar{\mathbf{v}} \\ \tau_{\rho \mathbf{v} \mathbf{v}} = \overline{\rho \mathbf{v} \otimes \mathbf{v}} - \bar{\rho} \bar{\mathbf{v}} \otimes \bar{\mathbf{v}} \\ \tau_S = \overline{\mu \nabla \mathbf{v}} - \bar{\mu} \nabla \bar{\mathbf{v}} \\ \tau_\sigma = \overline{\sigma k \mathbf{n} \delta_\Gamma} \end{cases} \quad (2.34)$$



$\mathbf{n}$  is the normal pointing outward the interface, while  $\delta_\Gamma$  is a Dirac function identifying the interface. Respectively the different terms are:

- $R_{\alpha_l}$ : represents the contribution of the under resolved interface to the liquid dispersion.
- $\tau_{\rho v}$ : represents the sub-grid contribution to the temporal term in the momentum equation and it has been shown its importance in [Tav+15] and [Vin+18].
- $\tau_{\rho v v}$ : similar to the sub-grid stress term in the case of the *single-phase* flow. Of course it is expected to have a particular behaviour for turbulent liquid-gas flow due to the high density variation and because it includes the velocity fluctuations induced by the mean slip between phases. A definitive modeling of this term has not been produced yet, despite recent development (see [Pug18] and references therein).
- $\tau_S$ : sub-grid term of the laminar viscous forces.
- $\tau_\sigma$ : term related to the surface tension. This term represents the effect of surface tension force on the mean momentum. It is expected to have a negligible direct effect on the largest scale if the Weber number is high. However, it depends on the surface representation. Thus, even if the force induced per the surface tension are often weak, an indirect role can be expected through the interface behaviour. For instance, the disintegration of the large liquid structures during the atomization process can enhance the liquid dispersion thus the slip phase velocity and then modified the Reynolds stresses. Other discussions and approaches on this term have been proposed in [Her13] and [Pop18].

An in-depth study of the contribution of the different terms can be found in [Vin+18] and [Tav+15], where an *a priori* test is conducted on a 3D Direct Numerical Simulation (DNS) configuration.

All these terms requires model in order to close the transport equations. Practical closure are still missing for *multi-phase* flows, so many *one-fluid* formalism closures have been tested by several authors ([Ane18], [Ahm19] among the others, but also [Lub+06], [CD01]). We have decoupled the description of flow dynamic to the surface representation. This is often the case in many applications in the literature: once an approach has been designed for the liquid-gas surface representation, it is attracting to complete the approach with classical modeling for the flow dynamic based mostly on *one-fluid* turbulence models. There are two main reasons. Firstly the turbulence in liquid-gas flows is very complex and not fully elucidated yet. Secondly there are plenty of cases where such separation gives good results. However, the coupling between the dynamic of the flow and of the interface is most probably a reality as suggested by the analysis of the unclosed terms. From the pionneerign work of Vallet and Borghi [VB99], it is even possible to represent certain surface phenomena such as the liquid dispersion and the turbulent liquid flux. These approaches have also provided good results ([Che+11]). In the next section we will take advantage of the turbulence modeling framework to introduce an Eulerian model able to handle liquid-gas turbulent flows, at least in the case where the length-scale of resolution is greater than the droplet length-scale.

### 2.2.5 ELSA

This approach, first introduced in [VB99], is based on the mixed phases formulation supplemented by the liquid volume fraction  $\alpha_l$  as numerical method to represent the liquid and gas phase behaviour. The modeling of the interface with respect to the nomenclature developed here is a mixed phases (FIT ) coupled with the incompressible form. Thus density  $\rho$  is constant for each phase and the following relationship for the mixture is the equivalent EOS:

$$\rho = \alpha_l \rho_l + (1 - \alpha_l) \rho_g \quad (2.35)$$



This approach has been mostly used for iso-thermal flow, where the energy equation is not considered, but it is possible to include energy also, see [Leb+09].

Another transport equation for a new variable is added, namely the interface area density  $\Sigma$ . This variable considers the portion of interface area in a certain volume. The transport equations are averaged or filtered. We finally get the following system of equations ([Ane+19b]):

$$\begin{cases} \nabla \cdot \bar{\mathbf{v}} = 0 \\ \frac{\partial(\bar{\rho} \bar{\mathbf{v}})}{\partial t} + \nabla \cdot [\bar{\rho} \bar{\mathbf{v}} \otimes \bar{\mathbf{v}}] = -\nabla \bar{p} + \mu \nabla^2 \bar{\mathbf{v}} - \nabla \cdot \boldsymbol{\tau}^R \\ \frac{\partial \bar{\alpha}_I}{\partial t} + \nabla \cdot [\bar{\mathbf{v}} \bar{\alpha}_I] = -\nabla \cdot \mathbf{R}_{\alpha_I} \\ \frac{\partial \bar{\Sigma}}{\partial t} + \nabla \cdot [\bar{\mathbf{v}} \bar{\Sigma}] = -\nabla \cdot \mathbf{R}_{\Sigma} + S_{\Sigma} \end{cases} \quad (2.36)$$

With respect to the filter applied, the modelling terms ( $\boldsymbol{\tau}^R$ ,  $\mathbf{R}_{\alpha_I}$ ,  $\mathbf{R}_{\Sigma}$ ,  $S_{\Sigma}$ ) have different formulations. In the RANS framework, considering the *Boussinesq* hypothesis, the Reynolds stress tensor is considered to be proportional to the mean gradient of velocity. The same formulation has been proposed for  $\mathbf{R}_{\alpha_I}$  in [Dem+07]. Physically this can be seen mainly as the dispersion of liquid thanks to the turbulent motion. This formulation does not take into account the slip-velocity among the two phases. A different formulation taking into account this effect has been proposed in [And+16]. The typical way to model these two terms can be resumed as:

$$\begin{cases} \boldsymbol{\tau}^R = \overline{\mathbf{v} \otimes \mathbf{v}} - \bar{\mathbf{v}} \otimes \bar{\mathbf{v}} \approx \frac{\nu_t}{S_{C_t}} (\nabla \mathbf{v} + \nabla^T \mathbf{v}) \\ \mathbf{R}_{\alpha_I} = \overline{\mathbf{v} \alpha_I} - \bar{\mathbf{v}} \bar{\alpha}_I \approx \frac{\nu_t}{S_{C_t}} \nabla \alpha_I \end{cases} \quad (2.37)$$

Where  $\nu_t$  is representative of the *turbulent viscosity* in case of RANS framework, whereas is the eddy viscosity in the LES framework.  $S_{C_t}$  is the turbulent Schmidt number and describes the ratio between the rates of turbulent transport of momentum and the turbulent transport of mass.

All the other term mentioned in eq. (2.32) are either neglected or can be considered as included in the modelling of  $\boldsymbol{\tau}^R$  and  $\mathbf{R}_{\alpha_I}$ . This approach is of course oversimplified, but up to now it has provide acceptable results ([Leb+09],[Che10] among others).

Concerning the surface density transport equation it is worth to study it more in depth. In literature it is possible to find different works about the transport equation of  $\Sigma$ . The first formulation proposed in [Ish75] has been recovered in further works, starting from combustion community ([DVP93]), until *multi-phase* community ([VB99], [Dur+12], [Nin+09], [DHD15]):

$$\frac{\partial \Sigma}{\partial t} + \nabla \cdot [\mathbf{v} \Sigma] = S \quad (2.38)$$

The research activity related to the closure terms have been subject of huge developments, we can identify three main branches as proposed in [Pug18] and [Che10]:

- In the first approach, the exact geometric equation of the liquid-gas interface is established ([Pop88]). The identification of the different terms is still under construction and not completely assessed. For the interested reader it is suggested [Mor07]. This work inspired a 7-equation model presented in [Cha+13].
- For dispersed flows where the spray is composed of droplet described by a droplet size distribution, it is possible to associate to each droplet an area. Then by integrating this area with the known distribution we can recover the surface density equation ([Ish75] and [IA03]). This approach is a modelling attempt based on the kinetic approach presented in the sections above.

- Using the phenomenological approach used in the combustion and flame community for the flame surface-density ([CP90]) adapted by Vallet and Borghi [VB99] and Burluka, Vallet, Borghi in [BB+01] for liquid-gas interfaces.

All these approaches aims to represent a part of the information on the interface, lost with the mixed phases formulation, since the position of the interface is not set precisely. Among all the features of the interface that are lost, the approach based on  $\Sigma$  equation aims to recover the surface density or the probability to find an interface. The formulation presented in the eq. (2.47) has been filtered or averaged, modelled, and leads to:

$$R_{\Sigma} = \overline{\Sigma \mathbf{v}} - \overline{\Sigma} \overline{\mathbf{v}} \approx \frac{\nu_t}{S_{C_t}} \nabla \Sigma \quad (2.39)$$

In addition, the source term is modelled following the restoration of equilibrium among the liquid and the gas subjected to turbulence motion as:

$$S_{\Sigma} = \frac{\overline{\Sigma}}{\tau_{eq}} \left( 1 - \frac{\overline{\Sigma}}{\overline{\Sigma}_{eq}} \right) \quad (2.40)$$

Where  $\tau_{eq}$  is a characteristic time-scale to reach the equilibrium. In turbulence dominated domains (high Weber  $We$  and Reynolds  $Re$  numbers) this is taken as proportional to a turbulent time-scale  $\tau_t$  ([Dur+13]).  $\overline{\Sigma}_{eq}$  is estimated considering the equilibrium state where the surface tension force balances the break-up due to the Turbulent Kinetic Energy (TKE)  $k$ . To define this quantity it is necessary first to define an equilibrium Weber number  $We^*$ . A first attempt has been done by Lebas et al. in [Leb+09] and later improved in [Dur+12] to take into account the very dense part of the flow field:

$$We^* = 4 \frac{0.5(\rho_l + \rho_g)\alpha_l(1 - \alpha_l)k}{\sigma \overline{\Sigma}_{eq}} \quad (2.41)$$

Setting the equilibrium Weber number  $We^* = 1.63$  ([Dur+13]), it is possible to retrieve  $\overline{\Sigma}_{eq}$ . The source term of eq. (2.41) can be recasted in order to define a  $\Sigma \rightarrow \overline{\Sigma}_{eq}$ .

$$S_{\Sigma} = \frac{1}{\tau_{eq}} \frac{\overline{\Sigma}}{\overline{\Sigma}_{eq}} (\overline{\Sigma}_{eq} - \overline{\Sigma}) \quad (2.42)$$

This model of the source term takes into account only the atomization in the near field region. Other effects can be accounted in the source term. For a complete overview of all the physical effects that it is possible to account, the reader can refer to [Bea+05], [Bea06] and [Leb+09]. To finalize the model, considering the eq. (2.41) it is possible to observe that eq. (2.42) tends to 0 when the TKE tends to 0. In this case the  $\overline{\Sigma}_{eq}$  should be limited by the minimum interface area in an unit volume. As derived in [Che10] for a typical length-scale sizing of  $\Delta x$  of the control volume, it is possible to write:

$$\Sigma_{min} = 2.4 \frac{\sqrt{\alpha_l(1 - \alpha_l)}}{\Delta x} \quad (2.43)$$

A different formulation has been proposed in [Pal21] in connection with the direct definition of the interface area density. The minimum area interface density is defined as the magnitude of the gradient of the liquid volume fraction .

$$\Sigma_{min} = |\nabla \alpha_l| \quad (2.44)$$

Hence for the *turbulent kinetic energy* tends to 0 we can state  $\overline{\Sigma}_{eq} \geq \Sigma_{min}$ . Considering the LES formalism, it is possible to decompose  $\Sigma$  in two parts: the minimum

area interface density  $\Sigma_{min}$  and the sub-grid interface area density i.e the additional interface area density due to sub-filter turbulence  $\Sigma'$ , hence:

$$\Sigma = \Sigma_{min} + \Sigma' \quad (2.45)$$

Chesnel et al. in [Che10] proposed, for numerical consistency with the whole LES framework, to substitute the evolution equation of the filtered surface area density  $\bar{\Sigma}$ , eq. (2.47), by the transport equation of the sub-grid interface area density  $\Sigma'$ .

$$\frac{\partial \Sigma'}{\partial t} + \nabla \cdot [\bar{\mathbf{v}} \Sigma'] = -\nabla \cdot \mathbf{R}_{\Sigma'} + S_{\Sigma} \quad (2.46)$$

The final system of equation for the ELSA model can be rewritten as:

$$\begin{cases} \nabla \cdot \bar{\mathbf{v}} = 0 \\ \frac{\partial(\bar{\rho} \bar{\mathbf{v}})}{\partial t} + \nabla \cdot [\bar{\rho} \bar{\mathbf{v}} \otimes \bar{\mathbf{v}}] = -\nabla \bar{p} + \bar{\mu} \nabla^2 \bar{\mathbf{v}} - \nabla \cdot \boldsymbol{\tau}^R \\ \frac{\partial \bar{\alpha}_l}{\partial t} + \nabla \cdot [\bar{\mathbf{v}} \bar{\alpha}_l] = -\nabla \cdot \mathbf{R}_{\alpha_l} \\ \frac{\partial \Sigma'}{\partial t} + \nabla \cdot [\bar{\mathbf{v}} \Sigma'] = -\nabla \cdot \mathbf{R}_{\Sigma'} + S_{\Sigma} \end{cases} \quad (2.47)$$

### 2.2.6 Multi-scale modeling

The previous discussion shown that to different modeling length-scales correspond different physical effects to be taken into account. As mentioned at the beginning of the chapter, the atomization problem is characterized by a great range of length-scales. In order to simulate the whole atomization problem there are different alternatives:

- A unified modeling approach able to handle the length-scale related to the separated and to the disperse phase zone. Different works go in this direction. The interested reader can refer to [Cor+20a] and to [DB+19].
- A coupling between different of the approaches just presented above, mainly through the source terms of the equations.
- Clear separation of the physical domain in different zones (static or dynamic) where one or the other model is employed with respect to the level of modelling required.

The typical case referring to the second point of the list it is what is called the coupling between different length-scales frameworks. A numerical model with a typical length-scale capable to model the interface and the flow dynamic is coupled with a kinematic model, where the modeling length-scale is set upper to the diameter of the droplets length-scale. The *ELSA* model presented above is coupled with a stochastic Lagrangian model in [Bea06] and in [Ane18]. An interesting study based on how it is possible to switch to a kinetic approach has been done [Can+18], where curvature computation is exploited to gain geometrical information to better understand how droplet size distribution is generated. References [Her08] and [Her10] present an approach where a CLSVOF interface treatment is coupled with a stochastic approach. Another similar approach is pursued in [ZED18] and for VOF resolved interface approach to Lagrangian kinetic approach [Fus+09]. In the recent years one of the most important focus in the coupling framework has been how to switch from the length-scale of the interface modeling to the length-scale of the Kinetic approach. For the interested reader it is suggested the review and improvements in [Ché+19].

Somehow in the context of the *ELSA* approach the description of the liquid-gas flow is based only the dynamic (velocity), the liquid volume fraction and the amount of surface density. This formalism does not specify the morphology of the interface (assuming spherical droplet

for instance) and since it is a mixed phases FIT approach it can be used for any resolution length-scale. Of course the unresolved part require physical modelling adapted to any situation. For instance it is expected for a resolution length-scale smaller than any length-scale of the flow that the sub-filter turbulent dispersion should vanish or, that the equilibrium surface has to be bigger than the minimum surface density. On top of that it is expected to recover the numerical method designed for tracking the interface whenever the resolution is sufficient. This is not the case for the *ELSA* approach. In [Ane+19b] the *InterFoam* model is coupled with the *ELSA* framework. To do this the transport equation for the liquid volume fraction presented in eq. (2.47) is modified. We have the liquid dispersion term in the *ELSA* model and a counter-flux part sharpening term for the *InterFoam* model. This two terms are incompatible and it has been proposed to switch the formulation to the other based on indicator of the interface resolution quality (*IRQ*). In the next section we will present in details this model.

### 2.2.7 ICM-ELSA

In the previous section we introduced the LES framework. Starting from the *single-phase* formulation we extended it to the *multi-phase*. We mentioned that we are going to use an *implicit filtering* technique, where the filter is directly the cell used during the discretization procedure. It is expected, as a characteristic of the LES modeling, that for increasing resolution the Sub-Grid Scale (SGS) model vanish and the LES simulation tends to the DNS. The perfect match would arise when we reach the so-called *Kolmogorov scale*. For *multi-phase* flows it is still not possible to define which is the smallest length-scale (the equivalent of the Kolmogorov scale), and for which length-scale the entire dynamic of the flow and of the interface is solved. The problems come from the presence of the interface. The phase indicator has no molecular diffusion since the phase are not miscible, then it is not possible to define the scalar Batchelor length-scale ([Bat59]). Other scales like the Hinze scales have been tested [Lin+19] with poor results. As highlighted in [GH08], nowadays only few studies about mesh convergence allows to access to the minimum length-scale based on the resolution ([SU10]).

#### Interface Resolution Quality (IRQ)

$IRQ_{\Sigma}$

This parameter relies on the interface area resolved and it is defined as the ratio of the minimum interface area resolved ( $\Sigma_{min}$ ) given a certain amount of liquid volume fraction to the actual interface area ( $\Sigma$ ). The interface area is actually the interface area density and it is defined as the amount of interface area in the control volume. This criteria has been introduced in [Ane+19a]. We can define a threshold corresponding to the proportion of interface resolved. This *IRQ* is close to unity where most of the interface is described at the mesh resolution ( $\Sigma_{min}$ ) and goes to zero when most of the interface area is at the sub-grid level ( $\Sigma'$ ), each part is illustrated on fig. 2.8.

$$IRQ_{\Sigma} = \frac{\Sigma_{min}}{\Sigma_{min} + \Sigma'} = \frac{\Sigma_{min}}{\Sigma} \quad (2.48)$$

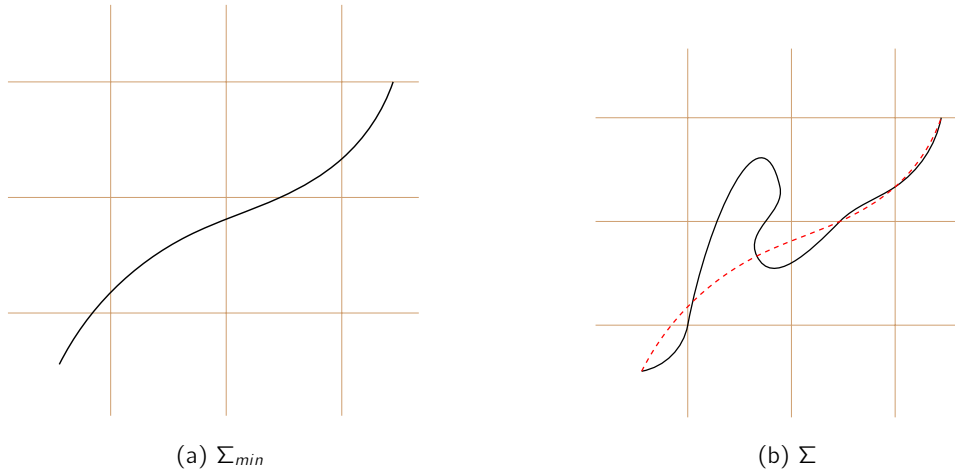


Figure 2.8 – Given the computational grid, on the left the interface reconstruction provides a certain  $\Sigma_{min}$ , on the right the real interface  $\Sigma$ . The difference of area is  $\Sigma'$

### $IRQ_K$

An in-depth study about this parameter has been carried out in [Can]. It is based on a geometrical property of the interface: the curvature. We will not enter in the main text in details about the curvature, but for more information and for a possible implementation carried out during the development of the thesis of the Gaussian curvature in the *OpenFoam* library, we suggest the reading of the appendix A. In [Can] two possible formulation of the parameter  $IRQ_K$  have been proposed, dependent on the two principal curvatures  $(k_1, k_2)$ . A first definition:

$$IRQ_K = \frac{1}{\Delta x |k_1 + k_2|} \quad (2.49)$$

and a more restrictive one:

$$IRQ_K^{max} = \frac{1}{2\Delta x \max(|k_1, k_2|)} \quad (2.50)$$

Considering the first definition it is possible to make an example to better understand this indicator. We consider a sphere of radius  $r = 1$ . The analytical solution of the curvature of the sphere is  $k = k_1 + k_2 = \frac{2}{r}$  and hence  $k = 2$ . We can compute the indicator as defined in eq. (2.49) as  $IRQ_K = 1/(2\Delta x)$ . The smaller is  $\Delta x$ , the higher is  $IRQ_K$ . The threshold between well resolved and not well resolved interface is dependent on the configuration chosen. Up to now a parametric study has been performed on a HIT configuration in [Can] and a value of  $IRQ_K = 2$  has been chosen, but it is worth to say that other studies are necessary to validate this value.

### Connection between InterFoam and ELSA formalism

In the previous section we introduced two criteria to state if the interface is well resolved. For well resolved cases, the LES SGS model become less and less relevant and the solution tends to the solution of the direct simulation (DNS), where a sharp transition between the phases should be recovered. For this reason we keep inside the transport equation of the liquid volume fraction, the formulations of the *InterFoam* and *ELSA* model, using one of the  $IRQ$  criteria to switch among them. The resulting transport equation for the liquid volume

fraction  $\alpha_l$  will be:

$$\frac{\partial \bar{\alpha}_l}{\partial t} + \nabla \cdot (\bar{\mathbf{v}} \bar{\alpha}_l) + \underbrace{\nabla \cdot C_\alpha \mathbf{U}_r \bar{\alpha}_l (1 - \bar{\alpha}_l)}_{ICM} = \underbrace{-(1 - C_\alpha) \nabla \cdot \{R_{\alpha_l}\}}_{ELSA} \quad (2.51)$$

The parameter  $C_\alpha$  takes the following possible values:  $C_\alpha = 0$  or  $C_\alpha = 1$ . In case of  $C_\alpha = 0$ , the sharpening counter-flux is turned off and the turbulent liquid flux part is turned on. In this case the transport equation is equivalent to the liquid volume fraction transport equation of the *ELSA* model (eq. (2.37)).

$$\frac{\partial \bar{\alpha}_l}{\partial t} + \nabla \cdot (\bar{\mathbf{v}} \bar{\alpha}_l) + \nabla \cdot \{R_{\alpha_l}\} = 0 \quad (2.52)$$

In case of  $C_\alpha = 1$  the turbulent liquid flux term is turned off. In this case the transport equation is equivalent to the liquid volume fraction transport equation of the *InterFoam* model (eq. (2.15)).

$$\frac{\partial \bar{\alpha}_l}{\partial t} + \nabla \cdot (\bar{\mathbf{v}} \bar{\alpha}_l) + \nabla \cdot \mathbf{U}_r \bar{\alpha}_l (1 - \bar{\alpha}_l) = 0 \quad (2.53)$$

Intermediate value of  $C_\alpha$  would not be possible, because it would mean to keep in the equation a sharpening term and a dispersion term that are in principle incompatible.

#### Complete model

$$\left\{ \begin{array}{l} \nabla \cdot \bar{\mathbf{v}} = 0 \\ \frac{\partial (\bar{\rho} \bar{\mathbf{v}})}{\partial t} + \nabla \cdot [\bar{\rho} \bar{\mathbf{v}} \otimes \bar{\mathbf{v}}] = -\nabla \bar{p} + \bar{\mu} \nabla^2 \bar{\mathbf{v}} - \nabla \cdot \boldsymbol{\tau}^R \\ \frac{\partial \bar{\alpha}_l}{\partial t} + \nabla \cdot (\bar{\mathbf{v}} \bar{\alpha}_l) + \underbrace{\nabla \cdot C_\alpha \mathbf{U}_r \bar{\alpha}_l (1 - \bar{\alpha}_l)}_{ICM} = \underbrace{-(1 - C_\alpha) \nabla \cdot \{R_{\alpha_l}\}}_{ELSA} \\ \frac{\partial \Sigma'}{\partial t} + \nabla \cdot [\bar{\mathbf{v}} \Sigma'] = -\nabla \cdot \mathbf{R}_{\Sigma'} + S_\Sigma \\ C_\alpha (IRQ) \end{array} \right. \quad (2.54)$$

### 2.3 Map of the models

In this chapter we presented different numerical models that is possible to deploy to simulate the atomization phenomenon, highlighting, for each model, the reference modeling length-scale. In fig. 2.9 and table 2.1 it is possible to find a map of the different modeling techniques explored along the chapter, and the different specific methods classified for the modeling level chosen. In table 2.1 we report only some examples of methods, explained previously in the text, while it can be completed with the available literature. In fig. 2.9 it is possible, starting with compressible or incompressible formalism and set the model of interface we want to use (separated or mixed phases, differentiating among the FIT and CIT family of methods), to move the modeling length scale, choosing the physical effects we are willing to model.

It remains one open question: which is the metric to compare the different models just proposed? In the recent past rarely a metric has been proposed to compare different models with the same modelling length scale. In literature we can find an example in [MIM19], where a *sharp interface* model is compared with a *diffuse interface* model, based on their mathematical structure. In this work a deformable droplet ([TB00]), a standing wave [PZ99] and a Rayleigh-Taylor instability ([BM92]) have been taken into account and a test is performed, analysing deterministic parameters such as error on surface tension force representation. This comparison does not focus on the non deterministic nature of a turbulent flow, having as a reference

classical test cases for assessing new numerical models or methods.

Our purpose is to assess the statistical behaviour of a test case of practical interest in order to evaluate the performance of the different modeling strategies, and to further understand the interaction among phases. This topic will be addressed in the next chapter.

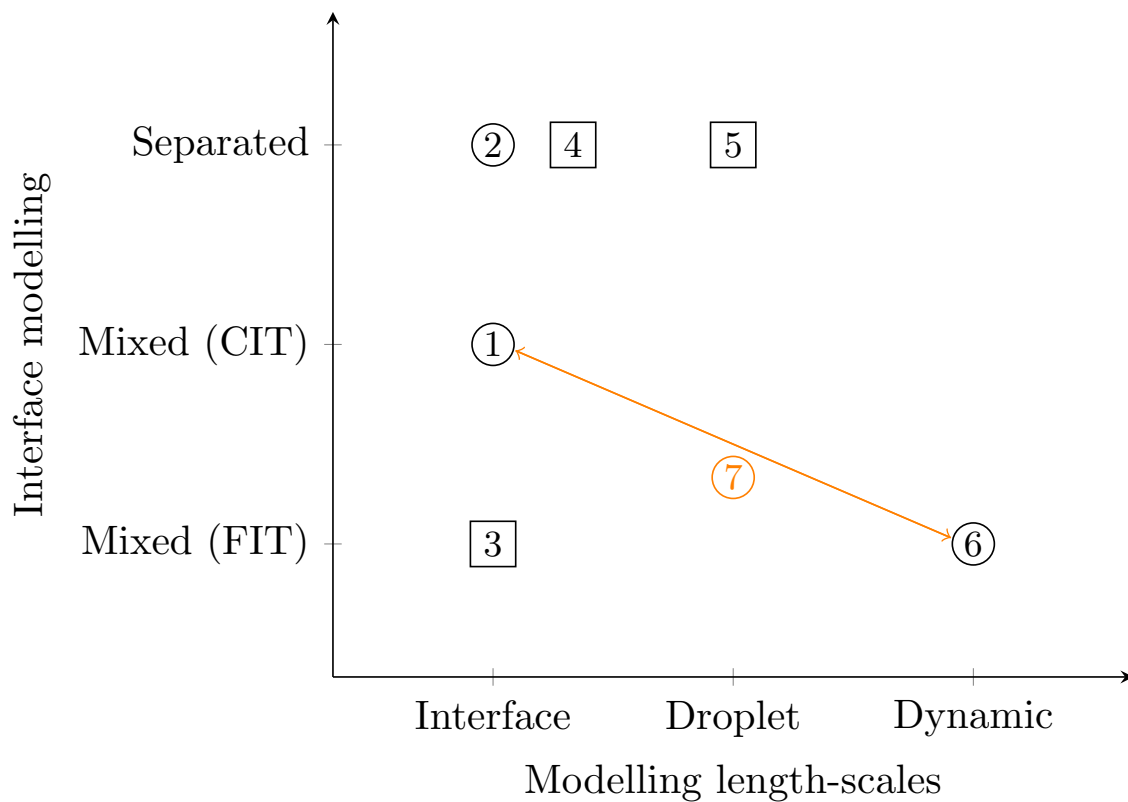


Figure 2.9 – Map of the modeling possibilities for the atomization problem. The 2 dimensional modeling space couples the modeling length scales chosen and the type of interface modeling chosen.  $\square$  represents the compressible flow models and the  $\circ$  the incompressible flow ones. In table 2.1 the reference to the different point represented in the modeling space.

①	<i>InterFoam</i> ([Rus02]);
②	Level-Set ([OS88]), VOF ([HN81]), CLSVOF ([MTB07]);
③	Baer-Nunziato ([BN86]), Cordesse ([Cor20]), Saurel ([SP18]), Cahn-Hilliard([EII89]);
④	Canu([Can19]), Zou-Grenier ([Zou+20]);
⑤	Kinetic Approach ([Wil58]);
⑥	<i>ELSA</i> ([VB99],[Che10]);
⑦	<i>ICMelsa</i> ([Ane+19a]).

Table 2.1 – Table with the resume of the map of the models referred to fig. 2.9. Are represented some examples of models relative to the classification discussed along the chapter.





## Chap. 3 | Numerical models comparison: the air-assisted liquid sheet test case

In the previous chapter we highlighted how important it is to define a metric to compare different numerical models. In this chapter we define this metric in order to compare different way to model the multi-scale atomization phenomenon. The plan of the work is to compare different interface treatment modeling approaches. For this purpose three different codes will be considered:

- *ARCHER* : will be the reference code. The code is developed at CORIA (<https://www.coria-cfd.fr/index.php/Archer>) and an incompressible model with separated phases representation (CLSVOF+PLIC reconstruction) is used ([MTB07], [Vau+17]).
- *CEDRE* : in this code developed at ONERA (<https://cedre.onera.fr/>) the compressible mixed phases model in this code and the results of the simulations post-processed and used in this thesis have been achieved by Pierre Cordesse in his PhD manuscript ([Cor20]). The subsequent validation of the model have been achieved in [Cor+20b].
- *OpenFoam* : in the multi-physics *C++* library (<https://cfd.direct/openfoam/>) three different model will be tested: *InterFoam* solver where a mixed phases CIT approach is applied ([Wel]); *ELSA* and *ICMelsa* that have in common to complement the approach by additional physical model, where the mesh resolution is not sufficient to capture properly all the interface. In both cases part of the dynamic of the flow is described with a LES turbulence modeling approach. The difference among *ELSA* and *ICMelsa* lies in the interface treatment. While *ELSA* implements a mixed phases FIT model, *ICMelsa* (as presented in the previous chapter) considers an hybrid interface treatment that switches from a mixed phases CIT model to a mixed phases FIT representation.

In the first part of the chapter we introduce the different codes used for this comparison, presenting models implemented in the different codes and the numerical methods associated to them. In the second part we build a meaningful configuration for our tests. It should be representative of the atomization that can be encountered in an aeronautical industrial set-up but at the same time simple enough and flexible to allow the simulations with the different codes. In the third part we define the metrics and in the last part we present the post-processing results, pointing out how the different interface representation influences the statistics related to the different quantities characterizing the flow field.

The work hereafter presented is part of the following publications: [Rem+19], [Cor+20b].

### 3.1 Modeling the interface

In the chapter 2 we introduced two main models for the interface treatment in flow: mixed phases model and separated phases model. In the second case we have highlighted that we can classify them as *sharp interface* approaches, due to the discontinuity among properties caused by the interface model. There are in literature also mixed phases models that aims to reproduce the *sharp interface* behaviour of the separated phases models, by implementing a numerical counter-flux ([Rus02]). In this thesis they will go under the family of mixed phases CIT approaches.

In the next sections we will present the code used for the reference simulation (*ARCHER*), the code implementing a FIT approach with the mixed phases formalism (*CEDRE*) and the code implementing a counter-flux interface sharpening CIT approach using the mixed phases formalism (*InterFoam*). We'll go through the numerical models and methods used.

#### 3.1.1 ARCHER

*ARCHER* is a DNS code developed in CORIA laboratory in Rouen. The equations that are discretized and solved inside the solver are the incompressible N-S system supplemented by a coupled level-set VOF approach (CLSVOF) with interface reconstruction through a PLIC strategy [MTB07].

In *ARCHER* the equations are discretized through a finite difference approach ([QQ09], [FP12]) on a staggered grid, where the velocities are placed at the faces of the cells, while the other variables are placed at the center of the cells. In the *ARCHER* code structured grids are considered. The level-set function  $\phi(x, y)$  is a distance signed function. The interface  $\Gamma$  location is defined as  $\phi(x, y) = 0$ . Mathematically the properties of the distance function can be written as  $|\nabla\phi(x, y)| = 1$ . The equation of the level-set (see chapter 2) is discretized with a Weighted Non-Oscillatory Scheme (WENO) [Shu98] scheme. This scheme has the advantage to combine accuracy and robustness and is of 5th order accurate.

After every iteration of transport, the level-set loses its distance function property  $|\nabla\phi| \neq 1$ . This property is of critical importance for the computation of normals, and hence of the curvature, that has to be the most precise possible in the computation of surface tension force ([Vau15]). A re-distancing algorithm is implemented:

$$\frac{\partial d(x, y, \tau)}{\partial \tau} = \text{sgn}(\phi(x, y, t))(1 - |\nabla d(x, y, \tau)|) \quad (3.1)$$

With the initial condition of:

$$d(x, y, \tau = 0) = \phi(x, y, t) \quad (3.2)$$

The *sign* function is defined as:

$$\text{sign}(\phi(x, y, t)) = \frac{\phi(x, y, t)}{\sqrt{\phi(x, y, t)^2 + dx^2}} \quad (3.3)$$

$\tau$  is the fictitious time-scale used to reach the steady state and hence the distance function. Eventually we obtain:

$$\phi(x, y, t) = d(x, y, \tau_{end}) \quad (3.4)$$

The equation is discretized in space with a WENO scheme of order 5 and the temporal integration is performed with a Runge-Kutta scheme of order 2. The discretization of this equation can bring to a mass-loss more or less important. To try to contain this effect, the level-set method is coupled with the VOF method in the CLSVOF method.

The VOF transport equation, introduced in chapter 2 can be resolved in its discretized form using two different approaches:

- Using high order numerical scheme for spatial and time resolution in order to limit the numerical diffusion;
- reconstructing geometrically the interface.

In the *ARCHER* code the approach used is the second one. The reconstruction of the interface has a crucial role in the computation of fluxes inside the finite volume method. The method used to reconstruct the interface is the PLIC method. This method allows to reconstruct the interface starting from the VOF function, considering the normal to the plane. The coupling between the VOF and level-set method is performed in two different steps:

- A level-set is determined in a cell and it is possible to reconstruct the corresponding volume of the liquid.
- After the advection of the level-set and the re-distancing algorithm, the VOF function is used to adjust the interface position in order to assure that the liquid corresponding to the reconstructed level-set function is the same of the one defined by the VOF function (more details in [MTB07] and [Mén07])

To compute velocity and pressure, the momentum transport equation eq. (2.2) is solved using a standard projection method. This method allows to decouple velocity and pressure. An intermediate velocity is first calculated without the pressure term  $-\nabla p$  and the surface tension term

$$\mathbf{v}^* = \frac{\rho^n \mathbf{v}^n}{\rho^*} - \Delta t \underbrace{\frac{\nabla \cdot ((\rho \mathbf{v})^n \otimes \mathbf{v}^n)}{\rho^*}}_I + \Delta t \underbrace{\frac{\nabla \cdot (2\mu \mathbf{D})}{\rho^*}}_{II}, \quad (3.5)$$

where  $\rho^*$  corresponds to the density calculated with the new value of  $\alpha_l$  obtained after the interface resolution,  $\rho^* = \alpha_l^{n+1} \rho_l + (1 - \alpha_l^{n+1}) \rho_g$ ,  $\mathbf{D}$  is the strain rate tensor ( $\mathbf{D} = [\mu(\nabla \mathbf{v} + \nabla^T \mathbf{v})]$ ). Regarding the convection term *I*, the method of Vaudor et al. [Vau+17] has been used ensuring consistent mass and momentum fluxes computation. The mesh is an Eulerian staggered grid so the velocity is computed on the faces of the cells and the other variables (pressure, density, liquid volume fraction, ...) are computed in the center of the cells. This method initially proposed in [Rud98] consists in calculating the mass flux  $\rho \mathbf{v}$  in the center of the cell by using the continuity equation. The mass flux has to be known in the center of the cell in order to have a second order centered scheme for the divergence operator. This procedure allows mass and momentum to be transported in a consistent manner thereby enabling flows with large liquid/gas density ratios to be simulated accurately. A detailed explanation of the algorithm can be found in Vaudor et al. [Vau+17].

Following the procedure of Sussman et al. [Sus+07], The dynamic viscosity used in the viscous term *II* ( $\mu_l$  or  $\mu_g$ ) depends on the sign of the level-set function. In mixed cells, a specific treatment is performed to evaluate the dynamic viscosity. This method takes into account directly the viscous tensor jump across the interface.

Then, the momentum equation is discretized in the following way by using the intermediate velocity obtained previously,

$$\mathbf{v}^{n+1} = \mathbf{v}^* - \Delta t \frac{\nabla P}{\rho^*} \quad (3.6)$$

By applying the divergence operator to eq. (3.6), an Helmholtz equation for the pressure is obtained

$$\nabla \cdot \left( \frac{\nabla P^{n+1}}{\rho^*} \right) = \frac{\nabla \cdot \mathbf{v}^*}{\Delta t}. \quad (3.7)$$

Equation (3.7) is solved using a MultiGrid preconditioned Conjugate Gradient (MGCG) algorithm [Zha96]. The  $\nabla \cdot \mathbf{v}^*$  term is solved with a second order centered scheme. A Ghost

Fluid Method (GFM) [Fed+99] is used to apply the pressure jump due to the presence of surface tension [MTB07]. The advantage of the GFM is a more realistic representation of the interface (sharp, infinitely thin): jump conditions are directly added at the interface position through a local modification of the numerical scheme. The distance of the interface is provided by the level-set function. The final velocity is computed by eq. (3.6) using a second order centered scheme for the pressure gradient. A second order predictor-corrector Runge Kutta scheme have been used for temporal integration. Concerning the time step calculation, a  $CFL$  condition similar to the one used by [KFL00] is used. For  $CFL = 1$ , the  $CFL$  condition can be written as:

$$\Delta t \left( \frac{(C_{cfl} + V_{cfl}) + \sqrt{(C_{cfl} + V_{cfl})^2 + 4(S_{cfl})^2}}{2} \right) \leq 1 \quad (3.8a)$$

with:

$$C_{cfl} = \frac{\max(|u_x|)}{\Delta x} + \frac{\max(|u_y|)}{\Delta y} + \frac{\max(|u_z|)}{\Delta z}, \quad (3.8b)$$

$$V_{cfl} = \left( \frac{2}{\Delta x^2} + \frac{2}{\Delta y^2} + \frac{2}{\Delta z^2} \right) \times \max \left( \frac{\mu_l}{\rho_l}, \frac{\mu_g}{\rho_g} \right), \quad (3.8c)$$

$$S_{cfl} = \sqrt{\frac{\gamma|H|}{\min(\rho_g, \rho_l) \times \min(\Delta x, \Delta y, \Delta z)^2}}, \quad (3.8d)$$

$$H = \frac{k_1 + k_2}{2} \quad (3.8e)$$

### 3.1.2 CEDRE

#### The model

The mixed phases FIT model proposed by Baer-Nunziato and already presented in the previous chapter is implemented in the fluid dynamic software CEDRE working on general unstructured meshes and implementing a set of solvers developed at the french aerospace lab (ONERA). The solver SEQUOIA is in charge of the mixed phases FIT model. The model has been developed in [Cor20].

At the top of the hierarchy of *diffuse interface* models ([SP18]) stands the Baer-Nunziato model, also called the *seven equation model*, accounting for full disequilibrium of the phases. This first-order non-linear non-conservative system of partial differential equations is composed of a mass, momentum and energy equation for each phase and a seventh equation on the volume fraction  $\alpha$  to reconstruct the interface. The extended form proposed in [SA99] introduces an interfacial pressure,  $p_l$ , and an interfacial velocity,  $v_l$ , that need to be closed. The quasi-linear form of the system in the one-dimensional case takes the form

$$\partial_t q + \mathcal{A}(q)\partial_x q = r(q), \quad (3.9a)$$

with  $\mathcal{A}(q) = \partial_q f(q) + \mathcal{N}(q)$  and

$$\partial_q f(q) = \begin{pmatrix} 0 & 0 & 0 \\ 0 & \partial_{q_2} f_2(q_2) & 0 \\ 0 & 0 & \partial_{q_1} f_1(q_1) \end{pmatrix}, \quad \mathcal{N}(q) = \begin{pmatrix} v_l & 0 & 0 \\ n_2 & 0 & 0 \\ n_1 & 0 & 0 \end{pmatrix}, \quad (3.9b)$$

$$q_k = \begin{pmatrix} \alpha_k \rho_k \\ \alpha_k \rho_k v_k \\ \alpha_k \rho_k E_k \end{pmatrix}, \quad f_k(q_k) = \begin{pmatrix} \alpha_k \rho_k v_k \\ \alpha_k (\rho_k v_k^2 + p_k) \\ \alpha_k (\rho_k E_k + p_k) v_k \end{pmatrix}, \quad n_k(q) = \epsilon_k \begin{pmatrix} 0 \\ p_l \\ \rho_l v_l \end{pmatrix}, \quad (3.9c)$$

where the column vector  $q \in \mathbb{R}^7$  is defined by  $q^t = (\alpha_2, q_2^t, q_1^t)$ , the conservative flux  $f : q \in \Omega \mapsto \mathbb{R}^7$  reads  $f(q)^t = (0, f_2(q_2)^t, f_1(q_1)^t)$  and  $\mathcal{N} : q \in \Omega \mapsto \mathbb{R}^{7 \times 7}$  is the matrix containing the non-conservative terms. Furthermore we have  $\epsilon_k = (-1)^{k+1}$ . Then,  $\alpha_k$  is the volume fraction of phase  $k \in [1, 2]$ ,  $\rho_k$  the partial density,  $v_k$  the phase velocity,  $p_k$  the phase pressure,  $E_k = e_k + v_k^2/2$  the total energy per unit of mass and  $e_k$  the internal energy. Concerning the relaxation source term,  $r(q)$ , it decomposes into

$$r = \lambda r^v + \mu r^p, \quad r^v = \begin{pmatrix} 0 \\ r_2^v \\ r_1^v \end{pmatrix}, \quad r^p = \begin{pmatrix} p_d \\ r_2^p \\ r_1^p \end{pmatrix}, \quad (3.10a)$$

$$(r_k^v)^t = -\epsilon_k (0, v_d, v_l v_d), \quad (r_k^p)^t = -\epsilon_k (0, 0, p_l p_d), \quad (3.10b)$$

where we have introduced the pressure difference  $p_d = p_2 - p_1$  and the slip velocity  $v_d = v_2 - v_1$ . An expression for the relaxation parameters  $\lambda$  and  $\mu$  have been derived for example using the DEM technic in [SGR03]. Hereafter, we will consider the phase 1 to be the gaseous phase and the phase 2 to be the liquid phase. We will thus explicit the subscripts by using  $g$  and  $l$ . From this seven-equation model, the instantaneous relaxation of the pressures and the velocities leads to the *five-equation* model [Kap+01] and relaxing also instantaneously the temperatures, one obtains the compressible multi-species N-S equations referred as the *four-equation* model. These three models define a hierarchy of *diffuse interface* model and each of them are hyperbolic and appropriate for reactive two-phase flow or interface problems. In cryogenic applications, the pressure of the phases may be considered to relax instantaneously, but due to the strong velocity and temperature gradients at the interface, it is unrealistic to assume hydrodynamic and thermal instantaneous relaxations. Whereas single velocity models are sufficient in the separated zone with an adapted resolution mesh, it is not the case in the mixed region and thus fail at predicting the atomization process. Therefore the B-N model (eq. (3.9)) appears as the best candidate for the present study. Nonetheless, stemming from rational thermodynamics, the macroscopic set of equations can not be derived from physics at small scale of interface dynamics and thus require closure of interfacial pressure and velocity as well as to postulate the thermodynamics. The theory on the existence of a supplementary conservative equation to first-order order system of partial differential equation including non-conservative terms [CM20] has brought about supplementary conservative equations together with constraints on the interfacial quantities and the definition of the thermodynamics of the mixture. In the present work, we use a non-miscible fluid thermodynamics, where the mixture entropy is defined by the mass averaged sum of the phasic entropies with no mixing effect, together with a closure proposed in [FS15] obtained through a discrete element method approach [SGR03]. Only mechanical and hydrodynamic relaxations are accounted for in the present study. They are modeled as in [FS15] through a pressure difference term and a drag term as in Equation (3.10). Each term is driven by a characteristic time, which can be finite to account for disequilibrium. In the limit of an instantaneous relaxation, any disequilibrium disappear. We have used an instantaneous pressure relaxation but a finite velocity relaxation.

**The numerical method** The numerical methods employed to solve the Baer-Nunziato model eq. (3.9) are implemented in the multiphysics computational fluid dynamics software CEDRE [Gai+16] working on general unstructured meshes and organized as a set of solver

[Gai+16] developed at the french aerospace lab ONERA. The solver *SEQUOIA* is in charge of the mixed phases FIT model. The implementation and the simulation have been done by Pierre Cordesse in the context of his PhD. For more information refer to [Cor20]. The Strang splitting technique applied on a HLLC solver proposed in [FS15] has been successfully implemented in the solver *SEQUOIA* of the CEDRE CFD code. Second-order extension is achieved using a second-order Runge-Kutta scheme for the time discretization of each sub-system together with a multislope MUSCL second-order space discretization [LTMG14]. The technique consists in computing two dedicated slopes for each face of each mesh cell. It uses the vertex neighbors and ensures the  $L^\infty$  norm stability on the scalar advection. The issue encountered when discretizing the non-conservative terms is tackled in [FS15] by assuming (1) the interfacial quantities  $\rho_I$  and  $\mathbf{v}_I$  to be local constants in the Riemann problem, (2) the volume fraction to vary only across the interfacial contact discontinuity  $\mathbf{v}_I$ . As a result, the non-conservative terms vanish,  $\mathbf{v}_I$  and  $\rho_I$  are determined locally by Discrete Equation Method (DEM) [SGR03] at each time step and stay constant during the update. Thus, phases are decoupled, the system splits into two conservative sub-systems to which we apply the multi-slope HLLC with hybrid limiter solver.

Depending on the application, the relaxations are assumed either instantaneous or finite in time. In the present test case, it is reasonable to assume a instantaneous pressure relaxation,  $\mu \rightarrow +\infty$ , but one need to consider a finite velocity relaxation since the interface dynamic is mainly driven by the shear stress induced by a high velocity difference between the phases at the injection.

To obtain the relaxed pressure, since the characteristic time is taken to be infinitely small, the problem reduces to apply an iterative procedure as a Newton method to solve a second order ordinary differential equation (ODE). The iterative procedure returns a single equilibrium pressure. Detailed equations can be found in [FS15]. As for the velocities, since we want to account for finite relaxation time, the associated ODE takes the form

$$\partial_t \mathbf{v}_d - \frac{A^\circ}{\epsilon_v} \mathbf{v}_d = 0, \text{ with } A^\circ = \frac{\rho^\circ}{\alpha_I^\circ \rho_I^\circ \alpha_G^\circ \rho_G^\circ}, \quad (3.11)$$

where  $\epsilon_v$  is the characteristic relaxation time,  $\epsilon_v = 1/\lambda$ , superscript  $^\circ$  denotes the state before relaxation and  $\rho$  is the mixture density,  $\rho = \alpha_I \rho_I + \alpha_G \rho_G$ . A first numerical approach is to fix a remaining slip velocity ratio target at each computational time step  $\Delta$ . It defines the characteristic relaxing time as

$$\frac{\epsilon_v}{A^\circ} = \ln \left( \frac{v_d(\Delta t)}{v_d^\circ} \right) \Delta t. \quad (3.12)$$

An instantaneous velocity relaxation is in practice also possible and manipulating the ODE leads to a unique relaxed velocity, which is the mass weighted average of the two velocities before relaxing. In the present simulation, we have however been using the finite velocity relaxation.

### 3.1.3 InterFoam

The *InterFoam* model is a mixed phases CIT model that point to reproduce the *sharp interface* shape of a separated phases formalism, through the use of a numerical sharpening flux in the liquid volume fraction transport equation.

The discretization is performed through the finite volume method ([QQ09], [FP12]), considering the unstructured grid formalism. The algorithm to solve the incompressible N-S equations system is the well known Pressure-Implicit with Splitting of Operators (PISO) algorithm introduced in [Iss86].

**PISO algorithm**

Representative of a segregated approach, the solution of the system is found by solving in an iterative manner the equations for velocity and for pressure.

a. **Velocity predictor:**

It is possible to find a first prediction of the velocity field based on the solution at the previous time step. This is not a compulsory step but helps in the convergence process.

b. **Compute pseudo-velocity:**

Using either the predicted velocity or the previous time step velocity it is necessary to compute the new velocity, not considering the pressure term. This is the first step of the classical *projection methods* (e.g [Cho68]).

c. **Pressure direct solution:**

The pressure at the current time step is obtained by solving the Poisson equation obtained by taking the divergence of the correction equation (eq. (3.7)).

d. **Explicit velocity corrector:**

The new pressure has been computed and the velocity can be corrected.

e. **Flux corrector:**

The flux must be corrected taking into account the pressure computation: point from b. to e. must be re-iterated to get as close as possible to the solution.

**Phase equation** The classical VOF method requires an equation of transport for the liquid volume fraction  $\alpha_l$ :

$$\frac{\partial \alpha_l}{\partial t} + \nabla \cdot (\alpha_l \mathbf{v}) = 0 \quad (3.13)$$

In order to keep the interface sharp, a conservative version of the equation eq. (3.13) has been implemented, with an additional *compression term* weightened in a way that acts only at the interface (with the weight  $\alpha_l(1 - \alpha_l)$ ). The implementation and more theoretical details can be found in ([Rus02]).

$$\frac{\partial \alpha_l}{\partial t} + \nabla \cdot (\alpha_l \mathbf{v}) = -\nabla \cdot [\mathbf{U}_c \alpha_l (1 - \alpha_l)] \quad (3.14)$$

Analysing the compression term:

- $\alpha_l(1 - \alpha_l)$  is the contribution that force the term to be activated only in the neighbourhood of the interface;
- $U_c$  is the term that modulate the compression. It is defined as the relative velocity between two phases  $\mathbf{U}_r$  multiplied by  $C_\alpha$ , and it is usually defined in the code as:

$$\mathbf{U}_c = C_\alpha \mathbf{U}_r = C_\alpha |\mathbf{v}| \cdot \mathbf{n} \quad (3.15)$$

where  $\mathbf{n}$  is the normal to the liquid-gas interface directed toward it,  $C_\alpha$  is a parameter that in literature is always set to 1 (for an example where the value is varied, see [WW13]).

In order to understand fully the resolution method used for the liquid volume fraction evolution equation, in the following paragraphs we will go through the whole discretization procedure.

**Discretization of the phase indicator** The eq. (3.14) for the evolution of the liquid volume fraction  $\alpha_l$  can be discretized in time, considering as  $\alpha_l^{n+1} = \alpha_l(x, t^{n+1})$ ,  $\alpha_l^n = \alpha_l(x, t^n)$  the liquid volume fraction value evaluated respectively at time  $t^n$  and  $t^{n+1}$  at the center of the computational volume, and  $\Delta t = t^{n+1} - t^n$ .

$$\alpha_l^{n+1} = \alpha_l^n - \Delta t \{ \nabla \cdot [\mathbf{v} \alpha_l + U_c \alpha_l (1 - \alpha_l)] \} \quad (3.16)$$



The time discretization performed in eq. (3.16) is first order accurate in time and recover a typical forward Euler scheme ([BG08]). Following the discretization in time, it is possible to proceed to the discretization of the equation following the finite volume formalism, for a control volume  $V$ . We define with the notation  $\alpha_{l,f}$  the liquid volume fraction value evaluated at the control volume faces and we denote with  $\sum_f$  the sum operation over all the faces of the control volume.

$$\alpha_l^{n+1} = \alpha_l^n - \frac{\Delta t}{V} \sum_f [F \alpha_{l,f} + F_c \alpha_{l,f} (1 - \alpha_{l,f})] \quad (3.17)$$

For the sake of simplicity the flux terms are grouped together in the flux  $F_{\alpha_l}$  as:

$$F_{\alpha_l} = F \alpha_{l,f} + F_c \alpha_{l,f} (1 - \alpha_{l,f}) \quad (3.18)$$

So finally it is possible to write the equation in the canonical discretized form ([LeV02]) as:

$$\alpha_l^{n+1} = \alpha_l^n - \frac{\Delta t}{V} \sum_f F_{\alpha_l} \quad (3.19)$$

**FCT and MULES for the solution of  $\alpha$  equation** The pressure-velocity coupling is solved using the PISO algorithm described previously, while it is necessary to add a method for solving the discretized equation of liquid volume fraction (eq. (3.17)). The one used in the *OpenFoam* implementation is the Multidimensional Universal Limiter for Explicit Solution (MULES) and it is an Flux-Corrected Transport (FCT) algorithm. This technique was first introduced by [BB73] and ameliorated by [Zal79], it guarantees the boundedness of the solution of hyperbolic problems.

The principle of FCT is that given a transport equation for a variable  $\phi$ :

$$\frac{\partial \phi}{\partial t} + \nabla \cdot \mathbf{F} = 0 \quad (3.20)$$

Considering a 1D case, given the index  $i$  that determines the cell and  $n$  the temporal step, the eq. (3.20) can be discretized as:

$$\frac{\phi_i^{n+1} - \phi_i^n}{\Delta t} V + \sum_f (\mathbf{F}^n \cdot \mathbf{S})_f = 0 \quad (3.21)$$

Isolating the center of a cell labelled as  $i$ , it is possible to write (as for a Godunov first order accurate scheme [LeV92]):

$$\phi_i^{n+1} = \phi_i^n - \frac{\Delta t}{V} (F_{i+1/2}^n - F_{i-1/2}^n) \quad (3.22)$$

The boundedness of the temporal solution can be obtained via face value limiting, or limiting face fluxes. A classical Total Variation Diminishing (TVD) scheme algorithm is defined as following:

- Compute  $F^L$ , flux computed with a low order scheme;
- compute  $F^H$ , flux computed with an high order scheme;
- Define an anti diffusive flux  $A = F^H - F^L$
- compute a corrected flux  $F^C = F^L + \lambda_i A$ , with  $\lambda_i$  is defined for each cell and we call it *flux limiter* [LeV02].
- solve the equation (in this case it has been chosen a particular time scheme):

$$\phi_i^{n+1} = \phi_i^n - \frac{\Delta t}{V} (F_{i+1/2}^C - F_{i-1/2}^C) \quad (3.23)$$

For the particular case of application to *InterFoam* the authors suggest the reading of [Ahm19]. We recap the organization of the algorithm in fig. 3.1.

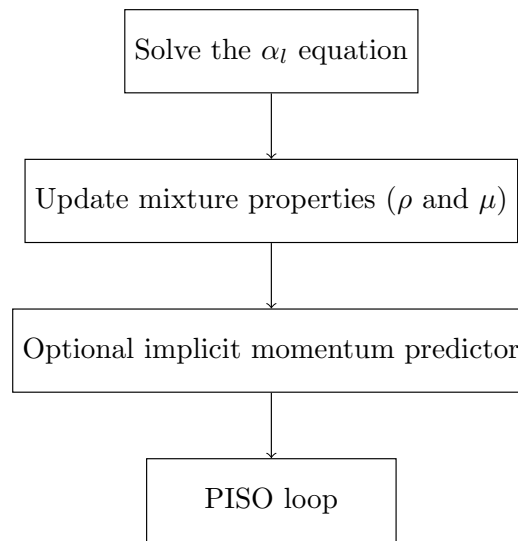


Figure 3.1 – Flow chart of the step for the solution of the incompressible multiphase system issued by an interface compression model inside the *InterFoam* solver.

## 3.2 Physical model of sub-grid interface

In the previous section we introduced 3 different codes implementing two different interface modelling approaches.

As already presented in chapter 2 it is possible to raise further the modeling length-scale, taking inside the model part of the effect of the dynamic of the flow. In the next sections the interface modeling will be supplemented by the LES modeling technique as was introduced previously in section 2.2.7. From the point of view of the interface treatment, two different models will be presented. A first mixed phases FIT approach (*ELSA*) and an hybrid mixed phases CIT - FIT model (*ICMelsa*) already discussed in section 2.2.7.

### 3.2.1 ELSAFoam

The *ELSA* approach was first developed by Borghi in [VB99] following a time-averaging approach and later extended in [Bea06] to the LES formalism. The model itself was presented in chapter 2. It follows the mixed phases approach and adds to the filtered N-S incompressible equation system the filtered liquid volume fraction transport equation:

$$\frac{\partial \bar{\alpha}_l}{\partial t} + \nabla \cdot (\bar{\alpha}_l \bar{\mathbf{v}}) = -\nabla \cdot \mathbf{R}_{\alpha_l} \quad (3.24)$$

where on the RHS we find the turbulent liquid flux  $\mathbf{R}_{\alpha_l} = \overline{\mathbf{U}'\alpha'_l}$  that must be modeled. As suggested in section 2.2.5, this term is modeled following the gradient hypothesis as:

$$\mathbf{R}_{\alpha_l} = \frac{\nu_t}{Sc_t} \nabla \alpha_l \quad (3.25)$$

Another equation is added to the set: the transport of the interface area density function. For further details, it is suggested to the reader to refer to section 2.2.5. The  $\nu_t$  depends on the filter used to average equations (spatial or time) and on the turbulence modeling approach used. In our case an implicit LES filter is used and a Smagorinsky approach is deployed [Sma63].

The algorithm to solve the system of the equations is the same used for the *InterFoam* approach previously introduced, the slight difference is in the solution procedure. A step

is added after the transport of the liquid volume fraction to solve implicitly the RHS part. A further step is added at the end of the algorithm to solve the transport of the sub-grid interface area density  $\Sigma'$ , along with the formulation for the minimum interface area density  $\Sigma_{min} = |\nabla\alpha_l|$ . It is possible to have a complete overview of the algorithm in the flow chart proposed in fig. 3.2.

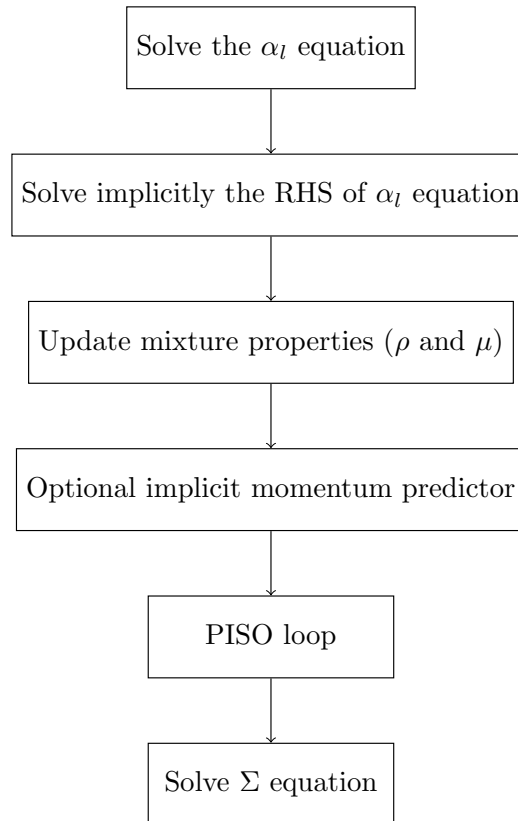


Figure 3.2 – Flow chart of the step for the solution of the incompressible multiphase system issued by the ELSA model inside the *ElsaFoam* solver.

### 3.2.2 ICMelsa Foam

The complete *ICMelsa* model was previously introduced and discussed in section 2.2.7. It is a multi-scale approach that unifies the DNS like approach of the mixed phases CIT model *InterFoam* and the LES approach of the *ELSA* mixed phases FIT model, pointing to a full description of the evolution of the interface along all the atomization process. The equations are discretized using the finite volume formalism. The coupling among velocity and pressure is solved through the PISO algorithm, while the hybrid evolution equation for the liquid volume fraction is solved through the use of the MULES algorithm reported in the previous sections. The liquid volume fraction equation can switch from *InterFoam* to *ELSA* mode with respect to the  $C_\alpha$  variable which depends on the *IRQ* (for the different definitions of *IRQ* the reader can refer to section 2.2.7). The *IRQ* is evaluated immediately after the resolution of the evolution equation for the interface area density. The *IRQ* chosen to determine if the dynamic of the interface is well resolved or not and hence to evaluate the  $C_\alpha$  is the  $IRQ_\Sigma$  and the limit value has been chosen to  $IRQ_\Sigma = 0.65$ . This value has been chosen in relation to a numerical parametric study on a simplified configuration (for the interested reader refer to appendix B). It is possible to have a complete overview of the algorithm in the flow chart

proposed in fig. 3.3.

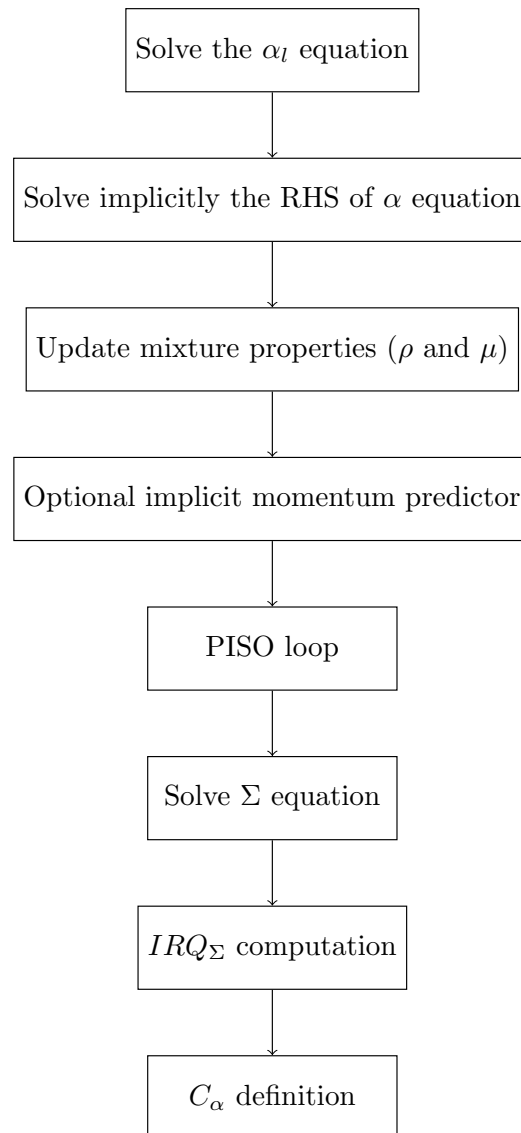


Figure 3.3 – Flow chart of the step for the solution of the incompressible multiphase system issued by the ICM model inside the *ICMEIsaFoam* solver.

### 3.3 Configuration

#### 3.3.1 Bibliography about the air assisted liquid sheets

In the industrial framework (e.g aeronautic and agricultural) are commonly used injectors in which the liquid is surrounded by moving air: the so-called air-blast atomizer. Even if most of the configurations are axis-symmetric, in the literature there is plenty of studies using the planar liquid sheet configuration. This is because of the relative experimental simplicity of such kind of geometry ([Loz+01]).

A first experimental study of a liquid sheet breaking into droplets was performed by Savart. He studied a simple process where a round liquid jet impacted on a flat circular surface ([Sav33]). A century later, Taylor in [Tay59a] and [Tay59b] reproduced a similar configuration in the so-called *water bell* configuration. A complete review of all experiences and studies using this configuration has been done recently in [VC02].

After the experiences of Taylor, a wide number of experiments have been performed, mostly based on visual observations and, along with it, was studied the linear stability ([Squ53]). The first linear stability analysis were conducted in quiescent air. In the following years, an interesting geometry was proposed by Dombrowski ([DHW60],[DJ63]): namely the so-called *water fans*. The authors stated the importance of viscosity in the instability of the liquid jet. Until that point the dynamic of the gas was completely ignored by imposing a non-shear boundary condition at the interface. A first attempt to model the viscosity of both fluids was performed in [CDJ75]. After that important achievements a long series of experiments with large aspects liquid sheets were carried out ([RL80],[Ara86]) until the first case with an air-assisted sheet atomization that can be found in [SS90]. In these seminal works, a phenomenological observation of the flow field was performed, in order to predict the droplet size characteristics. In particular Strapper and Samuelsen described the breakup process, noticing that it is dependents more on the velocity ratio among the two jets  $U_G/U_L$  than of two fluids properties ([SSS92]). In particular they noticed two breakup regimes:

- at low  $U_G/U_L$  what they refer to as *cellular breakup regime*, where the sheet oscillates with low amplitude growth. The penetration of the core it's high and the angle is low. The instability of the coherent liquid structure is due to slowly growing spanwise and streamwise ligaments;
- at higher  $U_G/U_L$  what they refer to as *ligament breakup regime*. The streamwise velocity becomes more important and the breakup is dominated by streamwise ligaments and sinusoidal lateral oscillations.

While the breakup regimes are independent on the fluid's properties, it is not the case for the droplet dimension (as reported in [SC95]). Successively the different kind of jet destabilizations were further analysed in [CD96] where it has been stated clearly that the breakup can be caused only by the sinusoidal or by non-symmetric perturbation, with the two parallel interfaces that oscillates in phase. For the interested reader a wide review about experimental work on liquid sheets atomization can be found in [Dum08] and for an interesting guide on destabilization mechanisms at different regimes it can be referred to [CHS02] (fig. 3.5).

Starting from the work of Lozano ([Loz+96],[Loz+01]) the attention of most of the works has been driven to a more precise identification of the breakup phenomena. This achievement was reached thanks to the use of numerical simulation. The final goal was to understand which of the instability phenomena just cited prevails with respect to the other, changing the fluid characteristics. The most recent work reported are from Zandian ([ZSH16],[ZSH17a],[ZSH17b],[ZSH18]). Through the vortex dynamics they identified three different breakup regimes that can occur at different density ratio, gas Weber number and liquid Reynolds number.

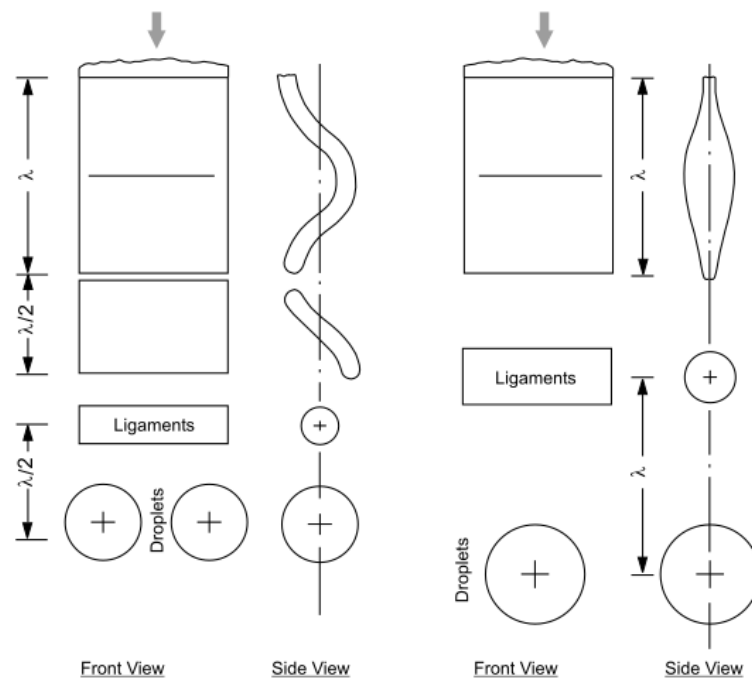


Figure 3.4 – Instabilities that brings to the film disintegration in an air assisted liquid sheet configuration [CHS02].

### 3.3.2 Building a benchmark configuration

The present configuration has been set by adjusting flow parameters in order to promote a fast atomization, limit the liquid core penetration and having a density ratio realistic for aircraft engines. A reasonably high momentum  $M = \frac{\rho_g v_g^2}{\rho_l v_l^2} = 18.7$  is obtained with a moderately high velocity ratio,  $v_g/v_l = 43$  and a density ratio  $\frac{\rho_g}{\rho_l} = 1/100$ . To reduce the role played by the surface tension, since it is not solved by the mixed phases model CEDRE, we have chosen a high relative gaseous Weber number,  $We_R = 403$ .

### 3.3.3 Geometry and description of various meshes

The simulated domain described in fig. 3.5. The gas velocity profile  $v_g$  given in eq. (3.26) is

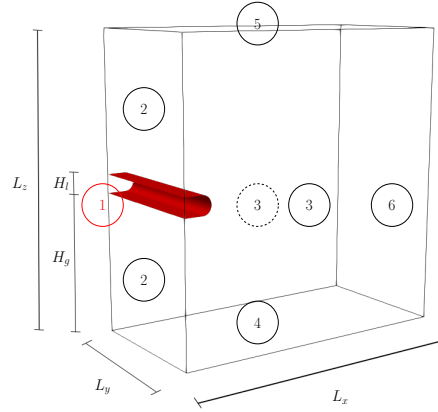


Figure 3.5 – Geometry of the configuration. (1) is the liquid injection plane. (2) is the gas injection plane. (4)(5)(6) are the outlet planes. (3) are the periodic planes.

units	$H_l$	$H_g$	$L_x$	$L_y$	$L_z$
(mm)	1	7.5	16	4	16

(a) Dimensions

Phase	$\rho$ (kg/m <sup>3</sup> )	$p$ (MPa)	$\gamma$ (N/m)	$\mu$ (Pa.s)
Liquid	100	0.1	0.01	0.0001
Gas	1	0.1	0.01	0.0001

(b) Fluids physical properties

Table 3.1 – Dimensions and physical properties of the configuration.

typical for turbulent pipe flow [Sch74].

$$v_g = v_g^{avg} \frac{7}{6} \left( \frac{2|z| - H_g}{H_g - H_l} \right)^{\frac{1}{6}} + v_l. \quad (3.26)$$

The average gas velocity  $v_g^{avg}$  is 65 m/s. An offset equal to  $v_l = 1.5$  m/s ensures the continuity of the velocity profile at the injection plan. The *ARCHER* simulations are performed on a Cartesian mesh  $512 \times 128 \times 512$  with a cell size equal to  $\Delta x = 3.125 \cdot 10^{-5}$  m, so a total of 101M faces, 33.6M cells and 32 cells in the liquid slot. In terms of degrees of freedom, which is defined as the product of the number of variables solved and the number of cells, *ARCHER* solves 42.0M. *CEDRE* simulations have been performed on two meshes composed of tetrahedral cells. The first, referred later on as *CEDRE (MR)*, proposes a medium refinement level with 148k faces, 71.7k cells and 788k degrees of freedom, and the second, referred later on as *CEDRE (HR)*, a high refinement level with 1.11M faces, 546k cells, thus 6.01M

degrees of freedom. *CEDRE (MR)* has only 10 cells in the slit, while *CEDRE (HR)* has 20 cells. The *InterFoam* simulation is performed on the same mesh as *ARCHER*. For the *ELSA* and *ICMelsa* solver it has been used a structured mesh with 24M faces, and hence 1/5 with respect of the number of faces of the *ARCHER* simulation. In the vicinity of the injection *ELSA* meshes have been built to have a mesh resolution comparable to the *CEDRE (HR)* one. The data are summarized in Table 3.2. In order to compare the results of the *ARCHER*

	Face number	Cell number	$d_l / \min(\Delta x)$
<i>CEDRE (MR)</i>	0.148M	71.7k	10
<i>CEDRE (HR)</i>	1.11M	546k	20
<i>ARCHER</i>	101M	33.6M	32
<i>InterFoam</i>	101M	33.6M	32
<i>ELSA</i>	24M	8M	20
<i>ICMelsa</i>	24M	8M	20

Table 3.2 – Mesh statistics of the simulations.

simulation to the results obtained with *CEDRE*, one must consider the fact that the *ARCHER*, *InterFoam*, *ELSA*, *ICMelsa* solvers are incompressible, thus there is no acoustic impacting the liquid sheet and both gas and liquid densities are constant. To restrain the acoustic role in the *CEDRE* compressible solver, we have enlarged the computational domain by a factor 5 in the  $x$  and  $z$  direction.

Another important factor to take into account is the fact that the *ELSA* and *ICMelsa* solver have been used considering a LES approach for the modelling of the turbulence. As far as there is no solid wall in this configuration, a classical implicit filter with Smagorinsky approach has been used (for more details about Smagorinsky model refer to chapter 2). Considering the configuration designed and the *ELSA* model described in the previous section, it is interesting to notice that the turbulent liquid flux modeling term, present in the liquid volume fraction transport equation, has been developed with the assumption of high Weber and Reynolds numbers. Thus this model is somehow here applied out of his domain of application for the purpose to test it.

### 3.4 Metric of comparison

The comparison among the different interface treatment strategies is done taking into account that we are in a turbulent flow and hence it is necessary to give relevance to the non-deterministic description. In this sense it is necessary for the reader to introduce some glossary in order to avoid confusion about the terminology used inside the following sections. In the analysis of the results we will follow a statistical approach. A very complete review about the averaging approaches used in *multi-phase* flow is given in [Ish75]. Here We will use different type of statistical operator for the different variables:

- Time averaging : given a field  $\phi(\mathbf{x}, t)$  the time average can be defined like

$${}^t\bar{\phi}(\mathbf{x}) = \frac{1}{\Delta t} \int_{\Delta t} \phi(\mathbf{x}, t) dt \quad (3.27)$$

where  $\Delta t = t_f - t_i$  is the time-scale of the regularization kernel. In the temporal averaging case for stationary process the  $\Delta t \rightarrow \infty$ . In the real case it is not possible but we chose an averaging time  $\Delta t$  that is sufficiently long to achieve a reasonable statistical convergence.



- Space averaging : given a field  $\phi(\mathbf{x}, t)$  the time average can be defined like

$${}^x\bar{\phi}(t) = \frac{1}{\Delta x} \int_{\Delta x} \phi(\mathbf{x}, t) dx \quad (3.28)$$

where  $\Delta x = \mathbf{x}_f - \mathbf{x}_i$  is the length of the regularization kernel.

- Ensemble or statistical averaging : considering a set of  $N$  similar physical system, the statistical averaging is defined by considering the arithmetic averaging among them (for a discussion about what does it mean similar system, we rely on [Ish75]).

$$\langle \phi \rangle (\mathbf{x}, t) = \frac{1}{N} \sum_{i=0}^N \phi_i(\mathbf{x}, t) \quad (3.29)$$

When not specified, the symbol  $\bar{\cdot}$  would signal an averaged value and the type of averaging operation performed will be specified in the text.

Once these elements have been defined, we can determine the different steps of the analysis:

- Time sequence of the dynamic of the interface, performing a comparison among the *diffuse interface* approach and the *sharp interface* approach.
- First order statistics comparison: we compare how the time and space average of liquid volume fraction and velocities are reproduced by different modelling strategies.
- Second order statistics comparison: we compare how Reynolds stress are captured by different strategies.

This statistical analysis will be called *classical analysis*, because of it follows the classical path of a turbulent flow analysis ([Vin+16]). We will call the second step *phase analysis* (chapter 4). In order to perform this kind of analysis, a new multi-purpose post-processing tool has been developed: REMODARCO. The time average is performed run-time from one relaunch to another of the simulation and successively, the different chunks of statistics are averaged together. The fact of having split chunks of statistics gives the advantage to choose which part of the flow history to use (and hence from which time to start the statistics collection) in order to perform the averaging.

### 3.5 Statistical convergence

An important concept in the study of statistics is the *statistical convergence* of the time series of a random variable ([Pro56]). In turbulence literature guidelines for *single-phase* configurations has been described to reach convergence (for instance in case of wall-bounded flows ([Vin+16])). In case of *multi-phase* flow it is hard to find a complete description of statistical convergence in case of coherent structures of one of the phases composing the system. We propose in this work a definition for the relative statistical convergence of flow variables.

Let's consider the domain depicted in fig. 3.5. It is possible to compute the liquid mass through the layer placed at  $L_y/2$  of width  $\Delta y$  as the integral of the liquid volume fraction multiplied by the layer width.

$$m_{tot} = \left( \int_0^{L_z} \int_0^{L_x} \alpha_l dx dz \right) \Delta y \quad (3.30)$$

It is possible to compute the time average of this quantity as it follows.

$${}^t\overline{m_{tot}} = \left( \int_0^{L_z} \int_0^{L_x} {}^t\overline{\alpha_l} dx dz \right) \Delta y \quad (3.31)$$

The configuration presented is a plane-symmetric configuration the domain is cut in half along the  $y$  direction, and the average liquid mass unbalance  $|{}^t\overline{m}_{up} - {}^t\overline{m}_{low}|$ , where:

$${}^t\overline{m}_{up} = \left( \int_{L_z/2}^{L_z} \int_0^{L_x} {}^t\overline{\alpha}_l dx dz \right) \Delta y \quad (3.32)$$

$${}^t\overline{m}_{low} = \left( \int_0^{L_z/2} \int_0^{L_x} {}^t\overline{\alpha}_l dx dz \right) \Delta y \quad (3.33)$$

Should verify the following relationship:

$$\Delta m = \lim_{t \rightarrow \infty} |{}^t\overline{m}_{up} - {}^t\overline{m}_{low}| = 0 \quad (3.34)$$

Following this idea, it is possible to determine a relative parameter  $\epsilon$  that evaluates the percentage of unbalance of mass among the upper and the lower part.

$$\epsilon = \frac{|{}^t\overline{m}_{up} - {}^t\overline{m}_{low}|}{{}^t\overline{m}_{tot}} \quad (3.35)$$

the parameter  $\epsilon \rightarrow 0$  as  $t \rightarrow \infty$  as a consequence of eq. (3.34). In fig. 3.6 it is possible to observe the evolution of the parameter  $\epsilon$  for a run of the *ARCHER* simulation.  $\epsilon$  start from

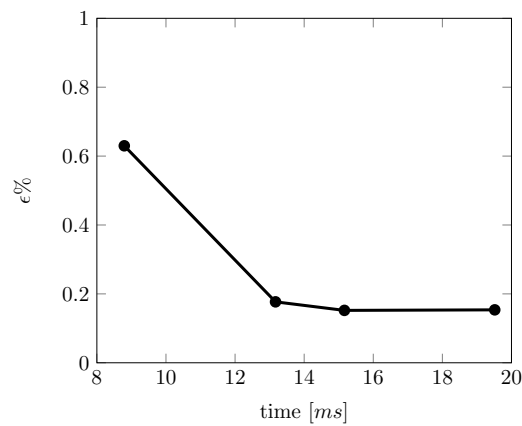


Figure 3.6 – Evolution of the parameter  $\epsilon$  for the *ARCHER* simulation.

a value of 0.6% at 8.7[ms] and eventually drops to a value around 0.2% at 22[ms]. As far as the simulation performed using *ARCHER* is the reference simulation, we will use it as a reference also for the convergence of the other simulations. In table 3.3 it is possible to find the value of the convergence parameter for the different simulation analysed in the next sections. It is possible to observe, how the parameter  $\epsilon$  is around 3% for each simulation apart from the CEDRE(HR) case where the parameter is around 14%. It has not been possible to add further averaging time to the CEDRE simulations because the simulations have been run by Pierre Cordesse in the context of his PhD work ([Cor20]).

	Average Time	$\Delta t_{avg}$	CPU cost for 9[ms] in hours	$\epsilon(\%)$	$d_l / \min(\Delta x)$
CEDRE (MR)	2[ms] – 11[ms]	9[ms]	$8.54 \cdot 10^3$	2.0	10
CEDRE (HR)	2.3[ms] – 10.5[ms]	8[ms]	$69.3 \cdot 10^3$	14.8	20
<i>ARCHER</i>	3.8[ms] – 21.2[ms]	17.4[ms]	$98.3 \cdot 10^3$	0.2	32
<i>InterFoam</i>	3.8[ms] – 19[ms]	15.2[ms]	$86.0 \cdot 10^3$	2.4	32
<i>ELSA</i>	3.8[ms] – 19[ms]	15.2[ms]	$10.7 \cdot 10^3$	3.5	20
<i>ICMelsa</i>	3.8[ms] – 19[ms]	15.2[ms]	$10.7 \cdot 10^3$	3.7	20

Table 3.3 – Average time and convergence results for the database of simulations we have built

### 3.6 Region of validity of the results

In order to perform the comparison among the different numerical models, we have to determine a region of validity in which make the comparison. We will perform the comparison where we can say that state that the resolution is sufficient for our case of reference, namely *ARCHER* simulation. The problem of under resolution is a real issue in general for simulation of turbulent gas-liquid interfacial flows. The resolution required to solve completely most of atomization processes, even with moderate Weber number, is often skyrocketing. Solving entirely a two-phase flow of an atomization process would require several mesh cell per diameter of any droplet, a condition that is hardly met in practice and leads to the question of mesh convergence. Even with the most intensive computational effort [SU10], the full resolution is not necessarily guaranteed and statistical analysis is often intractable. The strategy developed in the present work is to reduce the zone of analysis to a restricted area where the mesh resolution is high enough to accurately capture the two-phase flow. This is among the first attempts to determine which part of the flow is well-resolved based on numerical criterium characterizing the Interface Resolution Quality (*IRQ*). This approach is based on previous work performed, on a simplified problem [Can19] where the statistical analysis of this *IRQ* criterium has been carried out by comparing several level of grid refinement leading up to mesh convergence. The main advantage of this criterium is to evaluate the quality of complex configuration simulations, such as the present one, without running the simulation with several levels of mesh resolution to achieve a proper mesh convergence study. This criterium is defined as  $IRQ_K = \frac{1}{(\Delta x^2 H)}$ , where  $\Delta x$  is the grid size and  $H$  the mean curvature (for more details see section 2.2.7). This criterium highlights the under-resolved regions of the simulation where its value diminishes. For instance, a droplet described with 4 mesh cells along its radius has an  $IRQ_K = 2$ , though with 2 mesh cells along the diameter means  $IRQ_K = 1$ . Therefore, the lower the *IRQ* is, the lower is the resolution of the liquid (or gas) structure highlighted. Note that the threshold value of 2 chosen here is arbitrary and the user is expected to choose a value that is the most adequate to a given simulation. Instead of investigating the individual  $IRQ_K$  for each structure, the  $IRQ_K$  Probability Density Function (PDF) can be studied to obtain a better picture of the resolution level of the overall simulation. Since the *ARCHER* simulation is the reference one,  $IRQ_K$  criterium is analysed with this code. The  $IRQ_K$  is extracted from two specific regions of the jet: in the vicinity of the main liquid core, where the criterium should behave perfectly since most wrinkling of the interface are expected to be captured, and in the most critical secondary atomization region, where liquids structures encounter fragmentation/breakup processes that can lead to under-resolved liquids structures.

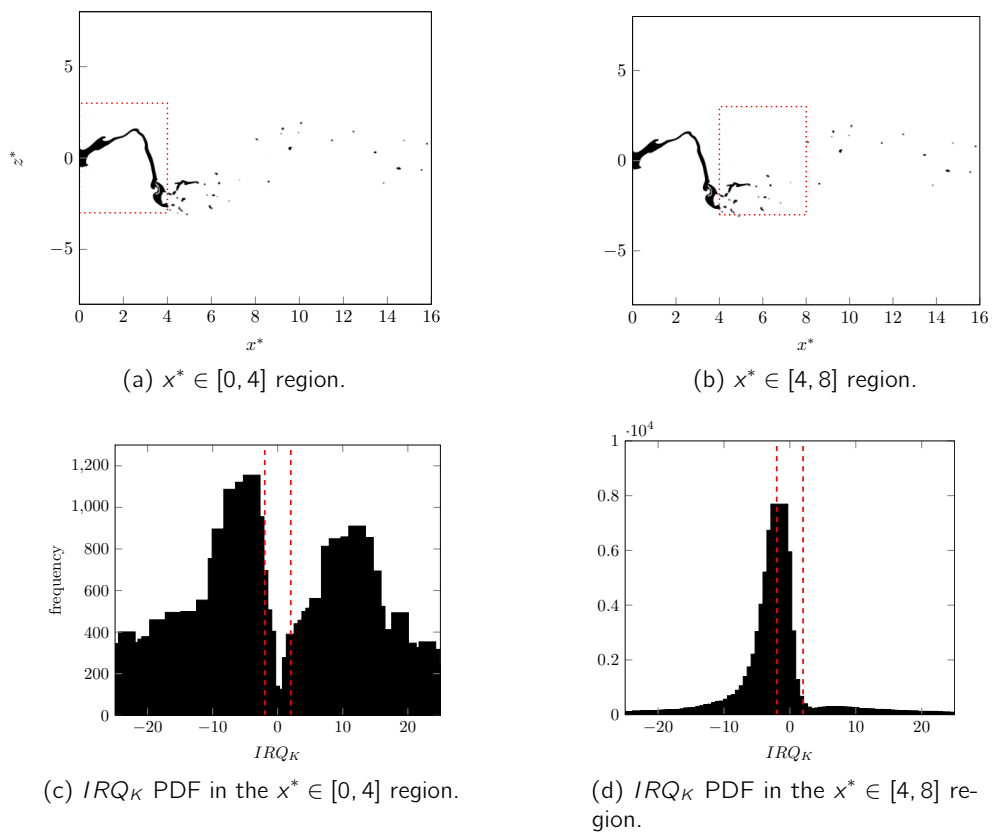


Figure 3.7 –  $IRQ_k$  PDF analysis at time  $t = 12 \text{ ms}$  (bottom), in two regions identified by the red dashed rectangles drawn on the plan  $y^* = 0$  showing liquid volume fraction  $\alpha_l$  (top).

The PDF of  $IRQ_K$ , shown in Figures 3.7c, 3.7d, gives useful information about the quality of the interface resolution. In the first region of the liquid sheet, most of the IRQ values of the PDF (around 95%) are located beyond the critical zone of low IRQ,  $IRQ_K \in [-2 : 2]$ , as shown in Figure 3.7c. This range is indicated by two red dotted lines in the figure. Thus, in this zone, the interface resolution is high enough to capture the largest part of the curvature distribution. A residual of the distribution for absolute value of  $IRQ_K$  less than 2 exist. This is an inherent behaviour of atomization process that can produce nearly an infinite curvature for instance at the pitching of a ligament just before the breakup. However the percentage of curvature that are less than 2 is small and, above all, there is no accumulation of low resolved surface. This behaviour would have been a marker, with this kind of approach, that mesh resolution is limiting the production of small length scale. Further discussion have been developed in [Can]. In the second region, Figure 3.7d, the PDF is compressed close to the critical  $IRQ_K$  zone, hence only around 60% of the interface is well resolved, and there is an accumulation of weakly resolved interface. It indicates that the *ARCHER* results should be taken with caution for large  $x^*$ . This can be explained by the production of droplets of small scale due to atomization of the flapping sheet. Note that this kind of simulations at high Weber and Reynolds numbers are quite challenging in term of computational costs, explaining the difficulty to reach higher IRQ in the most atomized or dispersed region. Besides, we specifically have chosen two different regions with opposite behavior to assess the pertinence of the criterion. Consequently, the *ARCHER* simulation appears sufficiently trustworthy until the jet become more dispersed, due to the presence of very small droplets. In addition, in the present work, CEDRE simulation has not been coupled with any specialized reduced-order model, relying on kinetic approach, to better describe the dispersed flow. The same can be said for the other model implemented in *OpenFoam*. It is unlikely that the mixed phases model or a reduced order model alone will capture properly the dispersed part of the flow. The following analysis will therefore be conducted in the zone  $x^* \in [0, 4]$  along the streamwise axis where the *ARCHER* simulation can be considered as the reference simulation.

Even if in the confidence zone, we would expect a different level of error for each code tested. *ARCHER* is conserving sharp the interface thanks to the separated phases model and conserves the volume thanks to the CLSVOF method, thus it conserve the interface at the level of the mesh resolution. *InterFoam* that is a mixed phases model with a counter-flux that aims to mimic the *sharp interface* representation, will limit the curvature somehow due to the numerical diffusion above the level of resolution. The *diffuse interface* approaches (*ELSA* and *CEDRE*), where the interface is a mixture zone and the position is not well defined, will be affected by an higher error on the curvature.

### 3.7 Classical analysis

In the next paragraphs we'll analyse the flow field and the quantities that characterize it by doing a phenomenological observation of the phase marker evolution. Later we'll analyse first and second order statistics along with the Turbulent Kinetic Energy (TKE). The title of the section is "*classical analysis*" because it is an analysis that is common to different turbulent flow configuration, *single-phase* (e.g [Nic99]) and *multi-phase* and we want to distinguish it from the analysis that we'll do in the next section, more focused on the position of the interface and the interaction of the two phases.

In the next sections will be showed iso-surfaces and slices of the averaged quantities. While the iso-surfaces represent the time averaged quantities (denoted with  $\bar{\cdot}$ ), the slices have been also space-averaged in the statistically homogeneous direction ( $y$ ), and the procedure will be denoted with  $\bar{\cdot}$ . This choice has been made to gain statistical convergence and has not been

done for the iso-surfaces to save computational time.

### 3.7.1 Phenomenological observation

The different simulations have been synchronized at an initial time value, identified with  $t_0$ , observing where the flapping cycle was starting for each simulation. This time varies from simulation to simulation. One possible explanation for this phenomena is the difference in the processes that trigger instabilities due to the difference in the interaction among the two phases, as it is possible to see in the *phase analysis* (section 4.2).

From the initial time  $t_0$  it has been considered a time step of  $\delta t \approx 0.1[ms]$  for a total of 9 frames sequence, in order to observe the cyclic behaviour of the flapping jet. The macroscopic behaviour of the big features of the flow in the sequence proposed can be split in two different parts. A first part ranging from  $t_0$  to  $t_0 + 4\delta t$  where the flapping of the liquid sheet prevails. A second part ranging from  $t_0 + 4\delta t$  to  $t_0 + 8\delta t$  where the so-called *dripping regime* prevails ([Dum08]). It refers to a condition in which the ligaments are released from the nozzle without a continuity of the liquid column.



Figure 3.8 – Instantaneous picture of the flapping liquid sheet. On the left CEDRE(HR) simulation. The colorscale goes from low levels of  $\alpha_l$  (blue) to high levels (red). On the right ARCHER simulation. The iso-contour represents the 0 iso-value of the *level-set distance function*.

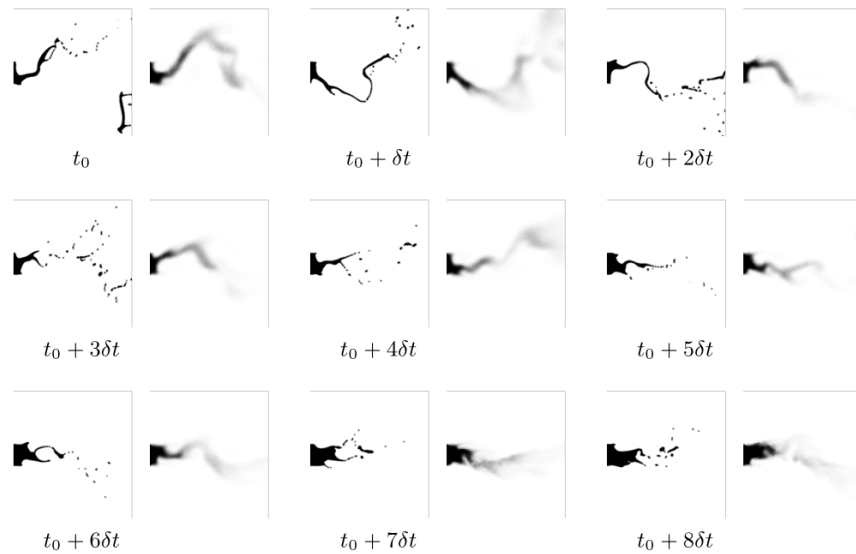


Figure 3.9 – Transient evolution of the plane  $y^* = 0$  of liquid volume fraction near the injector,  $\alpha_l = 0$  to 1. Left: *ARCHER*, right: *CEDRE*. We define  $t_0$  as the starting time and  $\delta t$  as the progression time step. The window showed is in the range  $x^* = [0, 5.5]$ .

In fig. 3.8 it is possible to observe a contour plot of the phase marker for the *CEDRE* code and *ARCHER* code. The difference among a mixed phases approach and a separated phases is demonstrated. While for the *ARCHER* liquid-gas interface plot it is possible to observe also the small scales of the liquid interface, in the *CEDRE* code small liquid structures are represented as a diffuse phase marker field.

In fig. 3.9 it is possible to observe how the dynamic of the first part of the sequence is reproduced in the same way by the two different models. It is possible to recognise in the same time frames the flapping regime and the dripping regime as explained at the beginning of the paragraph. In *CEDRE*, the smaller features of the liquid are not represented due to the diffusion and the absence of the surface tension in the model (fig. 3.8). This phenomena is clearly shown in the frames from  $t_0 + 6\delta t$  to  $t_0 + 8\delta t$ . It is possible also to observe, through the convexity of the liquid leap how the dynamic of the flow is completely maintained.

The phenomenological observation of the flow rising from the injector shows that in case of the separated phases model and mixed phases model the dynamic of the flow is well captured and in the nine time sequence analysed, the qualitative behaviour reproduced is the same.

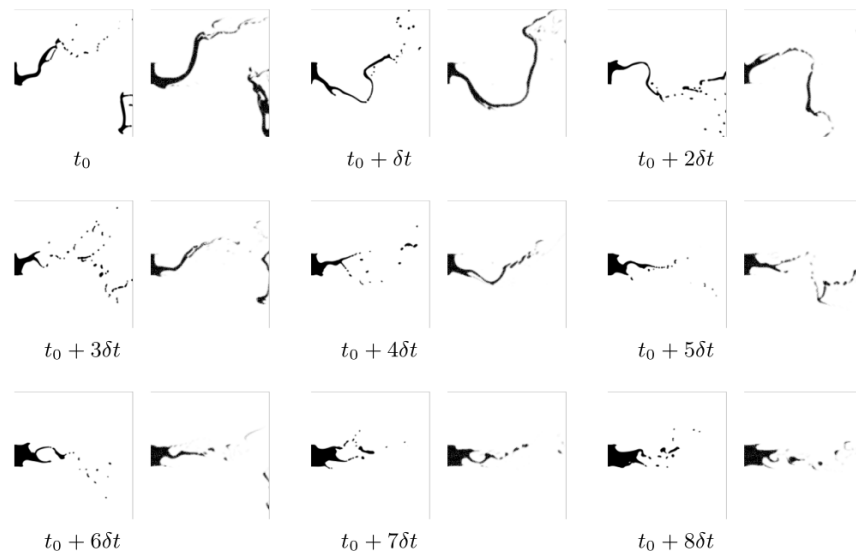



Figure 3.10 – Transient evolution of the plane  $y^* = 0$  liquid volume fraction near the injector,  $\alpha_l = 0$   1. Left: *ARCHER*, right: *InterFoam*. We define  $t_0$  as the starting time and  $\delta t$  as the progression time step. The window showed is in the range  $x^* = [0, 5.5]$ .

The comparison of the liquid film dynamic between *ARCHER* and *InterFoam* shows that the two phases behaviour (flapping and dripping) is represented following the same pattern. In case of *InterFoam* simulation the *compression flux* showed in eq. (3.14) tends to prevent the atomization and to cluster the particles in bigger structure with respect to what is happening in the *ARCHER* simulation. It is possible to observe in the *InterFoam* sequence that the phase transition, where  $\alpha$  is changing from 0 to 1, requires a finite length-scale. Thus this representation rely on a mixed phases model with an interface thickness that is bounded to length related to the mesh size ( $\Delta x$ ). For the smallest, most constrained interface, the interface tends to increase. The *sharpening terms* tends to maintain the interface sharp but does not prevent completely the diffusion. The interface is commonly spread among 2-3 cells. It is still possible to observe the difference with respect to the *diffuse interface* representation in fig. 3.9, where the smaller features of the flow are completely absent in all the time frames.



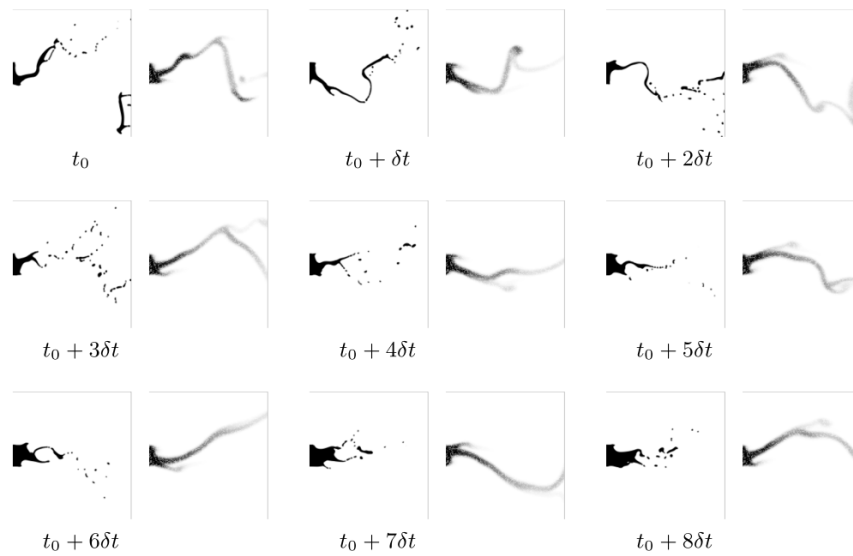



Figure 3.11 – Transient evolution of the plane  $y^* = 0$  liquid volume fraction near the injector,  $\alpha_l = 0$   1. Left: *ARCHER* , right: *ELSA* . We define  $t_0$  as the starting time and  $\delta t$  as the time step. The window showed is in the range  $x^* = [0, 5.5]$ .

On the comparison between *ELSA* and *ARCHER* code results, it is possible to observe the same global behaviour with respect to the two previous comparisons. The same flapping and dripping phases are reported. The diffusion of the flapping jet is further enhanced due to the additional physical model diffusion term (see eq. (3.24)) that is an attempt to model the *turbulent liquid flux*. This somehow prevents the atomization of the jet that appears as a diffuse liquid field showing much less structure. It is still possible to report the same dynamics, even if the convexity of the liquid leap is not completely conserved as in the case of *CEDRE*.

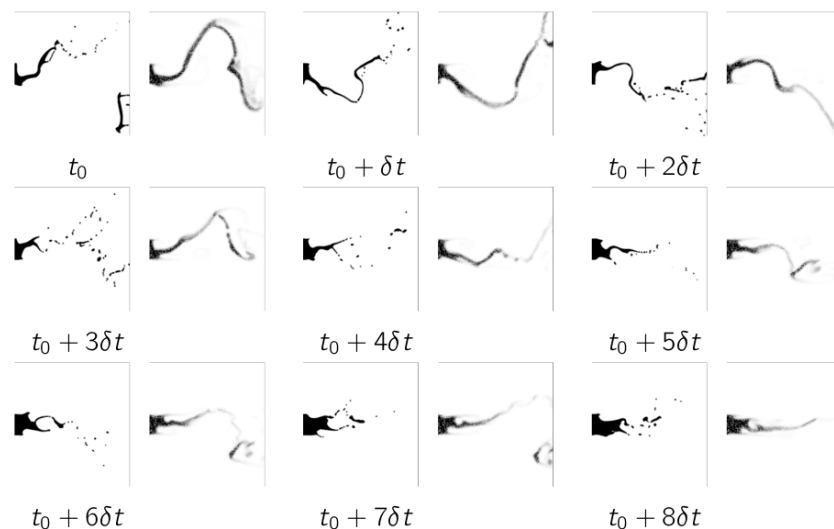
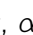


Figure 3.12 – Transient evolution of the plane  $y^* = 0$  of liquid volume fraction near the injector,  $\alpha_l = 0$   1. Left: *ARCHER* , right: *ICMelsa* . We define  $t_0$  as the starting time and  $\delta t$  as the time step. The window showed is in the range  $x^* = [0, 5.5]$ .

In the comparison between *ICMelsa* model and *ARCHER* it is possible to observe that the two phases of flapping and dripping are maintained. The features of the flow that can be observed are a mix among the features that have been reported for the *InterFoam* and *ELSA* model. Near the outlet the structure of the liquid leap is maintained sharp by the numerical counter-flux, while after it is spread and the small features of the flow are not represented anymore. This is due to the switch of the model to the *ELSA* formalism. There the turbulent liquid flux plays an important role, with the physical model based on liquid sub-grid dispersion.

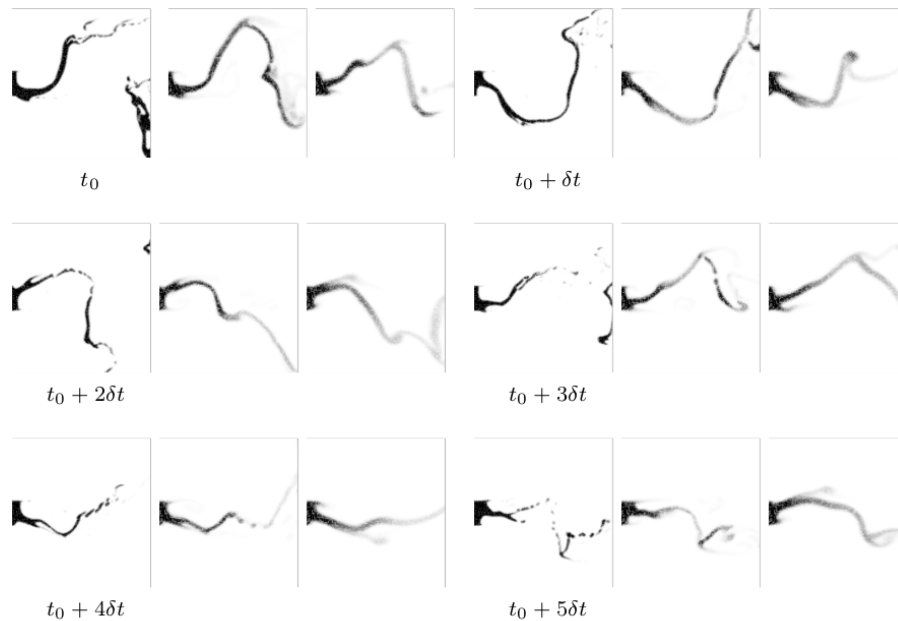



Figure 3.13 – Transient evolution of the plane  $y^* = 0$  of liquid volume fraction near the injector,  $\alpha_l = 0$   1. Left: *InterFoam*, center: *ICMelsa*, right: *ELSA*. We define  $t_0$  as the starting time and  $\delta t$  as the time step. The window showed is in the range  $x^* = [0, 5.5]$ .

In fig. 3.13 it is possible to observe the progression among *InterFoam* (on the left), *ICMelsa* (on the center) and *ELSA* (on the right) for 5 different time steps. This figure highlights how the dynamic of the flow is well captured by the three models and confirms what has been already presented in fig. 3.10, fig. 3.11 and fig. 3.12. It is possible also to observe the hybrid nature of *ICMelsa* model, which tends to maintain the interface sharp near the entrance of the domain, where the resolution is sufficient to capture the interface, while it recovers the *ELSA* feature of the flow farther away, attempting to physically model the interface dynamic that happen below the mesh resolution.

### 3.7.2 Averaged liquid volume fraction

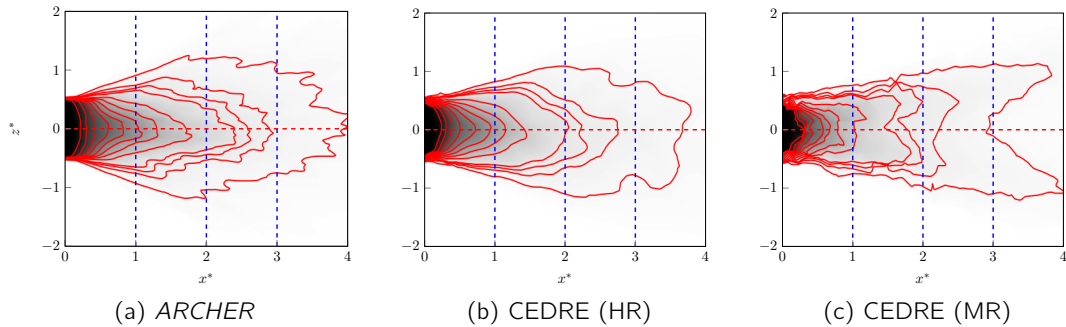


Figure 3.14 – Averaged liquid volume fraction isolines  $\overline{\alpha}_l^t = 0.1$  to  $1$  at the  $y^* = 0$  plane. Dashed lines located at  $x^* \in \{1, 2, 3\}$ .

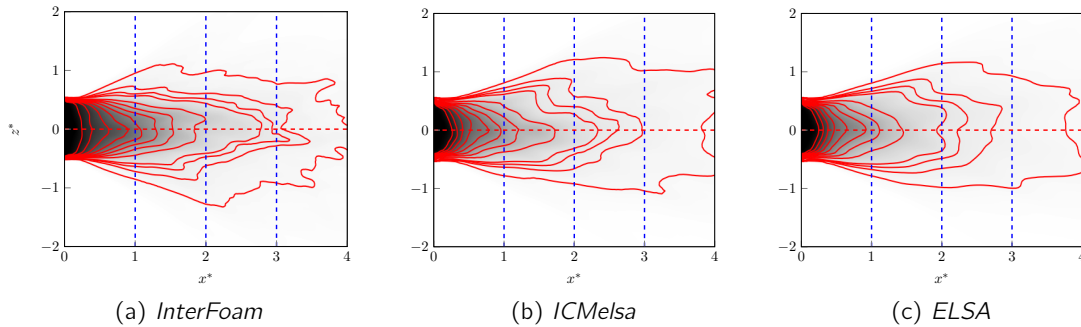


Figure 3.15 – Averaged liquid volume fraction isolines  $\overline{\alpha}_l^t = 0.1$  to  $1$  at the  $y^* = 0$  plane. Dashed lines located at  $x^* \in \{1, 2, 3\}$ .

The average liquid volume fraction is a key quantity to evaluate the penetration of the liquid inside the quiescent environment together with the liquid dispersion. Figure 3.14 and fig. 3.15 it is represent a slice of the fluid domain at  $y^* = 0$ , representing contour lines of the liquid volume fraction from  $\overline{\alpha}_l^t = 0.1$  until  $\overline{\alpha}_l^t = 1$ . In the different codes the  $\overline{\alpha}_l^t = 1$  iso-line appears to follow the same behaviour. following the other iso-lines we notice a different trend for the different models tested. The *sharp interface* approaches (*ARCHER* and *InterFoam*) shows less spreading of the liquid with respect to the *diffuse interface* ones (*CEDRE* and *ELSA*) for which the iso-lines are smoother. We notice furthermore a tendency in the *InterFoam* model to cluster the liquid near the center-line  $z^* = 0$ . The *ICMelsa* behaviour can be considered in between among *InterFoam* and *ELSA*. We can observe that the iso-lines near the inlet recover the behaviour of the *sharp interface* approaches and in particular of the *InterFoam* model, while farther away, for the iso-lines corresponding to a more dispersed liquid phase, the behaviour is very similar to the *ELSA* case. The fig. 3.16 shows the averaged liquid volume fraction trend along the streamwise axis  $z^* = 0$ . it is possible to observe the characteristic behaviour of the different models. It is confirmed that the interface model of *InterFoam*, with the presence of the sharpening term, tends to cluster the liquid along the central axis, with respect to the CLSVOF model of *ARCHER*. At the contrary the *diffuse interface* models tends to disperse more the liquid, and so we will find less liquid at the central axis. The *ICMelsa* model line lies nearer to the *InterFoam* line for  $x^* = [0, 2]$ , while it tends to approach to the *ELSA* line for higher values of  $x^*$ . This behaviour is in line with what has

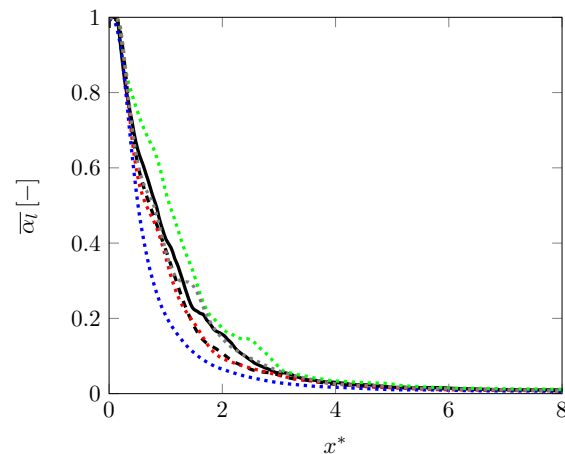


Figure 3.16 – Averaged liquid volume fraction  $\bar{\alpha}_l$  along streamwise axis. — *ARCHER*, ..... *CEDRE (HR)*, ..... *CEDRE (MR)*, ..... *InterFoam*, ..... *ELSA*, ..... *ICMelsa*.

been observed in fig. 3.14 and fig. 3.15. Table 3.2 shows the different mesh characteristics of the different simulation. In fig. 3.16 it is possible to observe how in the streamwise plane, the effect of the grid refinement for the *CEDRE* case, brings to reduce the liquid dispersion. In fig. 3.15 and fig. 3.14 we observe that the *CEDRE (MR)* and *ELSA* simulations follow the same behaviour, enhancing the dispersion of the liquid in the upper and lower part of the domain and opening up the spray angle. The difference among the two is that one is due to numerical diffusion (*CEDRE*) and the other one is based on physical model that aims to represent sub-grid dispersion (*ELSA*). The idea that numerical diffusion can be used to mimic the sub-grid dispersion have been studied by certain group, at least in *single-phase* flows ([Ege+14],[BB10]). It would be interesting in future works to test the different simulations with the same mesh at a different level of refinement. In Figure 3.17 represents the averaged profiles of the  $\bar{\alpha}_l$  respectively at the locations  $x^* = 1, 2, 3$  of the domain. It is possible to draw the same conclusions of the previous analysis. The magnitude of the average liquid volume fraction  $\bar{\alpha}_l$  near the centre-line is more accentuated for the *InterFoam* simulation with respect to the *ARCHER* simulation, while for the *diffuse interface* models it is less. This is due to the fact that in case of the interface model implemented in *InterFoam*, the sharpening counter-flux tends to cluster the liquid near the centre-line, while in case of the *diffuse interface* approaches, the diffusion, tends to spread the liquid more far away. The mesh refinement effect of *CEDRE (MR)* and *ELSA* is more evident for the  $x^* = 3$  slice. While for  $x^* = 1$  we can notice only a difference in the magnitude. With increasing  $x^*$  we can notice the effect of the dispersion, due to the flapping and the dynamic of the configuration.

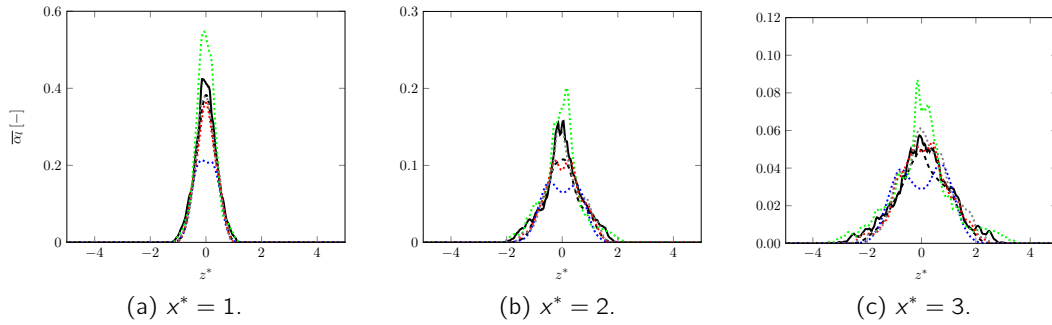


Figure 3.17 – Averaged liquid volume fraction  $\bar{\alpha}_l$  along fig. 3.14 and fig. 3.15 dashed lines. — ARCHER, ---- CEDRE (HR), ..... CEDRE (MR), ..... InterFoam, ..... ELSA, ..... ICMelsa. Reader must take care to the fact that the  $\bar{\alpha}_l$  range is different for the three slices.

### 3.7.3 Averaged velocities

In this paragraph we compare the streamwise ( $\overline{v_x}$ ) and spanwise averaged velocities ( $\overline{v_z}$ ). Figure 3.18 and fig. 3.19 present the time averaged slice at the plane  $y^* = 0$  of the streamwise velocity  $\overline{v_x}$ . The global behaviour appears to be the same for the different interface model tested. The same for the different velocity profiles in fig. 3.20 for the different location  $x^* = 1, 2, 3$ . In the *ELSA* code we notice a different behaviour among the slice and the space-averaged lines. This difference can be justified by two effects. First is the space averaging procedure. The second is the color scale of the contour plot in fig. 3.19. This has been chosen to be more saturated near the low value of the streamwise velocity and hence it appears qualitatively different from the behaviour shown in fig. 3.20.

Figure 3.21 and fig. 3.22 present the time averaged slice at the plane  $y^* = 0$  of the spanwise velocity  $\overline{v_z}$ . More difference with respect to the streamwise velocity can be noticed. This is an effect mainly due to the numerical domain itself and its boundary conditions (fig. 3.5). The principal direction of the flow is the streamwise direction where at the patch inlet ② in fig. 3.5 we impose a mean velocity profile. The injection of momentum at the inlet in the streamwise direction is mostly dominated by the boundary condition. The velocity in the spanwise direction is caused by the instabilities and liquid dispersion that produce relatively small transverse velocity and produce few differences on the axial velocity. The spreading of what we can call "the velocity cone" appears to be different in the different approaches (fig. 3.23). The averaged spanwise velocity profiles at location  $x^* = 1, 2, 3$  are shown in fig. 3.23. While for  $x^* = 1$  the profiles appears not to present huge differences, for bigger value of  $x^*$  the differences accentuates.

There is a tendency of the *sharp interface* models (*ARCHER* and *InterFoam*) to spread the velocity more far away with respect to the central axis ( $z^* = 0$ ) with an increasing  $x^*$  location. With the increasing  $x^*$  location the peak tends also to decrease, apart for the *ELSA* model. A possible explanation can be the difference in the spreading of the liquid volume fraction (fig. 3.14 and fig. 3.15), as far as what we are observing here is the complete averaged transversal velocity, where the averaged component can be written as:

$$\overline{v_z} = \overline{\alpha_l v_{zl}} + \overline{(1 - \alpha_l) v_{zg}} \quad (3.36)$$

Where with the subscript  $l$  we refer to the velocity associated to the liquid phase and with  $g$  the velocity associated to the gas phase. In case of CEDRE, as far it is taken into account

the compressibility of the fluids, the average velocity can be written as:

$$\overline{v_z} = \frac{\overline{\rho_l v_{zl} \alpha_l + \rho_g v_{zg} \alpha_g}}{\overline{\rho_l \alpha_l + \rho_g \alpha_g}} \quad (3.37)$$

Where all these information can be retrieved, solving the equation of the model presented in the introduction of this chapter. The analysis of the different components of eq. (3.36) and eq. (3.37) to understand the differences in  $v_z$  can represent an extension of the present work. For more information about the decomposition refer to chapter 4.

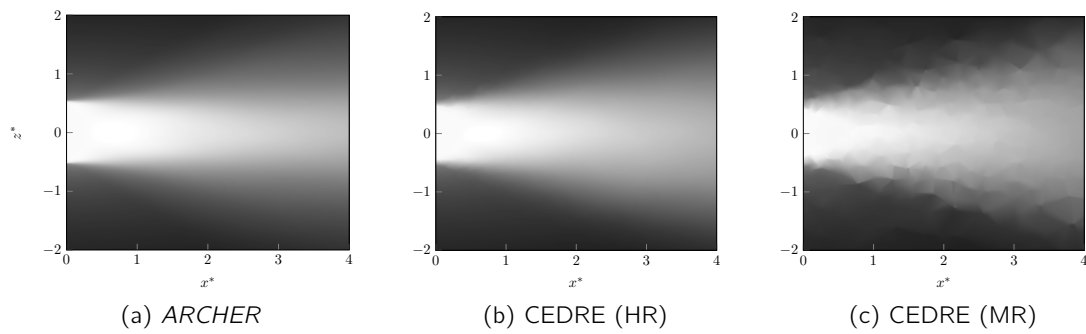


Figure 3.18 – Averaged axial velocity  $\overline{v_x} = 0$  to  $70 \text{ m/s}$  at the  $y^* = 0$  plane.

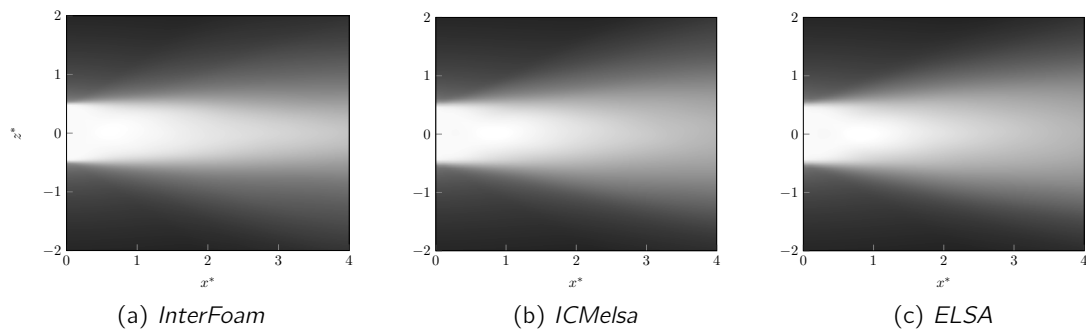


Figure 3.19 – Averaged axial velocity  $\overline{v_x} = 0$  to  $70 \text{ m/s}$  at the  $y^* = 0$  plane.

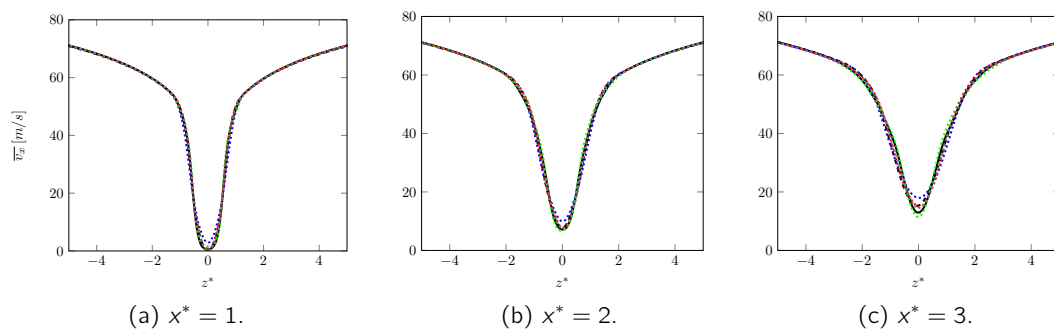


Figure 3.20 – Averaged axial velocity  $\overline{v_x}$  along fig. 3.14 and fig. 3.15 dashed lines. — ARCHER , - - - CEDRE (HR), ···· CEDRE (MR), ···· InterFoam , ···· ELSA , ···· ICMelsa .

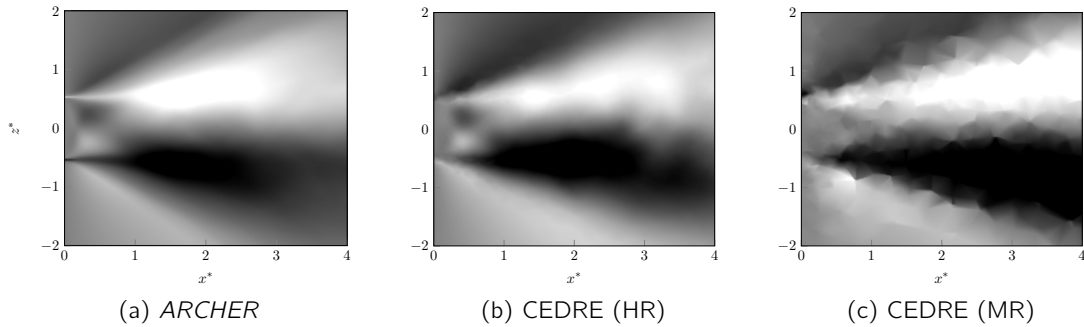


Figure 3.21 – Averaged transversal velocity  $\overline{v_z} = -3$  to  $3$  m/s at the  $y^* = 0$  plane.

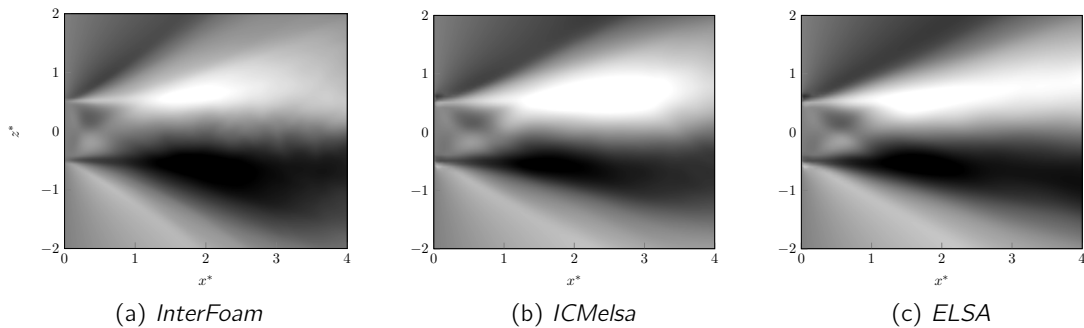


Figure 3.22 – Averaged transversal velocity  $\overline{v_z} = -3$  to  $3$  m/s at the  $y^* = 0$  plane.

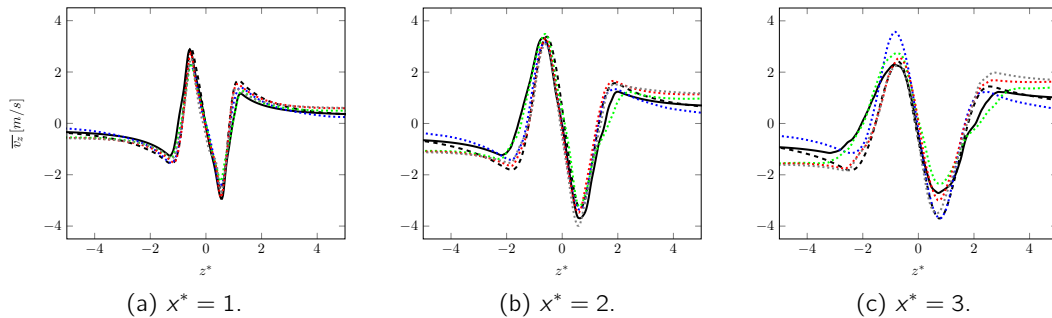


Figure 3.23 – Averaged transversal velocity  $\overline{v_z}$  along Figure fig. 3.14 and fig. 3.15 dashed lines. — ARCHER , ---- CEDRE (HR), ..... CEDRE (MR), -.-.- InterFoam , ..... ELSA , ..... ICMelsa .

### 3.7.4 Turbulent Kinetic Energy (TKE) and Reynolds stress components

Having a look at the TKE we can analyse more in-depth the statistics of the flow. Figure 3.24 and fig. 3.25 present the time averaged slice at the plane  $y^* = 0$  of the TKE  $1/2\overline{v_i'v_i'}$ , where with  $ii$  we denote the *Einstein notation* that implies the summation over the components  $xx$ ,  $yy$  and  $zz$ . It is not possible to see a huge difference among the *sharp interface* approach of *InterFoam* and the *diffused* one of *ELSA* as it is possible to observe in fig. 3.14. It is possible to notice the difference of magnitude between the *diffuse interface* representation and the *sharp interface* representation. The TKE values in case of the *ARCHER* code and

*InterFoam* model appear to be spread on a larger range over the  $z^*$  axis. These statements are confirmed by the averaged slice of TKE at the locations  $x^* = 1, 2, 3$  represented in fig. 3.26. The global trend of the TKE is to have two peaks and a saddle in the middle of the  $z^*$  domain. While the peaks magnitude is captured for all the codes at each location (in exception of CEDRE (MR) case, probably due to the under-refinement of the mesh), the saddle magnitude varies from code to code.

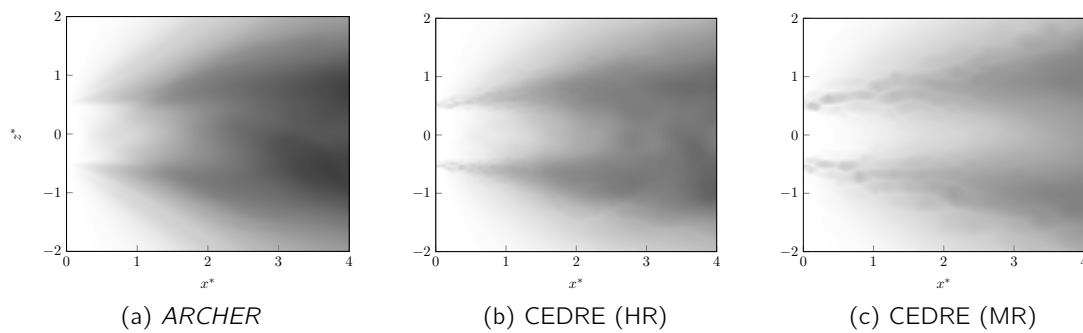


Figure 3.24 – Turbulent Kinetic Energy (TKE)  $1/2\overline{v'_i v'_i} = 0$   $\blacksquare$   $380 \text{ m}^2/\text{s}^2$  at the  $y^* = 0$  plane.

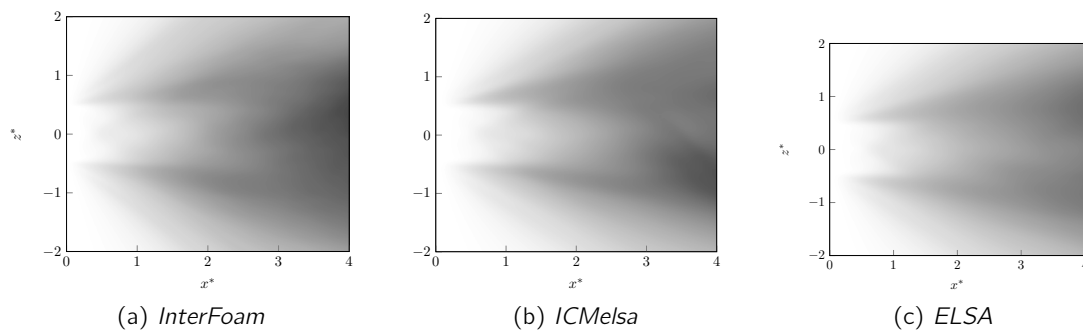


Figure 3.25 – Turbulent Kinetic Energy (TKE)  $1/2\overline{v'_i v'_i} = 0$   $\blacksquare$   $380 \text{ m}^2/\text{s}^2$  at the  $y^* = 0$  plane.

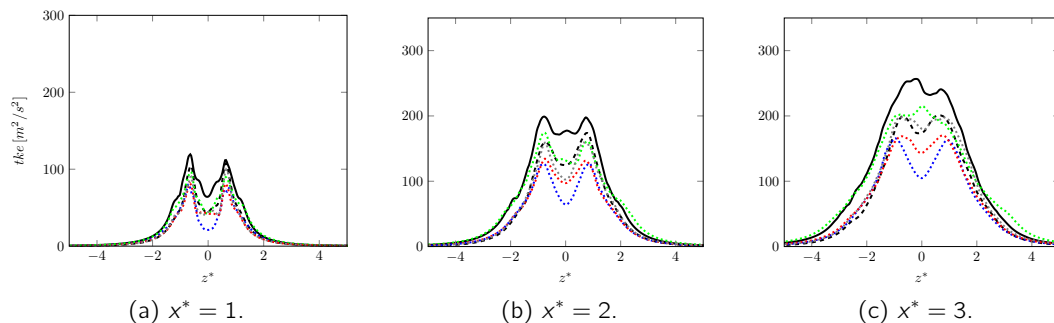


Figure 3.26 – Turbulent Kinetic Energy (TKE)  $(1/2)\overline{v'_i v'_i}$  along Figure fig. 3.14 and fig. 3.15 dashed lines. — *ARCHER*, - - - *CEDRE (HR)*, ···· *CEDRE (MR)*, - - - *InterFoam*, ···· *ELSA*, - - - *ICMelsa*.



Figure 3.27 and fig. 3.28 present the time averaged slices at the plane  $y^* = 0$  of the  $xx$  Reynolds stress component  $\overline{v'_x v'_x}$ . The differences observed among the different interface models are more evident with respect to the previous comparisons. While the contour shape of the results is similar, the magnitude is different, mainly if we compare the *sharp interface* and *diffuse interface* representations. This difference is even more significant in fig. 3.30 and fig. 3.31 that present the time average slices at the plane  $y^* = 0$  of the  $zz$  component of the Reynolds stress  $\overline{v'_z v'_z}$ .

The fig. 3.29 present the averaged profiles of the  $xx$  Reynolds stress respectively at the locations  $x^* = 1, 2, 3$ . By increasing the  $x^*$  location the maximum values of the *diffuse interface* approaches are reduced with respect to the maximum values of the *sharp interface* approaches. Another effect it is possible to notice with the increasing  $x^*$  for the *ARCHER* simulation, the range is less close to the center-line  $z^* = 0$ . The fig. 3.32 presents the averaged of  $zz$  component of the Reynolds stress respectively at the locations  $x^* = 1, 2, 3$ . The range of values around the center-line  $z^* = 0$  is less spread, but as it was shown in fig. 3.30 and fig. 3.31 it is possible to observe a difference among the maximum value of the models tested. In order to analyse more in-depth these results it is useful to proceed with the phase analysis (chapter 4. This kind of analysis will be performed in section 4.2. To conclude the analysis we observe the  $zx$  component of the Reynolds stress tensor. The fig. 3.33 and fig. 3.34 present the time averaged slices at  $y^* = 0$  of the  $xz$  Reynolds stress component. From these plot it is possible to observe no relevant difference among the different representations. Observing the averaged profiles at the locations  $x^* = 1, 2, 3$  in fig. 3.35 it is possible to conclude the same. The only difference that we observe can be seen for the slice  $x^* = 1$ . Here the *ELSA* and *ICMelsa* model capture around  $z^* = 0$  a double variation of the value, not captured by the other models.

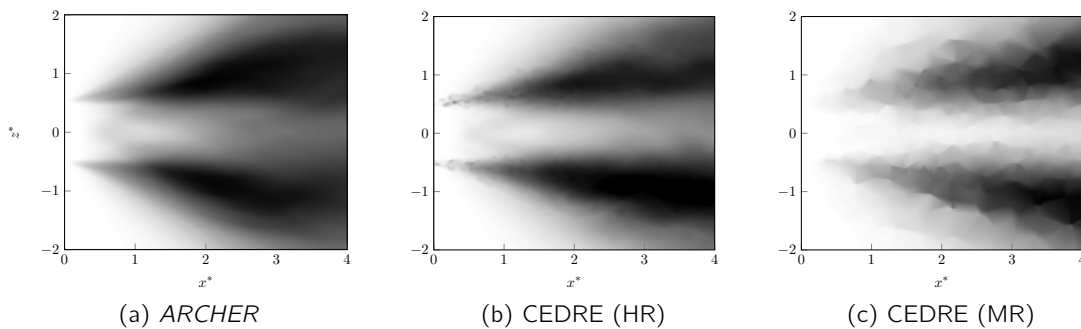



Figure 3.27 – Reynolds stress tensor component  $\overline{v'_x v'_x} = 0$    $350 \text{ m}^2/\text{s}^2$  at the  $y^* = 0$  plane.

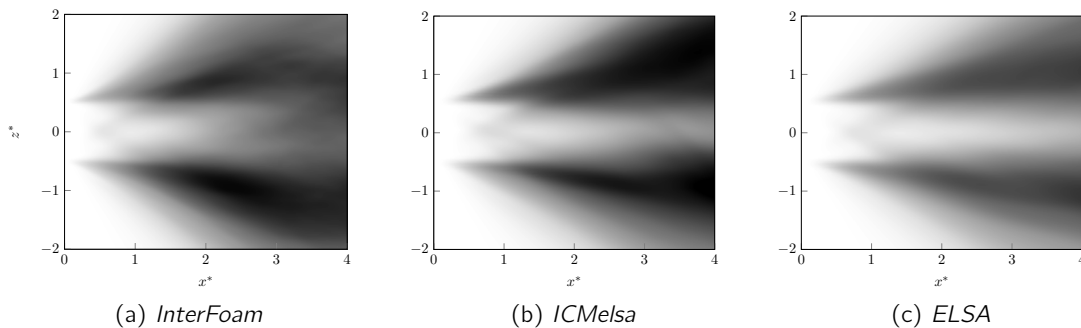



Figure 3.28 – Reynolds stress tensor component  $\overline{v'_x v'_x} = 0$    $350 \text{ m}^2/\text{s}^2$  at the  $y^* = 0$  plane.

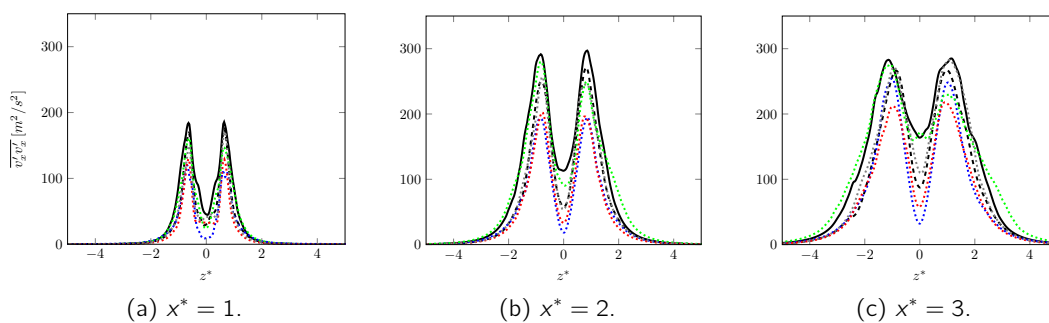


Figure 3.29 – Reynolds stress tensor component  $\overline{v'_x v'_x}$  along fig. 3.14 and fig. 3.15 dashed lines. — ARCHER , - - - - CEDRE (HR), - . - . - CEDRE (MR), - . - . - InterFoam , - . - . - ELSA , - - - - ICMelsa .

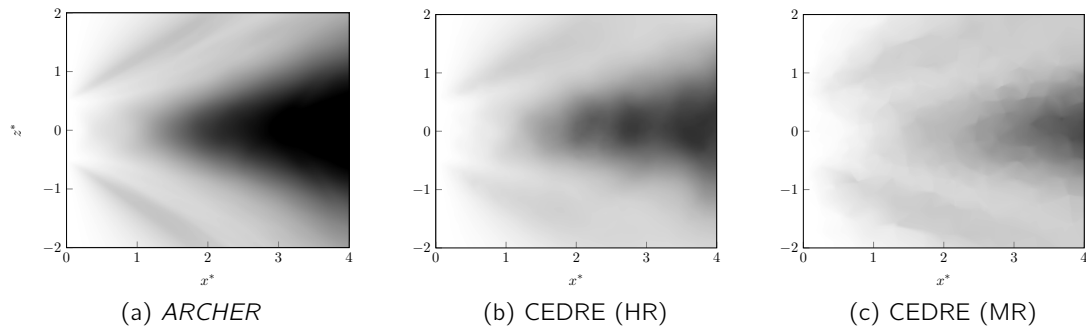


Figure 3.30 – Reynolds stress tensor component  $\overline{v_z'v_z'}$  at the  $y^* = 0$  plane.  $\blacksquare$   $350 \text{ m}^2/\text{s}^2$

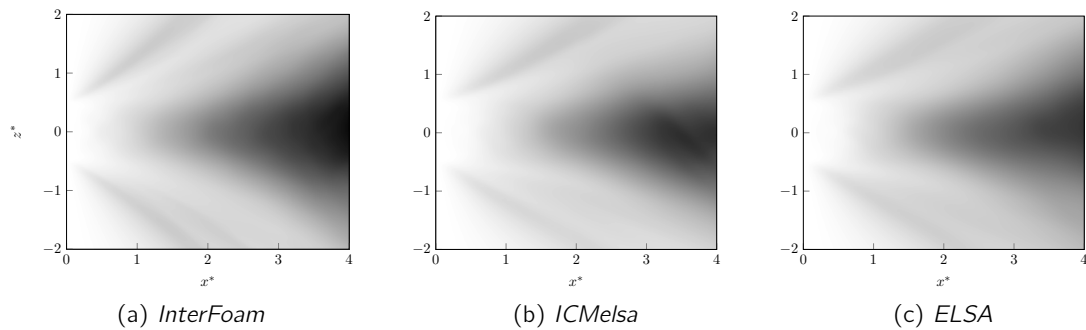


Figure 3.31 – Reynolds stress tensor component  $\overline{v_z'v_z'}$  at the  $y^* = 0$  plane.  $\blacksquare$   $350 \text{ m}^2/\text{s}^2$

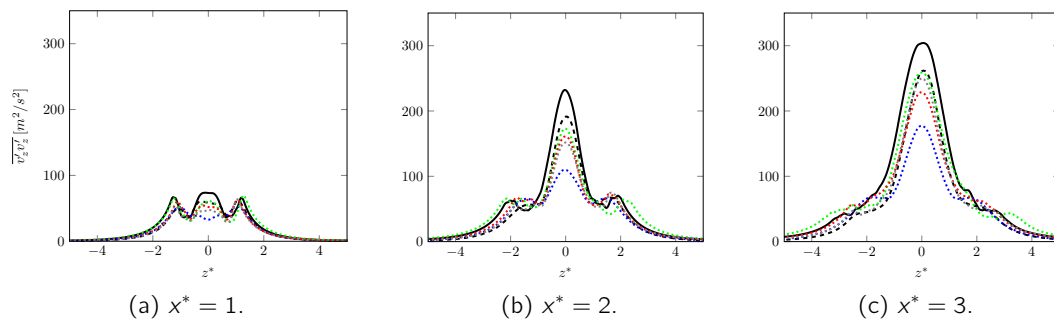


Figure 3.32 – Reynolds stress tensor component  $\overline{v_z'v_z'}$  along fig. 3.14 and fig. 3.15 dashed lines. — ARCHER, - - - CEDRE (HR), - - - CEDRE (MR), - - - InterFoam, - - - ELSA, - - - ICMelsa.

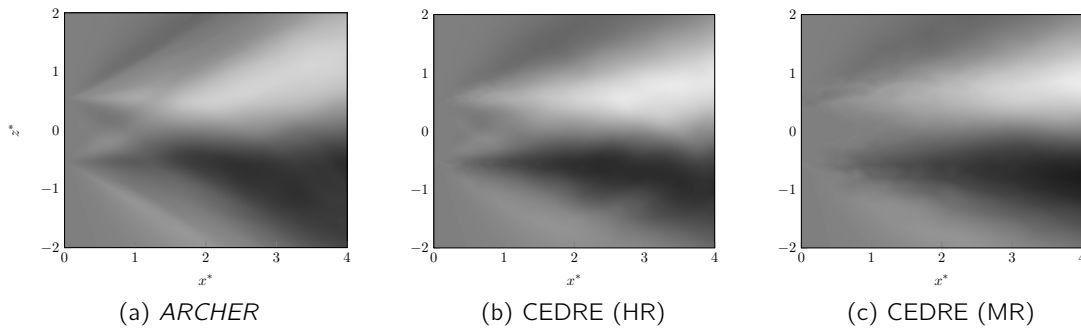


Figure 3.33 – Reynolds stress tensor component  $\overline{v'_z v'_x} = -150 \text{ } \blacksquare \text{ } 150 \text{ m}^2/\text{s}^2$  at the  $y^* = 0$  plane.

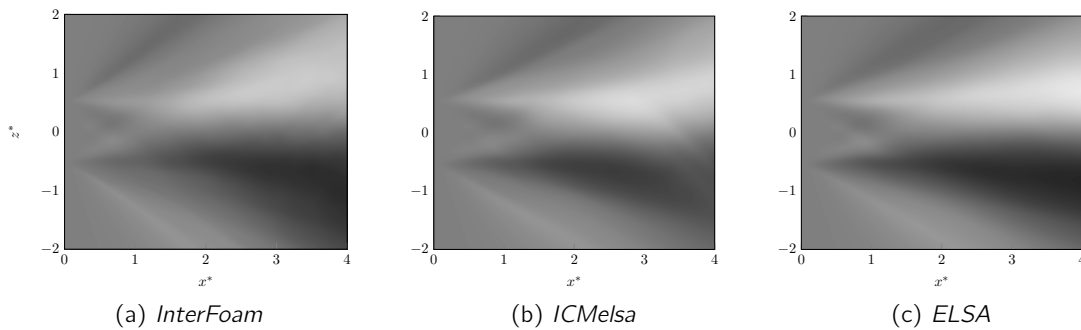


Figure 3.34 – Reynolds stress tensor component  $\overline{v'_z v'_x} = -150 \text{ } \blacksquare \text{ } 150 \text{ m}^2/\text{s}^2$  at the  $y^* = 0$  plane.

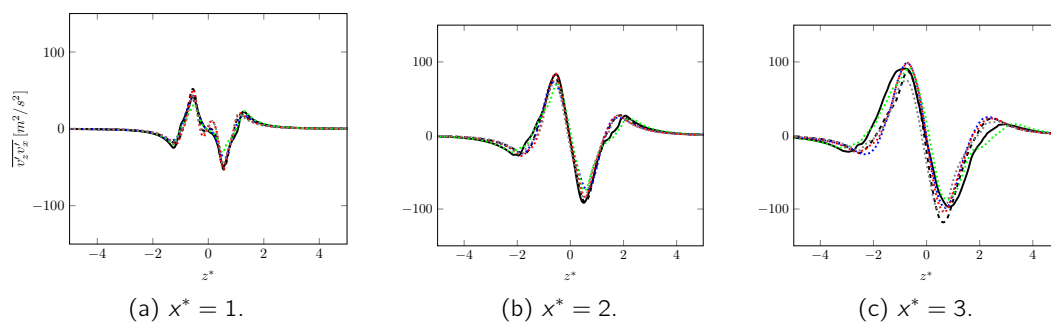


Figure 3.35 – Reynolds stress tensor component  $\overline{v'_z v'_x}$  along fig. 3.14 and fig. 3.15 dashed lines. — ARCHER , ..... CEDRE (HR), ..... CEDRE (MR), ..... InterFoam , ..... ELSA , ..... ICMelsa .

### 3.8 Conclusion

Observing the first order and second order statistics we notice that all the models represent in the same way the global dynamics of the flow. We can observe the first part of the flapping cycle, where the flapping phenomenon prevails, and a second part, where the so-called dripping regime is predominant. All the models represents similarly the liquid dispersion at large length-scale. However the different interface representations plays a role for the distribution of the phase marker. In particular we observe how the liquid volume fraction is spread farther away from the center-line in case of the *diffuse interface* representation, while it is kept near the center-line in case of *sharp interface* representation. In order to analyse the difference related to the smaller scales, we refer to the second order statistics and the TKE. There we can notice a significant difference between the approaches even quantitatively for the range of variation. As highlighted previously and in [Cor+20b] the difference are due to the different representation of transition among phases and the way in which the mixture velocities are recovered in the models. Thus, it is worth to go more in-depth and analyse the second order statistics related to the phase marker. This is the motivation for the next chapter where an analysis of the different approaches is attempted, based on signal analysis, related to the structure of the phase marker.

## Chap. 4 | Phase analysis

In the previous chapter we highlighted that for the different models tested we reached differences in terms of the second order statistics. Hereafter, we propose an analysis in order to understand the nature of these differences. This type of analysis is called "*phase analysis*", because it is related to the phases interaction and to the representation of interface.

It is already possible to find a great number of studies based on the phase analysis in literature (e.g see [Ish75]). In this chapter we will focus on the segregation of the flow field, by defining when a flow can be defined as segregated and when it is considered not segregated.

Indeed, in the previous chapter we have studied an academic test representative of an air assisted atomization with different methods covering a wide scope of interface representation. Despite an expected dependency on the mesh resolution, overall the large scale features of the flow have been recovered by all the methods for statistical quantity up to first order. The first analysis of second order statistics (Reynolds Stress components and the TKE) have shown more pronounced differences. Thus it is expected that second order statistics are related to the interface representation. To understand this relation, in this chapter, we propose to analyse a 1D signal extracted from previous simulations. This simpler statistical analysis will provide us some guidelines to finally analyse the full 3D second order statistics obtained on the air-blast configuration.

### 4.1 The statistical tools

In order to proceed to the phase analysis, we must add two statistical tools to those introduced in the previous chapter. These tools take advantage of the formalism proposed in [Ish75]:

- Conditional averaging: the conditional averaging takes into account only a part of the signal that respect a certain condition. Given a field  $\phi(\mathbf{x}, t)$  it is possible to define a conditional averaging with a condition called test as:

$${}^t\bar{\phi}_{|\text{test}} \quad (4.1)$$

In the following paragraph the test will be related to signals with three possible states and hence three possible conditional averaging cases. In particular we will analyse the phase marker signal  $\alpha$  and hence we will consider: the case in which  $\alpha = 1$  (pure liquid phase), the case in which  $\alpha = 0$  (pure gas phase), the case in which  $0 < \alpha < 1$  (transition between gas and liquid phase : the interface zone). Given a variable  $\phi(\mathbf{x}, t)$ , three conditional averages are defined:

$${}^t\bar{\phi}_{|\alpha=0}, {}^t\bar{\phi}_{|\alpha=1}, {}^t\bar{\phi}_{|0<\alpha<1} \quad (4.2)$$

- Weighted averaging: regarding the weighted averaging operator we consider the statistics of any variable  $\phi$  multiplied by the phase marker. In this sense we can introduce the weighted mean value of a variable  $\phi(\mathbf{x}, t)$  with the phase marker  $\alpha$  as:

$${}^t\tilde{\phi}(\mathbf{x}) = \frac{{}^t\bar{\phi\alpha}}{{}^t\bar{\alpha}} \quad (4.3)$$

In the next sections we will use the notation  ${}^t\tilde{\phi}_l$  and  ${}^t\tilde{\phi}_g$  to refer to the weighted average with respect to  ${}^t\bar{\alpha}$  and  ${}^t\overline{1-\alpha}$  respectively.

## 4.2 Analysis on 1D signal

We can observe the temporal evolution of the phase marker at a specific location in the domain. In particular in case of the ARCHER simulation we will have two markers to track the evolution of the liquid phase:

- The level-set distance function: in this case the presence or not-presence of the liquid phase is determined by the sign of the level-set distance function and the interface is located by definition at the level-set 0 is a value of the distance function.
- The liquid volume fraction : it represents the ratio of the liquid volume to the total cell volume. This quantity is obtained at the level of the mesh resolution on a control volume  $\Delta x^3$ . Thus, it depends on the mesh resolution. The values can be 1 in pure liquid, 0 in pure gas and any value in between, if the control volume is crossed by the interface. Consequently the precise localization of the interface is lost if we consider only the local value of the liquid volume fraction . Notice, that in numerical methods for liquid-gas flow, this local value is not considered alone and hence, a more precise reconstruction of the interface is achieved (see PLIC and SLIC in chapter 2).

In the next paragraphs we will call the phase marker (either the level-set distance function, either the liquid volume fraction ) as  $\alpha$  and we will focus on the case in which  $\alpha$  is only time-dependent. A point is considered in the computational domain:  $\mathbf{x}_0 = (x_0, y_0, z_0)$  with  $x_0 \in L_x$ ,  $y_0 \in L_y$ ,  $z_0 \in L_z$ . The phase marker considered will have the following dependency  $\alpha(\mathbf{x}_0, t)$ . In the next sections  $\mathbf{x}_0 = (L_x/6, L_y/2, L_z/2)$  and the representation of the points with respect to the flapping liquid sheet is reported in fig. 4.1.

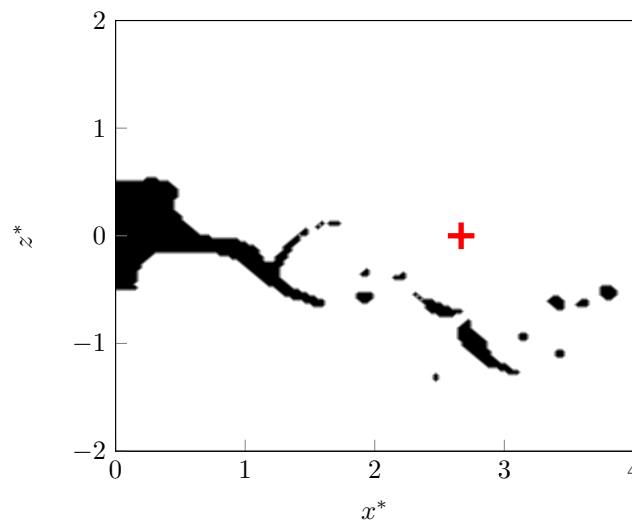


Figure 4.1 – Localisation of the point ( + ) used to extract the 1D signal of the phase marker  $\alpha$ . Here, the phase marker field is extracted from the level-set distance function.

### 4.2.1 Fully segregated flow field

Figure 4.2 reports the evolution of the marker based on the level-set distance function sign in time from 8[ms] to 11[ms]. As we can observe the signal is a purely *telegraphic signal*. We can define the Probability Density Function PDF  $f(\alpha)$  to be in three different states:  $\alpha = \mathcal{H}(\phi) = 1$ ,  $\alpha = \mathcal{H}(\phi) = 0$ ,  $0 < \alpha = \mathcal{H}(\phi) < 1$ , where  $\mathcal{H}(\phi)$  is the Heaviside function that has value 1 when the sign of the level-set distance function is positive (and hence we are in the liquid) and 0 when the sign of the level-set distance function is negative (and hence we are in the gas). In particular it is possible to associate a probability to be in each of the state. In case of this telegraphic signal we can join together the  $p(\alpha = 0)$  and  $p(\alpha = 1)$  to build the PDF  $f(\alpha)$  through the use of the Dirac function  $\delta$ , while the probability  $p(0 < \alpha < 1) = 0$  as far as it is possible for the signal to be only in two different states. Hence, having only a binary state possible, we can write the PDF  $f(\alpha)$  for the phase marker  $\alpha$  as:

$$f(\alpha) = p(\alpha = 0)\delta(\alpha) + p(\alpha = 1)\delta(\alpha - 1) \quad (4.4)$$

In order to find the two probabilities we use the 0-order and first order statistical moments.

$$\int_0^1 f(\alpha)d\alpha = 1 \rightarrow p(\alpha = 0) + p(\alpha = 1) = 1 \quad (4.5)$$

$$\int_0^1 \alpha f(\alpha)d\alpha = {}^t\bar{\alpha} \rightarrow p(\alpha = 1) = {}^t\bar{\alpha} \quad (4.6)$$

Eventually we can re-write the  $f(\alpha)$  defined in eq. (4.4) as:

$$f(\alpha) = ({}^t\bar{\alpha} - 1)\delta(\alpha) + {}^t\bar{\alpha}\delta(\alpha - 1) \quad (4.7)$$

Figure 4.3 shows the PDF  $f(\alpha)$  for the signal captured from 3.8[ms] to 30[ms]. The data in the range  $[0[ms], 3.8[ms]]$  has been discarded, to avoid the transitory period corresponding to the flow establishment. Figure 4.4 presents the Cumulative Density Function (CDF)  $\mathcal{C}(\alpha)$ .

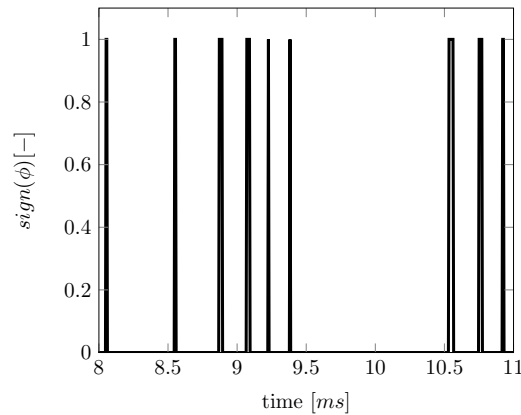


Figure 4.2 – Signal of the level-set distance function sign at a probe placed at  $(L_x/6, L_y/2, L_z/2)$  in the domain. The interval taken is from 8[ms] to 11[ms].



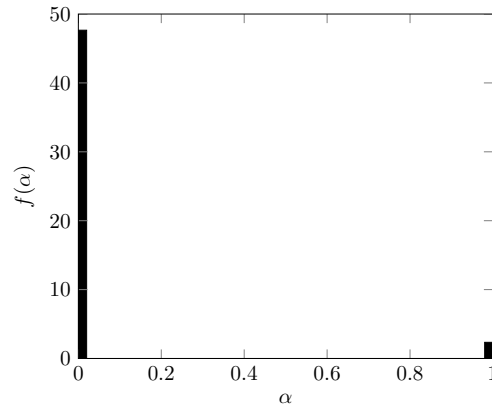


Figure 4.3 – PDF ( $f(\alpha)$ ) of the level-set distance function Heaviside function  $\mathcal{H}(\phi)$  at a probe placed at  $(L_x/6, L_y/2, L_z/2)$  in the domain. The time range extends from 3.8 to 30[ms]. Bins interval is of  $\Delta\alpha_{\text{bins}} = 0.02$ , and hence  $n.\text{bins} = 50$ .

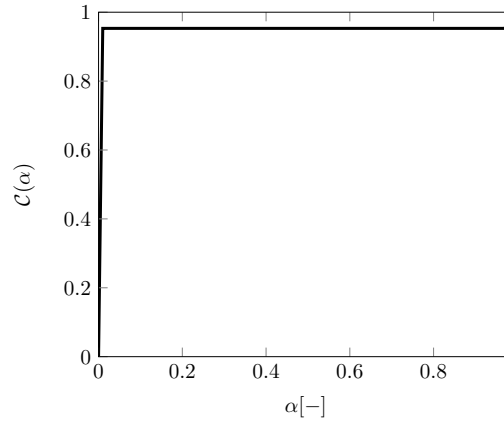


Figure 4.4 – CDF ( $\mathcal{C}(\alpha)$ ) of the level-set distance function Heaviside function  $\mathcal{H}(\phi)$  at a probe placed at  $(L_x/6, L_y/2, L_z/2)$  in the domain. The time range extends from 3.8 to 30[ms]. Bins interval is of  $\Delta\alpha_{\text{bins}} = 0.02$ , and hence  $n.\text{bins} = 50$ .

In this case the measured probability  $p(0 < \alpha < 1) = 0$ , thus, the flow field is said fully segregated. The  $p(\alpha = 1)$  is exactly the probability for the signal to be in the liquid state and the  $p(\alpha = 0)$  is exactly the probability for the signal to be in gas state. The interface has 0 thickness, its location can be determined with precision and the jump conditions are required to describe flow properties. This is exactly the case for the separated phase models we have introduced in chapter 2.

In this particular case the conditional average process and the weighted average (for the definitions refer to eq. (4.3) and eq. (4.1)) gives the same results when applied on any field  $\psi(\mathbf{x}, t)$ . Considering for example  $\psi(\mathbf{x}, t) = \mathbf{v}(\mathbf{x}, t)$ , it is possible to write:

$${}^t\bar{\mathbf{v}}_{|\alpha=1} = {}^t\tilde{\mathbf{v}}_l = \frac{{}^t\overline{\mathbf{v}\alpha}}{{}^t\overline{\alpha}} = \text{The liquid velocity} \quad (4.8)$$

$${}^t\bar{\mathbf{v}}_{|\alpha=0} = {}^t\tilde{\mathbf{v}}_g = \frac{{}^t\overline{\mathbf{v}(1-\alpha)}}{{}^t\overline{(1-\alpha)}} = \text{The gas velocity} \quad (4.9)$$

This happens because the  $p(0 < \alpha < 1) = 0$  for a segregated flow and the two averages give equivalent results. This will not be the case for the not segregated flow field, as will be better explained in the next section.

#### 4.2.2 Not segregated flow field, diffuse interface

There are cases in which the phase marker can reach values between 0 and 1, leading to a certain uncertainty on interface position. This can be due either to the model itself (as it is for the mixed phase models introduced in chapter 2), either to the numerical method and the mesh resolution. In this case the flow is called not segregated or diffused. We can have an example of not segregated flow by observing the signal of the liquid volume fraction coming from the ARCHER simulation (probe placed at  $(L_x/6, L_y/2, L_z/2)$ ) represented in fig. 4.5. As it is possible to observe, values of the phase marker  $\alpha$  that are between 0 and 1 are possible. Hence we will have a different distribution of PDF  $f(\alpha)$ . The signal can be in three different states:

- $\alpha = 1$  and hence it is possible to associate to this particular event a probability  $p(\alpha = 1)$ .
- $\alpha = 0$  and hence it is possible to associate to this particular event a probability  $p(\alpha = 0)$ .
- $0 < \alpha < 1$  and hence it is possible to associate to this particular event a probability  $p(0 < \alpha < 1)$ .

Finally in case of not segregated flow it is possible to write the PDF  $f(\alpha)$  as:

$$f(\alpha) = p(\alpha = 1)\delta(\alpha - 1) + p(\alpha = 0)\delta(\alpha) + p(0 < \alpha < 1)f_s(\alpha) \quad (4.10)$$

where  $f_s(\alpha)$  is the PDF of  $\alpha$  in the transition zone. Figure 4.6 shows the PDF  $f(\alpha)$  for the signal captured from 3.8[ms] to 30[ms]. The level of the PDF between 0 and 1 is not null anymore (see also the zoom on fig. 4.7).

It is important to highlight, here that with respect to the segregated case, where it is possible to say that when the phase marker  $\alpha = 1$  corresponds to the presence of the liquid, while when  $\alpha = 0$  corresponds to the presence of gas, here it is not strictly the case. Neither it is possible to affirm that in case of  $0 < \alpha < 1$  we are at the interface. The zone in which the phase marker fulfill the relation  $0 < \alpha < 1$  is a region that includes a part of gas and a part of the liquid and where it is not possible to define precisely an interface.

- a. The liquid weighted quantity does not correspond anymore to the conditional average. For instance, for the liquid velocity:

$$t\tilde{\mathbf{v}}_l \neq t\bar{\mathbf{v}}_{|\alpha=1} \quad (4.11)$$

This inequality is due to the liquid that is contained in the transition zone. Thus the probability  $p(\alpha = 1)$  corresponds only to the part of the liquid that is completely segregated, but an additional part is now included in the transition zone.

- b. The transition zone does not correspond actually to an interface in the sense of the transition to one phase to the other. Indeed, some transition start from 0 to 1 but before to complete they decrease back to 0 (see fig. 4.5 around 10[ms]). At the contrary any transition is completed for the fully segregated signal (see fig. 4.2). The incomplete transition may be due to the passage of very small liquid structures that are not sufficient to fill up the control volume completely with liquid. There is also a 3D effect. On the liquid volume fraction signal the control volume may be filled partially by the edge of a liquid structure.

Finally, it is important to support the idea that even if it is not fully segregated, the *diffuse interface* signal, still carry the essential information for the large liquids structures passing

through the control volume (see the nine liquid inclusions observed in both fig. 4.5 and fig. 4.2). In this particular 1D analysis based on CLSVOF *ARCHER* simulation we have been able to analyse a fully segregated signal with respect to a diffuse interface signal based on the control volume used to reconstruct the liquid volume fraction. This allows to distinguish between resolved transition and unresolved transition, but the actual challenge is to establish this distinction on fully 3D results. To explore this possibility in the next section an analysis is conducted based on the variance of the phase marker.

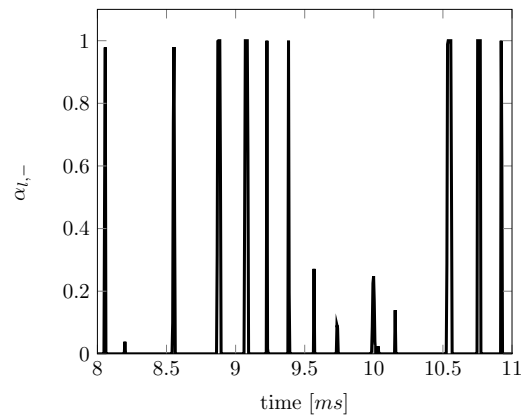


Figure 4.5 – Signal of the liquid volume fraction at a probe placed at  $(L_x/6, L_y/2, L_z/2)$  in the domain. The time interval is taken from 8[ms] to 11[ms].

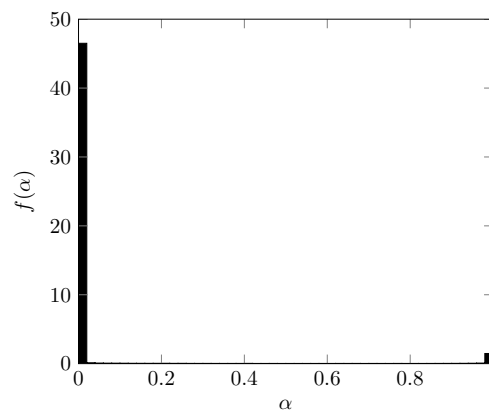


Figure 4.6 – PDF ( $f(\alpha)$ ) of the liquid volume fraction at a probe placed at  $(L_x/6, L_y/2, L_z/2)$  in the domain. The time interval is taken from 3.8 to 30[ms]. Bins interval is of  $\Delta\alpha_{\text{bins}} = 0.02$ .

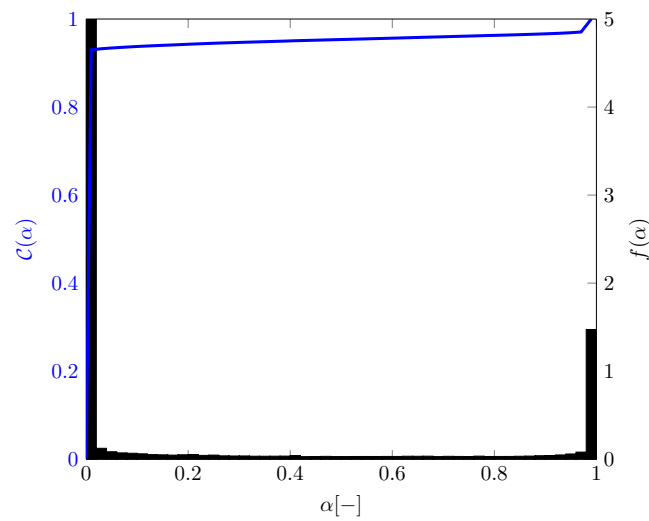


Figure 4.7 – CDF ( $\mathcal{C}(\alpha)$ ) of the liquid volume fraction at a probe placed at  $(L_x/6, L_y/2, L_z/2)$  in the computational domain. The time interval is taken from 3.8 to 30[ms]. The transitory has been considered in the range  $[0[ms], 3.8[ms]]$ . On the background a zoom of the probability density function  $f(\alpha)$  is reported. Bins interval is of  $\Delta\alpha_{\text{bins}} = 0.02$ .

### 4.2.3 Probability of presence

An important parameter to characterize the signal, is the Probability Density Function of the time interval lasted in the gas or in the liquid phase. Figure 4.8 and fig. 4.9 show time duration PDF  $f(\Delta t)$  and CDF  $\mathcal{C}(\Delta t)$  of these intervals respectively for the liquid and the gas phase. Time intervals are related to the size of liquid and gas inclusions through the velocity field. The inversion process to recover a length-scale distribution is not straightforward since the velocity may vary at the probe location during the time interval. In addition, the shape of liquid or gas inclusion is not spherical (droplet or bubble) and even if it would have been the case the probe time lasted on one phase will depend on the trajectory of the probe in the liquid or gas structure. Thus these distributions are not directly related to the diameter distribution of the spray, but they have related features. The probe has been set at  $(L_x/6, L_y/2, L_z/2)$  where the mean liquid volume fraction is equal about 4.8%. Thus the time intervals are much shorter in the liquid phase than in the gas phase. The overall sampling time is not yet sufficient to establish the mathematical form of such distribution, this would be a nice perspective of this work. A first attempt has been done in collaboration with Ludovic Goudenège (CentraleSupélec) that we would like to acknowledge for his help. This collaboration has started at the end of this PhD and it has not been possible to go further on the analysis of this signal. However, it has been possible to observe the impact of the interface representation when it is based on a non segregated phase representation. Thus, we have measured the time interval statistics at the same location but using a not fully segregated approach, similar to the one explained on the previous section, see fig. 4.10 and fig. 4.11. Despite the thickness of the *diffuse interface* approach that is relatively small (it is related to the mesh size  $\Delta x$  of the most refined case done with ARCHER as explained on the previous section), there is a clear impact of the statistics. Table 4.1 shows the total percentage of time devoted to each zone of the flow: in the pure liquid phase, in the pure gaseous phase and in the transition zone. With respect to the fully segregated case and for this probe the time lasted in the transition becomes comparable to the time spent in the pure liquid phase. Accordingly it would have been necessary to account of the transition zone for

any liquid statistic. Indeed the conditional mean for instance in the liquid phase ( $\alpha = 1$ ) will not be appropriate. Given the total time in liquid  $\Delta t_l$  and the time interval of the averaging window  $\Delta t$ , the time average of the phase marker can be evaluated as:

$$t_{\bar{\alpha}} \approx t_{\bar{\alpha}|_{\alpha=1}} = \frac{\Delta t_l}{\Delta t} = 0.028 \quad (4.12)$$

We can observe the value of the approximate time average underestimate the value computed using the definition given in eq. (3.27):  $t_{\bar{\alpha}} = 0.048$ . Considering also the transition time  $\Delta t_t$  and using a weight of  $\alpha_t = 0.5$  we obtain:

$$t_{\bar{\alpha}} \approx \frac{\Delta t_l + \alpha_t \Delta t_t}{\Delta t} = 0.05 \quad (4.13)$$

On the contrary the mathematical shape of the both PDF and CDF seems preserved. This first glance at liquid and gas time distribution shows the possibility to explore this kind of signal to make it clear which features of the liquid-gas flow are preserved and lost by using mixed phases formulation. It is expected that the main structure of the flow is preserved until the interface thickness representation interact with the characteristic length-scale of liquid and gas elements, but it is observed also that even with a very thin diffuse interface approach some key statistics can be affected if the averaging process is not appropriate.

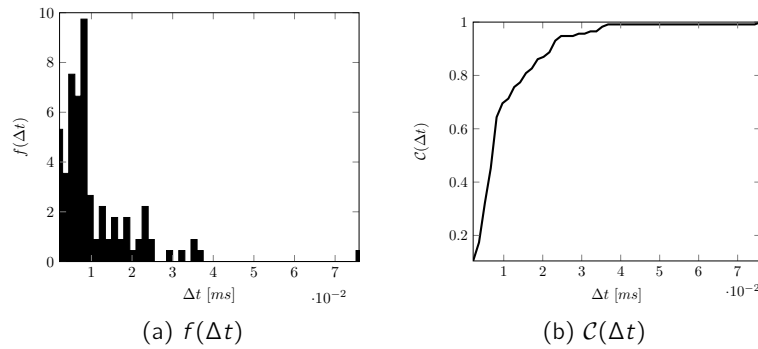


Figure 4.8 – Liquid time interval PDF ( $f(\Delta t)$ ) on the left and CDF ( $C(\Delta t)$ ) on the right for a segregated signal similar to fig. 4.2.

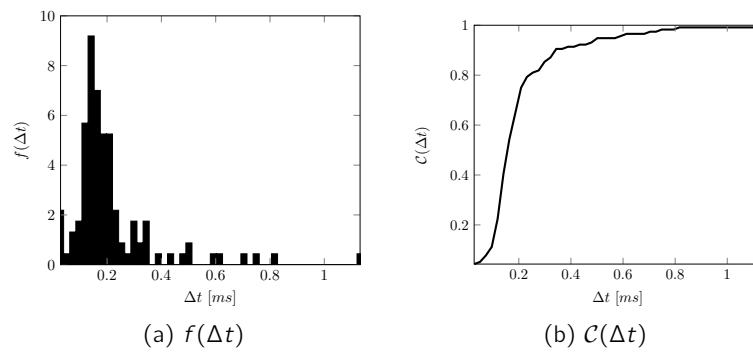


Figure 4.9 – Gas time interval PDF ( $f(\Delta t)$ ) on the left and CDF on the right for a segregated signal similar to fig. 4.2.

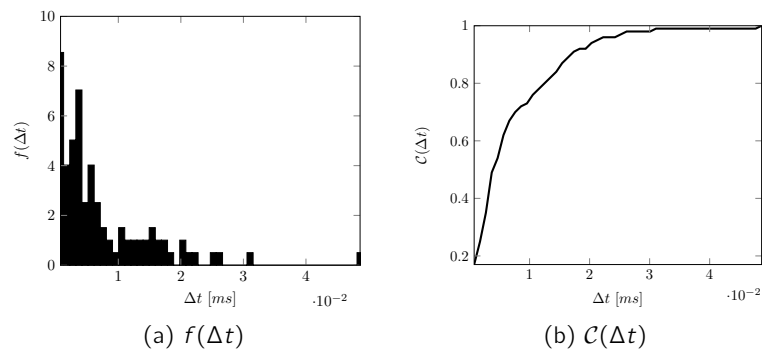


Figure 4.10 – Liquid time interval PDF ( $f(\Delta t)$ ) on the left and CDF ( $\mathcal{C}(\Delta t)$ ) on the right for a not segregated signal similar to fig. 4.5.

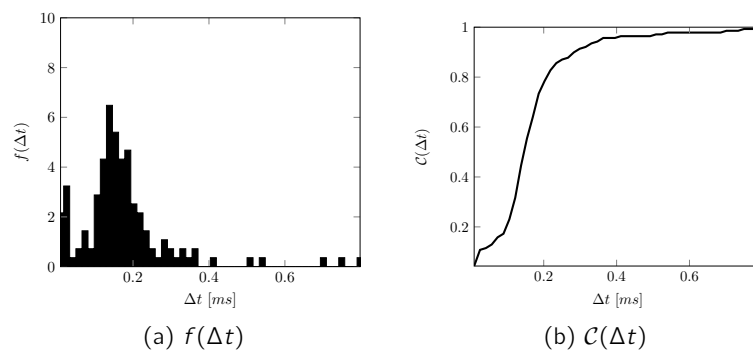


Figure 4.11 – Gas time interval PDF ( $f(\Delta t)$ ) on the left and CDF ( $\mathcal{C}(\Delta t)$ ) on the right for a not segregated signal similar to fig. 4.5.

	time gas %	time liquid %	time transition %
segregated	95.26	4.74	0
diffused	92.74	2.87	4.39

Table 4.1 – Percentage of the total time for which the signal is in one of the three states.

### 4.3 The phase marker variance

A key quantity for the phase analysis is the phase marker variance. This quantity is very important to define the level of segregation of the flow field, given a certain marker and drives the evolution of each second order moment.

Given a generic variable  $\phi$  in a fully segregated flow, and the phase marker  $\alpha$ , due to equivalence of the conditional averaging process and the weighted averaging process, it is possible to write:

$${}^t\overline{\alpha\phi} = {}^t\overline{\alpha} {}^t\overline{\phi}_{|\alpha=1} \quad (4.14)$$

Following the same method it is possible to obtain statistics related to the gas phase:

$${}^t\overline{(1-\alpha)\phi} = (1 - {}^t\overline{\alpha}) {}^t\overline{\phi}_{|\alpha=0} \quad (4.15)$$

It is possible to apply this concept to the derivation of the phase marker variance, namely  ${}^t\overline{\alpha'\alpha'}$ . This quantity can be obtained in two different ways:

- From the Reynold's decomposition definition as a *computed variance*:

$${}^t\overline{\alpha'\alpha'} = {}^t\overline{\alpha\alpha} - {}^t\overline{\alpha} {}^t\overline{\alpha} \quad (4.16)$$

- Considering the  $f(\alpha)$  for a segregated flow introduced in eq. (4.14):

$$\begin{aligned} {}^t\overline{\alpha'\alpha'} &= {}^t\overline{\alpha\alpha} - {}^t\overline{\alpha} {}^t\overline{\alpha} = \\ &= {}^t\overline{\alpha} {}^t\overline{\alpha}_{|\alpha=1} - {}^t\overline{\alpha} {}^t\overline{\alpha} = \\ &= {}^t\overline{\alpha}(1 - {}^t\overline{\alpha}) \end{aligned} \quad (4.17)$$

Using these two definitions, it is possible to introduce the *segregation factor*  $S$  that can be defined as the level of segregation of the flow.

$$S = \frac{{}^t\overline{\alpha\alpha} - {}^t\overline{\alpha} {}^t\overline{\alpha}}{{}^t\overline{\alpha}(1 - {}^t\overline{\alpha})} \quad (4.18)$$

In case of fully segregated flow field  $S = 1$  otherwise  $S < 1$ .

We can go further in our analysis and try to see if it is possible to define relations for other second order statistics using the PDF  $f(\alpha)$  of the segregated flow introduced in eq. (4.14). First we can analyse the *turbulent liquid flux*  ${}^t\overline{\alpha'\mathbf{v}'}$ , fundamental term from the modeling point of view, since it describes the sub-grid dispersion.

$$\begin{aligned} {}^t\overline{\alpha'\mathbf{v}'} &= {}^t\overline{\alpha} {}^t\overline{\mathbf{v}}_{|\alpha=1} - {}^t\overline{\alpha} {}^t\overline{\mathbf{v}} = \\ &= {}^t\overline{\alpha} {}^t\overline{\mathbf{v}}_{|\alpha=1} - {}^t\overline{\alpha} [{}^t\overline{\alpha} {}^t\overline{\mathbf{v}}_{|\alpha=1} + (1 - {}^t\overline{\alpha}) {}^t\overline{\mathbf{v}}_{|\alpha=0}] = \\ &= ({}^t\overline{\alpha} - {}^t\overline{\alpha}^2) {}^t\overline{\mathbf{v}}_{|\alpha=1} - {}^t\overline{\alpha}(1 - {}^t\overline{\alpha}) {}^t\overline{\mathbf{v}}_{|\alpha=0} = \\ &= {}^t\overline{\alpha}(1 - {}^t\overline{\alpha}) [{}^t\overline{\mathbf{v}}_{|\alpha=1} - {}^t\overline{\mathbf{v}}_{|\alpha=0}] \\ &= {}^t\overline{\alpha'\alpha'} [{}^t\overline{\mathbf{v}}_{|\alpha=1} - {}^t\overline{\mathbf{v}}_{|\alpha=0}] \end{aligned} \quad (4.19)$$

We can see how the variance of the flow drives the representation of the *turbulent liquid flux* as far as the phase marker variance is a factor of the difference of velocity among liquid and gas phase.

We can perform a similar derivation for the Reynolds stress components. Notice that beyond the method used to represent the interface, the flow is actually segregated (except if the mesh is sufficient to resolve the physical interface thickness, see discussion of chapter 2)

$$\begin{aligned}
{}^t\overline{\mathbf{v}'\mathbf{v}'} &= {}^t\overline{\mathbf{v}'\mathbf{v}'} - {}^t\overline{\mathbf{v}}{}^t\overline{\mathbf{v}} \\
&= {}^t\overline{\alpha\mathbf{v}\mathbf{v}} + {}^t\overline{(1-\alpha)\mathbf{v}\mathbf{v}} - {}^t\overline{\mathbf{v}}[{}^t\overline{\alpha}{}^t\overline{\mathbf{v}}|_{\alpha=1} + (1-{}^t\overline{\alpha}){}^t\overline{\mathbf{v}}|_{\alpha=0}] \\
&= {}^t\overline{\alpha}{}^t\overline{\mathbf{v}\mathbf{v}}|_{\alpha=1} + ({}^t\overline{1-\alpha}){}^t\overline{\mathbf{v}\mathbf{v}}|_{\alpha=0} - {}^t\overline{\mathbf{v}}{}^t\overline{\alpha}{}^t\overline{\mathbf{v}}|_{\alpha=1} + {}^t\overline{\mathbf{v}}(1-{}^t\overline{\alpha}){}^t\overline{\mathbf{v}}|_{\alpha=0} \\
&= {}^t\overline{\alpha}{}^t\overline{\mathbf{v}'\mathbf{v}'}|_{\alpha=1} + ({}^t\overline{1-\alpha}){}^t\overline{\mathbf{v}'\mathbf{v}'}|_{\alpha=0} \\
&\quad + {}^t\overline{\alpha}{}^t\overline{\mathbf{v}}|_{\alpha=1}{}^t\overline{\mathbf{v}}|_{\alpha=1} + (1-{}^t\overline{\alpha}){}^t\overline{\mathbf{v}}|_{\alpha=0}{}^t\overline{\mathbf{v}}|_{\alpha=0} \\
&\quad - {}^t\overline{\mathbf{v}}{}^t\overline{\alpha}{}^t\overline{\mathbf{v}}|_{\alpha=1} - {}^t\overline{\mathbf{v}}(1-{}^t\overline{\alpha}){}^t\overline{\mathbf{v}}|_{\alpha=0} \\
&= {}^t\overline{\alpha}{}^t\overline{\mathbf{v}'\mathbf{v}'}|_{\alpha=1} + {}^t\overline{1-\alpha}{}^t\overline{\mathbf{v}'\mathbf{v}'}|_{\alpha=0} \\
&\quad + {}^t\overline{\alpha}{}^t\overline{\mathbf{v}}|_{\alpha=1}[{}^t\overline{\mathbf{v}}|_{\alpha=1} - {}^t\overline{\mathbf{v}}] + (1-{}^t\overline{\alpha}){}^t\overline{\mathbf{v}}|_{\alpha=0}[{}^t\overline{\mathbf{v}}|_{\alpha=0} - {}^t\overline{\mathbf{v}}]
\end{aligned} \tag{4.20}$$

From eq. (4.19) we derived the following relationships:

$${}^t\overline{\alpha'\mathbf{v}'} = {}^t\overline{\alpha}[{}^t\overline{\mathbf{v}}|_{\alpha=1} - {}^t\overline{\mathbf{v}}] \tag{4.21}$$

$${}^t\overline{\alpha'\mathbf{v}'} = (1-{}^t\overline{\alpha})[{}^t\overline{\mathbf{v}}|_{\alpha=0} - {}^t\overline{\mathbf{v}}] \tag{4.22}$$

Using this relationships inside eq. (4.20) it is possible to arrive to a decomposition of the Reynold's stresses by phases.

$${}^t\overline{\mathbf{v}'\mathbf{v}'} = \underbrace{{}^t\overline{\alpha}{}^t\overline{\mathbf{v}'\mathbf{v}'}|_{\alpha=1}}_{\text{liquid}} + \underbrace{({}^t\overline{1-\alpha}){}^t\overline{\mathbf{v}'\mathbf{v}'}|_{\alpha=0}}_{\text{gas}} + \underbrace{{}^t\overline{\alpha}(1-{}^t\overline{\alpha})({}^t\overline{\mathbf{v}}|_{\alpha=1} - {}^t\overline{\mathbf{v}}|_{\alpha=0})^2}_{\text{slip tke}} \tag{4.23}$$

In eq. (4.23) we recognize clearly a contribution to the full Reynolds stresses of the liquid Reynolds stresses, of the gas Reynolds stresses and of the velocity differences. Also in this case we can observe the influence of the phase marker variance on the mixed terms of the Reynolds stress components.

Since the variance of the phase marker is so important, it would be interesting to understand if it has a connection with the numerical method and model. In the next sections we will study it more in-depth. For the interested reader, other results regarding the different terms decomposition are reported in appendix D.

### 4.3.1 Results

Hereafter we analyse the phase marker variance computed on the whole computational domain. In the following analysis, along this section, we consider as the phase marker the liquid volume fraction variable.

Figure 4.12 and fig. 4.13 present on the plane  $y^* = 0$  the liquid volume fraction variance  ${}^t\overline{\alpha'_j\alpha'_j}$ . The repartition of this field is globally the same for all the different approaches but it is possible to observe a difference in the magnitude. We have the peak values around  $z^* = 0$  and  $x^* = [0.5, 2]$  and then the fluctuations are dissipated for  $x^* > 2$ . Since it is possible to observe a clear difference between the *diffuse interface* approaches and those with a *sharp interface* representation. A continuous progression in the intensity is observed as the approaches change from *InterFoam* to *ICMelsa* and the most diffuse *ELSA* approaches. The



same effect was possible to observe for the 0-order statistics cases in the previous chapter. The trend is confirmed with the profiles of the phase marker variance represented in fig. 4.14. The peak value is the same for *ARCHER* code and *InterFoam*. The two *sharp interface* representations and thickened interface representations match in pairs, while the *ICMelsa* line lies in between. The CEDRE (MR) simulation has a remarkably lower magnitude, probably due to the low resolution that enhance numerical diffusion.

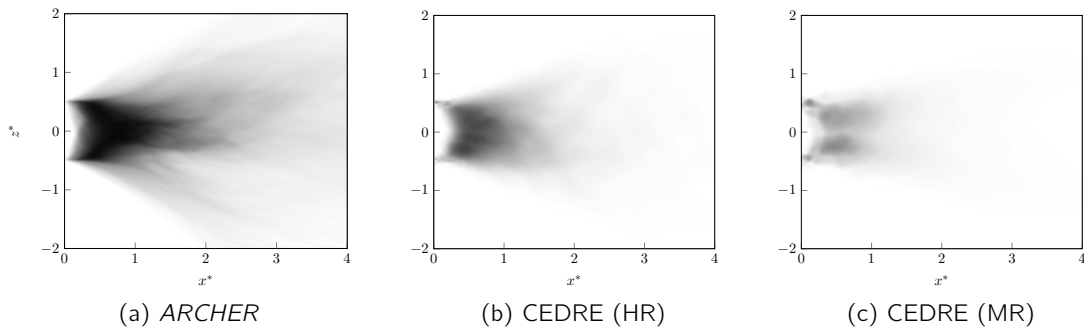



Figure 4.12 – Liquid volume fraction variance  $\overline{t\alpha'_i\alpha'_i} = 0$   0.250 at the  $y^* = 0$  plane.

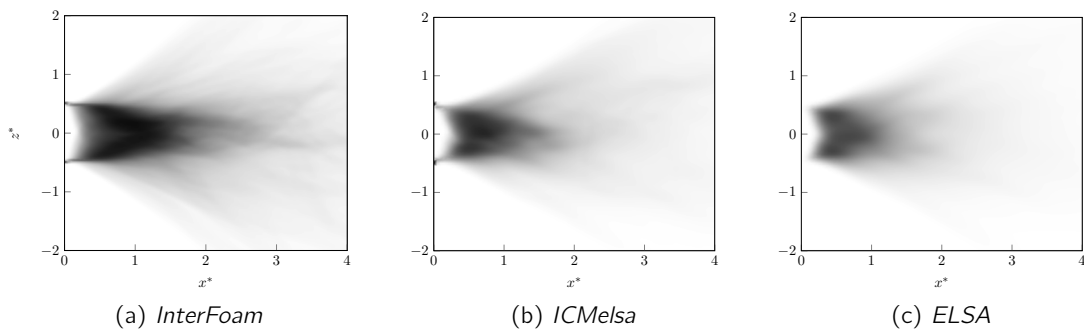



Figure 4.13 – Liquid volume fraction variance  $\overline{t\alpha'_i\alpha'_i} = 0$   0.250 at the  $y^* = 0$  plane.

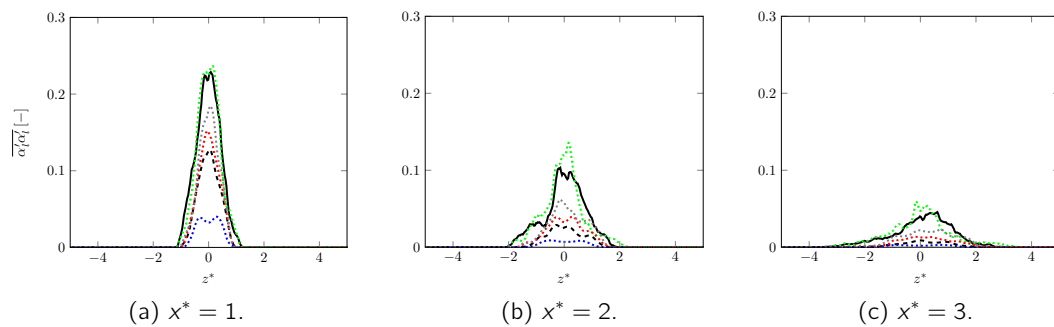


Figure 4.14 – Liquid volume fraction variance  $\overline{\alpha'_i\alpha'_i}$  along Figure fig. 3.14 and fig. 3.15 dashed lines. — *ARCHER*, ---- *CEDRE (HR)*, ..... *CEDRE (MR)*, -.-.- *interFoam*, ..... *ELSA*, ..... *ICMelsa*.

**ARCHER** In the *ARCHER* code a CLSVOF method is used. This means that we can compute the liquid dispersion using two different interface representation: the liquid volume fraction and the level-set distance function. Actually, both approaches are combined to compute the liquid flux when solving the liquid volume fraction transport equation, and both approaches are consistent by using the CLSVOF method. However, it is still possible to use one or the other field to analyse the results. By using the liquid volume fraction field integrated over a computational cell, the phase transition is spread over the cell ( $\Delta x$ ), this phase marker is called hereafter  $\alpha_{VOF}$ . At the contrary when the level-set 0 of the distance function is used, the interface thickness is reduced to zero, this phase marker is called hereafter  $\alpha_{LS}$ . Accordingly, in order to compute the statistics we assigned a value of 1 to the marker, where the sign of the distance function is positive and a value of 0 where it is negative. In the following analysis we compare the variance obtained with one phase marker field to the relation that holds exactly for a fully segregated liquid-gas flow (eq. (4.17)).

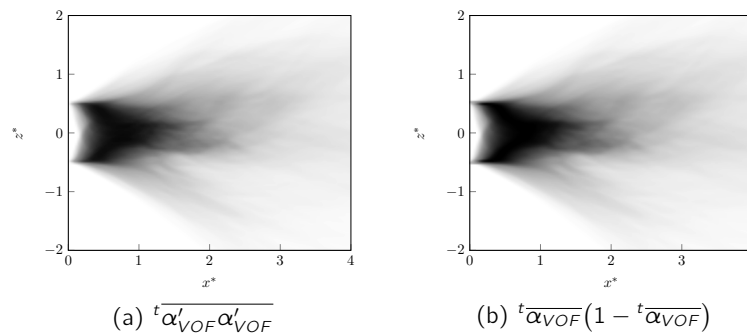



Figure 4.15 – Phase marker variance for the ARCHER code using  $\alpha_{VOF}$ . 0  0.250 at plane  $y^* = 0$ . On the left the representation of the variance field, on the right the representation of the variance computed in the segregated way.

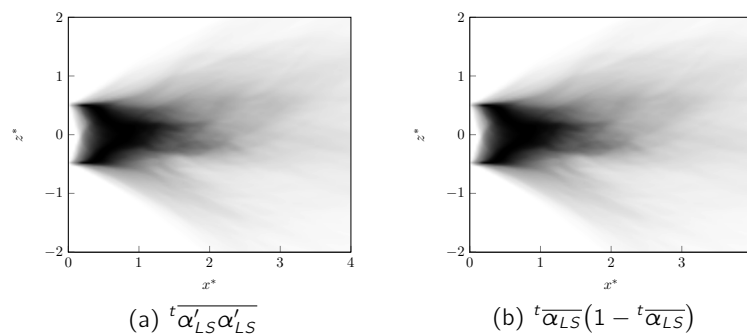



Figure 4.16 – Phase marker variance for the ARCHER code using  $\alpha_{LS}$ . 0  0.250 at the  $y^* = 0$  plane. On the left the representation of the variance field, on the right the representation of the variance computed in the segregated way.

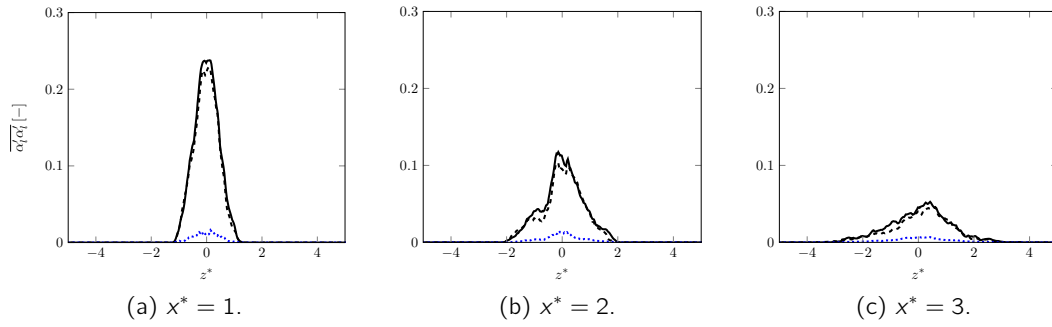


Figure 4.17 – Phase marker variance computed using the  $\alpha_{VOF}$  along slices at  $x^* = 1, 2, 3$ . —  $\overline{\alpha_{VOF}}(1 - \overline{\alpha_{VOF}})$ , .....  $\overline{\alpha'_{VOF}\alpha'_{VOF}}$ , ..... residual difference.

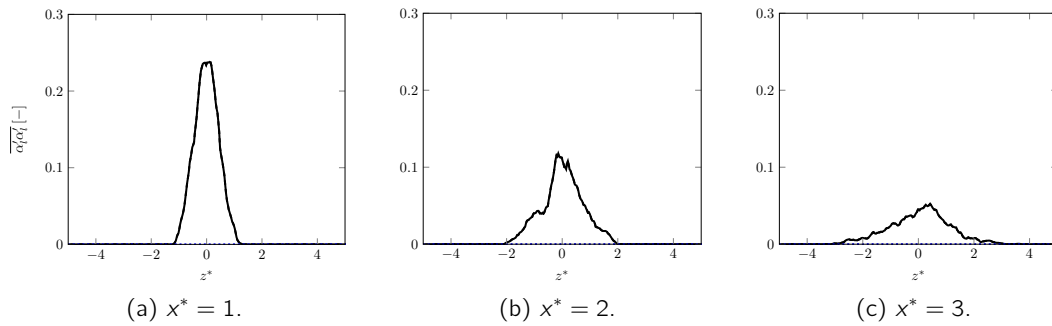


Figure 4.18 – Phase marker variance computed using the  $\alpha_{LS}$  along slices at  $x^* = 1, 2, 3$ . —  $\overline{\alpha_{LS}}(1 - \overline{\alpha_{LS}})$ , .....  $\overline{\alpha'_{LS}\alpha'_{LS}}$ , ..... residual difference.

Figure 4.15 represents at plane  $y^* = 0$  the variance and the maximum variance represented by  $\overline{\alpha_{VOF}}(1 - \overline{\alpha_{VOF}})$ , using the liquid volume fraction  $\alpha_{VOF}$ . Figure 4.16 represents the same case but based on phase marker  $\alpha_{LS}$ . Looking at the contour plot, it is not possible to notice any relevant difference. On fig. 4.17 and fig. 4.18 the equivalent vertical profiles  $x^* = 1, 2, 3$  are drawn. It is possible to observe, some differences among the two methods used to compute the variance. With the fully segregated method based on the level-set distance function, the variance and the maximum variance are perfectly identical and no residual error is produced. This is coherent with this representation  $\alpha_{LS}$  that is fully segregated with a null interface thickness. The interface transition between the two phases is a true discontinuity with a well defined position. The liquid volume fraction describes a phase transition over a length-scale of the order of  $\Delta x$ . It is interesting to see that even this relatively small interface thickness (of the order of  $\Delta x$ ) for the most refined test case has already a noticeable effect on the variance when compared to the maximum one. This can play a role on any second order statistic, since the variance is part, for instance, of any Reynolds stress component and of the turbulent liquid flux, as shown previously. If we consider that the transition between phase is actually sharp (i.e. the physical interface thickness is negligible with respect to all the other scales of the flow, see chapter 2), it follows that the evaluation of second order statistics by mean of *diffuse interface* approach have to account for an hidden part of the fluctuation below the interface thickness. In this case, even if we consider a separated phases model (CLSVOF in ARCHER), the not segregated flow behaviour is caused by the approximation of the phase marker  $\alpha_{VOF}$ , which is at the order of  $\Delta x$ .

**InterFoam** Figure 4.19 presents the plane  $y^* = 0$  of the liquid volume fraction variance field. Overall the behaviour of the variance based on the *InterFoam* description is very similar to the one obtained with *ARCHER* when the phase marker is  $\alpha_{VOF}$ . Remember that the representation of the interface with *ARCHER* is more precise since it is based on a coupled CLSVOF approach. Thus with *InterFoam* the sharpening term is quite able to sustain the interface transition to a thickness of the order of the mesh size ( $\Delta x$ ). In fig. 4.20 it is possible to observe that for the farthest ( $x^* = 3$ ) profile of the variance, a more important residual difference start to appear showing that the sharpening term becomes insufficient to preserve the interface transition at the order of the mesh resolution due to the production of very small structure at the interface, effect of the atomization process.

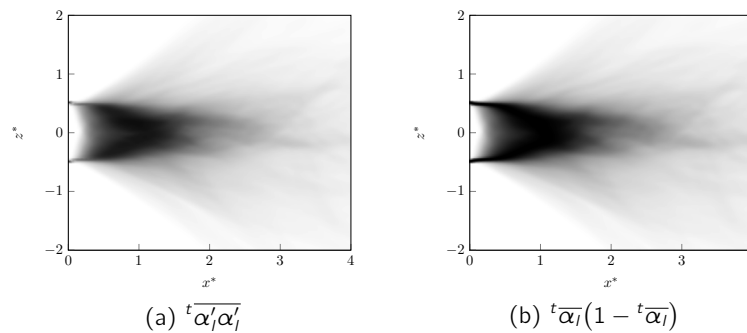


Figure 4.19 – Liquid volume fraction variance for the *InterFoam* model. 0 0.250 at plane  $y^* = 0$ . On the left the representation of the variance field, on the right the representation of the variance computed in the segregated way.

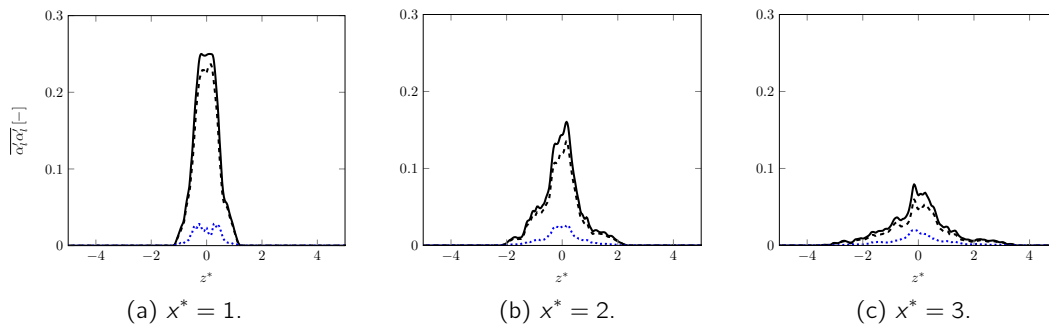


Figure 4.20 – Liquid volume fraction variance for the *interFoam* model along slices at  $x^* = 1, 2, 3$ . —  $\overline{\alpha_i} (1 - \overline{\alpha_i})$ , - - -  $\overline{\alpha'_i \alpha'_i}$ , ···· residual difference.

**ICMelsa** Figure 4.21 presents the plane  $y^* = 0$  of the liquid volume fraction variance field. It shows a departure from the fully segregated variance becoming more and more pronounced as we go down stream. This is related to the diffuse interface behaviour that increase during the atomization process. The *IRQ* sensor detects the under resolution of the interface, and activate the *diffuse interface* approach. Accordingly the *ELSA* model is used leading to a more important part of the interface described through sub-grid physical models: liquid dispersion through the presence of a sub-grid model for the turbulent liquid flux and sub-grid surface density. In fig. 4.20 it is interesting to notice that even for the first profile, where the *ICMelsa* approach rely mainly on the *InterFoam* representation, the departure to the fully segregated variance is more important than for the *InterFoam* approach. We believe this is an effect of the mesh resolution since in the test case of *ICMelsa* it is less, and we have demonstrated before that for a mixed phases model even if a sharp profile is sustained through a sharpening term, the residual difference between the variance and the maximum variance is related to the mesh size  $\Delta x$ .

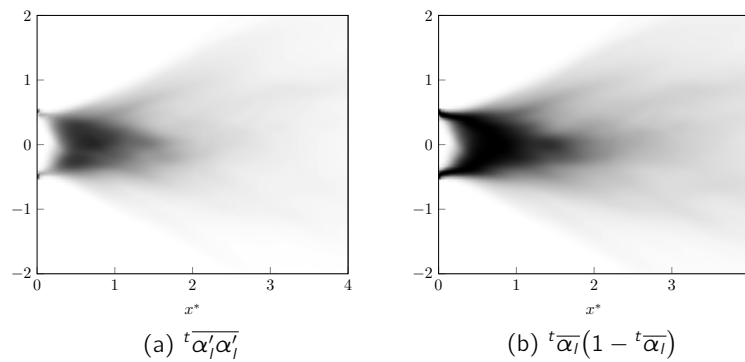


Figure 4.21 – Liquid volume fraction variance for the *ICMelsa* model. 0 0.250 at plane  $y^* = 0$ . On the left the representation of the variance field, on the right the representation of the variance computed in the segregated way.

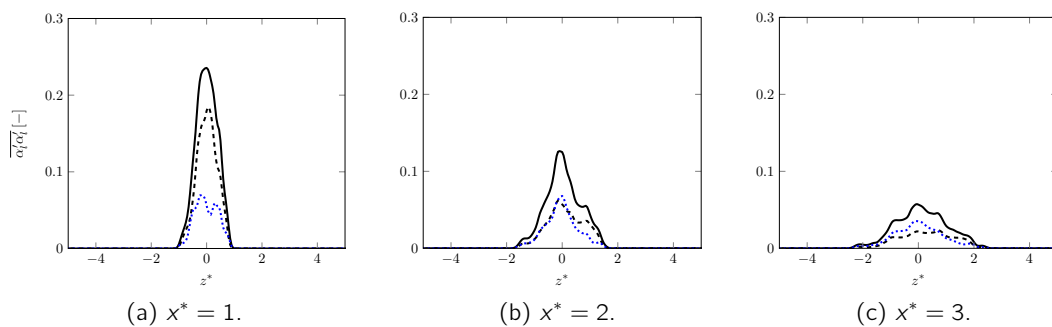


Figure 4.22 – Liquid volume fraction variance for the *ICMelsa* model along slices at  $x^* = 1, 2, 3$ . —  $\overline{\alpha_i} (1 - \overline{\alpha_i})$ , - - -  $\overline{\alpha'_i \alpha'_i}$ , ···· residual difference.

**ELSA** Figure 4.23 presents the plane  $y^* = 0$  of the liquid volume fraction variance field and in fig. 4.24 the slices at  $x^* = 1, 2, 3$ . The *diffuse interface* effect on the variance induced by the modelling of the sub-grid dispersion is clearly visible. The residual difference between the variance and the fully segregated variance is more important than for *ICMelsa* and *InterFoam*. This sub-grid effect is most probably overestimated showing that in one hand, the physical models may be not appropriate (they have been designed for high Weber and Reynolds number flows which is not the case here) and in the other hand, the numerical approach is most probably not able to maintain a sufficiently thin interface. Even in the vicinity to the injection plane the interface thickness is too large with respect to the mesh resolution to keep a variance in level and thus level of segregation comparable to the one produce with *ICMelsa*. Thus, there is a clear advantage to use the *ICMelsa* approach to benefit of the numerical representation of the interface developed in *InterFoam* for the well resolved zone.

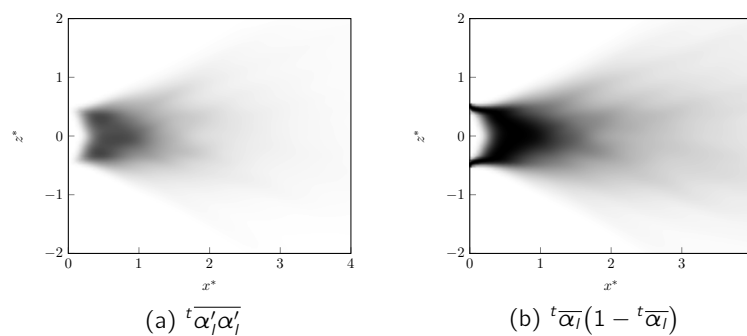


Figure 4.23 – Liquid volume fraction variance for the *ELSA* model. 0 0.250 at plane  $y^* = 0$ . On the left the representation of the variance field, on the right the representation of the variance computed in the segregated way.

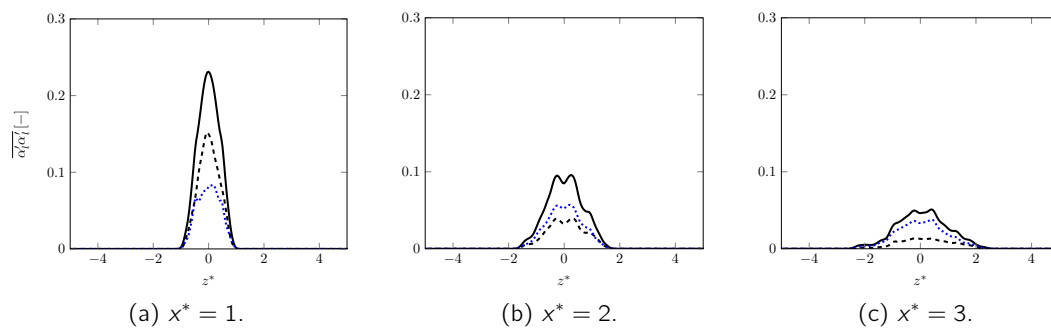


Figure 4.24 – Liquid volume fraction variance for the *ELSA* model along slices at  $x^* = 1, 2, 3$ . —  $\alpha_i(1 - \alpha_i)$ , - - -  $\alpha'_i \alpha'_i$ , ···· residual difference.

**CEDRE** (fig. 4.25, fig. 4.26) The diffuse interface approach and the numerical method associated brings the residual to be comparable with results obtained with the *ELSA* method.

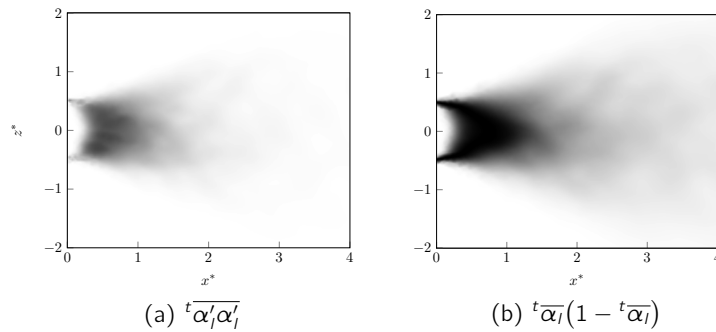


Figure 4.25 – Liquid volume fraction variance for the CEDRE model with the HR mesh. 0 0.250 at plane  $y^* = 0$ . On the left the representation of the variance field, on the right the representation of the variance computed in the segregated way.

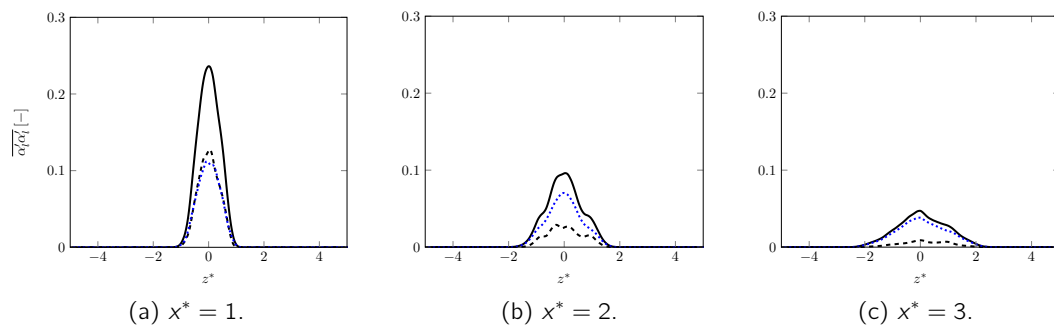


Figure 4.26 – Liquid volume fraction variance for the CEDRE model along slices at  $x^* = 1, 2, 3$  with the HR mesh. —  $\overline{\alpha_l(1-\alpha_l)}$ , .....  $\overline{\alpha'_l\alpha'_l}$ , - - - residual difference.

### 4.3.2 Conclusion about the phase marker variance analysis

In this section we highlighted the importance of the phase marker variance term and analysed this term for the simulation proposed in chapter 3. The variance has been compared for the various approaches that have various diffuse interface behaviour with respect to the variance corresponding to a fully segregated flow. The more or less pronounced effect of the diffuse interface approach has been related to the interface thickness (i.e. the size of the phase transition zone).

In case of the segregated flow there is no difference in computing the phase marker variance in one of the two ways proposed. On the contrary, in case of not fully segregated flow, it is possible to remark a residual difference. One of the main result is that using the liquid volume fraction as a phase marker even in the case of *ARCHER* still produces a residual, showing the interest of using the variance and the segregation level as a sensible analysis to evaluate the effect of the interface thickness. These results show that the effect on the variance is both related to the physical modelling of the sub-grid dispersion and to the numerical method used to characterize the interface.

In the *InterFoam*, *ICMelsa*, *ELSA* and *CEDRE* simulations we observed how mixed phases modeling approach coupled with the particular method chosen can create a different level of segregation of the flow field. One question rises from this analysis: how much the residual (and hence the segregation) is connected with the filtering related to the mesh resolution with respect to the length-scale of interface variation. In order to start answering this question a simple 1D model is developed and discussed in the next section.

## 4.4 1D model

Starting from the telegraphic signal given by the level-set distance function, we create a synthetic mixed phase signal by doing a convolution with a top-hat filter.

Given the discrete signal fig. 4.2, we have a time resolution based on the time step of the signal as  $\Delta t$ . To generate the synthetic mixed phase signal we should define the kernel for the convolution. We start by using a top-hat filter as a regularization kernel. The width of the kernel is related to  $\Delta t$  and will be assigned as  $\lambda = k\Delta t$  with  $k$  a multiplier. The designed top-hat filter will have the following shape:

$$H(t) = \begin{cases} 0, & |t| \geq \lambda/2 \\ 1, & |t| < \lambda/2 \end{cases} \quad (4.24)$$

The convoluted synthetic mixed phase signal of fig. 4.2 is represented in fig. 4.27 with  $k = 20$ . As we can observe in fig. 4.27 we obtain linear transitions between the states  $\alpha = 0$  that means absence of liquid and  $\alpha = 1$  that means presence of liquid. The transition thickness is, by definition of the convolution operator, equal to  $\lambda$  and so it can be identified as the mixed phases model interface thickness. In this 1D signal, it is possible to define an equivalent *surface density*  $\Sigma$  as the number of time the interface is crossed per unit of time over all the time interval considered.

$$\Sigma = \frac{n_i}{t_{end} - t_{start}} \quad (4.25)$$

Recalling the definition of the PDF given in eq. (4.10), it is possible to obtain the probability for the phase marker to be between 0 and 1 as:

$$p(0 < \alpha < 1) = \frac{n_i}{t_{end} - t_{start}} \lambda = \lambda \Sigma \quad (4.26)$$



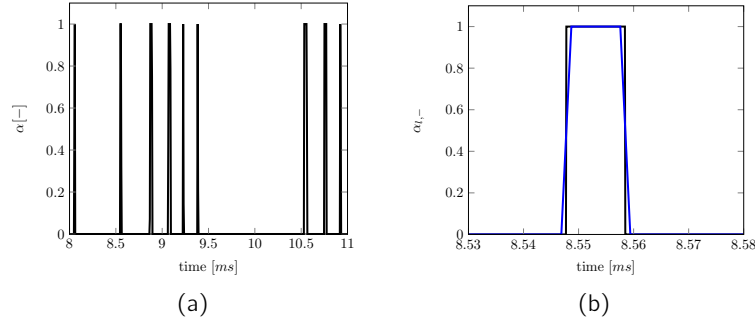


Figure 4.27 – The convoluted signal using the kernel represented in eq. (4.24) of the level-set distance function signal in fig. 4.2 at a probe placed at  $(L_x/6, L_y/2, L_z/2)$  in the domain. On the left: interval taken is from 8[ms] to 11[ms]. On the right: zoom on one transition.

Since any value of  $\alpha$  in the transition have the same probability, due to the fact that this simple model considers a linear transition, we can say that  $f_s(\alpha) = f_s$ , so it is constant. Furthermore  $f_s(\alpha)$  is normalized such that  $\int_0^1 f_s(\alpha) d\alpha = 1$  and hence  $f_s = 1$ . Thus the complete PDF  $f(\alpha)$  for any value of  $\alpha$ , becomes:

$$f(\alpha) = P_0\delta(\alpha) + P_1\delta(\alpha - 1) + \Sigma\lambda \quad (4.27)$$

Where  $P_0 = p(\alpha = 0)$  and  $P_1 = p(\alpha = 1)$ , in analogy with eq. (4.10). In order to find the coefficient  $P_0, P_1$  we consider the 0-order and first order statistical moments:

$$\int_0^1 f(\alpha) d\alpha = 1 \quad (4.28)$$

$$\int_0^1 \alpha f(\alpha) d\alpha = {}^t\bar{\alpha} \quad (4.29)$$

By solving the system of eq. (4.28) and eq. (4.29) we obtain:

$$P_0 = 1 - {}^t\bar{\alpha} - \frac{\Sigma\lambda}{2} \quad (4.30)$$

$$P_1 = {}^t\bar{\alpha} - \frac{\Sigma\lambda}{2} \quad (4.31)$$

$$f(\alpha) = \left(1 - {}^t\bar{\alpha} - \frac{\Sigma\lambda}{2}\right)\delta(\alpha) + \left({}^t\bar{\alpha} - \frac{\Sigma\lambda}{2}\right)\delta(\alpha - 1) + \Sigma\lambda \quad (4.32)$$

Built the model, it is possible at this point to evaluate the convoluted phase marker variance, and to compare it with the one computed for the fully segregated flow (and hence the telegraphic signal), reported in eq. (4.17).

$$\begin{aligned} {}^t\overline{\alpha'\alpha'} &= \int_0^1 (\alpha - {}^t\bar{\alpha})^2 f(\alpha) d\alpha \\ &= \int_0^1 (\alpha^2 - 2\alpha {}^t\bar{\alpha} + {}^t\bar{\alpha}^2) f(\alpha) d\alpha \\ &= {}^t\bar{\alpha}(1 - {}^t\bar{\alpha}) - \frac{\Sigma\lambda}{6} \end{aligned} \quad (4.33)$$

For a segregated flow, it is valid the following equation:

$${}^t\overline{\alpha'\alpha'} = {}^t\overline{\alpha}(1 - {}^t\overline{\alpha}) \quad (4.34)$$

This linear model has been tested with different  $\lambda$  and the results are shown in fig. 4.28. This figure confirms the accuracy of the model that evaluate accurately the segregation directly computed on the convoluted signal, for relatively low value of  $\lambda$ . However if the regulation kernel becomes larger, a discrepancy starts to appear and continue to increase. The explanation of this effect relies on the relative kernel size with respect to the interface one between two transition. In fact whenever the transition zone becomes large enough to interact each other the reasoning behind the linear model does not hold anymore, since the PDF  $f(\alpha)$  in the transition zone is not anymore constant. Thus it is interesting that this simple model comparison is able to reproduce the expected effect of the thickness of the interface with respect to the size of the interface fluctuations. Of course this simple model is based on a 1D time signal, but the mechanism should be essentially the same for a 3D interface simulation. The size of the kernel can be associated to the interface thickness and the interval between two transitions to the distance between two surfaces that can be the size of a droplet or the distance between two droplets. Indeed, the interface thickness of a *diffuse interface* approach play a role at two different levels. If it is small it simply damps the level of fluctuations (i.e. it reduces the segregation level) by adding a mixture layer around the surface. The structure of the surface is still essentially preserved. If the interface thickness is large enough to interact with the surface structure (for example drop size) then another effect takes place and additional features of the interface are lost.

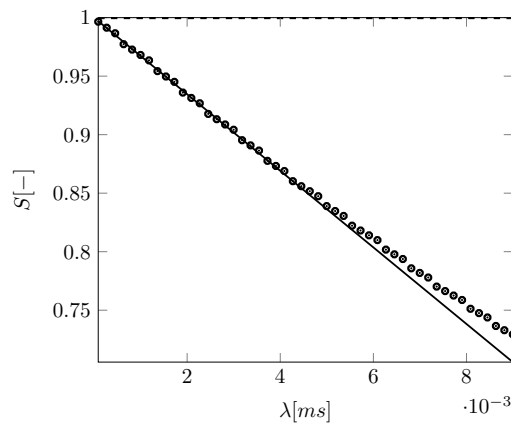


Figure 4.28 – Results of the segregation ( $S$ ) of the convoluted phase marker with respect to the linear model for different  $\lambda$ . ---- Completely segregated signal, — Ideal linear model, • convoluted signal values.

## 4.5 Conclusion and perspectives

In the present chapter we analysed the phase marker variance to understand the difference between a segregated and not segregated flow representations. We rely first on a simple 1D analysis obtained by a probe, set in the *ARCHER* simulation, to obtain a phase marker signal in time. The *ARCHER* simulation combines both liquid volume fraction and level-set of the distance function to localize the liquid-gas interface. It is still possible to use the level-set function only to recover a fully segregated representation and to integrate the liquid volume fraction on a computational cell to obtain a *diffuse interface* representation with

an interface thickness of the order of the mesh resolution. This signal has been analysed in term of statistics of the phase marker and for the time interval distribution lasted in each phase. The appearance of a non negligible transition zone between pure liquid and gas phase has been shown for the non segregated representation. This analysis of the 1D signal is corroborated by the direct analysis of the phase marker variance used for the different methods studied in the previous chapter. It is remarkable that even a very thin interface results brings to a noticeable difference of the phase marker variance with respect to a fully segregated representation. This can be important since the phase marker variance play a role on all second order statistics: turbulent liquid flux and Reynolds stress components. For statistical analysis, the conditional mean to be in one phase is different from the phase marker weighted mean for a non fully segregated representation. Overall the non segregated representation has to be handled with care for second order statistics, but it is expected to carry the main structure of the flow as soon as the liquid-gas interface thickness remain smaller than any gas and liquid elements. To have a better understanding of this limitation, coming back to the 1D signal of the fully segregated representation a filter or regularisation kernel with different sizes is applied to produce a synthetic signal, representative of a non segregated form. Somehow in these cases we can play with the interface thickness. A linear model is built to recover the variance departure with respect to a fully segregated representation. This simple linear model match well the variance obtained for different kernel size up to a point where this size interact with the size of liquid and gas structures. This confirm the expected limitation of the non segregated representation that would require additional information to describe the under resolved scale. Overall, this chapter address only partially the dependency on the respective scales of the interface with respect to the scale of liquid and gas elements. It is mostly a starting point for further works, with several perspectives, among them:

- The segregation of the physical models and numerical methods is expected to change in with the localization of the probe used to measure the 1D signal. For this reason at the present time a simulation with 25 probes have been launched (fig. 4.29). The goal is to use the post processing developed here to define in different part of the flow the respective weight of the modeling and numerical method on the segregation measured by the variance.
- The mathematical nature of the 1D signal could be analysed with respect to the signal theory to check if it is possible to put forward particular statistical properties.
- The linear model could be used to determine if the thickness of the interface interacts with the length-scale of the liquid and gas element.
- Since we have an access to the velocity field and even to the distance function, further studies may use this information to reconstruct a length-scale distribution for the time interval distribution. Thus we can study in the future the link with the drop size distribution.

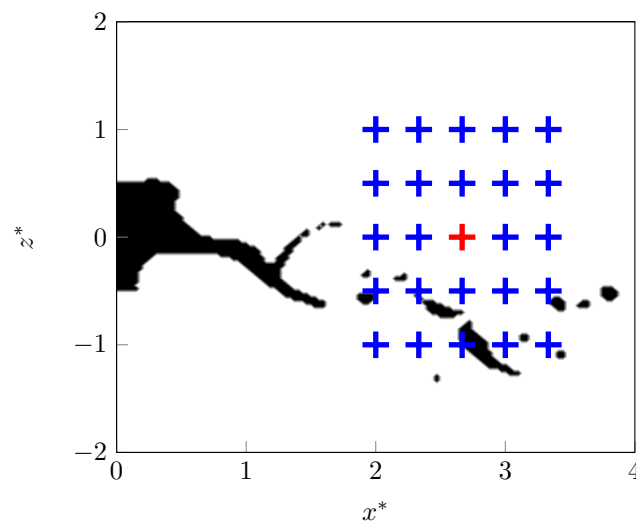


Figure 4.29 – Snapshot of the sign level-set distance function for the *ARCHER* simulation. The red cross  $+$  indicates the point in which the 1D signal has been extracted for the analysis proposed in this chapter, the blue crosses  $+$  represent the location of the probes for the future analysis.



## Chap. 5 | Silvercrest

The previous analysis performed on the air assisted liquid sheet academic configuration presents the different numerical model available and a detailed description on their advantages and drawbacks. This chapter is devoted to going further toward the final application which is the numerical simulation of a realistic aeronautical injector. Numerical formalism used in this section will be similar to the ones used in the previous chapter, allowing to extend and benchmark their capabilities to a more complex configuration.

The configuration studied here has been proposed by *SAFRAN Aircraft Engines* and is representative of an aeronautical injection system. This chapter is dedicated to the primary injector of the C42 configuration of the *Silvercrest* engine.

Due to the requirements of European norms becoming more and more stringent over the years, aeronautic engine design needs to be optimized constantly to reduce their greenhouse gas emission. The pollutant emission are related to the combustion process occurring in aeronautical engines. In the combustion chamber the fuel injection system is expected to play a more crucial role in emissions since the chamber is becoming more compact to reduce the plane weight. Consequently, the flame is closer to the injector. This phenomena leads engineers and researchers to work further on this topic.

The injectors are mostly designed in a continuous process of slight modifications of the previous geometries based on empirical considerations. The goal of this chapter is to evaluate the ability of numerical simulation to predict accurately the spray characteristics based on the internal design of the injector. Ultimately, it is expected to complete the classical design approaches by numerical simulation of the injectors to speed up the whole design process. Complementing the experiments results with predictive numerical studies would allow *SAFRAN Aircraft Engines* to optimize its design process and greatly reduce its experimental campaigns costs.

In the first part of the chapter we will introduce the pressure swirl-atomizer and the related challenges. The analytical and empirical models present in literature that are mostly used in the design process of the injector will be reviewed.

In the second part of the chapter we will present the available experimental results along with the related experimental setup.

In the last part of the chapter we will present the results of the simulation performed. Due to the complex geometry that requires an adapted mesh, three models (*InterFoam* , *ELSA* , *ICMelsa* ) have been used for this configuration. In addition, this configuration lead us to propose an improvement of the *ICMelsa* framework, in order to take into account the effect of the different modeling and of the minimum interface density area term. Finally recent strategy developed in [Fer22] and [Pal21] will be used to predict the Sauter Mean Diameter.

## 5.1 The pressure-swirl atomizer

In a pressure-swirl atomizer, liquid is delivered in the swirling chamber through tangential ports. It starts to rotate and, under the action of the centrifugal forces, spreads out in the form of a conical sheet as it leaves the orifice. The liquid sheet experience instabilities that disintegrate it and generate a series of droplets (fig. 5.1).

One advantage of this kind of configuration is to reach larger cone angles respect to common pressure atomizers, due to the action of the centrifugal forces. However the hydrodynamic processes happening inside a pressure-swirl atomizer are very complex. The single swirling atomizer is commonly called *simplex* injector. Another type of swirling injector is commonly called *duplex*. In this case the fuel is delivered to the combustion chamber through a set of two co-axial swirling injectors (a primary and a secondary), fed by two different circuits. At low flow rate requirements, all the fuel is delivered through the primary injector, while for high flow rate requirements also the secondary injector starts to work.

Inside the jet engines it has been common practice to install pressure-swirling injectors. With respect to internal combustion engines, where the combustion chamber is closed and the mixture is done through the piston motion, in the case of Jet engines we have an annular, constant volume combustion chamber, and hence the atomizer must:

- Provide a fine atomization;
- Provide the mixing without the help of any mechanical component.

Though the pressure swirling atomizer is the common solution, new technologies have been developed. The interested reader can refer to the chapter 1 for more details.

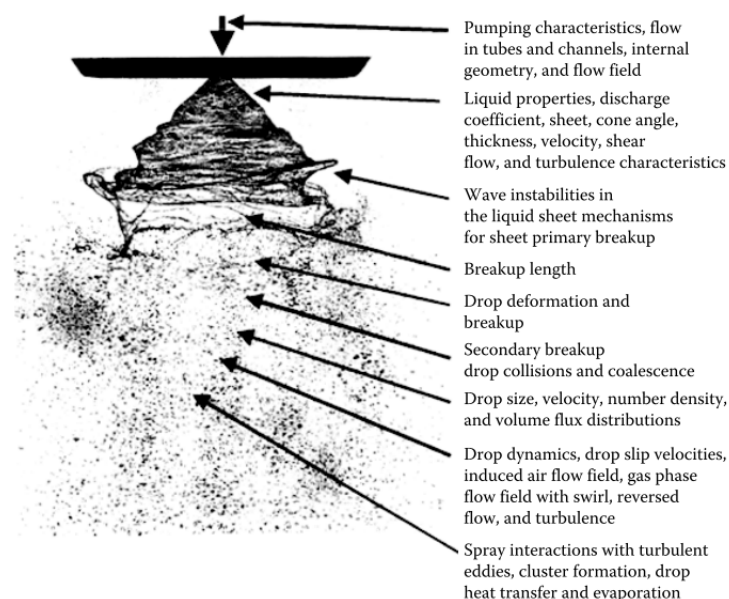


Figure 5.1 – Important quantities characterizing the flow field outside the pressure-swirl atomizer from [LM88]

## 5.2 Performance and Physical phenomena of a Pressure-Swirl atomizer

In the following section we will exploit the different parameters that are useful to characterize the performance of a pressure-swirl atomizers, highlighting the physical process happening inside and outside the swirling chamber.

### 5.2.1 Inside the swirling chamber

The liquid is fed into the swirling chamber by tangential ports and discharged in the combustion chamber through the outlet orifice. The swirling movement causes the creation of an air-core vortex at the center of the swirling chamber.

The most important feature of the flow inside the swirling chamber is the formation of the air core because it determines the most important performance parameters of the injector. During the recent years different studies about the air-core dimension and dynamic have been conducted. The pioneering work about treatment of the potential flow (inviscid theory) in a simplified cylindrical swirling chamber has been conducted by Taylor in [Tay48], where he predicted the air core diameter and atomizer performances. In [Tay50] a new study extended the validity to a viscous case and predicted the boundary layer growth in a convergent nozzle. During this period a wide range of studies based on Taylor's theory and boundary layer analysis have been performed (among the others [BH50]). The experimental work of Kutty in [KNN78] allowed a wide number of theoretical studies. Furthermore, the two main experimental techniques for the measurements of the liquid film thickness have appeared in this period. The first one (e.g used in [KNN78]) uses a photographic technique, with optical access to the injector, by tacking photos upstream through the nozzle outlet. The optical access poses mainly two issues. First of all the dimension of the injector must be increased, and second, the material for the model must be chosen carefully in order to take into account the refraction index ([TY07]). The second technique was introduced in [SL86]. Water is injected and the electrical conductance between two electrodes located at the discharge orifice is measured. Since water conductance is known, it is possible to directly determine the average liquid film thickness among the two electrodes.

The theoretical works produced during these years provided to be the most relevant and are still today widely used to evaluate the performance of an injector. The evaluation of the air core dimensions and non viscous empirical framework was built by Lefebvre, Rizk in [RL85], [RL87] and by Suyari in [SL86] covering the most of industrial injection pressure (from 1 to 3 [atm]) using water as discharged liquid, to allow the measurement. These results have been verified and discussed in [DS00] where they computed the air core diameter in a two-dimensional axis-symmetric conical swirl spray nozzle, with the help of least resistance theory. The analysis with pressure injection up to 1 [bar] and typical length-scales of  $l = 10^{-3}[m]$  performed considering injectors of industrial interest, showed how the theoretical predictions are not capable to represent an uniform and steady air core diameter at the nozzle. In [HDS02] the evolution of the formation of liquid core has been shown, performing an experimental campaign on injector of different dimension (typical length scale of the order of  $10^{-3}[m]$ ). One of the first characterization using numerical method can be found in [Das+01]. During the most recent years further experimental studies have been performed in order to better understand the air-core formation process. One of the most relevant work has been [MASB10]. Here different relationships from literature have been tested, with a varying injection pressure (up to 7 [bar]). In the last decade a huge focus has been given to the dynamic of the inner air core (in [Chi+16] for instance).

In the following paragraphs we will present the main parameters characterizing the performance of the atomizer.



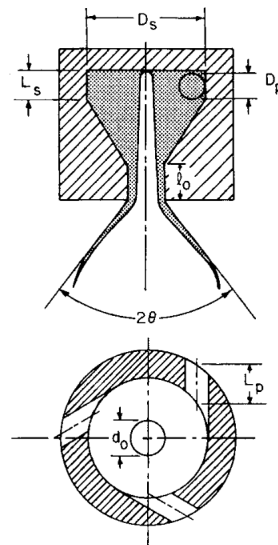


Figure 5.2 – Schematic representation of the simplex swirl atomizer ([RL85]).  $D_p$  represents the diameter of a single circular inlet port,  $L_p$  represents the length of the inlet port,  $L_s$  represents the width of the swirling chamber sky,  $D_s$  represents the diameter of the swirling chamber sky,  $d_0$  represents the diameter of the outlet orifice,  $l_0$  represents the length of the outlet orifice throat,  $2\theta$  represents the double of the cone angle created by the discharged liquid sheet.

**Flow number** The effective flow area of a pressure atomizer (swirl and non swirl) is defined by a *flow number* ( $FN$ ). The definition is given by:

$$FN = \frac{\dot{m}_L}{(\Delta P)^{0.5}(\rho_L)^{0.5}} \quad (5.1)$$

where  $\dot{m}_L$  is the liquid mass flow rate,  $\Delta P$  is the injection pressure differential and  $\rho_L$  is the liquid density. the empirical relation for the pressure-swirl atomizers is given in [RL85]:

$$FN = 0.395 \left[ \frac{A_p^{0.5} d_0^{1.25}}{D_s^{0.25}} \right] \quad (5.2)$$

where, referring to fig. 5.2 from [RL85],  $A_p$  is the total inlet ports area,  $d_0$  is the outlet orifice diameter and  $D_s$  is the swirling chamber sky diameter.

**Discharge coefficient** The discharge coefficient ( $C_D$ ) is defined as the ratio of the actual discharge flow rate to the maximum discharge flow rate, neglecting the viscous effects. It can be related to the mass flow rate injected into the swirling chamber as:

$$C_D = \frac{\dot{m}_L}{A_0 \sqrt{2\rho_L \Delta P}} \quad (5.3)$$

Where, referring to fig. 5.2 from [RL85],  $A_0$  is the area of the outlet orifice of diameter  $d_0$ ,  $\dot{m}_L$  is the liquid mass flow rate,  $\rho_L$  is the liquid density,  $\Delta P$  is the injection pressure differential. For the pressure-swirl injectors, it is influenced by the presence of the air core and hence the value will be very low with respect to the one of the simple pressure atomization, with no swirling. In [RL85] the following relationship for the  $C_D$  was derived. Following the non

viscous theory presented in [GM50] and correcting it with experimental results derived, we obtain:

$$C_D = 0.35 \left( \frac{A_p}{D_s d_0} \right)^{0.5} \left( \frac{D_s}{d_0} \right)^{0.25} \quad (5.4)$$

Where, referring to fig. 5.2 from [RL85],  $A_p$  is the total inlet ports area,  $D_s$  is the diameter of the swirling chamber sky,  $d_0$  is the diameter of the outlet orifice. The discharge coefficient ( $C_D$ ) is usually defined as a value between 0.60 and 0.62 and is characteristic of the atomizer geometry (independent from the flow condition but dependent only on the atomizer geometry). For understanding better the influence of different geometrical and fluid parameters, Jones conducted a wide experimental campaign in [Jon82]. For the interested reader it is recommended to have a look at [LM88].

Starting from the non viscous theory of [GM50], we report here the derivation of an empirical law that bounds the discharge coefficient with the injector's geometry and will be useful for the derivation of the liquid film thickness empirical law.

Considering a simplex swirl-pressure atomizer as in fig. 5.2 (a simply convergent pressure-swirl atomizer), it is possible to write the conservation of angular momentum considering non-viscous conditions. Considering the tangential velocity  $v$ , a radius  $r$  inside the swirling chamber, and assuming a solid spin or solid body rotation, it is possible to write:

$$vr = v_i R_s \quad (5.5)$$

$R_s$  is the diameter of the swirling chamber in correspondence of the inlet.  $v_i$  is the inlet velocity and hence, knowing the mass flow rate  $\dot{m}_L$ , the total injection surface  $A_p$ , we have:

$$v_i = \frac{\dot{m}_L}{\rho_L A_p} \quad (5.6)$$

Where  $A_p = \sum_i A_i$ , with  $i$  iterating on the total number of inlet tangential inlet ports (usually are from 1 to 4). Considering to be in a constant total enthalpy condition ([QA13]), the total pressure  $P_0$  is conserved throughout all the swirling chamber, and so, for the liquid, it is possible to write the following equation:

$$P_0 = p + \frac{1}{2} \rho_L u_x^2 + \frac{1}{2} \rho_L u_y^2 = \text{constant} \quad (5.7)$$

Considering to be in the condition of having a free vortex with an air core, two statements can be asserted:

- the axial velocity  $u_x$  is constant for every point inside the swirling chamber;
- the pressure of the air core is the back pressure of the ambient, and hence  $p = 0$ ;

A relation for the total pressure of a particle of liquid on the interface with the air core can be derived as:

$$P_0 = 0.5 \rho_L (v_{r_a}^2 + u_x^2) \quad (5.8)$$

Where  $v_{r_a}$  is the velocity of a point on the external radius of the air core.

Respectively the two components of the velocity are:

$$u_x = \frac{\dot{m}_L}{\rho_L (A_0 - A_a)} \quad (5.9)$$

Where  $\rho_L$  is the liquid density,  $A_0$  is the area of the outlet orifice with diameter  $d_0$  and  $A_a$  is the area of the gas core.

$$v_{r_a} = \frac{\dot{m}_L R_s}{\rho_L A_p r_a} \quad (5.10)$$

Where  $\dot{m}_L$  is the liquid mass flow rate,  $R_s$  is the radius of the swirling chamber sky,  $\rho_L$  is the liquid density,  $A_p$  is the inlet ports area and  $r_a$  is the radius of the gas core.

Substituting the two formulations in eq. (5.7), we obtain:

$$P_0 = \frac{1}{2}\rho_L \left[ \left( \frac{\dot{m}_L}{\rho_L(A_0 - A_a)} \right)^2 + \left( \frac{\dot{m}_L R_s}{\rho_L A_p r_a} \right)^2 \right] \quad (5.11)$$

From the definition of the discharge coefficient given in eq. (5.3), and using the hypothesis we have just described, it is possible to rewrite:

$$\dot{m}_L = C_D A_0 \sqrt{2\rho_L P_0} \quad (5.12)$$

We can substitute eq. (5.12) in eq. (5.11). Calling  $X = A_a/A_0$ , and  $K_1 = \frac{A_p}{\pi r_a R_s}$  it is possible to define the discharge coefficient  $C_D$  as:

$$\frac{1}{C_D^2} = \frac{1}{K_1^2 X} + \frac{1}{(1-X)^2} \quad (5.13)$$

It is useful to express the discharge coefficient as dependent only from one characteristic of the injector, i.e we would like to get rid of one parameter among  $X$  and  $K_1$ . We can apply the condition that for any given value of  $K_1$ , the size of the air core will give always the maximum flow, and hence  $\frac{d}{dX} \left( \frac{1}{C_D^2} \right) = 0$ .

By considering the system:

$$\begin{cases} \frac{1}{C_D^2} = \frac{1}{K_1^2 X} + \frac{1}{(1-X)^2} \\ \frac{d}{dX} \left( \frac{1}{C_D^2} \right) = 0 \end{cases} \quad (5.14)$$

the following relation is obtained:

$$C_D = \left[ \frac{(1-X)^3}{1+X} \right]^{0.5} \quad (5.15)$$

**Velocity coefficient** The velocity coefficient ( $K_v$ ) is defined as the ratio of the actual discharge velocity to the theoretical one generated thanks to the injection pressure differential  $\Delta P$ .

$$K_v = \frac{u\sqrt{\rho_L}}{\sqrt{2\Delta P}} \quad (5.16)$$

where  $u$  is the real discharge velocity in a geometry of the type shown in fig. 5.2,  $\rho_L$  is the liquid density and  $\Delta P$  is the injection pressure drop. In [RL87] it has been checked that  $K_v$  is related to the geometry of the atomizer and hence:

$$K_v = \frac{C_D}{(1-X)\cos\theta} \quad (5.17)$$

where  $\theta$  is the semi-angle of the cone generated by the discharged liquid sheet.

The value of this coefficient is heavily influenced by:

- the geometry;
- the pressure differential;
- the liquid properties.

**The liquid film thickness** Different formulations for the liquid film thickness estimation exist in literature. Here after we propose the derivation of the most used mathematical relation in the design process of the injectors ([RL85]).

Referring to fig. 5.2, we can consider an element of the liquid film flowing in the nozzle. This element will have length  $dx$ , depth  $dy$  and unit value in the direction tangential to the motion. Only pressure and viscous forces are considered to act to the element. These two forces should balance each others.

$$dp \cdot dy = d\tau \cdot dx \quad (5.18)$$

where  $\tau$  is the shear stress that, given  $\mu$  the dynamic viscosity of the liquid, can be defined as:

$$\tau = \mu \frac{du}{dy} \quad (5.19)$$

while  $dp$  is the local pressure gradient acting in the  $x$  direction.

Considering the pressure gradient constant across the film thickness, it is possible to integrate the eq. (5.18), and it would give:

$$\begin{cases} u = \frac{1}{\mu} \left( \frac{dp}{dx} \right) \frac{y^2}{2} + C_1 y + C_2 \\ u = 0 & y = 0 \\ u = U_s & y = t \end{cases} \quad (5.20)$$

With the constant  $C_1$  and  $C_2$  determined by the two boundary conditions and  $t$  the liquid film thickness:

$$u = \frac{1}{\mu} \frac{dp}{dx} \left( \frac{y^2}{2} - \frac{ty}{2} \right) + \frac{U_s y}{t} \quad (5.21)$$

$U_s$  being the maximum flow velocity attained at the liquid interface, obtained by differentiating the equation of the velocity and equating to zero:

$$U_s = -\frac{1}{\mu} \frac{dp}{dx} \frac{t^2}{2} \quad (5.22)$$

Averaging the eq. (5.21) in the  $y$  direction through the liquid film ( $\bar{u} = \int_0^t u dy / t$ ) it is possible to obtain:

$$\bar{u} = -\frac{1}{\mu} \frac{dp}{dx} \frac{t^2}{12} + \frac{U_s}{2} \quad (5.23)$$

Substituting the eq. (5.22), it is possible to obtain:

$$\bar{u} = -\frac{1}{\mu} \frac{dp}{dx} \frac{t^2}{3} \quad (5.24)$$

Now, referring again to fig. 5.2, the single liquid element, will be aligned with the streamlines, hence, considering  $l$  a typical length scale of the geometry, it is possible to write:

$$\bar{u} = \frac{\Delta p t^2 \cos \theta}{3\mu l} \quad (5.25)$$

Where we identify  $\Delta p$  the pressure drop along the path  $l / \cos \theta$  and  $\theta$  the cone angle. To identify a value for the length scale  $l$  we should consider that proportional, through a constant  $A$  to the outlet orifice  $d_0$  (fig. 5.2), i.e.  $l = A d_0$ . Furthermore the pressure drop  $\Delta p$  along the path direction  $l / \cos \theta$  is considered proportional to the injection pressure drop along

the whole injector through a constant  $B$ , i.e.  $\Delta p = B\Delta P$ . Substituting the relationships in eq. (5.25), we obtain:

$$\bar{u} = \frac{\Delta P t^2 \cos \theta}{3\mu d_0(A/B)} \quad (5.26)$$

Since the pressure drop is proportional to the length scale  $l$  considered, we assume that the ratio  $A/B$  remain fairly constant and around the value of  $A/B = 400$  from the experimental values ([RL85]).

Recalling the axial velocity at the outlet orifice, defined in eq. (5.9), substituting inside  $X = A_a/A_0$ , with  $A_a$  the gas core area,  $A_0$  the orifice area, and considering the relationship among the averaged velocity in the flow path direction and the axial velocity as  $\cos \theta = \frac{u_x}{\bar{u}}$ , the following relation is obtained:

$$\cos^2 \theta = \frac{12\dot{m}_L \mu(A/B)}{\pi \rho_L d_0 \Delta p t^2 (1 - X)} \quad (5.27)$$

To find a general equation for the semi cone angle  $\theta$  it is necessary to recall the relationship we have found previously for the discharge coefficient  $C_D$  in eq. (5.15). The flow was considered to be inviscid. To take into account the viscosity effect we correct it using the velocity coefficient  $K_V$  as:

$$C_D = K_V \left[ \frac{(1 - X)^3}{1 + X} \right]^{0.5} \quad (5.28)$$

Along with this mathematical expression we have the y-averaged velocity  $\bar{u}$  defined starting from the velocity coefficient definition in eq. (5.16):

$$\bar{u} = K_V \left[ \frac{2\Delta P}{\rho_L} \right] \quad (5.29)$$

where  $\Delta P$  is the total pressure jump,  $K_V$  is the velocity coefficient and  $\rho_L$  is the liquid density. The mass flow rate, defined through the volume flow rate  $Q$  as  $\dot{m}_L = \rho_L Q$ , can be hence expressed as:

$$\dot{m}_L = \rho_L Q = \rho_L A_0 C_D \left[ \frac{2\Delta P}{\rho} \right]^{0.5} = A_0 C_D \frac{\bar{u}}{K_V} \quad (5.30)$$

Now it is matter of combining the different relation we have found going through the following path:

- using the relationship  $\cos \theta = \frac{u_x}{\bar{u}}$  and substituting eq. (5.30) in eq. (5.9), we obtain eq. (5.17);
- from eq. (5.28) and eq. (5.17) we obtain:

$$\cos^2 \theta = \frac{1 - X}{1 + X} \quad (5.31)$$

Finally equalizing eq. (5.31) and eq. (5.27) it is possible to arrive firstly to:

$$t^2 = \frac{1560 F N \mu}{\rho^{0.5} d_0 \Delta P^{0.5}} \frac{1 + X}{(1 - X)^2} \quad (5.32)$$

and by substituting:

$$X = \frac{A_a}{A_0} = \frac{(d_0 - 2t)^2}{d_0^2} \quad (5.33)$$

to the final equation for the liquid film thickness  $t$ :

$$t = 3.6 \left[ \frac{d_0 F N \mu}{(\rho \Delta P)^{0.5}} \right]^{0.25} \quad (5.34)$$

As mentioned in [LM88] and [SL86] through experimental and dimensional analysis it is possible to modify the 3.6 constant to the value of 2.7:

$$t = 2.7 \left[ \frac{d_0 F N \mu}{(\rho \Delta P)^{0.5}} \right]^{0.25} \quad (5.35)$$

This relation is still used nowadays in the industry to predict the liquid sheet thickness at the outlet of the atomizers.

### 5.2.2 Outside the swirling chamber

When a sheet of liquid emerges from a nozzle, its subsequent development is influenced mainly by:

- Its initial velocity
- the physical properties of the liquid and the ambient gas

To expand the sheet against the *tension-forces*, a minimum sheet velocity is required and, in this case, it is given by the centrifugal motion induced by the swirling chamber. Increasing the initial velocity expands and lengthens the sheet until a leading edge is formed where the equilibrium exists between surface tension and inertial forces.

Fraser and Eisenklam defined in [Fra53] three main modes of sheet disintegration:

- *Rim* (fig. 5.3): forces created by surface tension cause the free edge of a liquid sheet to contract into a thick rim, which then breaks up by a mechanism corresponding to the disintegration of a free liquid jet. When this occurs, the resulting drops continue to move in the original flow direction, but they remain attached to the receding surface by thin threads that also rapidly break up into rows of drops. This mode of disintegration is most prominent where both the viscosity and surface tension of the liquid are high.

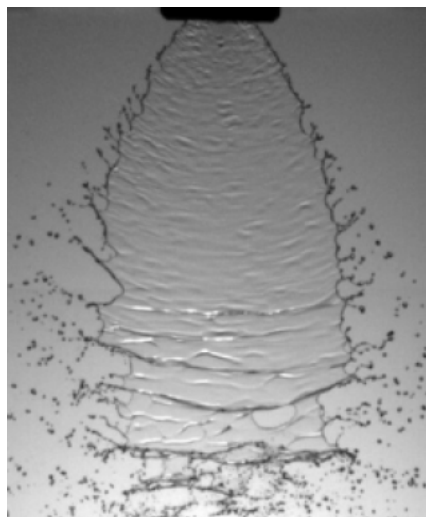


Figure 5.3 – Shadowgraphy of a jet with the rim disintegration mode ([ARA11]).

- *Wave* (fig. 5.4): the liquid undergoes to wave motion. The zone in which this happens, rapidly contract under the action of the surface tension, but disintegration can happen, due to the turbulence of the liquid flow.

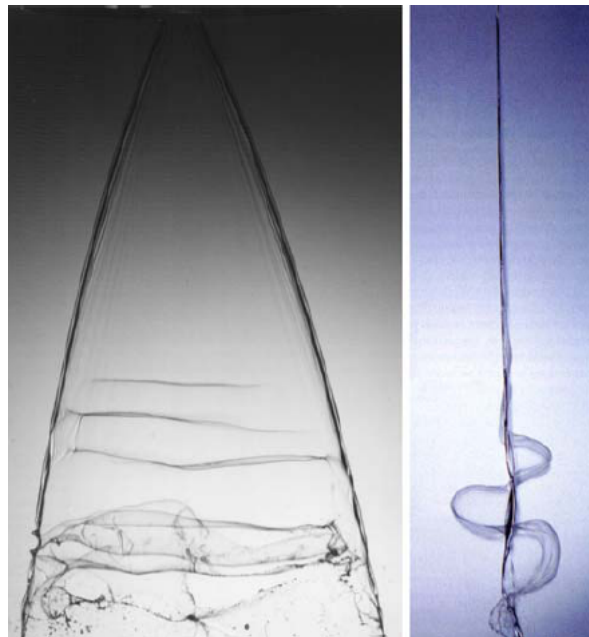


Figure 5.4 – Shadowgraphy of a jet with the wave disintegration mode ([Dum05]).

- *Perforated-hole* (fig. 5.5): holes appear in the sheet and are delineated by rims formed from the liquid that was initially included inside. These holes grow rapidly in size until the rims of adjacent holes coalesce to produce ligaments of irregular shape that finally break up into drops of varying size.

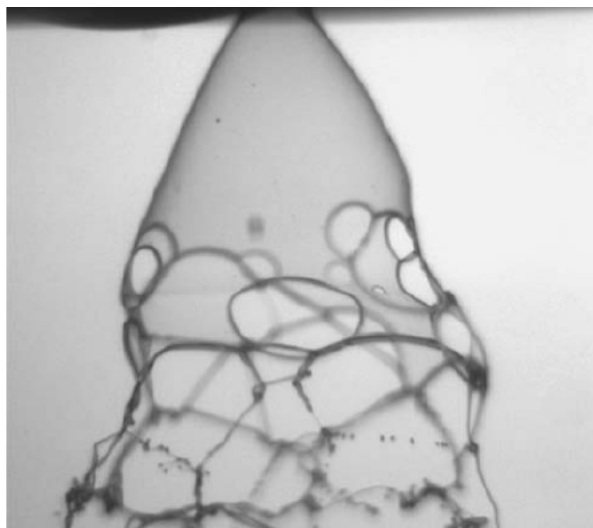


Figure 5.5 – Shadowgraphy of a jet with the perforated hole disintegration mode ([MD01]).

Atomizers that discharge the liquid in the form of a sheet are usually capable of exhibiting all three modes of sheet disintegration. Sometimes two different modes occur simultaneously, and their relative importance can greatly influence both mean drop size and the drop size distribution.

Further study about the instabilities that brings to liquid film disintegration in free swirling flows, have been carried out in [FL77] and later recalled in [Fal13]. They identified the classical mechanism of vortex breakdown that takes place when a reverse flow happens at the central

axis of the injector ([BCH98]). In [FL77] have been identified 23 different modes of vortex breakdown. The most common gives origin to a flow topology of bubble and spirals. The different modes are really dependent on the pressure and velocity field as well on the geometry of the orifice (if we have or not a divergent and the diameter of the outlet).

The orderliness of the disintegration process and the uniformity of production of threads have a large influence on the drop size distribution ([Fra63]).

**The breakup of a liquid sheet** Considering a liquid sheet, at the interface separating the liquid and the air, the jump of pressure due to surface tension force, can be described by:

$$p_L - p_A = -\sigma \frac{d^2 h}{dx^2} \quad (5.36)$$

Where  $h$  is the amplitude of the disturbance with respect to a perfectly flat interface. Surface tension forces try to return the protuberance back to its original position, but the air experiences a local decrease in static pressure (corresponding to a local increment of the velocity) that tends to expand the protuberance (positive  $h$ ) farther outward. This corresponds to the normal pattern of wind-induced instability, where surface tension forces oppose any movement of the interface from its initial planar state and attempt to restore equilibrium, while the aerodynamic forces increase any deviation from the interface and thereby promote instability. Considering a 2 dimensional liquid sheet an exponential increase in wave amplitude occurs under certain conditions. The amplitude increase is given by:

$$h_t = Ae^{\beta t} \quad (5.37)$$

This is called Kelvin-Helmoltz (K-H) instability and has been widely described in literature, since the first work of Lord Kelvin in [Tho71] and of Helmholtz in [Hel68].

Lefebvre and Rizk examined the mechanism of sheet disruption and drop formation using very high-speed flash photography 0.2  $\mu s$  of exposure ([RL80]). It is observed that liquid air interaction produces unstable waves that disintegrates into *fragments*. These *fragments* become ligaments that eventually brake into droplets. From this analysis a clear dependence of the length-scale of the instability have been observed with respect to the shear that is due to the difference between gas and liquid velocity. The higher is the difference, the smaller is the length-scale, thus the ligament, and then the droplets eventually formed.

With liquids of high viscosity, the wavy-surface mechanism is dissipated before significant deformation of the interface occurs. Instead, the liquid is drawn out from the atomizing lip in the form of long ligaments.

Thicker liquid film thickness produces bigger droplets. This explains the importance of having a thin liquid sheet for a controlled droplets distribution.

**The breakup length** Breakup length decreases with the increase in the relative velocity between the liquid and the air. An empirical relation that relates the film thickness and the Reynolds number to the breakup length in planar liquid sheet is reported in [AH85] and a lot of other relations can be found in different studies (a classical example is [DH62]). These empirical relation are valid mostly for planar liquid sheet. A lot of other specific case can be found but a general relation for different liquid sheet shape (conical or planar) is still missing in literature to the author's knowledge. In this work we will follow the guidelines of [RN01] where the breakup length is identified with the distance where the liquid sheet is first seen with perforations.



**Mean diameter** In many calculations of mass transfer and flow processes, it is convenient to simplify the spray description by working only with mean or average diameters instead of the complete drop size distribution. The concept has been presented for the first time in [ME51]. In general we have:

$$D_{ab} = \left[ \frac{\int_{D_0}^{D_m} D^a \left( \frac{dN}{dD} \right) dD}{\int_{D_0}^{D_m} D^b \left( \frac{dN}{dD} \right) dD} \right]^{\frac{1}{a-b}} \quad (5.38)$$

Where  $D_0$  is the minimum diameter considered and  $D_m$  is the maximum diameter considered. From this general definition any combination of  $a$  and  $b$  (except  $a = b$ ) can be used to define a mean diameter. Among them the most used are the mean diameter  $D_{10}$  based on the number of droplet, the  $D_{30}$  is base on the volume of droplet, the  $D_{20}$  is base on droplet surface area,  $D_{32}$ , also called Sauter Mean Diameter (SMD), is the diameter of the drop whose ratio of volume to surface area is the same as that of the entire spray.

### 5.3 Silvercrest engine

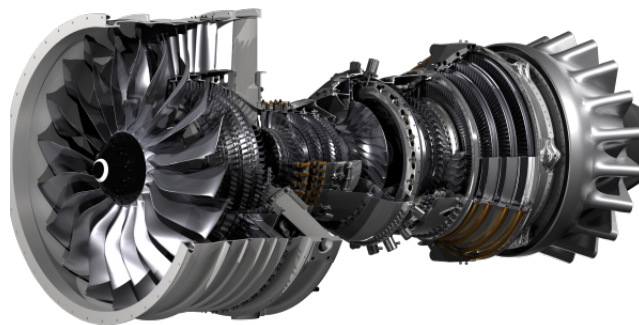


Figure 5.6 – picture of the Silvercrest engine.

Silvercrest's SAFRAN engine (fig. 5.6) is a research and development (R&T) engine and it is intended to be a demonstrator and a reference for the future. At the beginning of the combustion chamber are placed 18 duplex injectors (fig. 5.7).

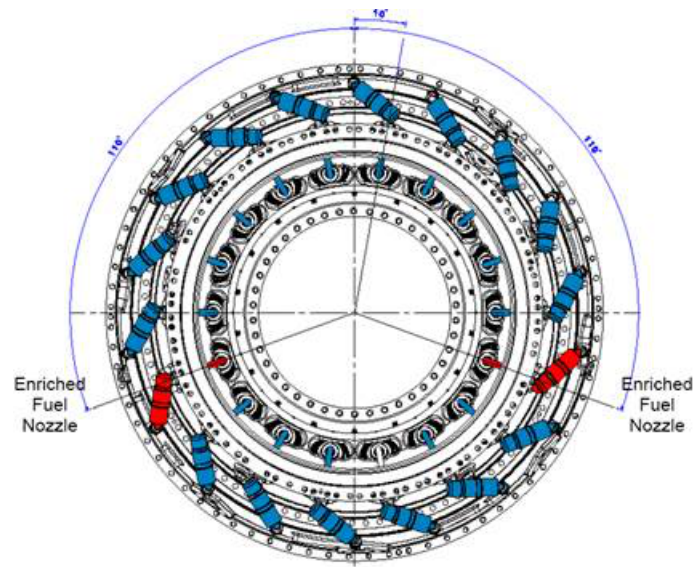


Figure 5.7 – Silvercrest’s front view of the combustion chamber with the highlight on the injectors and on the spark plugs.

In the case of the Silvercrest engine the duplex injector is deployed as a simplex injector in the most of the cases, while it is deployed as duplex only when the maximum power is required. It is for this reason, and for matter of simplicity, that our study will be focused only on the primary injector.

### 5.3.1 Experimental Campaign

The experimental campaign for the visualization of the flow was conducted considering 4 different test cases at rising injection pressures. For all the four different cases has been used JP5 (table 5.1) fuel is injected in still air at  $T = 293[K]$ . The same fuel properties have been used for the experimental campaign conducted successively for the determination of the spray characteristics.

	$\nu[m^2/s]$	$\rho[kg/m^3]$	$\sigma[kg/s^2]$	$T[K]$
JP5	$2.1 \cdot 10^{-6}$	801	0.026	293.15
Air	$1.53 \cdot 10^{-5}$	1.2		293.15

Table 5.1 – Properties of the Fuel and air used during the experimental campaign.

### Experimental setup

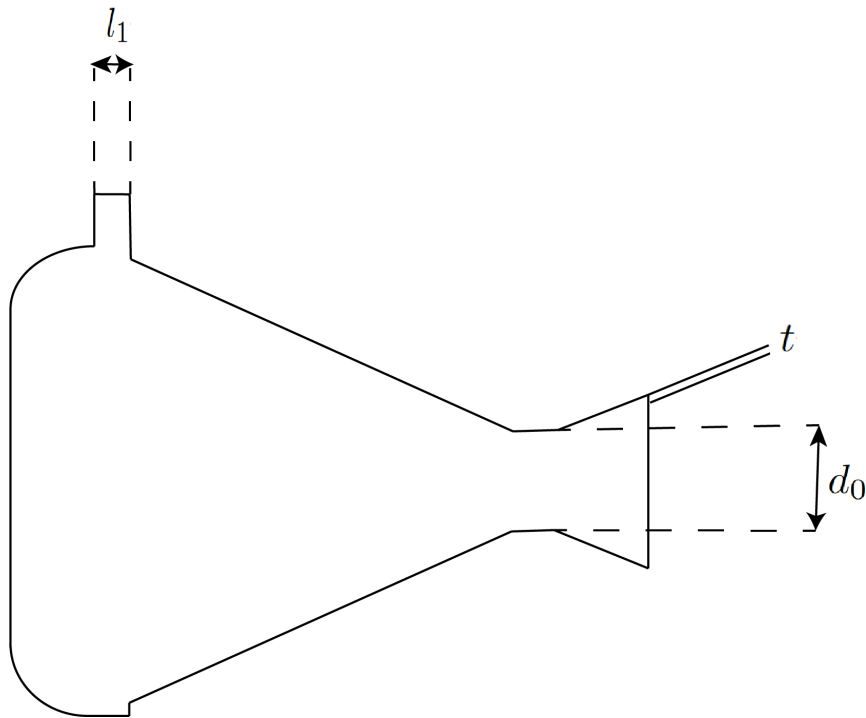


Figure 5.8 – Slice of the *Silvercrest* injector with reference names. With  $l_1$  we denote the diameter of the inlet, with  $d_0$  the diameter of the throat of the swirling chamber, with  $t$  the liquid film thickness.

The experimental campaign was conducted at the CORIA laboratory. Two different setups have been mounted for the shadowgraphy visualization and for the granulometry.

The shadowgraphy as reported in [TY07] is a particular experimental technique that does not need a special optical component. The light coming from a point source is transmitted through the test object and a shadow map due to difference in density of the medium can be collected by a camera. In the experimental campaign for the C42 injector a Phantom V2512 camera (sensor CMOS 12 bits with a pixel of  $28 [\mu m]$ ) has been used. The setup of the camera is to use a frequency of 99000 fps and  $4 [\mu s]$  of exposure time. Finally, we want to remark that part of the outflow is covered by the presence of the injector cap. All the analysis of the images we will do, will consider the origin of the axis at the tip of the injector cap (fig. 5.9).

The granulometry is done using the Phase Doppler Analysis (PDA) technique. For the interested reader, we suggest the dedicated monography [Alb+13]. For this experimental campaign a Dantec Dynamic P800 apparatus has been used. It is a system with a continuous argon laser with a power of  $0.6 [W]$  and it is possible to measure droplets in the range of  $1 - 280 [\mu m]$ . The measuring point has been placed at  $20 [mm]$  and  $30 [mm]$  from the injector cap exit. The choices of this plane, far away from the injector's outlet is common in PDA measurements. The spray should be completely developed in order to have a relatively low level of noise in the results. The granulometry results can be found in table 5.3. The experimental campaign was conducted considering different test cases at different injection pressure ( $\Delta P$ ) conditions and hence different flow rate conditions ( $\dot{m}_L$ ). Other 4 conditions have been tested to extrapolate a visualization of the flow at different regimes. It is possible to compute the

following dimensionless parameters, used to characterize the flow field (consider fig. 5.8):

$$Re_{in} = \frac{l_1 u_{in}}{\nu_{ke}} \quad (5.39)$$

$$Re_0 = \frac{t u_0}{\nu_{ke}} \quad (5.40)$$

$$We_0 = \frac{\rho_a u_0^2 t}{\sigma_{ke}} \quad (5.41)$$

Considering  $u_{in}$  the inlet velocity,  $u_0$  the velocity at the outlet orifice,  $t$  the film thickness,  $\rho_a$  the air density,  $\nu_{ke}$  the fuel kinematic viscosity and  $\sigma_{ke}$  the fuel surface tension, referring to table 5.1. The different conditions and results can be found in table 5.2. The film thickness predicted by the Lefebvre empirical relation decreases with the increasing flow rate, while the cone angle increases.

Table 5.3 presents the SMD results with increasing injection pressure. The results have been obtained through the PDA technique previously introduced. In Figure 5.10 presents the trend of the SMD with increasing injection flow rate. In table 5.2, we observe that the film thickness decreases with the increasing injection flow rate. In the introduction of this chapter we have shown that to decreasing film thickness corresponds decreasing values of droplets' diameter. In fig. 5.10 this trend is verified.



Figure 5.9 – Slice of the *Silvercrest* C42 injector. In is possible to observe the primary injector covered by the injector cap.



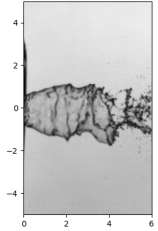
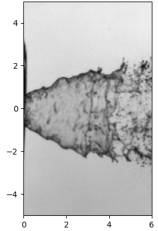
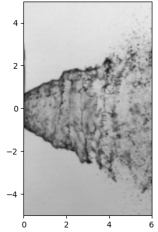
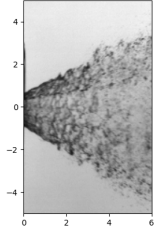
	$\Delta p$ [bar]	$\dot{m}_L$ [kg/h]	$Re_{in}$	$Re_0$	$We_0$	$t$ [m]	$A_a$ [m <sup>2</sup> ]	$K_v$	$\alpha$ [°]	$U_o$ [m/s]
	1.48	2.08	1566	293	0.14	$8.9 \cdot 10^{-5}$	$4.1 \cdot 10^{-8}$	0.30	11	5.8
	3.18	2.98	2241	424	0.3	$8.1 \cdot 10^{-5}$	$4.7 \cdot 10^{-8}$	0.33	21	9.3
	5.93	3.99	2997	576	0.65	$7.5 \cdot 10^{-5}$	$5.2 \cdot 10^{-8}$	0.35	28	13.7
	13.67	5.58	4186	855	1.6	$6.7 \cdot 10^{-5}$	$5.8 \cdot 10^{-8}$	0.38	28	22.6

Table 5.2 – Different condition tested during the experimental campaign with the different performance indexes.

$\dot{m}_L$ [kg/h]	$D_{32}$ [ $\mu\text{m}$ ]
2.0	139.6
2.4	89.2
3.3	47.1
3.6	40.2
4.9	27.3
5.1	26.0
7.1	22.1

Table 5.3 – Sauter Mean Diameter ( $D_{32}$ ) data at different flow rate inlet conditions  $\dot{m}_L$ . The tests are made at the same condition of the table 5.1.

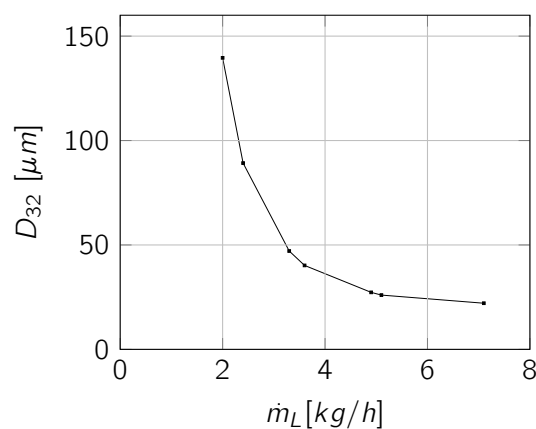


Figure 5.10 – Representation of the variation of the Sauter mean diameter ( $D_{32}$ ) with respect to the mass flow rate ( $\dot{m}_L$ ) for the *Silvercrest* engine's atomizer with the fuel properties reported in table 5.1. The detection point is placed at 20[mm].

### Design conditions

The condition studied in this work and to which it is posed the main focus during the design process are the critical ones for the engine. It is possible to identify mainly two critical conditions along the admissible flight path:

- **Re-light point:** In case of In-Flight Shut-Down (IFSD) occurrence, the injector must be capable to deliver the right amount of fuel so that the combustion can be performed in a way in which it is possible to re-light the engine. This condition is verified at a certain range of altitudes and speeds (fig. 5.11). For the *Silvercrest* injector this condition corresponds in table 5.2 to the flow rate  $\dot{m}_L = 2.98[\text{kg}/\text{h}]$ . The re-light point differentiate from the re-start point from the fact that, at the re-light point windmill restart can be attempted, at the re-start point a starter-assisted relight is required.
- **low temperature behaviour:** at high altitudes with low temperature, the properties of fuel can change. It is interesting to study how the atomization process changes accordingly to the change of properties like viscosity, density etc.

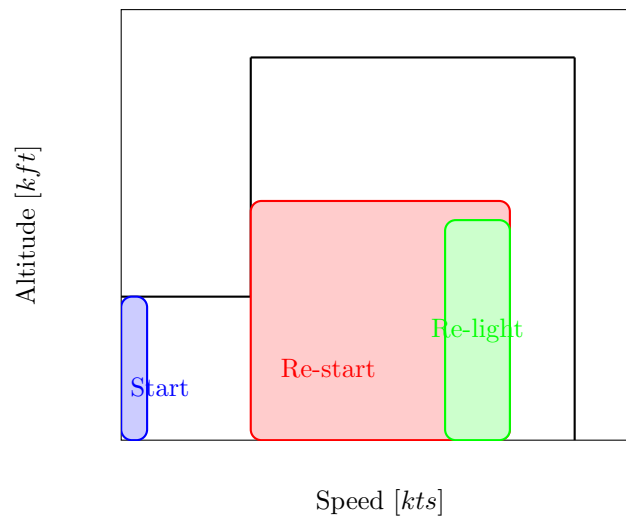


Figure 5.11 – Critical condition graph for the aircraft's engine during the admissible flight path, defined by analysing the aerodynamic performance, the engine performances, the structure performances and the load factor.

#### Flow pattern in the visualization

Once studied the quantitative parameters characterizing the swirling atomization, it is worth to have a look at the flow topology to understand better which one of the mechanism just recalled take place. Observing the shadowgraphy of the flow at the re-light point, it is possible to observe the basic mechanism of destabilization described in [BCH98]. In fig. 5.12 it is possible to observe a picture took from the seminal work of Billant [BCH98] and a snapshot of the side view of the *Silvercrest* injector's atomization process at the re-light point. It is possible to observe at the breakup point the typical two modes of vortex breakdown:

- The Kelvin-Helmoltz (K-H) instability that triggers the actual vortex breakdown.
- The spiral mode.

The flow field at the re-light point appears to be at the *tulip-stage* ([LM88])

It is not possible to go further in the analysis due to the fact that we don't have data about the velocity at the exit of the injector, so it is not possible for us to reconstruct the swirl number and to reconstruct the Reynolds number, even if for this last an attempt has been made in the table 5.2, starting from the analytical study proposed at the beginning of this chapter. These two numbers are fundamental to pursue the analysis proposed in [BCH98] and [RN01].



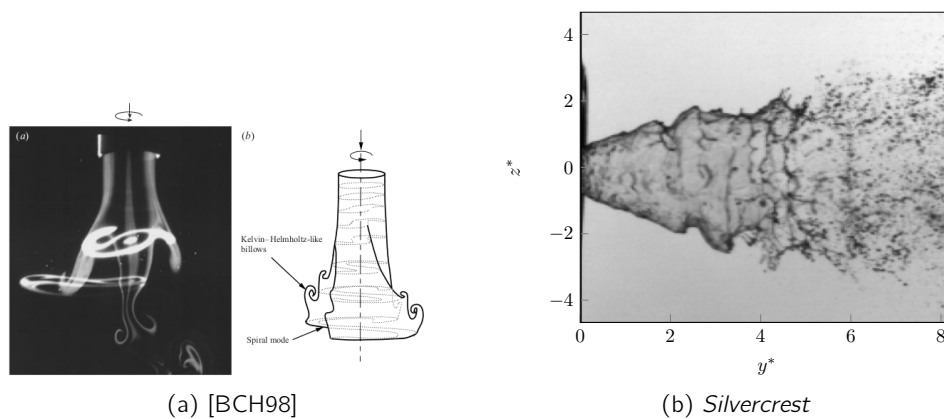


Figure 5.12 – On the left: illustration of the Kelvin-Helmholtz instability and spiral mode happening in the swirling injection by [BCH98]. On the right: Shadowgraphy of the *Silvercrest* at the re-light point.

## 5.4 The numerical process

In the previous sections we introduced the pressure swirl atomizers and their use inside the aeronautical engines. Starting from the experimental results from the *Silvercrest* case, the goal is to simulate the primary injector with an industrial oriented model that allows for a relatively fast simulation. With industrial model we address the numerical approaches available without or with very light development at the present time, able to work with a complex geometry and with a numerical simulation cost that remains affordable in term of computational resources and time consumed.

In the previous chapter we analyzed different numerical models able to handle the atomization problem, focusing on the different features of each technique. The *ARCHER* code with the CLSVOF approach and the reconstruction of the interface appear to be the most appealing, as we have observed in chapter 3. Even if the CLSVOF is the most accurate way for the interface dynamic's tracking (we used this model as the reference in chapter 3), the computational cost of a DNS is not affordable for an industrial configuration, because all the scales have to be computed to avoid any inaccuracy. The number of cells required to fully resolve the dynamic of the flow is too large and the computational time required would be not affordable (for a reference about the computational time see [Pop00]). The choice must be done among the different reduced order model that allows to reduce the number of degree of freedom of the problem and hence the number of computational cells. In the previous chapter we analyzed the 7 equations model implemented in the CEDRE code in [Cor20]. Even if this approach seems promising, it is still far from the possible use for the industrial application, and is still under development ([DB21]). Furthermore the computations performed in chapter 3, have been run with the help of Pierre Cordesse ([Cor+20b]). Due to the deadlines given by the PhD contract, he is not available for this part of the thesis. It would be interesting in future works to observe how this model is able to handle this type of geometry. In chapter 3 we analysed other three reduced order approaches based on *OpenFoam* library. Among them *InterFoam* demonstrated its ability to produce results that in terms of dynamic of the interface are comparable to the one of the DNS. The drawback is that the sharpening counter-flux tends to cluster structures of liquid when the resolution of the mesh does not allow to resolve completely the flow field. As already mentioned a mesh of DNS order of magnitude it is not affordable. Hence, the *InterFoam* model should be adapted with the use of the LES

---

formalism (chapter 2) in order to reduce the number of cells required for the computation. Nevertheless the drawback remains and, due to the reduced mesh resolution, it will be used slightly out of its range of application. The *ELSA* model tends to diffuse the interface, even if with a lower mesh resolution the approach is supplemented using a sub-grid liquid dispersion model combined with a sub-grid interface representation. However this approach is not able to recover a fully IC method (*InterFoam*). The model that unify the good features of both the models is the *ICMelsa* model. Even if it is still under development, in chapter 3 it showed great capability to reproduce the flow dynamic with an affordable computational cost.

The goal of the present study is to reproduce the most accurately possible the dynamic of the breakup that it is possible to observe in the shadowgraphy of the re-light point and to validate the film-thickness results obtained using the Lefebvre relation (eq. (5.35)). Finally it is interesting to give a prediction of the droplet size estimation, with a new technique developed in [Pal21]. After introducing all the steps necessary to define the computational domain, we will test the different models and we will analyse how the experimental results are recovered.

### 5.4.1 Solving strategy

The problem has been divided in work packages:

- Meshing process:** the primary atomizer of the *Silvercrest*'s injector has been extrapolated from the CAD sketch. An external volume has been added at the outlet, in order to simulate the outside environment. A process of mesh optimization started, in order to arrive to a final and optimal mesh.
- Simulation through IC method (InterFoam):** The first run of the simulation has been carried out using the IC method implemented in *OpenFoam*, *InterFoam*. This can be considered optimal choice to simulate the swirling chamber of the injector and to capture the first instability of the liquid sheet, but not to determine the droplet distribution. Several tests have shown that most of the interface length-scales are solved up to the injector exit. Thus this approach is suitable to determine the liquid film thickness, the global swirl motion among other characteristic feature of the internal flow.
- Simulation through ELSA:** we use *ELSA* formalism ([VB99], [Che10]) in order to gather more information to describe the poly-disperse spray.
- Simulation through the multi-scale model: ICMelsa:** with this approach the *ELSA* formalism is improved through the coupling with the interface capturing model. The details of the numerical model are explained in the section 2.2.7.

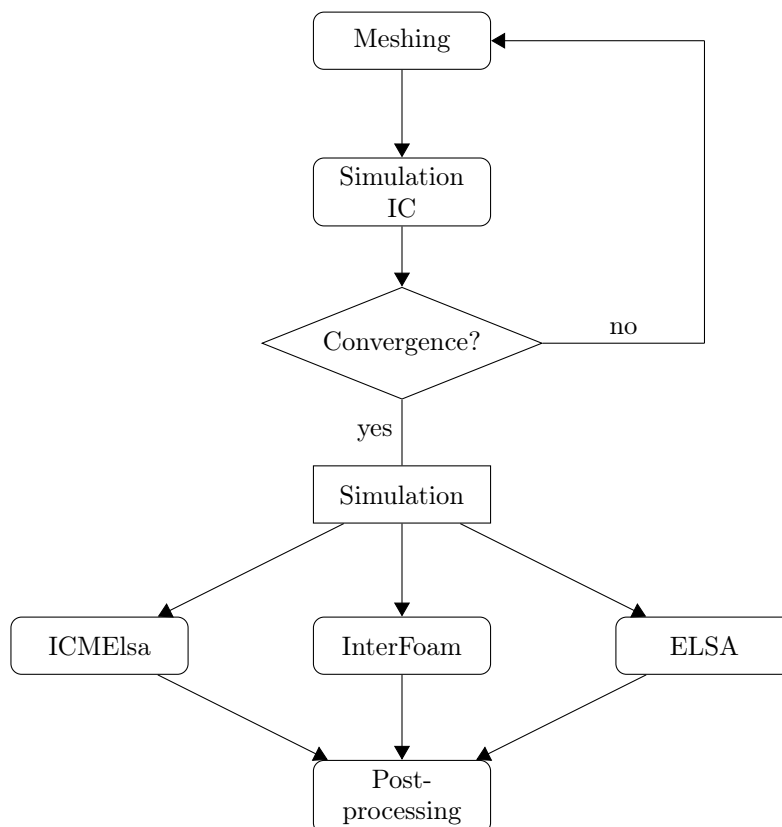


Figure 5.13 – Flow chart of the plan of the numerical study.

### 5.4.2 Meshing process

#### Geometry overview

In order to build the mesh it is necessary first of all to define the geometry in which we are interested. *SAFRAN Aircraft Engines* provided the geometry of the full *Silvercrest* injector named C42 (fig. 5.14).

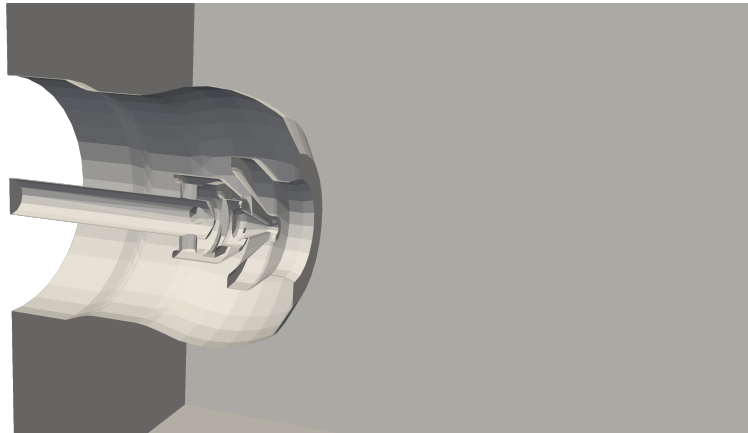


Figure 5.14 – Clip of the entire C42 duplex injector of the *Silvercrest* engine produced by *SAFRAN Aircraft Engines* .

We are interested in testing the *re-light* conditions and hence a condition in which only the primary injector is working. We want to extract only the primary injector from the entire geometry, in order to avoid useless mesh cells and hence further computational time required. In order to extract the primary injector we need to analyse further the geometry around the injector and hence, to identify in particular the inlet and the outlet. Taking a slice of the geometry at the inlet (fig. 5.15), we notice that the JP5 fuel is supplied to the primary injector through a circular crown.

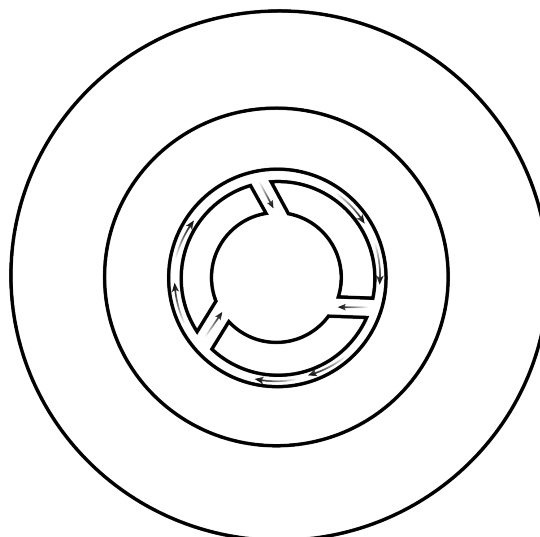


Figure 5.15 – Slice of the geometry at the level of the primary injector entrance. It is possible to observe the crown that brings to the inlet of the injector. The arrows indicates the direction of the flow of JP5 fuel.

We decide to extract the primary injector with straight entrance duct (fig. 5.16). With this choice the liquid has been supposed to enter normally to the swirling chamber and to have a simple and regular inlet patch. Even if this choice has been made, it would be interesting to make a study of the flow near the inlet's entrance in order to find the real distribution of velocity at the inlet patch.

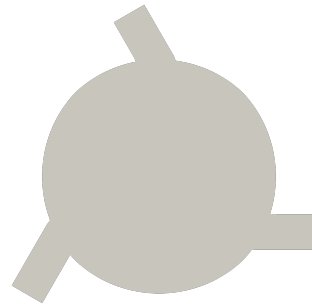


Figure 5.16 – Slice of the Silvercrest's primary injector's domain at the level of the inlet.

The numerical domain to simulate the external environment must be defined. A truncated cone of quiescent air is defined at the outlet of the primary injector, in order to have the environment where the liquid sheet issued from the injector will be atomized. A scheme of the numerical domain is defined at fig. 5.19.

#### Generation of the mesh and Numerical setup of the domain

The tool used to set up a structured mesh for the Silvercrest's injector is *BlockMesh*. It is integrated in *OpenFoam* C++ library and it allows to create a structured mesh by blocks. The philosophy of creation of the structured mesh for the Silvercrest case is to divide the geometry in blocks generating the circular shape with a square in the central part of the numerical domain. The goal of the present study is to address the film thickness raising from the swirling chamber. As we have already seen in the previous chapters, the scales involved in the atomization process are very different and a different mesh resolution should be set to solve the different constraints arising from the multi-scale problem. This will be one of the main matter of discussion in this chapter.

An analysis through 3 meshes, tested with the *InterFoam* solver has been performed. Starting from a highly refined mesh and unbalanced blocks (mesh A) we passed to a largely less refined mesh (mesh B) ending up to a mesh C which can be seen as a compromise between meshes A and B. The main improvement between the different meshes has been done in managing a more regular mesh resolution between the cone blocks and the outside environment through a grading strategy and in trying to avoid the merging of the different blocks. In fact the merging procedure in *BlockMesh* would bring to a hybrid structured/unstructured mesh and to a depreciation of the mesh quality. This value can be computed through the percentage of polyhedra with respect to the number of hexahedra. A qualitative comparison between the 3 meshes is represented in fig. 5.17. In table 5.4 it is possible to have a look to the number of cells of the different meshes in million ( $m/n$ ), the maximum and average wall distance of the first point of the mesh ( $y^+ = v_\tau y / \nu$ , where  $y$  is the wall normal coordinate,  $v_\tau$  is the velocity and  $\nu$  is the local mixture kinematic viscosity) at the inlet patch and at the end of the swirling chamber (denoted with outlet in the table). On the last line we have the CPU time to reach 1[ms] of physical time. The CPU time is computed by multiplying the number of core used by the time elapsed to complete 1[ms] of simulation.

	Mesh A	Mesh B	Mesh C
N. Cells	13.26 <i>mln</i>	2.3 <i>mln</i>	5.81 <i>mln</i>
$y_{avg}^+$ outlet	0.47	1.79	1.19
$y_{max}^+$ outlet	5.12	18.72	12.71
$y_{avg}^+$ inlet	2.11	11.63	1.98
$y_{max}^+$ inlet	6.28	22.33	5.02
Hexaedra	13.18 <i>mln</i>	2.28 <i>mln</i>	5.78 <i>mln</i>
Polyhedra	86994	24805	28615
CPU Time 1[ <i>ms</i> ] physical time (hours)	2688	384	768

Table 5.4 – Characteristics of the meshes A, B, C. Respectively in the table are reported the number of cells in the domain (in million, *mln*), the wall distance of the first point of the mesh in wall units, at the inlet and at the outlet patch (end of the swirling chamber), the number of hexaedra and polyedra and the CPU time elapsed to perform 1[*ms*] of physical time of simulation. The CPU time is computed by multiplying the number of cores used for the simulation by the time elapsed to perform it.

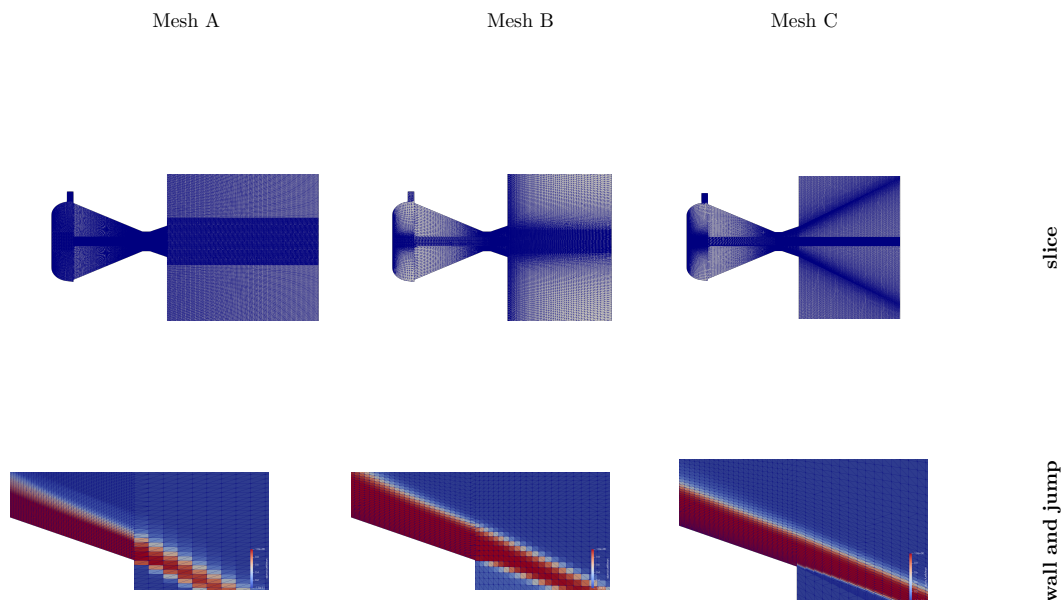


Figure 5.17 – Zoom of the outlet patch of the injector. A clear improvement is observed in the C configuration.

The mesh C still shows some lack of resolution in the environment patch. Furthermore we would like to simulate the injector starting from the inner flow up to the poly-disperse spray. To get a more regular mesh, the optimized mesh has been obtained by bounding the grading and the refinement of the different blocks composing the mesh (fig. 5.18). This is the mesh D and its characteristics are reported in table 5.5. This would bring to a more accurate results in terms of film thickness and of flow development in the quiescent environment. The huger number of mesh cells is given by the mesh refinement - grading connection, and to the heavily more refined outside environment. In the final mesh, the refinement level at the outlet allows to reach an  $y^+ = 1$  thanks to the moderate Reynolds number involved in this type of configuration (with respect to the not swirling atomizers, see e.g [Ane+19a]). The minimum cell dimension in this region is far below the *Taylor scale* limit ([Pop00]), allowing for a good capturing of the boundary layer profile and of the film thickness. The Taylor length-scale is

defined (values from table 5.2) as follow:

$$\lambda_g = D_0 \sqrt{10} Re_0^{-1/2} \approx 9.8 \cdot 10^{-5} [m] \quad (5.42)$$

Once defined the refinement level and the unbalance among the the injector and the

		Mesh D
N. Cells		54.121 <i>mln</i>
$y_{avg}^+$	outlet	0.12
$y_{max}^+$	outlet	1.02
$y_{avg}^+$	inlet	1.5
$y_{max}^+$	inlet	4.9
Hexaedra		54 <i>mln</i>
Polyhedra		121000
CPU Time 1[ <i>ms</i> ]	physical time (hours)	150528

Table 5.5 – Characteristics of the mesh D. Respectively in the table are reported the number of cells in the domain (in million, *mln*), the wall distance of the first point of the mesh in wall units, at the inlet and at the outlet patch (end of the swirling chamber), the number of hexaedra and polyedra and the CPU time elapsed to perform 1[*ms*] of physical time of simulation. The CPU time is computed by multiplying the number of cores used for the simulation by the time elapsed to perform it.

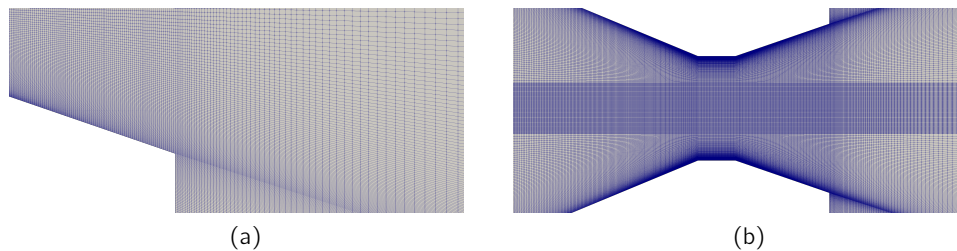


Figure 5.18 – z-normal slice of the mesh D. On the left representation of the connection among the primary injector and the outside environment. On the right representation of the throat and final part of the primary injector.

quiescent environment, it is important to set up the external domain's length. The script has been parametrized in order to have a variable external domain's length.

Once defined the mesh characteristics in the next sections we will introduce the setup used for the different models employed in the code to run the simulation progressively starting from *InterFoam* , passing through *ELSA* and finishing with *ICMelsa* . In all the different cases we will analyse three different aspect of the flow:

- Phenomenological analysis, with respect to the available experimental results, mainly shadowgraphy pictures.
- Liquid film thickness validation with respect to the eq. (5.35) that it is possible to find in [LM88].
- Breakup point analysis with respect to the experimental shadowgraphy.
- Sauter Mean Diameter analysis in line with the analysis performed in [Pal21].

In fig. 5.20, fig. 5.19 and table 5.6 are reported the geometry and the boundary conditions used for the following simulations.

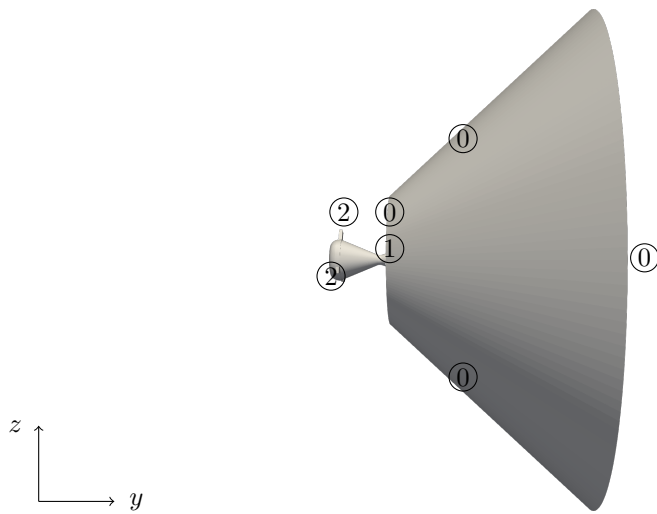


Figure 5.19 – Side view of the computational domain, marked with numbers to define the different boundary patch. ② : inlet, ① : air, ① : wall near the outlet and injector wall. For the boundary condition associated evaluate the table 5.6.



Figure 5.20 – Top view of the computational domain, marked with number to define the different boundary patch. On the left: top view of the primary injector. ② : inlet, ① : wall of the primary injector. On the right: top view of the external domain simulating the external environment. ① : air, ① : wall near the outlet of the injector.

	①	①	②
$\mathbf{v}$	Neumann: zero-gradient	Dirichelet: $\mathbf{v} = 0$	Dirichelet: imposed flux
$p$	Dirichelet: $\Delta p = 0$	Neumann: zero-gradient	Neumann: zero-gradient
$\alpha_l$	Neumann: zero-gradient	Neumann: zero-gradient	Dirichelet: $\alpha_l = 1$
$\Sigma'$	Neumann: zero-gradient	Neumann: zero-gradient	Dirichelet: $\Sigma' = 0$

Table 5.6 – Boundary condition assigned at the different boundary patch.



### 5.4.3 Simulation with interface capturing model

In the previous section we dealt with the geometry identification, mesh definition, boundary conditions. In this section we will recall the features of the industrial oriented model *InterFoam* and we will present the main results of the simulation.

#### The InterFoam model and the numerical method

In the previous chapter we introduced the *InterFoam* IC model, based on the *OpenFoam* library. We have explained the finite volume method along with the PISO algorithm to solve the incompressible N-S system and MULES algorithm for the liquid volume fraction transport equation. For more details on the theoretical and numerical methods, the reader is invited to address to the previous chapters (chapter 2, chapter 3).

We start by using this model as far as possible near to the IC method limits, with results mainly obtained at high resolution. The use of mesh D, with cells at the outlet that are verified to be in the range of  $y^+ = 1$  and lower than *Taylor scale* allows to consider the resolution big enough to capture the liquid film thickness, and to understand better the flow development inside the injector.

In order to perform the simulation, try to capture better the dynamic of the flow and match better the experimental condition and pressure loss we use the *InterFoam* model in the LES formalism. In fig. 5.21 we observe the eddy viscosity ( $\nu_t$ ) in the domain. It is an identifier of

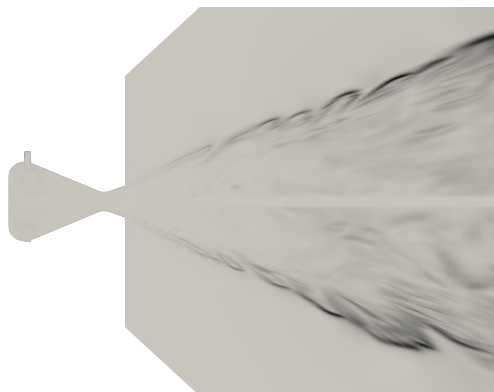


Figure 5.21 – Snapshot of the eddy viscosity  $\nu_t$  in the computational domain.  $\nu_t = 0[m^2/S]$    $1.1 \cdot 10^{-5}[m^2/s]$ .

where the LES model is actually playing a role, and gives information comparing with the kinematic viscosity ( $\nu$ ) of the liquid and gas. We observe that, while the mesh refinement inside the injector is actually good enough to not let the model play a role, in the quiescent environment, the value of  $\nu_t$  are comparable with the one of the liquid kinematic viscosity  $\nu_l$ . A filter is applied to the momentum equation, while the liquid volume fraction transport equation is not filtered (a nice review about the implication of this choice can be found in [Che+11] and on the section 2.2.7). An implicit LES method is applied with the use of a classical *Smagorinsky* model ([Sma63]) as explained in section 2.2.7. An interesting research point of view can be to test different LES models as has been done in [Ahm19] for pressure Diesel atomizers. Nevertheless the *Smagorinsky* model is a classical one and has been considered a good starting point and sufficient for the present analysis (for details about the Smagorinsky model, refer to chapter 2).

As far as the *OpenFoam* library has been designed to be easily used for industrial application, and as construction to be easy for the user to add new schemes without re-building the base elements, the order of the schemes implemented is maximum third order in space and second

order in time. We noticed also the recent concerns about the *Gauss* scheme convergence on unstructured grid [Syr+17]. In our simulations we use this scheme for gradient terms discretization, as far we have built the mesh as a structured mesh, but it could be interesting to see the differences with the least square method. More details about the accuracy in time and space for *OpenFoam* can be found in [Lee17]. The discretization schemes used in time and space are all of first and second order. The convection terms are discretized using TVD schemes (limited linear or Van Leer [VL74]). The discretization in time follows the backward scheme implemented in *OpenFoam* (a second order accuracy three point stencil scheme) for what it concerns the PISO algorithm while we use an implicit Euler scheme for the liquid volume fraction conservation equation.

#### Simulation strategy and phenomenological analysis

In the previous paragraph we reported the numerical model and method used in the simulation. In order to perform the simulation to study the film thickness, the breakup point and to save computational time, two choices are made from the setup point of view:

- The simulation start with all the cell inside the injector with  $\alpha_l = 1$ , hence with the injector full of liquid. We are not interested in the present study, to the initial unsteady process in which the injector is filled with liquid. Nevertheless it could be interesting to study this process in future works.
- The simulation starts with mesh C up to the development of the liquid film is completed. This allows to save computational time with a coarser mesh before using a finer mesh (mesh D) to obtain the proper results. The stabilization time has been chosen to 8[ms]. The flow development is reported on fig. 5.22 and fig. 5.23. Furthermore, we observe in fig. 5.24 the maximum pressure at the inlet ②. The plot shows the stabilization of the simulation and justifies our choice.



Figure 5.22 – Contour plot of the iso-surface defined by liquid volume fraction  $\alpha_l = 0.3$  of the *Silvercrest* primary injector. Startup phase on the mesh C. On the bottom left we can see the shadow of the liquid volume fraction .

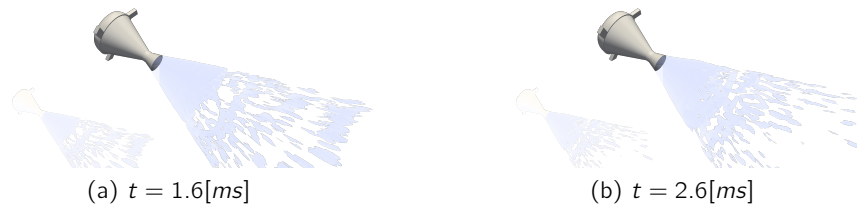


Figure 5.23 – Contour plot of the iso-surface defined by liquid volume fraction  $\alpha_l = 0.3$  of the *Silvercrest* primary injector. Startup phase on the mesh C. On the bottom left we can see the shadow of the liquid volume fraction .

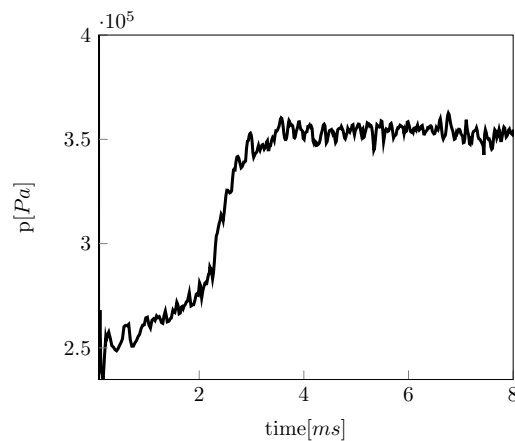


Figure 5.24 – Maximum pressure at the patch ② , with mesh C.

Starting from the physical time of 8[ms] we define the conditions to run the simulation on the mesh D. We consider a transitory time of 4[ms] before evaluating the results, in order to let the simulation stabilize.

In the atomization process (fig. 5.26) appears to show the similar dynamic of what it is shown in the experimental results. The wavy K-H instability that is shown in fig. 5.12 is partly recovered. The iso-surfaces represented in fig. 5.25 show only partly the dynamic of the flow, since they are not located at the same position (one iso-surface is at  $\alpha_l = 0.3$  and one at  $\alpha_l = 0.8$ ). This happens because, despite the interface capturing nature of the *InterFoam* model, the interface is not completely resolved, due to the mesh refinement. The reconstruction of the experimental images, starting from simulation results is still a field of open research. The built-in method proposed in *Paraview* is used here, the so-called volume rendering gives a global idea of the liquid pattern ([Aya15]).

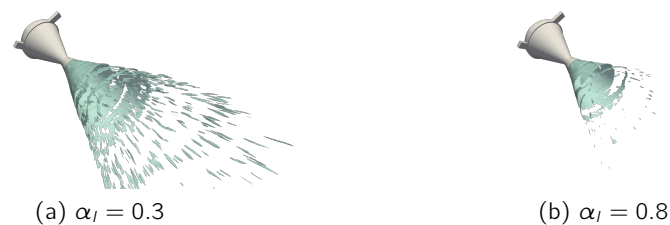


Figure 5.25 – On the left: Contour plot of the iso-surface defined by liquid volume fraction  $\alpha_l = 0.3$  of the *Silvercrest* primary injector. On the right: Contour plot of the iso-surface defined by liquid volume fraction  $\alpha_l = 0.8$  of the *Silvercrest* primary injector.

The amplitude of the waves appear less prominent, this is probably due partly to the mesh resolution that is not fine enough to capture fully the dynamic of the instability (other LES models could have been tested also but this has not been possible in the schedule of the present thesis). The effect of the numerical procedure used to keep the interface sharp in *InterFoam* has been studied in the previous chapter. It has been shown that a possible effect can be to limit the liquid dispersion and thus may be to decrease the amplitude of the instabilities. As already we mention in chapter 3, it tends to keep the liquid near the center line core, limiting the spreading and clustering the liquid structures. Interpreting the results it is possible to observe that the tulip behaviour of the liquid sheet possibly seen in the experimental results, is partially recovered. This again it could be due to the effect of the sharpening counter-flux present in the liquid volume fraction transport equation.

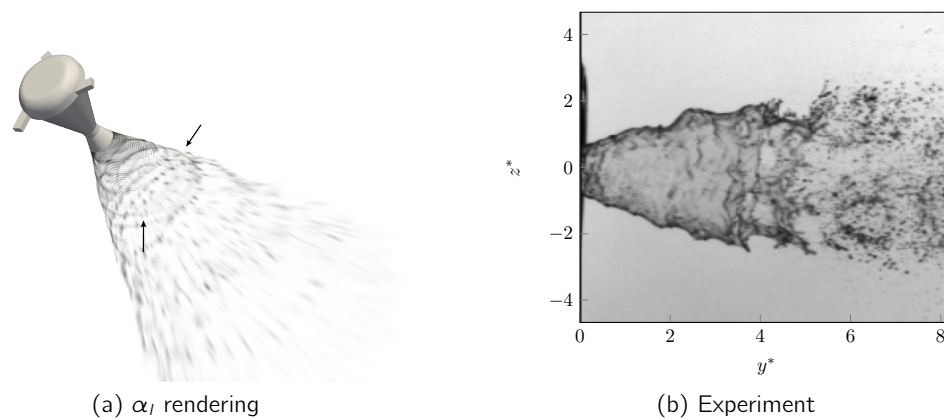


Figure 5.26 – On the left: Volume rendering of the liquid volume fraction field at  $t = 14.5[ms]$ ,  $\alpha_l = 0 \text{ --- } 1$ . The arrows point to the two main instabilities features. On the right: snapshot of the shadowgraphy of the *Silvercrest* injector at the re-light point

### Liquid film thickness

We proceed with the validation of the formulation presented in eq. (5.35). This equation is used for design purpose inside the *SAFRAN Aircraft Engines* offices. In order to compare between analytical and numerical values, we average the liquid volume fraction in time at the exit plane of the injector for  $\Delta t_{avg} = 2[ms]$  starting from the  $t_0 = 12[ms]$ . The assessment time, has been previously defined as  $8[ms]$  of simulation on the mesh C plus  $4[ms]$  of simulation on the mesh D. The choice of time averaging the liquid volume fraction has been done in order to perform the comparison of the liquid film thickness raising from a strongly unsteady process, and hence subject to temporal variation. The comparison is performed with the analytical formulation that is representative of a steady process and for this reason is a fixed value. Two perpendicular lines are used to extract the liquid volume fraction profiles (fig. 5.27). It is possible to weakly validate the axis-simmetry of the problem through the liquid volume fraction profiles that are nearly identical (see fig. 5.28). Despite the sharpening counter-flux, due to numerical diffusion, the transition of the liquid volume fraction at the interface is larger than one cell, we will consider the liquid film thickness as the position in which the liquid volume fraction reaches the value of 0.1. In fig. 5.27 it is possible to observe the contour of the time averaged liquid volume fraction and the profile of the time averaged liquid volume fraction in fig. 5.28. In both cases the liquid film thickness measured is of  $t/D = 0.077$ , where the coordinate  $t$  along the slice has been adimensionalized by the outlet diameter  $D$ . The difference with respect to the correlation value (eq. (5.35):  $t_{an}/D = 0.12$ ) is of  $|t - t_{an}|/t_{an} \approx 35\%$ . This value can be considered acceptable with respect to the design team objectives. In the future, it could be interesting to evaluate the opportunity to carry out film thickness measurements for the *Silvercrest* injector or for any swirling injector of aeronautical interest, in order to validate both the correlation model and the numerical model.

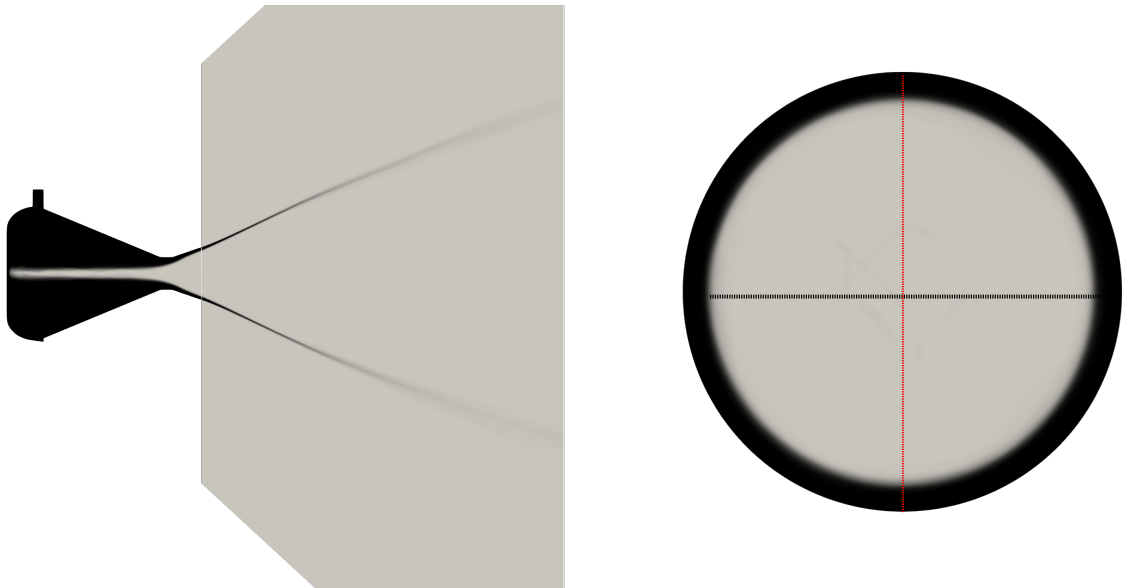


Figure 5.27 – On the left: side view of the time averaged liquid volume fraction,  ${}^t\bar{\alpha}_l = 0 \text{ --- } 1$ . On the right: view of the time averaged liquid volume fraction at the injector exit plane  ${}^t\bar{\alpha}_l = 0 \text{ --- } 1$ . ..... Line A, ..... line B.

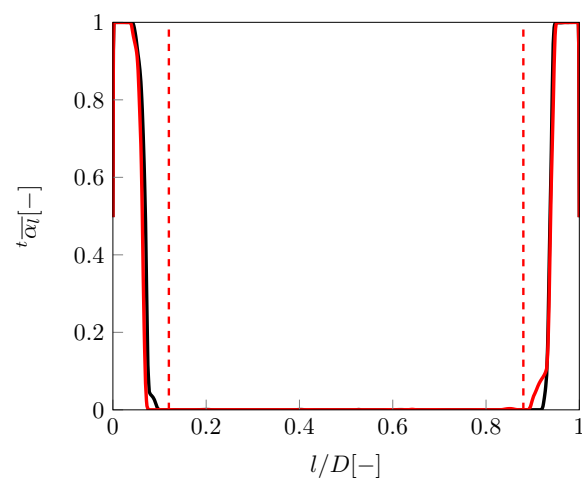


Figure 5.28 – Plot of the time averaged liquid volume fraction  ${}^t\bar{\alpha}_l$  along the two lines defined in fig. 5.27. — line A, — line B, ..... the empirical value. Distance are adimensionalized by the diameter of the injector  $D$

### Breakup point

The criteria to define breakup point is defined in section 5.3.1 as the first place where it is possible to see the first perforation holes in the liquid sheet. In the numerical case, the breakup point is strongly dependent on the value of the contour line chosen (e.g iso-line  $\alpha_l = 0.3$  in fig. 5.29), but in all the cases we can visualize a breakup happening around  $y^* \approx 2 - 2.5$  which is less with respect to the experimental value (fig. 5.30). The difference with the experimental and numerical case can be due mainly to two different causes:

- The shadowgraphy obtained has been taken from a previous work and dimensions have been recovered starting from the resolution of the CMOS sensor of the camera. The resolution  $256 \times 512$  pixels does not allow to recover the small features of the flow, neither to be precise on the big features. A more accurate experimental campaign should be planned, focused on the visualization of the flow near the exit of the injector, in order to validate the breakup point and the spray angle. Furthermore it is fundamental that the cap that covers the first part of the atomized flow (the interval  $y^* \in [-1.2, 0]$ ) is uncovered, in order to really understand the flow pattern in this region;
- As already stated along all the present work, the atomization problem is characterized by the strong multi-scale features. The *InterFoam* model with the sharpening term in the liquid volume fraction transport equation tends to cluster the structures where the resolution is not sufficient to recover all the interface dynamic. Hence, the coherent liquid film tends to go through a numerical breakup due to the resolution of the mesh. At a certain point it is possible to observe that in the width of the film there are less than 2 mesh cells. We can finally state that the mesh resolution is not enough to capture the physical breakup point with this approach. This is due mainly to the fact that in the mesh D, to maintain the coherence among the inner and outer environment as well as to have a regular mesh at the outlet, the mesh resolution is graded, having an high resolution at the outlet and less and less cells approaching to the outlet of the patch ②. Another possibility to obtain the right breakup point, and considering the multi-scale characterization of the problem, would be to decouple the problem. By running a first simulation of the entire injector we can recover the film thickness and later we can try to capture the breakup point by running a simulation on a more refined outside environment.

Other than the breakup point it is possible to observe in fig. 5.30 also that the predicted cone angle is slightly higher, and sharp, not typical of the re-light point condition reported by the experimental results (tulip stage). This could be always the effect of the sharpening term, already noticed in chapter 3. The further collapsing of the liquid sheet is due to its coherence. In one hand because it allows the large scale effect of surface tension force and in the other hand because the coherent liquid surface separate the gas flow in two zone that can have different pressure that can bend the liquid sheet. When holes occur on the liquid sheet the pressure re-balance and this last effect disappear. The compression flux that maintains the liquid sheet coherent prevent this effect.

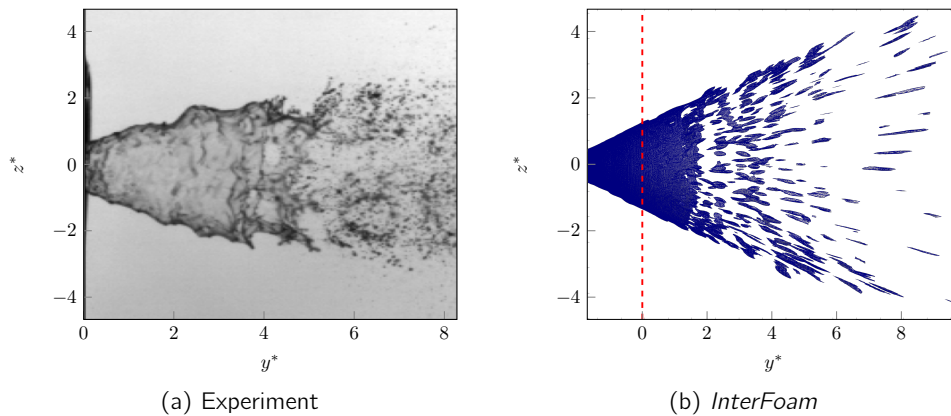


Figure 5.29 – On the left: snapshot of the shadowgraphy of the *Silvercrest* injector at the re-light point. On the right: Contour plot of the liquid volume fraction iso-surface defined by  $\alpha_l = 0.3$  of the *Silvercrest* simulation.

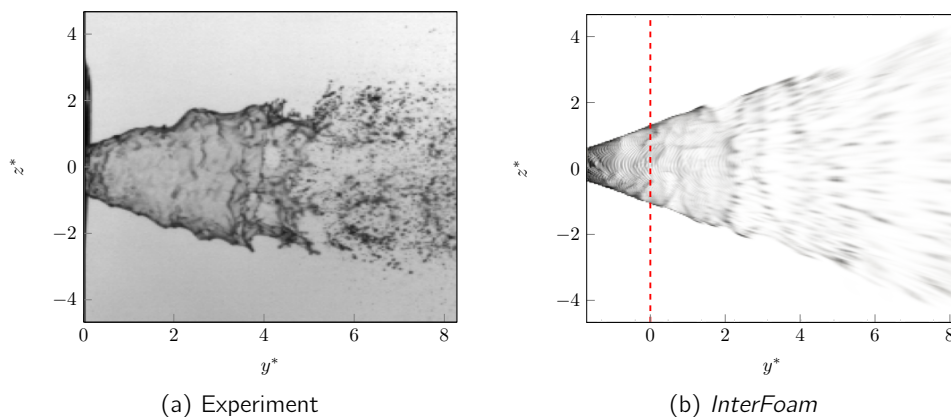


Figure 5.30 – On the left: snapshot of the shadowgraphy of the *Silvercrest* injector at the re-light point. On the right: volume rendering plot of the *Silvercrest* . Liquid volume fraction field.  $\alpha_l = 0$  to  $1$ .

### Sauter Mean Diameter prediction

The Sauter Mean Diameter (SMD or  $D_{32}$ ) is defined as the ratio of liquid volume to the liquid surface in a certain region of the domain. Where the flow is considered dispersed (see chapter 2) the following formulation based on droplet diameter can be used:

$$D_{32} = \frac{\sum_i D_{p,i}^3}{\sum_i D_{p,i}^2} \quad (5.43)$$

Where  $D_{p,i}$  is the the diameter of the particles present in the considered volume and with  $\sum_i$  the sum over all the particles. This method to evaluate the SMD is mostly used into switching modeling length-scale simulations simulation, and in interface modeling length-scale simulation coupled with droplet identification algorithm (see for example [AM+19]). In case of the *InterFoam* model a more generalized approach should be set up. If we look in details the eq. (5.43) we can recast the ratio between the total volume of liquid in a control volume



( $V_l$ ) and the total area of the interface ( $A_l$ ) of the liquid features:

$$D_{32} = 6 \frac{V_l}{A_l} \quad (5.44)$$

We can hence obtain the total volume of liquid in the control volume using the liquid volume fraction variable as:

$$V_l = \iiint_V \alpha_l dV \quad (5.45)$$

For the total area, we have introduced in the *ELSA* framework, the surface area density  $\Sigma$ . In case of the *InterFoam* model, the interface area, can be defined as the magnitude of the gradient of the liquid volume fraction .

$$\Sigma = |\nabla \alpha_l| \quad (5.46)$$

Hence it is possible to write the total liquid area as:

$$A_l = \iiint_V |\nabla \alpha_l| dV \quad (5.47)$$

It is possible to rewrite eq. (5.44) as follows:

$$D_{32} = 6 \frac{V_l}{A_l} = 6 \frac{\iiint_V \alpha_l dV}{\iiint_V |\nabla \alpha_l| dV} \quad (5.48)$$

As stated in [Pal21] it is more convenient for a simulation point of view to measure flow passing through a surface  $A$ . The eq. (5.48) can be recast in term of fluxes:

$$D_{32} = 6 \frac{\int_{\Delta t} \iint_A (\alpha_l \mathbf{v} \cdot \mathbf{n} dA) dt}{\int_{\Delta t} \iint_A (|\nabla \alpha_l| \mathbf{v} \cdot \mathbf{n} dA) dt} \quad (5.49)$$

Where  $A$  is the surface across which the average SMD is computed,  $\Delta t$  is the averaging time, and  $\mathbf{n}$  is the normal to the surface  $A$ . This output can be very similar to the value available from experiments, where the experiment aims to measure all the droplet at some distance of the injector. Then the experimental measure can be seen as the measurement of all droplet characteristics going through a cross sectional surface. It can be noticed that experimental measurement, to consider the drop size distribution, should have converged to the final state. In this work we set 5 different sampling planes and we compute there the SMD with the formulation proposed in eq. (5.48). In fig. 5.31 we can observe on the picture (a) the location where we evaluate the  $D_{32}$  and on part (b) the corresponding values of the SMD.

We can notice first an increase of the SMD moving along the  $y^*$  axis. The purpose to extract from the simulation the SMD is to compare with the reference obtained experimentally far downstream at  $y^* = 33$ . The experimental SMD is for this case  $D_{32} = 62[\mu m]$ . Of course the values obtained by simulation are not directly comparable, but it can be observed that even at this early stage of atomization, the ratio of the volume to surface for the spray is already in range of the experimental data. This means that most of the surface has been created in the initial stage of atomization. Following the work of [Pal21] it can be expected to extract from the simulation this ratio. However, in the simulation, the mesh resolution was fine enough to see a decrease of the SMD and then a plateau where it is proposed to measure it. In the present simulation, despite we are in the good range, the behaviour of the diameter with the distance from the injector is mostly increasing. This is surprising since a break up can be observed leading to more surface flux for the same liquid flux, thus it should decrease. This is where the method to determine the surface discussed all along this PhD

is important. We use an IC method and the surface is directly obtained by the integration of the gradient of the liquid volume fraction. This last quantity is strongly affected by the numerical model (mixed phases , separated phases and in this context *sharp interface* , *diffuse interface* ) and by the mesh resolution. In the present case we believe the mesh resolution is fine enough to capture the correct range of the interface area but not enough to obtain the correct value. It is expected that few additional mesh refinement will be sufficient, but this has not been possible to do in the present PhD. In addition the SMD most probably increases with the distance to the injector because of the mesh resolution is decreasing (due to the given grading).

To go further the additional amount of surface that is not captured by the numerical method should be obtained by implementing an additional physical model, this is the purpose of the *ELSA* model described in the following section.

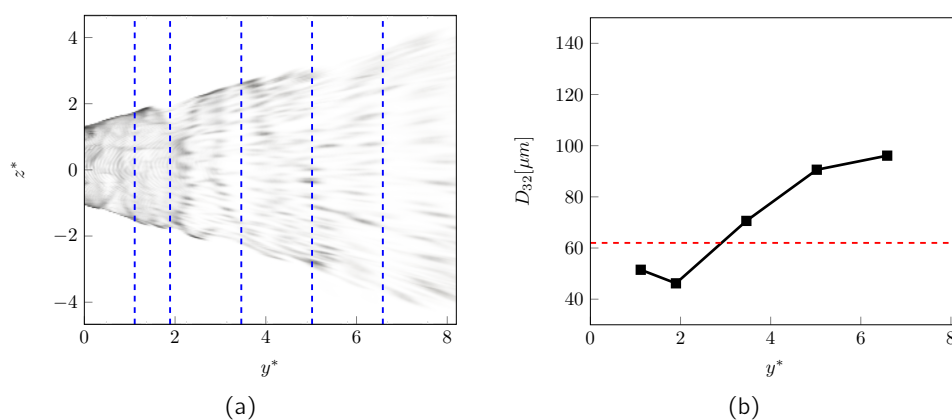


Figure 5.31 – On the left: rendering of the *InterFoam* liquid volume fraction field, and in dashed blue  $\text{---}$  the location in which we collect the  $D_{32}$  values.  $\alpha_l = 0$   $\blacksquare$   $1$ . On the right: plot of the  $D_{32}$  value post processed following the formulation proposed in eq. (5.48). In  $\text{---}$  the experimental value at  $y^* \approx 33$ .

#### 5.4.4 Simulation with ELSA model

By using the *InterFoam* model we tried to obtain results like the *ARCHER* CLSVOF model, following the methods developed on the academical testing configuration in chapter 3. On this industrial configuration the mesh resolution we can achieve has limited the accuracy of IC method: we lose information about the interface when the grid resolution is not sufficient to capture the interface dynamic. Hence, it is possible that the computational cell acts as a filter that is bigger than the actual liquid structure, or that the clustering induced by the sharpening counter-flux gives a false information about the surface evolution and makes impossible to retrieve further information, for example about the droplets distribution, or to capture correctly the breakup point. In order to continue to follow the interface and its evolution, also in case of insufficient resolution, we use the *ELSA* model that allows to recover more information about the different liquid structures thanks to an additional physical model for the surface density variable and for the liquid volume fraction transport equation sub-grid dispersion model. The advantage of introducing this model (we are using the Euler single phase mixture formulation of ELSA, without the Lagrangian dispersed phase) instead a coupled length-scale framework (such as the coupling of an interface modeling length-scale model with a kinetic approach), resides on the interface area density equation that allows to follow the interface dynamic of structures with different shapes, not only droplets. At the contrary a

coupling the IC framework with a kinetic approach allows to transform any liquid structure into spherical droplets follow their evolution ([Ane+19b]). Other than this we can find an advantage from the point of view of computational time, where the single modeling length scale models are in general less expensive than coupled length-scales modeling approaches ([Doi+13]).

### The ELSA model and the numerical method

In the previous chapters we introduced the *ELSA* model, implemented in the *OpenFoam* library [Ane18]. The model consists in a set of equations composed by the mass conservation and momentum conservation equations, along with the liquid volume fraction evolution equation and a supplementary equation that describes the evolution of the interface area density. The first implementation of the model was in the RANS framework ([VB99]). Hereafter, we will use the LES framework, introduced in [Che10] (details can be found in chapter 2). We remind to the reader that in case of *ELSA* framework, the implicit LES filtering procedure is applied also to the liquid volume fraction evolution equation and the *turbulent liquid flux* is modelled through a sub-grid dispersion term (other modeling strategies can be found in [Pug18]). Regarding the surface area density variable ( $\Sigma$ ) we consider the formulation with the minimum interface density area ( $\Sigma_{min}$ ) and the sub-grid interface area density ( $\Sigma'$ ) and hence we consider the transport equation only for  $\Sigma'$ . The minimum interface area density  $\Sigma_{min}$  is approximated through the magnitude of the gradient of the liquid volume fraction  $\Sigma_{min} = |\nabla\alpha_l|$ .


As for the *InterFoam* model, the equations are discretized using the finite volume method and PISO algorithm is used to solve the incompressible N-S system. The liquid volume fraction transport equation is solved using the MULES scheme to avoid overshoots or to underestimate the phase marker (for details see chapter 3).

### Simulation strategy and phenomenological analysis

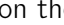
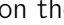


As for the *InterFoam* case, the simulation is restarted after 8[ms] of simulation performed using the *InterFoam* model on the mesh C. In order to analyse the results the simulation is run during 4[ms].

The dynamic of the flow in the external domain, appears to be similar to the experimental observations. It is possible to observe both the K-H instability and the spiral mode inside the cone (fig. 5.32). The difference with respect to the *InterFoam* simulation is that the destabilization of the liquid film appears to happen earlier and the amplitude of waves are more prominent. The tulip shape observed in the experimental results appears to be recovered. Most probably it is due to the diffusive nature of the *ELSA* that induce a more efficient air entertainment and liquid dispersion, as it has been already seen and highlighted in the chapter 3.



Figure 5.32 – Volume rendering of the liquid volume fraction field at  $t = 14.5[ms]$ ,  $\alpha_l = 0$   1.

#### Liquid film thickness

To analyse the liquid film thickness at the exit of the injector, we adopt the same strategy used for *InterFoam* simulations. We average the liquid volume fraction in time for a  $\Delta t_{avg} = 2[ms]$  starting from  $t_0 = 12[ms]$ . We take two perpendicular lines and we evaluate the film thickness on the two profiles (  line A and  line B reported in fig. 5.33). It is possible to arrive to the same conclusion that has been drawn in the chapter 3. The *diffuse interface* approach, brings to a smoother transition between the liquid film and the gas core, with respect to the sharp interface approach. The value of the film thickness is of  $t/D = 0.083$  for both  line A and  line B. The difference with respect to the correlation value (with eq. (5.35):  $t/D = 0.12$ ) is of  $|t - t_{an}|/t_{an} \approx 30\%$ . As a support of the previous observation we can state that the film thickness results to be 7% larger with respect to the value found in the *InterFoam* simulation.

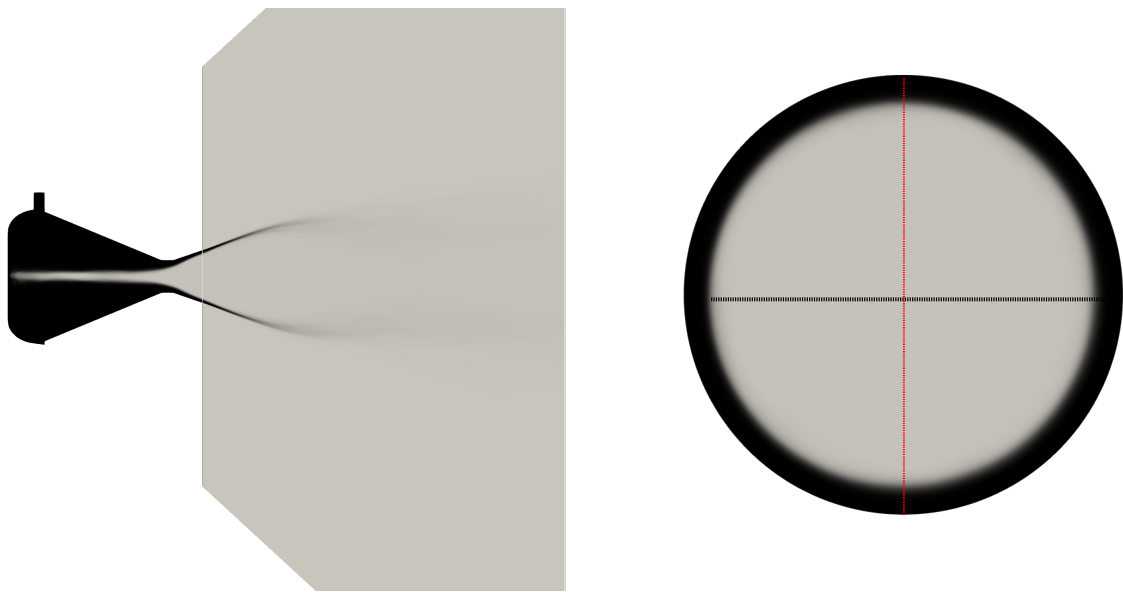


Figure 5.33 – On the left: side view of the time averaged liquid volume fraction,  ${}^t\overline{\alpha}_l = 0$  to  $1$ . On the right: view of the time averaged liquid volume fraction at the outlet  ${}^t\overline{\alpha}_l = 0$  to  $1$  and lines of where the liquid film thickness is evaluated. The averaging time is  $\Delta t_{avg} = 2[ms]$  starting from  $t_0 = 12[ms]$ . - - - - Line A, - - - - line B.

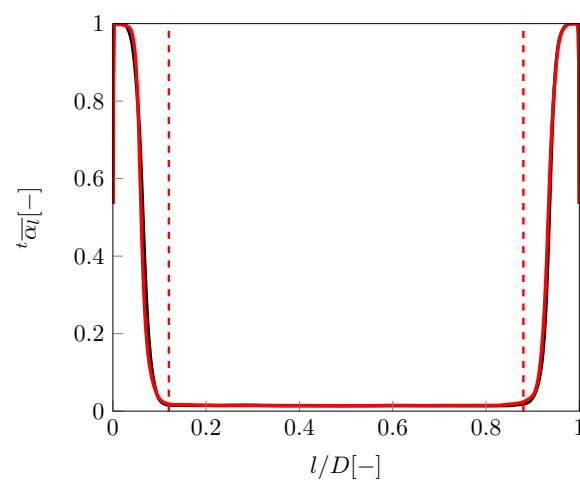


Figure 5.34 – Plot of the time averaged liquid volume fraction  ${}^t\overline{\alpha}_l$  for the two lines defined on fig. 5.27. — line A, — line B, - - - - the empirical value Length scale are adimensionalized by the diameter of the injector  $D$

### Breakup point

As for the *InterFoam* case, we consider the breakup point where it is possible to observe the first perforation holes in the liquid sheet. Having a look at the liquid volume fraction iso-lines (e.g  $\alpha_l = 0.3$  in fig. 5.35) the breakup seems to happen earlier with respect to what it was possible to observe in the *InterFoam* case. In fig. 5.35 (b) it appears to happen even before the end of the cover cap of the injector. This is due to the breakup point dependence on the iso-line value chosen. This effect is even more pronounced in case of diffuse interface model. For this reason we analyse the liquid volume fraction field volume rendering in fig. 5.36. It is

possible to observe that the breakup point appears to be around  $y^* \approx 2.5 - 3$ , recovering the results we have obtained with the *InterFoam* simulation.

The cone angle appears to be closer to the experimental observation with respect to the one observed with the *InterFoam* simulation. The particular tulip shape of the re-light point appears to be recovered.

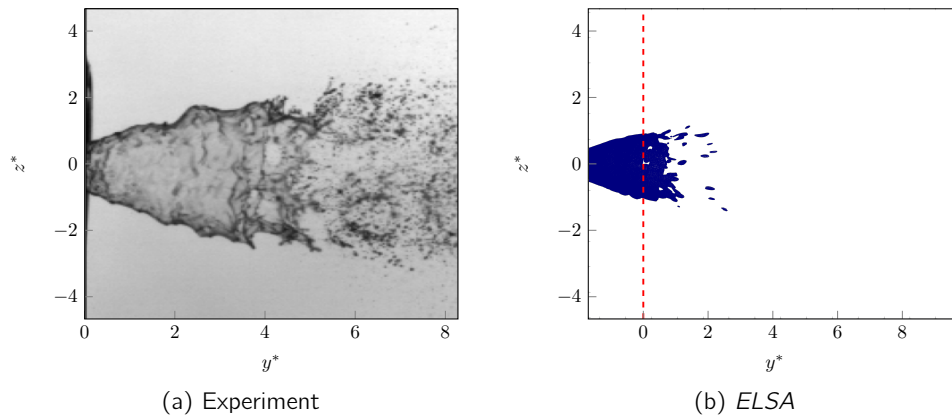


Figure 5.35 – On the left: snapshot of the shadowgraphy of the *Silvercrest* injector at the re-light point. On the right: Contour plot of the  $\alpha_l = 0.3$  of the *Silvercrest* primary injector.

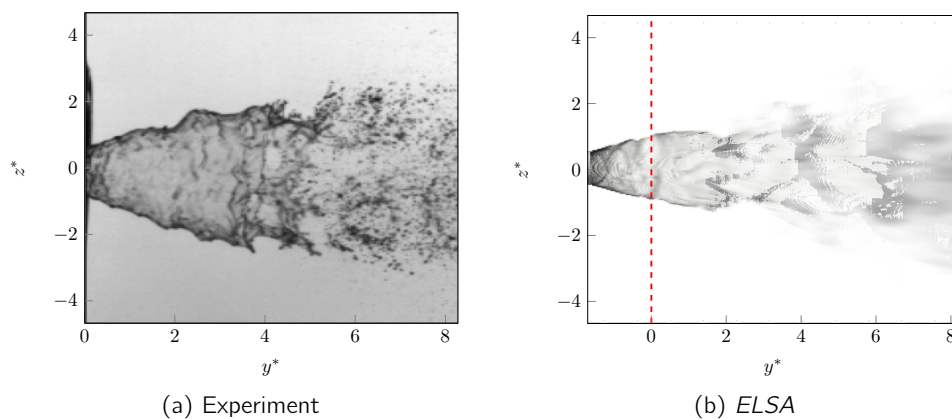


Figure 5.36 – On the left: snapshot of the shadowgraphy of the *Silvercrest* injector at the re-light point. On the right: volume rendering plot of the liquid volume fraction field of the *Silvercrest* primary injector.  $\alpha_l = 0$  to  $1$ .

### Sauter Mean Diameter prediction

With respect to the *InterFoam* case, the *ELSA* approach solves the equation for the sub-grid interface area density  $\Sigma'$ . As already stated before, it is possible to reconstruct the interface area density as  $\Sigma = \Sigma_{min} + \Sigma'$ . Recalling the eq. (5.49) used for the *InterFoam* case, and knowing the availability of the interface area density, it is possible to find the SMD through a surface  $A$  as:

$$D_{32} = 6 \frac{\int_{\Delta t} \iint_A (\alpha_l \mathbf{v} \cdot \mathbf{n} dA) dt}{\int_{\Delta t} \iint_A (\Sigma \mathbf{v} \cdot \mathbf{n} dA) dt} \quad (5.50)$$

Where  $\mathbf{n}$  is the normal to the surface  $A$ . The different slice in which we evaluate the  $D_{32}$  are reported in fig. 5.37 (a), while the values of Sauter Mean Diameter, evaluated through equation eq. (5.50) are reported in fig. 5.37 (b). It is possible to observe an increase in the value of the SMD. The estimation of the SMD with the *ELSA* approach leads to even larger values than for the *InterFoam* model. Thus the amount of surface is underestimated. Regarding the resolved part ( $\Sigma_{min}$ ) this is reasonable, since the diffuse interface behaviour is enforced due to the absence of any numerical method to control the interface thickness and by the sub-grid dispersion model. However in principle this should be compensated by the additional sub-grid interface model ( $\Sigma'$ ). This is clearly not the case for the present version of the model. The main reasons are most probably the physical model that have been designed for breakup processes occurring with large shear and turbulence. In the present test case the Reynolds and Weber numbers ( $Re_0 = 424$ ,  $We_0 = 0.3$ ) are pretty low, thus the modeling of related source term in the surface density equation have to be revisited. This has not been possible in the present thesis and should be the topic of further research.

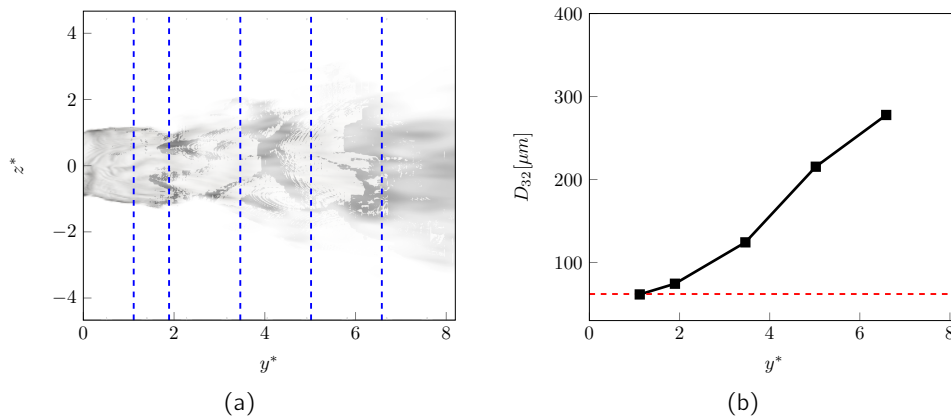


Figure 5.37 – On the left: rendering of the *ELSA* liquid volume fraction field, and in dashed blue ---- the location in which we collect the  $D_{32}$  values.  $\alpha_l = 0$  to 1. On the right: On the right: plot of the  $D_{32}$  value post processed following the formulation proposed in eq. (5.50). In ---- the experimental value at  $y^* \approx 33$ .

### 5.4.5 Simulation with ICMelsa model

In order to connect the positive aspects of both the models just introduced, we decided to apply the *ICMelsa* model. The main feature of this approach is its ability to switch for the *InterFoam* model when it is possible to preserve a sharp representation of the interface to a *diffuse interface* approach with additional physical model. To determine which model has to be used, different *IRQ* (Interface Resolution Quality) sensors have been designed (for more details see chapter 2). For the first part of the flow at the exit of the outlet, it is expected the

*IRQ* to state that the flow is well resolved. Thus the *InterFoam* model should be activated with the compression term. Farther away, where the resolution of the mesh does not allow to capture the liquid film, the *ELSA* approach is activated and the sharpening counter-flux is turned off. This should give the information about the evolution of the interface and mean diameter where the resolution is too low to use only the *InterFoam* model.

#### ICMelsa model and its improvements

We introduced the *ICMelsa* model in the chapter 2 of the present manuscript. It is composed of the momentum conservation equation, mass conservation equation, liquid volume fraction hybrid conservation equation (hybrid because can switch between the *ELSA* formalism and *InterFoam* formalism) and eventually the sub-grid interface area density transport equation. The system has been coupled with an Interface Resolution Quality (*IRQ*) sensor in order to switch among the *ELSA* formalism and *InterFoam* formalism. In this work (as we have already seen in chapter 3) it has been chosen to use the  $IRQ_{\Sigma}$  as interface resolution quality (for a parametric study see appendix B). Another choice should be done for what concerns the evaluation of the minimum interface area density ( $\Sigma_{min}$ ). One possibility has been presented and adopted in [Pal21], and in chapter 3 of this work, it has set the minimum interface area density  $\Sigma_{min}$  equal to the magnitude of the gradient of the liquid volume fraction ( $\Sigma_{min} = |\nabla\alpha_l|$ ). This approximation of the minimum interface area density fails when the interface is spread to include several phase inclusions. In this case the prediction of the minimum interface area density performed in [Che10] is more accurate than the prediction done by the magnitude of the gradient of the liquid volume fraction. Hence we decided to add to our model the capability to switch the method to evaluate  $\Sigma_{min}$  depending on the gradient of the liquid volume fraction with respect to the mesh resolution. When the  $\alpha_l$  is spread on less than 10 mesh cells ( $|\nabla\alpha_l| < 1/(10\Delta x)$ , where  $\Delta x$  is the characteristic dimension of one mesh cell), we can use the method to compute  $\Sigma_{min}$  proposed in [Pal21] and hence,  $\Sigma_{min} = |\nabla\alpha_l|$  else we use the definition of [Che10], and hence  $\Sigma_{min} = 2.4 \frac{\sqrt{\alpha_l(1-\alpha_l)}}{\Delta x}$ . Here we want to point out that, while the definition as interface area density given in [Pal21] is a direct definition, the minimum interface area proposed in [Che10] is a model proposition. An example of comparison of the two definition can be found in fig. 5.39. Another possible solution could be to set the minimum interface area density to 0 when liquid volume fraction is spread over more than 10 mesh cells. In connection with what we discussed in chapter 4, for *diffuse interface* approaches, when we have an extended interface we lose all the information about interface positioning and all the dynamic is given to the sub-grid contribution i.e.  $\Sigma'$ . This is the approach used in this work.

Another change has been done to the *ICMelsa* introduced in chapter 2. When the liquid volume fraction is spread among more than 10 mesh cells, automatically the transport equation switches to the *ELSA* formalism, which in the model means that the parameter  $C_{\alpha}$  is set to 0. The effect of this modification has been tested on the configuration we have used for models comparison in chapter 3. The results are reported in fig. 5.38-(b) where we can observe  $C_{\alpha}$  is set to unity (*InterFoam* mode) even also where the structure are not well refined and in clearly dispersed flow at the contrary after the modifications, in fig. 5.38-(c), the parameter  $C_{\alpha}$  is equal to unity only where the interface is well captured.



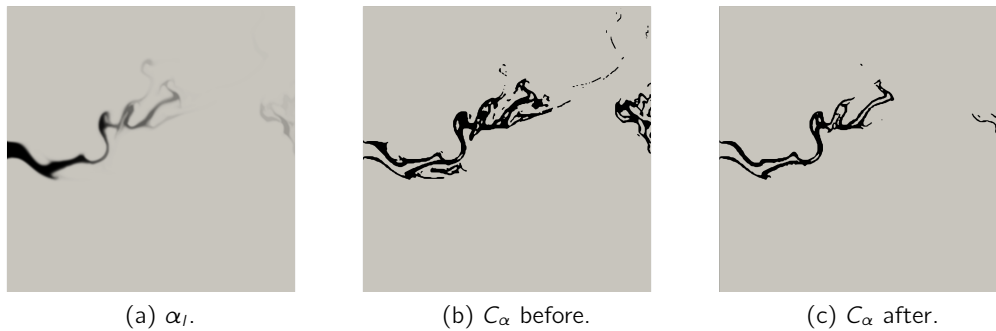


Figure 5.38 – On the left: slice of the domain presented in chapter 3, liquid volume fraction field.  $\alpha_l = 0 \text{ } \blacksquare \text{ } 1$ . On the center: Field of  $C_\alpha$  before the modification proposed.  $C_\alpha = 0 \text{ } \blacksquare \text{ } 1$ . On the right: Field of  $C_\alpha$  after the modification proposed.  $C_\alpha = 0 \text{ } \blacksquare \text{ } 1$ .

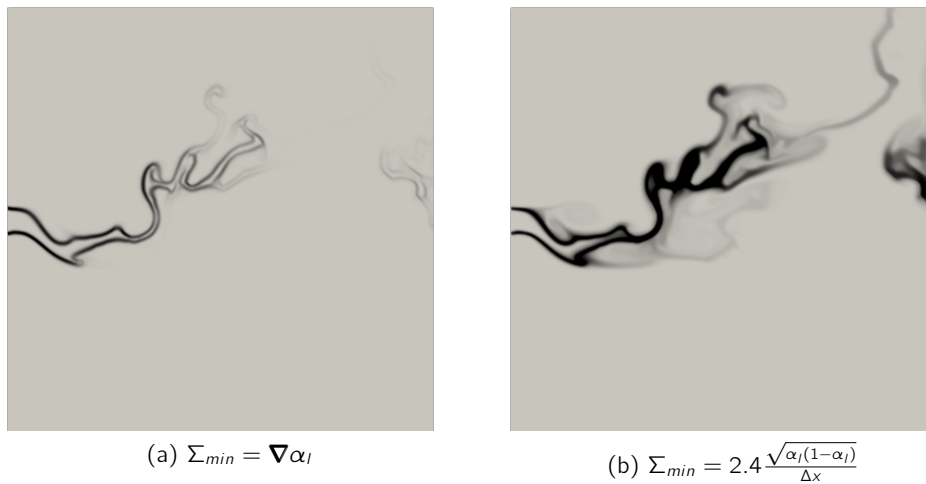



Figure 5.39 – On the left: slice of the minimum interface area computed as the magnitude of the gradient of the liquid volume fraction ([Pal21]). On the right: slice of the minimum interface area computed as defined in [Che10].  $\Sigma_{min} = 0[1/m] \text{ } \blacksquare \text{ } 7 \cdot 10^3[1/m]$

### Simulation strategy and phenomenological analysis

As for the *InterFoam* and *ELSA* cases, we start from the *InterFoam* simulation of mesh C and we run 4[ms] before analysing the results i.e we start the analysis at  $t_0 = 12$ [ms].

In fig. 5.40 it is possible to observe the dynamic of the interface, starting from the volume rendering of the liquid volume fraction field. The interface is maintained sharp at the immediate exit of the injector, where the *InterFoam* formalism is predominant for the liquid volume fraction transport equation, while farther away, the *ELSA* formalism is predominant, creating a diffuse field. Among the three models tested, the destabilization of the liquid film appears to be the most similar to the experimental case. In fig. 5.40 it is possible to distinguish qualitatively, both the sinusoidal breakup and the spiral mode. With respect to the *ELSA* model the classical tulip shape is recovered for a larger distance from the injector outlet.



Figure 5.40 – Volume rendering of the liquid volume fraction field at  $t = 14.5$ [ms],  $\alpha_l = 0$   1.

### Liquid film thickness

Like for the previous simulations, the liquid film thickness is evaluated averaging the liquid volume fraction field for  $\Delta t_{avg} = 2$ [ms] starting at 12[ms], over two lines ( - - - - line A and - - - - line B, represented in fig. 5.41). As already stated in chapter 3, the *ICMelsa* model leads to a transition between liquid and gas that is in between the *ELSA* model and *InterFoam* one. Following the *ICMelsa* model presentation, we would expect the behaviour of the *InterFoam* model close to the injector exit, since it is a well resolved region. While for the *InterFoam* model,  $C_\alpha = 1$  in all the computational domain, with the *ICMelsa* model  $C_\alpha$  is varying between 0 and 1 but it brings to the small differences it is possible to observe in the region where the interface is well captured.

The film thickness measured at  ${}^t\bar{\alpha}_l = 0.1$  is  $t/D = 0.086$  for both - - - - line A and - - - - line B. The difference with the correlation value of  $t_{an}/D = 0.12$  is  $|t - t_{an}|/t_{an} \approx 28\%$ .

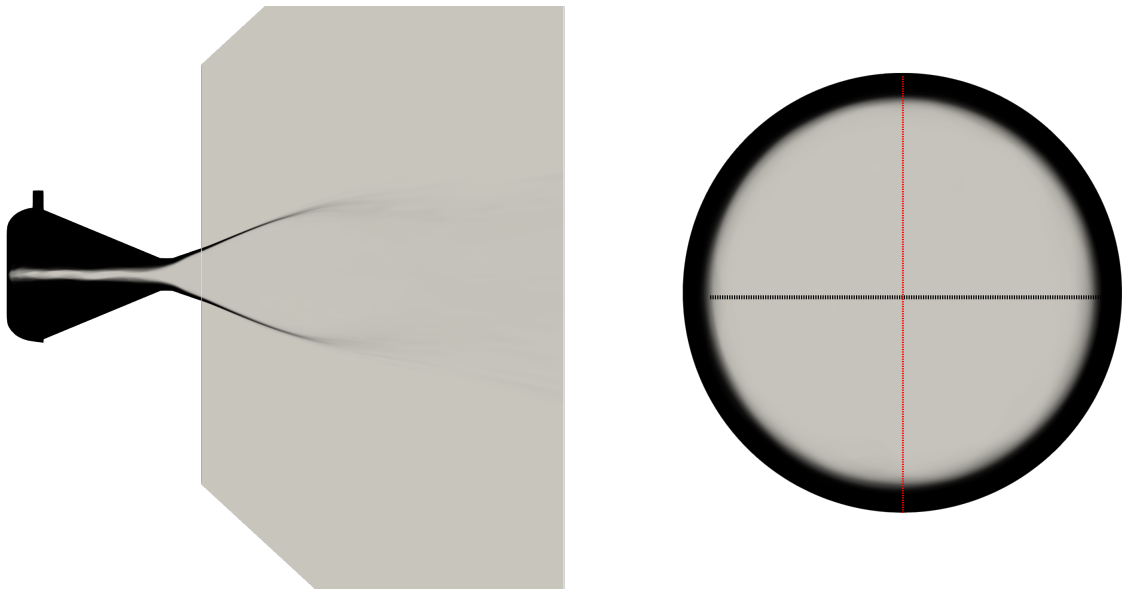


Figure 5.41 – On the left: side view of the time averaged liquid volume fraction ,  $\overline{\alpha}_l = 0 \text{ --- } 1$ . On the right: view of the time averaged liquid volume fraction at the outlet  $\overline{\alpha}_l = 0 \text{ --- } 1$  and lines where the liquid film thickness is evaluated. - - - - Line A, . . . . line B.

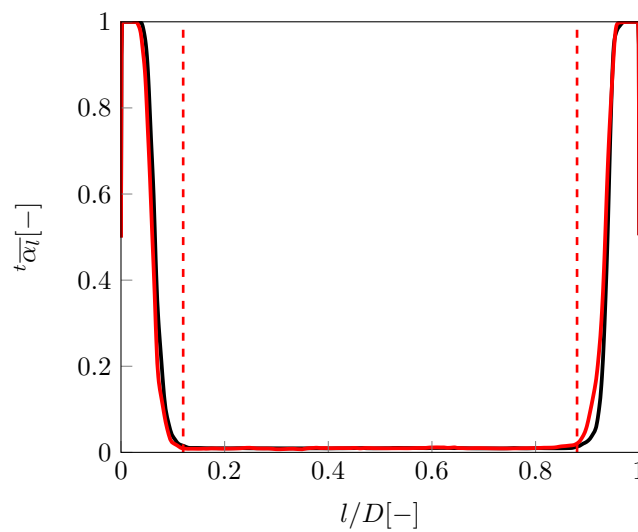


Figure 5.42 – Plot of the time averaged liquid volume fraction  $\overline{\alpha}_l$  along lines defined in fig. 5.27. — line A, — line B, . . . . the empirical value. The length are adimensionalized by the diameter of the injector  $D$

### Breakup point

We measure the breakup point as the first point where appears perforation holes in the liquid sheet. We saw in the previous cases that this value is strongly dependent on the iso-value of the liquid volume fraction (see also for *ICMelsa* the iso-value of  $\alpha_l = 0.3$  in fig. 5.43) hence we consider the volume rendering of the liquid volume fraction field in fig. 5.44. It is possible to observe that the breakup point is placed about at  $y^* \approx 3.5$ . Hence we can state that is in the range of the breakup point observed in the experimental results. Furthermore, as for the *ELSA* model, the spray tulip shape and angle is well recovered, due to the fact that after  $y^* = 0$ , the liquid volume fraction transport equation uses mostly the *ELSA* formalism, including diffuse interface approach and sub-grid liquid dispersion.

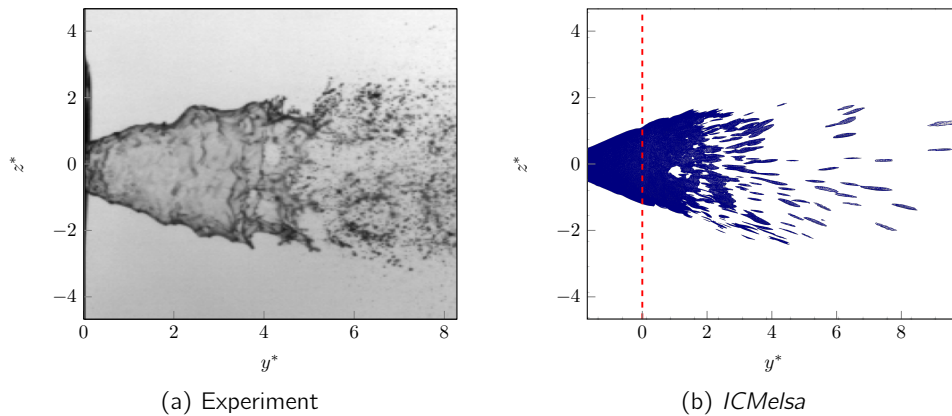


Figure 5.43 – On the left: snapshot of the shadowgraphy of the *Silvercrest* injector at the re-light point. On the right: Contour plot of the liquid volume fraction field  $\alpha_l = 0.3$  of the *Silvercrest* primary injector.

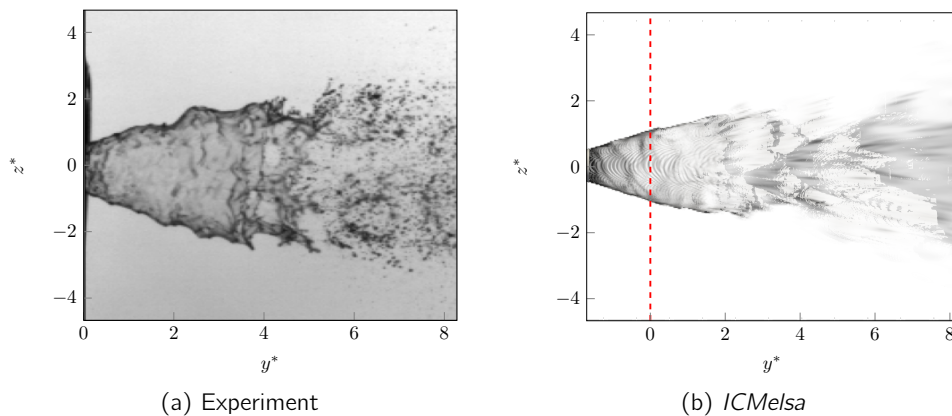


Figure 5.44 – On the left: snapshot of the shadowgraphy of the *Silvercrest* injector at the re-light point. On the right: volume rendering plot of the liquid volume fraction field  $\alpha_l$ .

### Sauter Mean Diameter

The Sauter Mean Diameter is evaluated using the formulation introduced in eq. (5.50). In fig. 5.45 it is possible to observe in (a) the location in which are evaluated the different  $D_{32}$  values and in (b) the plot of the values at the different  $y^*$  location. The  $D_{32}$  appears to increase and the value is far away from the interpolated experimental value of  $D_{32} = 62[\mu m]$  (obtained by interpolating the data of table 5.3).

The mesh resolution is the same as the previous simulation and not sufficient to catch the SMD with an SMD method. Clearly the physical models introduced with the *ELSA* approach are not sufficient to describe properly the correct amount of additional surface produced at the sub-grid scale. The *ICMelsa* formalism is nevertheless able to benefit of the first part of the well resolved simulation (*InterFoam* part) to provide a more appropriate value of the SMD (about at  $y^* = 2$ ) before to rely on the sub-grid *ELSA* model. Here the post processing method applied is still the one proposed in the *ELSA* simulation, i.e eq. (5.50), but the method to evaluate the Sauter Mean Diameter for the *ICMelsa* simulation is still not clear. The liquid volume fraction transport equation can switch between two different formalism, hence it is still not clear if to rely on the  $\Sigma$  evaluated as the gradient of the liquid volume fraction and then to apply the post-processing method of eq. (5.49), or to rely on the information got through the  $\Sigma'$  transport equation, then evaluate the interface area density as  $\Sigma = \Sigma_{min} + \Sigma'$  and finally apply the post-processing method of eq. (5.50). This is still under development and a complete study will be pursued in [Fer22].

At the present time, the best option, if it is affordable, is to increase the mesh resolution to base the spray analysis mostly on the *InterFoam* model. However it seems that the sub-grid dispersion term used for the liquid volume fraction transport equation is improving the global shape of the spray. Thus the main focus of further study would be to build physical models for the surface density equation compatible with the sub-grid atomization of the liquid sheet. The importance of the nature of the source term  $\Sigma'$  equation can be assessed by running a simulation with the *ICMelsa* framework, putting the source term of the equation to 0, and hence:

$$\frac{\partial \overline{\Sigma'}}{\partial t} + \nabla \cdot \overline{\mathbf{v} \Sigma'} = \nabla \cdot \mathbf{R}_{\Sigma'} \quad (5.51)$$

A first test has been run and the values of the SMD obtained, after a first increase along  $y^*$  different locations, falls to a value around  $D_{32} = 30\mu m$  at  $y^* = 7.6$ . This is an indication to the fact that a new source term for the equation should be studied to adapt the model to low Reynolds and Weber number conditions.

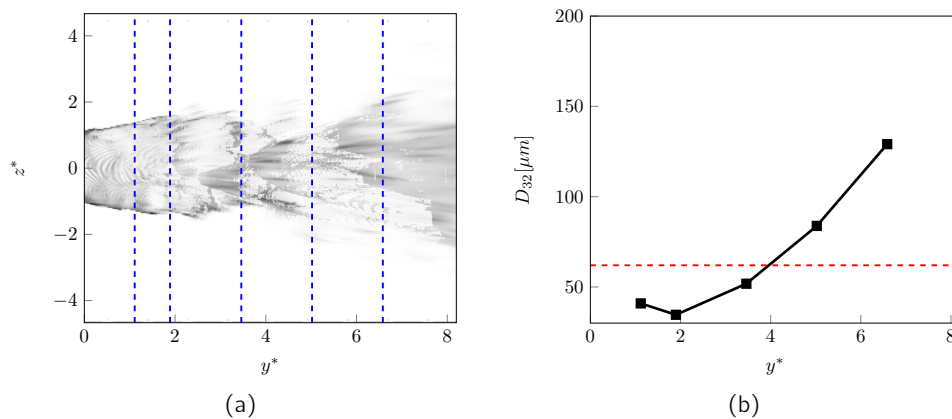


Figure 5.45 – On the left: rendering of the *ICMelsa* liquid volume fraction field, and in dashed blue  $\text{---}$  the location in which we collect the  $D_{32}$  values.  $\alpha_l = 0$   $\text{---}$   $1$ . On the right: On the right: plot of the  $D_{32}$  value post processed following the formulation proposed in eq. (5.50). In  $\text{---}$  the experimental value at  $y^* \approx 33$ .

## 5.5 Conclusion

With this chapter, we have tried to simulate an actual injection system based on the different methods that can be used for liquid-gas flow with a complex interface morphology and that have been studied extensively in the first part of this thesis. The main purpose is to understand the behaviour of the two main classes of approaches used: the *diffuse interface* and the *sharp interface* representations. From the previous chapter it has been possible to show that these approaches can lead to equivalent results when the thickness of the interface remains lower than the length-scale of liquid and gas inclusion (droplets or bubbles). However, when the mesh resolution is not sufficient some information on the position of the interface and thus on the morphology of the interface are lost. Though the *sharp interface* approach even with low resolution conserve still an interface morphology, this is not the real one. The *diffuse interface* approach rely on some interface thickness that may be used to define probability of presence of the interface. However, if the length-scale of liquid-gas inclusion is too small, then a part of the information is missing and additional physical model are required to describe the unresolved part (chapter 4).

On the actual application (a real configuration provide by *SAFRAN Aircraft Engines* and referred as *Silvercrest* ) the mesh resolution that we have been able to set up is high enough for the flow inside the injector and at the injector exit but then, it becomes insufficient to capture all the interface characteristics for the final spray. This situation is typical of the present status of the injector simulations in industry and many applications. Another characteristic concerns the complex geometry of the configuration, that requires a mesh strategy that excludes for the moment the possibility to use most advanced code like *ARCHER* . Thus for this study we rely on the free library *OpenFoam* with the built-in available solver. The first one aims to represent a *sharp interface* (*InterFoam* ), the second one is based on *diffuse interface* through the *ELSA* solver. This latest solver includes also additional physical models to describe the sub-grid spray where the resolution is not high enough. However, when the resolution is sufficient to capture the interface the *ELSA* solver is not able to recover a completely *sharp interface* approach thus a hybrid solver is used called *ICMelsa* .

Like for many industrial systems the experimental characterisation of the injector flow gives only partial information. It relies mainly on the shadowgraphy pictures and on the spray Sauter

Mean Diameter measurements far away from the injector, where the spray is dispersed. In complement, a correlation can be used for comparison of the liquid film thickness at the exit of the injector. Testing the three models: *InterFoam*, *ELSA* and *ICMelsa* it has been possible to draw several conclusions:

- Within the well-resolved area, all models lead to equivalent results that are in line with the correlation that determine the liquid film thickness (fig. 5.46). We retrieve here the result of the first chapters, for high resolution simulations. All the approaches are able to describe the main features of the liquid-gas flow and the interface characteristics.
- On the low-resolution zone, all models failed to represent accurately the flow, and in particular, the small-scale features like droplet size (fig. 5.48). Indeed, the computed SMD seems far away of the experimental one, even if they are not measured at the same distance of the injector.
- Regarding the large feature of the flow, spray angle, global shape of the liquid sheet and position of the liquid sheet break-up (fig. 5.47), *InterFoam* is the most affected by the low-resolution. By trying to preserve the *sharp interface* representation it produces artefacts even at large scales by triggering the break-up of the liquid sheet prematurely. The *ELSA* approach avoids this bias by its ability to carry a diffuse interface that does not need to specify exactly the interface position. However, this advantage in the low-resolution zone is counterbalanced by the diffuse description of the interface where sharp variation of variable occurs at the phase transition. More accurate *diffuse interface* approaches, such as the one used in chapter 3 (CEDRE), may reduce this effect, though it has not been possible to test it in this thesis. Instead, a hybrid approach *ICMelsa* has been used. It seems able to benefit of each description by switching from sharp to diffuse interface approach thanks to *IRQ* criteria.
- The optimisation of the *ICMelsa* approach has been achieved through an improved description of the minimum/resolved interface. This development is an original development of the present PhD that can have other applications regarding the *ICMelsa* model.
- Finally, these results have shown the limitation of the present source terms used for the transport of the sub-grid interface density area. This quantity aims to complete the flow description by physical models where the resolution is not fine enough to describe all the scales of the interface. However, at this stage these models have been developed for liquid-gas interfacial flow characterised by high Weber and Reynolds number. The present application deals with liquid sheet break-up that are clearly less dominated by turbulence. It has not been possible to address this problem for this thesis, but modelling of such terms could certainly be improved. For this topic, the air-blast configuration developed in chapter 3 could be a good candidate to test new modelling proposals.

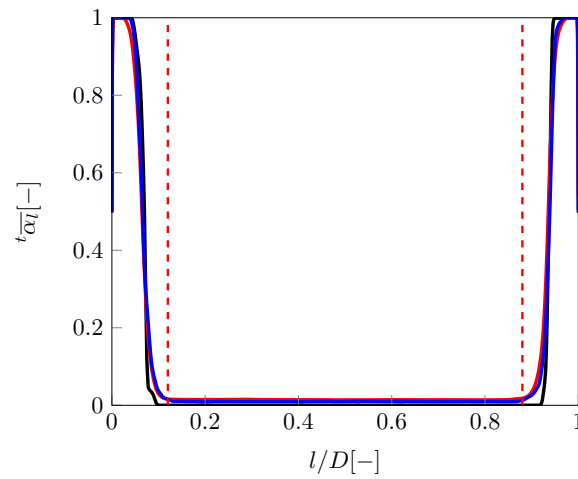


Figure 5.46 – Plot of the time averaged liquid volume fraction  $\overline{t\alpha_l}$  for the different models presented in the chapter. — *InterFoam* , — *ELSA* , — *ICMelsa* . The length adimensionalized by the diameter of the injector  $D$ . In - - - the empirical value.

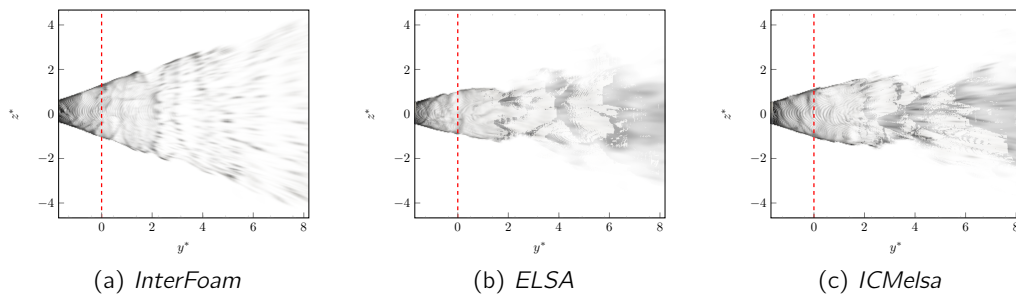


Figure 5.47 – Volume rendering of the liquid volume fraction field. On the left: *InterFoam* . On the center: *ELSA* . On the right: *ICMelsa* .  $\alpha_l = 0$   $1$ .

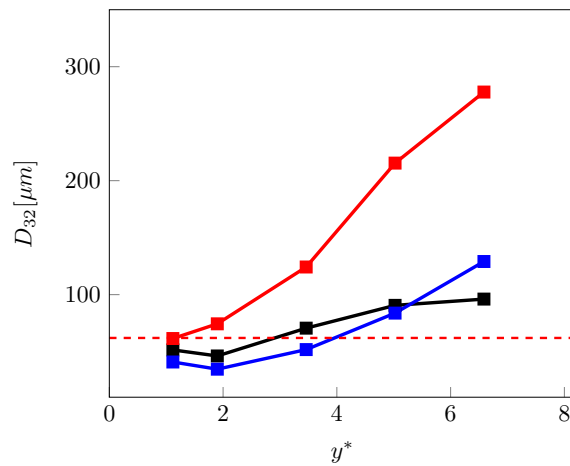


Figure 5.48 – Plot of the  $D_{32}$  value post processed following the formulation proposed in eq. (5.50) and eq. (5.49). — *InterFoam* , — *ELSA* , — *ICMelsa* , - - - the experimental value at  $y^* \approx 33$ .





# Chap. 6 | Conclusion and perspectives

## 6.1 Conclusion

The aim of this research is to study the atomization phenomena arising from an aeronautical injector. Due to the requirements of ICAO norms becoming more and more stringent over the years, aeronautic engine design needs to be optimized constantly to reduce their green house gas emission and require a predictive way to study the different flow characteristic. Different experimental studies have been conducted during the years, with very useful and considerable results. The development of numerical simulations can be very helpful to complete our knowledge and understanding of the atomization process. In this PhD we address numerical modelling through one of the atomization process: its multi-scale nature.

Indeed we started this research with an alternative review and classification of the models available, noticing that the works already present in literature ([MJD17],[SP18]) are frequently focused on one aspect of the multi-scale nature of the atomization phenomenon, being very specific and exhaustive on it. The classification we proposed is firstly based on the modeling length-scale chosen for the representation of the interface. The physical features under the modeling length-scale considered are represented by physical models, everything above is described by the transport equations of the variables. The models found in literature have been re-ordered by considering three representative length scales: interface length-scale, droplet length-scale, flow dynamic instability length-scale. For each modeling length-scale we have highlighted the models and methods present in literature, focusing on the interface representations and turbulence modeling techniques. The interface length-scale models can be split in the mixed phases and the separated phases models. At the droplet length scales most important approaches rely on the kinetic WBE. The flow dynamic instability length-scale represents the characteristics length scales related to the flow dynamic. This embodies in particular the turbulent nature of the flow that requires particular modelling treatment (RANS, LES, DNS). Most of the approaches consider these modelling techniques independent of the interface representation. For the sake of simplicity we keep this point of view by separating the dynamic length-scales from the other length-scales. We are well aware that, in reality, turbulent length-scale spectrum interact in many situation with the interface related length-scales but very few modelling approaches handle both phenomena. One attempt to progress in this direction is also presented based on the *ELSA* formalism (introduced in [VB99] and [Che+11]), and the *ICMelsa* model ([Ane+19a]) as practical examples.

A contribution of this thesis is the map which gathers all the modeling propositions and that allows to re-cast the methods available in literature.

A comparison between the different test cases has been defined in [MJD17] where *diffuse interface* approaches have been compared to the *sharp interface* approaches on some classical test cases examples. Most of the flows treated in atomization problems are turbulent flows, hence it is necessary to define a metric of comparison that takes into account the non-deterministic nature of the turbulent flows.

A simple test case configuration has been designed to test 5 methods, representative of the

different models we have introduced in the previous classification: *InterFoam* ([Rus02]) and *ARCHER* ([MTB07]) representative of the *sharp interface* approach, but with two different interface models (mixed phases for *InterFoam*, separated phases for *ARCHER*), CEDRE ([Cor20]) representative of the *diffuse interface* approach, *ELSA* ([Che+11]) representative of the turbulence modeling approach coupled with a mixed phases model and *ICMelsa* ([Ane18]) representative of the multi-scale approach, able to switch dynamically from a *diffuse interface* to *sharp interface* approach. The test case configuration is an air assisted liquid sheet with Reynolds and Weber numbers representative of the atomization for aeronautical engines. The comparison is restricted in a confidence zone of the domain assessed through the use of the  $IRQ_K$  criterion ([Can]), to understand how each model represents the different characteristics of the atomization problem.

By comparing the synchronized instantaneous liquid volume fraction fields of the different simulations, the large length-scales of the interface dynamic are well reproduced by all the numerical simulations. We can clearly distinguish 2 phases in the atomization process of the present configuration. A first phase in which it is possible to observe the oscillation of the liquid sheet and a second phase in which it is possible to observe the so called dripping regime ([Dum08]). The first order statistics appear to be reproduced mostly identically by the different models tested as soon as certain level of resolution are reached. A slight difference is visible in the liquid volume fraction time average  $\overline{\alpha}_l$ , where the characteristics of the different approaches show more or less liquid dispersion with respect to the center-line of the liquid sheet. The second order statistics and the Turbulent Kinetic Energy (TKE) are more sensible to the approaches used to represent the interface. This sensibility of the TKE to the small scale representation of the interface is initially surprising. The difference appears in terms of TKE spatial distribution but mostly on the magnitude of the TKE. we find, among others, differences in the magnitude and in the spreading around the central axis of the Reynolds stress components. To investigate this difference more in-depth we consider the analysis of the liquid-gas flow by phase. For this purpose we extracted the transient signal from the *ARCHER* phase markers with a probe located in the computational domain. As far as it relies on a CLSVOF method, it is possible to extract two different phase markers: the liquid volume fraction integrated over a computational cell to build a very thin *diffuse interface* signal and the level-set distance function, used to reconstruct a fully segregated representation. With the help of the introduction of the weighted average and the conditional average, we have highlighted the different representations between a segregated (level-set distance function) and a diffused (liquid volume fraction) flow field, showing the different Probability Density Functions (PDFs) of the phase markers. Then coming back to the 3D results, it is shown that The differences on the second order statistics are deeply bounded to the phase marker variance, thus it is important to study it for the different flow representations. Even with the well resolved *ARCHER* simulation, by computing the variance and comparing it with a segregated formulation we have found a noticeable residual difference. This is not the case of course when using the fully segregated representation based on the level-set distance function field. Computing the variance and hence the level of segregation with the different approaches, we have found more and more important residual difference with respect to the fully segregated representation. These results have shown the necessity to complete the *diffuse interface* representation by appropriate models to predict the second order statistics accurately. It is expected these models to be of different nature: reconstruction of the interface position if the diffuse interface thickness remains small with respect to the liquid-gas structures or physical modelling including sub-grid spray modelling when the interface thickness becomes larger than liquid size (droplets diameter for instance).

To better understand at which size this transition occurs, we introduced a simple linear model

based on a 1D representation. A filter or regularisation kernel is applied on a segregated field to produce a synthetic diffuse signal, representative of not segregated flow field. The linear model is built to recover the variance departure from the fully segregated representation. Once the differences in the modelling approaches have been explored, we test them for an industrial test case. One of the goals of this work was to test (and improve) the industrial oriented numerical models available in literature. Industrial oriented means: able to address complex geometries with an adapted computational cost. Among the different models tested on the air blast configuration, *ARCHER* represents a reference but requires a high number of computational nodes (and hence an high computational effort) to simulate a complex geometry. CEDRE model is a reduced order approach developed by Pierre Cordesse in his PhD work, still under development and not available at the final phase of the present work. *InterFoam*, *ELSA*, *ICMelsa* included physical models to represent sub-grid contributions and are based on the *OpenFoam* library that handles complex meshes. Thus this approaches can be tested on the swirl injector (the *Silvercrest* configuration provided by *SAFRAN Aircraft Engines*). The condition simulated is the re-light point of the flight path, most critical condition as far the compressor is rotating at a reduced rate, the combustion chamber is turned off and needs to be restarted. This particular condition has been experimentally tested in previous works, showing the typical tulip shape of a low injection pressure condition. This particular shape is well recovered with *ELSA* and *ICMelsa* model, while it is not for *InterFoam* with the same mesh resolution. The sharpening flux present in the liquid volume fraction transport equation plays the same role we have observed in the simple air-assisted liquid sheet configuration maintaining the liquid near the center axis of the sheet and preventing the liquid dispersion. The behaviour of the *ELSA* and *ICMelsa* model is different, where the liquid dispersion implied by the model increases the closure of the cone. The liquid film thickness at the injector exit has been shown to match the Lefebvre correlation with an uncertainty between 20 – 30%. In all the models we notice that the breakup length of the liquid sheet is primarily a matter of mesh resolution, even if the *ELSA* and *ICMelsa* show a better behaviour with respect to the *InterFoam* one (the most affected method by the low-resolution but all models) fail to retrieve the experimental SMD. In *ELSA* and *ICMelsa* the area density transport equation should complete the interface resolution with physical model. The present results showed the limitation of the source term. Indeed, this models have been developed for high Reynolds and Weber numbers and require further adaptation. The optimisation of the *ICMelsa* approach has been achieved through an improved description of the minimum/resolved interface. This development is an original development of the present PhD that can have other applications regarding the *ICMelsa* model.

## 6.2 Perspectives

The limited time a researcher have during its PhD does not allow to conclude all the topics opened and to solve all the issues. Here are some suggestions to pursue with this research work:

- The academical liquid sheet test case is really useful to perform an analysis on the first order and second order statistics and to pursue the phase analysis. All methods, even those using physical modelling for sub-grid resolution, are up to now dependent on the mesh resolution. This dependency on the resolution has been only partly explored during this PhD due to the important times required for such simulations. Thus other mesh resolutions test are expected to provide additional information. In particular, for *ARCHER* simulation, it would be interesting to double the resolution, to see if we would manage to extend the analysis zone. For the *ELSA* and *ICMelsa* models it would be

interesting to lower the mesh resolution, to have a better look to the sub-grid fluxes represented (an analysis of the turbulent liquid flux is proposed in appendix D).

- The phase analysis has brought new information and part of the work have been presented in [Cor+20b]. The amount of data produced is large and there has not been the time to post process the whole database. Other than the phase marker variance we have showed the decomposition of the Reynolds stress components. A proposal for a research activity could be to have a deeper look into this decomposition to understand from the phase analysis, the nature of the differences of the second order statistics.
- The segregation of the physical model is expected to change with the change in the position of the probe we use to retrieve the 1D signal. For this reason we have launched a simulation with 25 probes. Future objective will be to use the post processing developed in this work, to analyze the signal in different position.
- The 1D signal is a time signal, though the interface thickness is related to a spatial length scale. An idea could be to consider the velocity of the interface, and to use it to pass from a time signal to a spatial signal.
- Ludovic Goudenège helped in the identification of the important stochastic parameters to study. An example of this post processing has been set-up in the python notebook <https://gitlab.com/albiremo/1d-test>. The goal is to enlarge the study with more probe points and with the analysis of the signal coming from the simulation performed with the other methods (CEDRE, *ELSA*, *ICMelsa*, *InterFoam*). Furthermore an interesting research direction would be to use the machine learning *python* library *SciKit* [Ped+11] and the Bayesian unsupervised learning algorithms to deconvolve the liquid volume fraction diffuse signal in order to recover a fully segregated one.
- We simulated the *Silvercrest* injector with the *InterFoam*, *ELSA*, *ICMelsa* models. We have noticed the breaking length is not yet well reproduced. It would be interesting to further improve the resolution, to see if *InterFoam* and the other models are able to provide better results. It would be interesting to pursue the study of the breakup distance and the spray characteristic by simulating only the external environment, using as boundary the injection exit plan. This would allow less expensive simulation with an improved mesh refinement.
- The SMD post processing has shown the limitation of the present source terms used in the transport of sub-grid interface density area. It needs to be improved in order to take into account the physical phenomena happening in the transition and primary atomization zone, mainly for low Reynolds and low Weber number configurations. Some proposition have been already made in [Bea06], and needs to be tested and improved.
- The post processing of the spray characteristic can be understood more deeply and tested with the two formulation of the minimum interface area density  $\Sigma_{min}$  (the interface area density and the gradient of liquid volume fraction). The air blast configuration proposed in chapter 3 can be a good candidate to test the improvements in the future. Advancements from this point of view will be proposed by Ferrando in [Fer22].

# Bibliography

- [AH85] Takakage A. and Hiroyuki H. “Disintegration of Thin Liquid Sheet in Cocurrent Gas Stream : Wave Motion of Thin Liquid Sheet and Breakup Patterns”. In: *Transactions of the Japan Society of Mechanical Engineers Series B* 51.470 (1985), pp. 3336–3343 (cit. on p. 105).
- [Ahm19] A. Ahmed. “LES of atomization for diesel fuel injectors.” PhD thesis. University of Normandy, 2019 (cit. on pp. 25, 42, 122, 173).
- [Alb+13] H-E Albrecht, N. Damaschke, M. Borys, and C. Tropea. *Laser Doppler and phase Doppler measurement techniques*. Springer Science & Business Media, 2013 (cit. on p. 108).
- [AM+19] A. Asuri Mukundan, T. Ménard, A. Berlemont, and J.C.C Brändle De Motta. “A comparative study of DNS of airblast atomization using CLSMOF and CLSVOF methods”. In: *29th Annual Conference on Liquid Atomization and Spray Systems (ILASS19)*. ILASS19 Proceedings. Paris, France, Sept. 2019 (cit. on p. 129).
- [AMW98] D.M Anderson, G.B McFadden, and Adam A. Wheeler. “Diffuse-interface methods in fluid mechanics”. In: *Annual review of Fluid Mechanics* 30.1 (1998), pp. 139–165 (cit. on p. 8).
- [And05] J.D Anderson. *Introduction to Flight*. McGraw-Hill series in aeronautical and aerospace engineering. McGraw-Hill Higher Education, 2005 (cit. on p. 1).
- [And+15] A. Andreini, G. Caciolli, B. Facchini, A. Picchi, and F. Turrini. “Experimental investigation of the flow field and the heat transfer on a scaled cooled combustor liner with realistic swirling flow generated by a lean-burn injection system”. In: *Journal of Turbomachinery* 137.3 (2015), p. 031012 (cit. on p. 5).
- [And+16] A. Andreini, C. Bianchini, S. Puggelli, and F-X Demoulin. “Development of a turbulent liquid flux model for Eulerian–Eulerian multiphase flow simulations”. In: *International Journal of Multiphase Flow* 81 (2016), pp. 88–103 (cit. on pp. 5, 26).
- [Ane18] J. Anez. “Modélisation de l’injection de pétrole pour les procédés FCC (Fluid Catalytic Cracking)”. PhD thesis. University of Normandy, 2018 (cit. on pp. 25, 28, 132, 148).
- [Ane+19a] J. Anez, A. Ahmed, N. Hecht, B. Duret, J. Reveillon, and F-X. Demoulin. “Eulerian–Lagrangian spray atomization model coupled with interface capturing method for diesel injectors”. In: *International Journal of Multiphase Flow* 113 (2019), pp. 325–342 (cit. on pp. 29, 33, 119, 147, 173).
- [Ane+19b] J. Anez, S. Puggelli, N. Hecht, A. Andreini, J. Reveillon, and F. X Demoulin. “Liquid Atomization Modeling in OpenFOAM”. In: *OpenFOAM : Selected Papers of the 11th Workshop*. 2019, pp. 297–308 (cit. on pp. 26, 29, 132).

- [Ani11] W. Aniszewski. "Large eddy simulation of turbulent two-phase flow". PhD thesis. Czestochowa University of Technology, 2011 (cit. on pp. 9, 22).
- [ARA11] A. Altimira M. and Rivas, J.C Ramos, and R. Anton. "Disintegration regime of industrial fan-spray atomizers through CFD simulations". In: *ILASS-Europe 2011*. 2011 (cit. on p. 103).
- [Ara86] T Arai. "Disintegration of a Thin Liquid Sheet in a Cocurrent Air Stream". In: *International Journal of Turbo & Jet-Engines* 3 (1986), pp. 301–306 (cit. on p. 46).
- [Aya15] U. Ayachit. *The paraview guide: a parallel visualization application*. Kitware, Inc., 2015 (cit. on p. 125).
- [Bac00] W.D Bachalo. "Spray diagnostics for the twenty-first century". In: *Atomization and Sprays* 10.3-5 (2000), pp. 439–474 (cit. on p. 7).
- [Bac94] W.D Bachalo. "Experimental methods in multiphase flows". In: *International Journal of Multiphase Flow* 20 (1994), pp. 261–295 (cit. on p. 7).
- [Bat59] G.K Batchelor. "Small-scale variation of convected quantities like temperature in turbulent fluid Part 1. General discussion and the case of small conductivity". In: *Journal of Fluid Mechanics* 5.1 (1959), pp. 113–133 (cit. on p. 29).
- [BB+01] A.A Burluka, R. Borghi, et al. "Development of a Eulerian model for the "atomization" of a liquid jet". In: *Atomization and sprays* 11.6 (2001) (cit. on pp. 24, 27).
- [BB10] R.E Bensow and G. Bark. "Implicit LES predictions of the cavitating flow on a propeller". In: *Journal of fluids engineering* 132.4 (2010) (cit. on p. 61).
- [BB73] J.P Boris and D.L Book. "Flux-corrected transport. I. SHASTA, a fluid transport algorithm that works". In: *Journal of Computational Physics* 11.1 (1973), pp. 38–69 (cit. on p. 42).
- [BCB03] V.E Badalassi, H.D Cenicerros, and S. Banerjee. "Computation of multiphase systems with phase field models". In: *Journal of Computational Physics* 190.2 (2003), pp. 371–397 (cit. on p. 19).
- [BCH98] P. Billant, J-M Chomaz, and P. Huerre. "Experimental study of vortex breakdown in swirling jets". In: *Journal of Fluid Mechanics* 376 (1998), pp. 183–219 (cit. on pp. 105, 113, 114).
- [Bea+05] P.A Beau, M. Funk, R. Lebas, and F-X Demoulin. *Applying quasi-multiphase model to simulate atomization processes in Diesel engines: Modeling of the slip velocity*. Tech. rep. SAE Technical Paper, 2005 (cit. on p. 27).
- [Bea06] P-A Beau. "Modélisation de l'atomisation d'un jet liquide: Application aux sprays Diesel". PhD thesis. 2006 (cit. on pp. 27, 28, 43, 150).
- [Bek17] S. Bektas. "Curvature of the Ellipsoid with Cartesian Coordinates". In: *Landscape Architecture and Regional Planning* 2.2 (2017), p. 61 (cit. on p. 172).
- [BFR80] J. Bardina, J. Ferziger, and W. Reynolds. "Improved subgrid-scale models for large-eddy simulation". In: *13th fluid and plasmadynamics conference*. 1980, p. 1357 (cit. on p. 24).
- [BG08] J.C Butcher and N. Goodwin. *Numerical methods for ordinary differential equations*. Vol. 2. Wiley Online Library, 2008 (cit. on p. 42).



- [BH50] A.M Binnie and D.P Harris. “The application of boundary-layer theory to swirling liquid flow through a nozzle”. In: *The Quarterly Journal of Mechanics and Applied Mathematics* 3.1 (1950), pp. 89–106 (cit. on p. 97).
- [BM92] J.B Bell and D.L Marcus. “A second-order projection method for variable-density flows”. In: *Journal of Computational Physics* 101.2 (1992), pp. 334–348 (cit. on p. 31).
- [BN86] M.R Baer and J.W Nunziato. “A two-phase mixture theory for the deflagration-to-detonation transition (ddt) in reactive granular materials”. In: *International Journal of Multiphase Flow* 12.6 (1986), pp. 861–889 (cit. on pp. 8, 20, 33).
- [Cah59] J.W Cahn. “Free energy of a nonuniform system. II. Thermodynamic basis”. In: *The Journal of Chemical Physics* 30.5 (1959), pp. 1121–1124 (cit. on p. 20).
- [Can] “Curvature-based interface resolution quality (IRQ”. In: () (cit. on pp. 30, 54, 148, 173).
- [Can+18] R. Canu, S. Puggelli, M. Essadki, B. Duret, T. Menard, M. Massot, J. Reveillon, and F-X. Demoulin. “Where does the droplet size distribution come from?” In: *International Journal of Multiphase Flow* (2018) (cit. on p. 28).
- [Can19] R. Canu. “Développement d’une méthode compressible avec évaporation pour la simulation d’interface résolue dans le cadre de l’atomisation.” PhD thesis. University of Normandy, 2019 (cit. on pp. 33, 52, 173).
- [CD01] E.D Christensen and R. Deigaard. “Large eddy simulation of breaking waves”. In: *Coastal engineering* 42.1 (2001), pp. 53–86 (cit. on p. 25).
- [CD96] Norman Chigier and Christophe Dumouchel. “Atomization of liquid sheets”. In: *Recent advances in spray combustion: Spray atomization and drop burning phenomena*. 1 (1996), pp. 241–259 (cit. on p. 46).
- [CDJ75] G.D Crapper, N. Dombrowski, and W.P Jepson. “Wave growth on thin sheets of non-Newtonian liquids”. In: *Proceedings of the Royal Society of London. A. Mathematical and Physical Sciences* 342.1629 (1975), pp. 225–236 (cit. on p. 46).
- [CH58] J.W Cahn and J.E Hilliard. “Free energy of a nonuniform system. I. Interfacial free energy”. In: *The Journal of Chemical Physics* 28.2 (1958), pp. 258–267 (cit. on p. 19).
- [Cha+13] D.E.H Chawki et al. “Atomization modeling of liquid jets using an Eulerian-Eulerian model and a Surface Density Approach”. PhD thesis. Aix-Marseille, 2013 (cit. on p. 26).
- [Che10] J. Chesnel. “Simulation aux Grandes Échelles de l’Atomisation, Application à l’Injection Automobile.” PhD thesis. 2010 (cit. on pp. 22, 24, 26, 27, 28, 33, 116, 132, 137, 138).
- [Che+11] J. Chesnel, J. Reveillon, T. Menard, and F-X Demoulin. “Large eddy simulation of liquid jet atomization”. In: *Atomization and Sprays* 21.9 (2011) (cit. on pp. 9, 25, 122, 147, 148).
- [Ché+19] V. Chéron, J.C Brändle De Motta, G. Vaudor, T. Ménard, and A. Berlemont. “From droplets to particles: Transformation criteria”. In: *ILASS - Europe 2019, 29th Conference on Liquid Atomization and Spray Systems*. Paris, France, Sept. 2019 (cit. on p. 28).



- 
- [Chi+16] J.J Chinn, D. Cooper, A.J Yule, and G.G Nasr. “Stationary rotary force waves on the liquid–air core interface of a swirl atomizer”. In: *Heat and Mass Transfer* 52.10 (2016), pp. 2037–2050 (cit. on p. 97).
- [Cho68] A.J. Chorin. “Numerical solution of the Navier-Stokes equations”. In: *Mathematics of computation* 22.104 (1968), pp. 745–762 (cit. on p. 41).
- [CHS02] I.S Carvalho, M.V Heitor, and D. Santos. “Liquid film disintegration regimes and proposed correlations”. In: *International journal of multiphase flow* 28.5 (2002), pp. 773–789 (cit. on pp. 46, 47).
- [CM20] P. Cordesse and M. Massot. “Entropy supplementary conservation law for non-linear systems of PDEs with non-conservative terms: application to the modelling and analysis of complex fluid flows using computer algebra”. In: *Communications in Mathematical Sciences* 18.2 (2020), 515–534 (cit. on p. 39).
- [Cor20] P. Cordesse. “Contribution à l’étude des instabilités de combustion dans les moteurs-fusées cryotechniques : couplage entre modèles à interfaces diffuses et modèles cinétiques pour la simulation de l’atomisation primaire”. PhD thesis. Université Paris-Saclay, 2020 (cit. on pp. 8, 12, 17, 20, 33, 35, 38, 40, 51, 114, 148).
- [Cor+20a] P. Cordesse, R. Di Battista, S. Drui F.and Kokh, and M. Massot. “Derivation of a two-phase flow model with two-scale kinematics, geometric variables and surface tension using variational calculus”. en. In: *Proceedings of the NASA Summer Program*. Nasa Technical Memorandum. 2020 (cit. on pp. 12, 13, 28).
- [Cor+20b] P. Cordesse, A. Remigi, B. Duret, A. Murrone, T. Ménard, F-X Demoulin, and M. Massot. “Validation strategy of reduced-order two-fluid flow models based on a hierarchy of direct numerical simulations”. In: *Flow, Turbulence and Combustion* (2020), pp. 1–31 (cit. on pp. 35, 70, 114, 150).
- [CP90] S.M Candel and T.J Poinso. “Flame stretch and the balance equation for the flame area”. In: *Combustion Science and Technology* 70.1-3 (1990), pp. 1–15 (cit. on p. 27).
- [Das+01] S.K Dash, M.R Halder, M. Peric, and S.K Som. “Formation of air core in nozzles with tangential entry”. In: *The Journal of Fluids Engineering* 123.4 (2001), pp. 829–835 (cit. on p. 97).
- [DB+19] Ruben Di Battista, I. Bermejo-Moreno, T. Ménard, S. de Chaisemartin, and M. Massot. “Post-processing of two-phase DNS simulations exploiting geometrical features and topological invariants to extract flow statistics: application to canonical objects and the collision of two droplets”. In: 2019 (cit. on p. 28).
- [DB20] X. Deng and P. Boivin. “Diffuse interface modelling of reactive multi-phase flows applied to a sub-critical cryogenic jet”. In: *Applied Mathematical Modelling* 84 (2020), pp. 405–424 (cit. on p. 8).
- [DB21] R. Di Battista. “Towards a unified eulerian modeling framework for two-phase flow: geometrical subscale phenomena and associated highly-scalable numerical methods”. PhD thesis. Institut Polytechnique de Paris, 2021 (cit. on pp. 8, 114, 169, 171).
- [Dem+07] F-X Demoulin, P-A Beau, G. Blokkeel, A. Mura, and R. Borghi. “A new model for turbulent flows with large density fluctuations: Application to liquid atomization”. In: *Atomization and Sprays* 17.4 (2007) (cit. on pp. 24, 26).

- [DH62] N. Dombrowski and P.C Hooper. "The effect of ambient density on drop formation in sprays". In: *Chemical Engineering Science* 17.4 (1962), pp. 291–305 (cit. on pp. 7, 105).
- [DHD15] B.M Devassy, C. Habchi, and E. Daniel. "Atomization modelling of liquid jets using a two-surface-density approach". In: *Atomization and Sprays* 25.1 (2015) (cit. on p. 26).
- [DHW60] N. Dombrowski, D. Hasson, and D.E Ward. "Some aspects of liquid flow through fan spray nozzles". In: *Chemical Engineering Science* 12.1 (1960), pp. 35–50 (cit. on p. 46).
- [DJ63] N. Dombrowski and W.R Johns. "The aerodynamic instability and disintegration of viscous liquid sheets". In: *Chemical Engineering Science* 18.3 (1963), pp. 203–214 (cit. on p. 46).
- [Doi+13] F. Doisneau, J. Dupays, A. Murrone, F. Laurent, and M. Massot. "Eulerian versus Lagrangian simulation of unsteady two-way coupled coalescing two-phase flows in solid propellant combustion". In: *Comptes Rendus Mécanique* 341.1-2 (2013), pp. 44–54 (cit. on p. 132).
- [Dre83] D.A Drew. "Mathematical modeling of two-phase flow". In: *Annual review of fluid mechanics* 15.1 (1983), pp. 261–291 (cit. on p. 20).
- [Dru17] F. Drui. "Modélisation et simulation Eulériennes des écoulements diphasiques à phases séparées et dispersées: développement d'une modélisation unifiée et de méthodes numériques adaptées au calcul massivement parallèle". PhD thesis. 2017 (cit. on p. 20).
- [DS00] A. Datta and S.K Som. "Numerical prediction of air core diameter, coefficient of discharge and spray cone angle of a swirl spray pressure nozzle". In: *International journal of heat and fluid flow* 21.4 (2000), pp. 412–419 (cit. on p. 97).
- [DSG17] M. Dianat, M. Skarysz, and A. Garmory. "A Coupled Level Set and Volume of Fluid method for automotive exterior water management applications". In: *International Journal of Multiphase Flow* 91 (2017), pp. 19–38 (cit. on p. 19).
- [Dum05] C. Dumouchel. "Experimental analysis of a liquid atomization process at low Weber number". In: *Proceedings of international symposium on heat and mass transfer in spray systems, Antalya, Turkey. 2005*, pp. 5–10 (cit. on p. 104).
- [Dum08] C. Dumouchel. "On the experimental investigation on primary atomization of liquid streams". In: *Experiments in Fluids* 45.3 (2008), pp. 371–422 (cit. on pp. 46, 55, 148).
- [Dur+12] B. Duret, G. Luret, J. Reveillon, T. Ménard, A. Berlemont, and F-X. Demoulin. "DNS analysis of turbulent mixing in two-phase flows". In: *International Journal of Multiphase Flow* 40 (2012), pp. 93–105 (cit. on pp. 26, 27).
- [Dur+13] B. Duret, J. Reveillon, T. Menard, and F-X Demoulin. "Improving primary atomization modeling through DNS of two-phase flows". In: *International Journal of Multiphase Flow* 55 (2013), pp. 130–137 (cit. on p. 27).
- [DVP93] J.M Duclos, D. Veynante, and T. Poinso. "A comparison of flamelet models for premixed turbulent combustion". In: *Combustion and flame* 95.1-2 (1993), pp. 101–117 (cit. on p. 26).
- [Ege+14] C.P Egerer, S. Hickel, S.J Schmidt, and N.A Adams. "Large-eddy simulation of turbulent cavitating flow in a micro channel". In: *Physics of Fluids* 26.8 (2014), p. 085102 (cit. on p. 61).

- [Eli89] C.M Elliott. "The Cahn-Hilliard model for the kinetics of phase separation". In: *Mathematical models for phase change problems*. Springer, 1989, pp. 35–73 (cit. on pp. 20, 33).
- [Ess+17] M. Essadki, F. Drui, S. Chaisemartin, A. Larat, T. Ménard, and M. Massot. "Statistical modeling of the gas-liquid interface using geometrical variables: toward a unified description of the disperse and separated phase flows". en. In: (2017), p. 41 (cit. on p. 8).
- [Ess+18] M. Essadki, S. De Chaisemartin, F. Laurent, and M. Massot. "High Order Moment Model for Polydisperse Evaporating Sprays Towards Interfacial Geometry". In: *SIAM Applied Mathematics* 78.4 (2018), pp. 2003–2027 (cit. on pp. 11, 13, 20, 21).
- [Fal13] M. Falese. "A study of the effects of bifurcations in swirling flows using Large Eddy Simulation and mesh adaptation". PhD thesis. Université de Toulouse, 2013 (cit. on pp. 6, 104).
- [Fed+99] R.P Fedkiw, T. Aslam, B. Merriman, S. Osher, et al. "A non-oscillatory Eulerian approach to interfaces in multimaterial flows (the ghost fluid method)". In: *Journal of Computational Physics* 152.2 (1999), pp. 457–492 (cit. on pp. 19, 38).
- [Fer22] D. Ferrando. "Modélisation numérique avancée du processus d'atomisation : application à un système d'injection aéronautique". PhD thesis. University of Normandy, 2022 (cit. on pp. 95, 142, 150).
- [FHL71] J.A Fay, J.B Heywood, and Lawrence H. Linden. "Jet aircraft air pollutant production and dispersion". In: *AIAA Journal* 9.5 (1971), pp. 841–850 (cit. on p. 2).
- [FK95] U. Frisch and A.N Kolmogorov. *Turbulence: the legacy of AN Kolmogorov*. Cambridge university press, 1995 (cit. on p. 21).
- [FL77] J. Henry Faler and S. Leibovich. "Disrupted states of vortex flow and vortex breakdown". In: *The Physics of Fluids* 20.9 (1977), pp. 1385–1400 (cit. on pp. 104, 105).
- [FLM08] R.O Fox, F. Laurent, and M. Massot. "Numerical simulation of spray coalescence in an Eulerian framework: direct quadrature method of moments and multi-fluid method". In: *Journal of Computational Physics* 227.6 (2008), pp. 3058–3088 (cit. on p. 21).
- [FP12] J.H. Ferziger and M. Peric. *Computational methods for fluid dynamics*. 2012 (cit. on pp. 36, 40).
- [Fra53] R.P Fraser. "Research into the performance of atomizers for liquids". In: *Imperial College Chemical Engineering Science Journal* 7 (1953), pp. 52–68 (cit. on p. 103).
- [Fra63] R.P Fraser. "Liquid fuel atomization". In: *Imperial College Chemical Engineering Science Journal* 18.6 (1963), pp. 339–353 (cit. on p. 105).
- [FS15] D. Furfaro and R. Saurel. "A simple HLLC-type Riemann solver for compressible non-equilibrium two-phase flows". In: *Computers & Fluids* 111 (2015), pp. 159–178 (cit. on pp. 39, 40).

- [Fus+09] D. Fuster, A. Bagué, T. Boeck, L. Le Moyne, A. Leboissetier, S. Popinet, P. Ray, R. Scardovelli, and S. Zaleski. "Simulation of primary atomization with an octree adaptive mesh refinement and VOF method". In: *International Journal of Multiphase Flow* 35.6 (2009), pp. 550–565 (cit. on p. 28).
- [Gai+16] P. Gaillard, C. Le Touze, L. Matuszewski, and A. Murrone. "Numerical Simulation of Cryogenic Injection in Rocket Engine Combustion Chambers". In: *AerospaceLab* 11 (2016), p. 16 (cit. on pp. 39, 40).
- [Ger+91] M. Germano, U. Piomelli, P. Moin, and W.H Cabot. "A dynamic subgrid-scale eddy viscosity model". In: *Physics of Fluids A: Fluid Dynamics* 3.7 (1991), pp. 1760–1765 (cit. on p. 24).
- [GH08] M. Gorokhovski and M. Herrmann. "Modeling primary atomization". In: *Annual Review of Fluid Mechanics* 40 (2008), pp. 343–366 (cit. on p. 29).
- [GM50] E. Giffen and B.S Massey. "Report 1950/5". In: *Motor Industry Research Association* (1950) (cit. on p. 99).
- [Gra+07] V. Grandgirard, Y. Sarazin, P. Angelino, A. Bottino, N. Crouseilles, G. Darmet, G. Dif-Pradalier, X. Garbet, P.H Ghendrih, S. Jolliet, et al. "Global full-f gyrokinetic simulations of plasma turbulence". In: *Plasma Physics and Controlled Fusion* 49.12B (2007), B173 (cit. on p. 21).
- [Hag12] G. Hagler. *Modeling ships and space craft: the science and art of mastering the oceans and sky*. Springer Science & Business Media, 2012 (cit. on p. 1).
- [HDS02] M.R Halder, S.K Dash, and S.K Som. "Initiation of air core in a simplex nozzle and the effects of operating and geometrical parameters on its shape and size". In: *Experimental thermal and fluid science* 26.8 (2002), pp. 871–878 (cit. on p. 97).
- [Hel68] H. von Helmholtz. *über discontinuirliche Flüssigkeits-Bewegungen*. Akademie der Wissenschaften zu Berlin, 1868 (cit. on p. 105).
- [Her08] M. Herrmann. "A balanced force refined level set grid method for two-phase flows on unstructured flow solver grids". In: *Journal of Computational Physics* 227.4 (2008), pp. 2674–2706 (cit. on p. 28).
- [Her10] M. Herrmann. "A parallel Eulerian interface tracking/Lagrangian point particle multi-scale coupling procedure". In: *Journal of Computational Physics* 229.3 (2010), pp. 745–759 (cit. on p. 28).
- [Her13] M. Herrmann. "A sub-grid surface dynamics model for sub-filter surface tension induced interface dynamics". In: *Computers & Fluids* 87 (2013), pp. 92–101 (cit. on p. 25).
- [HN81] C.W Hirt and B.D Nichols. "Volume of fluid (VOF) method for the dynamics of free boundaries". In: *Journal of Computational Physics* 39.1 (1981), pp. 201–225 (cit. on pp. 18, 33).
- [IA03] V. Iyer and J. Abraham. "An evaluation of a two-fluid Eulerian-liquid Eulerian-gas model for diesel sprays". In: *The Journal of Fluids Engineering* 125.4 (2003), pp. 660–669 (cit. on p. 26).
- [Ica] *ICAO Enviromental Report*. Tech. rep. 2019 (cit. on p. 5).
- [Ish75] M. Ishii. "Thermo-fluid dynamic theory of two-phase flow". In: *NASA Sti/recon Technical Report A 75* (1975) (cit. on pp. 13, 15, 16, 20, 26, 49, 50, 71).

- [Iss86] R.I. Issa. "Solution of the implicitly discretised fluid flow equations by operator-splitting". In: *Journal of computational physics* 62.1 (1986), pp. 40–65 (cit. on p. 40).
- [Jed+18] J. Jedelsky, M. Maly, N.P del Corral, G. Wigley, L. Janackova, and M. Jicha. "Air–liquid interactions in a pressure-swirl spray". In: *International Journal of Heat and Mass Transfer* 121 (2018), pp. 788–804 (cit. on p. 6).
- [Jon82] A.R Jones. "Design optimization of a large pressure-jet atomizer for power plant". In: *Proceedings of ICLASS*. 1982, pp. 181–185 (cit. on p. 99).
- [Kah+12] D. Kah, F. Laurent, M. Massot, and S. Jay. "A high order moment method simulating evaporation and advection of a polydisperse liquid spray". In: *Journal of Computational Physics* 231.2 (2012), pp. 394–422 (cit. on p. 21).
- [Kap+01] A.K Kapila, R. Menikoff, J.B Bdzil, S.F Son, and D.S Stewart. "Two-phase modeling of deflagration-to-detonation transition in granular materials: Reduced equations". In: *Physics of fluids* 13.10 (2001), pp. 3002–3024 (cit. on pp. 20, 39).
- [Kat86] I. Kataoka. "Local instant formulation of two-phase flow". In: *International Journal of Multiphase Flow* 12.5 (1986), pp. 745–758 (cit. on p. 16).
- [KFL00] M. Kang, R.P. Fedkiw, and X-D. Liu. "A boundary condition capturing method for multiphase incompressible flow". In: *Journal of Scientific Computing* 15.3 (2000), pp. 323–360 (cit. on p. 38).
- [KG21] M. Klein and M. Germano. "Analysis and Modelling of the Commutation Error". In: *Fluids* 6.1 (2021), p. 15 (cit. on p. 22).
- [Kim98] Ron Kimmel. "Fast marching methods on triangulated domains". In: *Proc. Nat. Acad. Sci.* 95 (1998), pp. 8431–8435 (cit. on p. 19).
- [Kin+03] G. Kindlmann, R. Whitaker, T. Tasdizen, and T. Moller. "Curvature-based transfer functions for direct volume rendering: Methods and applications". In: *IEEE Visualization, 2003. VIS 2003*. IEEE. 2003, pp. 513–520 (cit. on pp. 169, 170).
- [KIS86] I. Kataoka, M. Ishii, and A. Serizawa. "Local formulation and measurements of interfacial area concentration in two-phase flow". In: *International Journal of Multiphase Flow* 12.4 (1986), pp. 505–529 (cit. on p. 16).
- [KNN78] S.P Kutty, M. Narasimhan, and K. Narayanaswamy. "Design and prediction of discharge rate, cone angle and air core diameter of swirl chamber atomizers". In: *Proceedings of the First International Conference on Liquid Atomization and Spray Systems*. 1978, p. 93 (cit. on p. 97).
- [Kol41a] A.N Kolmogorov. "Dissipation of energy in locally isotropic turbulence". In: *Dokl. Akad. Nauk SSSR*. Vol. 32. 1. JSTOR. 1941, pp. 16–18 (cit. on p. 22).
- [Kol41b] A.N Kolmogorov. "The local structure of turbulence in incompressible viscous fluid for very large Reynolds numbers". In: *Dokl. Akad. Nauk SSSR*. Vol. 30. 4. JSTOR. 1941, pp. 301–305 (cit. on p. 22).
- [LE92] E.K Longmire and J.K Eaton. "Structure of a particle-laden round jet". In: *Journal of Fluid Mechanics* 236 (1992), pp. 217–257 (cit. on p. 7).

- [Leb+09] R. Lebas, T. Ménard, P-A Beau, A. Berlemont, and F-X Demoulin. "Numerical simulation of primary break-up and atomization: DNS and modelling study". In: *International Journal of Multiphase Flow* 35.3 (2009), pp. 247–260 (cit. on pp. 26, 27).
- [Lee17] S.B Lee. "A study on temporal accuracy of OpenFOAM". In: *International Journal of Naval Architecture and Ocean Engineering* 9.4 (2017), pp. 429–438 (cit. on p. 123).
- [Leo75] A. Leonard. "Energy cascade in large-eddy simulations of turbulent fluid flows". In: *Advances in geophysics*. Vol. 18. Elsevier, 1975, pp. 237–248 (cit. on p. 23).
- [LeV02] R.J LeVeque. *Finite volume methods for hyperbolic problems*. Vol. 31. Cambridge university press, 2002 (cit. on p. 42).
- [LeV92] R.J LeVeque. *Numerical methods for conservation laws*. Vol. 3. Springer, 1992 (cit. on pp. 8, 42).
- [Li95] J. Li. "Calcul d'interface affine par morceaux". In: *Comptes rendus de l'Académie des sciences. Série II, Mécanique, physique, chimie, astronomie* 320.8 (1995), pp. 391–396 (cit. on p. 19).
- [Lin+19] Y. Ling, D. Fuster, G. Tryggvason, and S. Zaleski. "A two-phase mixing layer between parallel gas and liquid streams: multiphase turbulence statistics and influence of interfacial instability". In: *Journal of Fluid Mechanics* 859 (2019), 268–307 (cit. on p. 29).
- [LL59] L.D Landau and E.M Lifshitz. "Fluid mechanics. 1959". In: *Course of theoretical physics* (1959) (cit. on p. 20).
- [LM88] A.H Lefebvre and V.G McDonell. *Atomization and sprays*. CRC press, 1988 (cit. on pp. 7, 8, 11, 12, 96, 99, 103, 113, 120).
- [Loz+01] A. Lozano, F. Barreras, G. Hauke, and C. Dopazo. "Longitudinal instabilities in an air-blasted liquid sheet". In: *Journal of Fluid Mechanics* 437 (2001), pp. 143–173 (cit. on p. 46).
- [Loz+96] A. Lozano, C.J Call, C. Dopazo, and A. Garcia-Olivares. "Experimental and numerical study of the atomization of a planar liquid sheet". In: *Atomization and Sprays* 6.1 (1996) (cit. on p. 46).
- [LTMG14] C. Le Touze, A. Murrone, and H. Guillard. "Multislope MUSCL method for general unstructured meshes". In: *Journal of Computational Physics* 284 (2014), pp. 389–418 (cit. on p. 40).
- [Lub+06] P. Lubin, S. Vincent, S. Abadie, and J-P Caltagirone. "Three-dimensional large eddy simulation of air entrainment under plunging breaking waves". In: *Coastal engineering* 53.8 (2006), pp. 631–655 (cit. on p. 25).
- [Mal+18] M. Maly, J. Jedelsky, J. Slama, L. Janackova, M. Sapík, G. Wigley, and M. Jicha. "Internal flow and air core dynamics in Simplex and Spill-return pressure-swirl atomizers". In: *International Journal of Heat and Mass Transfer* 123 (2018), pp. 805–814 (cit. on p. 7).
- [MASB10] S. Moon, E. Abo-Serie, and C. Bae. "Liquid film thickness inside the high pressure swirl injectors: Real scale measurement and evaluation of analytical equations". In: *Experimental thermal and fluid science* 34.2 (2010), pp. 113–121 (cit. on pp. 7, 97).



- [MD01] H. Malot and C. Dumouchel. “Experimental investigation of the drop size distribution of sprays produced by a low-velocity Newtonian cylindrical liquid jet”. In: *Atomization and Sprays* 11.3 (2001) (cit. on p. 104).
- [ME51] R.A Mugele and H.D Evans. “Droplet size distribution in sprays”. In: *Industrial & Engineering Chemistry* 43.6 (1951), pp. 1317–1324 (cit. on p. 106).
- [Mén07] T. Ménard. “Développement d’une méthode level set pour le suivi d’interface. application de la rupture de jet liquide”. PhD thesis. University of Normandy, 2007 (cit. on p. 37).
- [MH92] D. Mitchell and P. Hanrahan. “Illumination from curved reflectors”. In: *Proceedings of the 19th annual conference on Computer graphics and interactive techniques*. 1992, pp. 283–291 (cit. on p. 169).
- [MIM19] S. Mirjalili, C.B Ivey, and A. Mani. “Comparison between the diffuse interface and volume of fluid methods for simulating two-phase flows”. In: *International Journal of Multiphase Flow* 116 (2019), pp. 221–238 (cit. on pp. 20, 31).
- [MJD17] S. Mirjalili, S.S Jain, and M. Dodd. “Interface-capturing methods for two-phase flows: An overview and recent developments”. In: *Annual Research Briefs* (2017), pp. 117–135 (cit. on pp. 8, 9, 11, 17, 147).
- [Mon03] H. Mongia. “TAPS: A fourth generation propulsion combustor technology for low emissions”. In: *AIAA International Air and Space Symposium and Exposition: The Next 100 Years*. 2003, p. 2657 (cit. on p. 5).
- [Mor07] C. Morel. “On the surface equations in two-phase flows and reacting single-phase flows”. In: *International Journal of Multiphase Flow* 33.10 (2007), pp. 1045–1073 (cit. on p. 26).
- [MR11] G.H McKinley and M. Renardy. “Wolfgang von ohnesorge”. In: *Physics of Fluids* 23.12 (2011), p. 127101 (cit. on p. 6).
- [MT03] J.E Marsden and A. Tromba. *Vector calculus*. Macmillan, 2003 (cit. on p. 169).
- [MTB07] T. Ménard, S. Tanguy, and A. Berlemont. “Coupling level set VOF ghost fluid methods: Validation and application to 3D simulation of the primary break-up of a liquid jet”. In: *International Journal of Multiphase Flow* 33.5 (2007), pp. 510–524 (cit. on pp. 19, 33, 35, 36, 37, 38, 148, 169).
- [Nic99] F.C Nicoud. *Numerical study of a channel flow with variable properties*. CTR Annual Research Briefs 1998. 1999 (cit. on pp. 24, 54).
- [Nin+09] W. Ning, R.D Reitz, R. Diwakar, and A.M Lippert. “An Eulerian-Lagrangian spray and atomization model with improved turbulence modeling”. In: *Atomization and Sprays* 19.8 (2009) (cit. on p. 26).
- [NP00] S. Nonnenmacher and M. Piesche. “Design of hollow cone pressure swirl nozzles to atomize Newtonian fluids”. In: *Chemical Engineering Science* 55.19 (2000), pp. 4339–4348 (cit. on p. 7).
- [NW76] W.F Noh and P. Woodward. “SLIC (simple line interface calculation)”. In: *Proceedings of the fifth international conference on numerical methods in fluid dynamics June 28–July 2, 1976 Twente University, Enschede*. Springer. 1976, pp. 330–340 (cit. on p. 19).
- [OS88] S. Osher and James A. Sethian. “Fronts propagating with curvature-dependent speed: algorithms based on Hamilton-Jacobi formulations”. In: *Journal of Computational Physics* 79.1 (1988), pp. 12–49 (cit. on pp. 19, 33).

- [Pal21] L. Palanti. “On the modelling of liquid fuel ignition and atomization in aero engine combustors”. PhD thesis. Università degli Studi di Firenze, 2021 (cit. on pp. 27, 95, 115, 120, 130, 137, 138).
- [Ped+11] F. Pedregosa, G. Varoquaux, A. Gramfort, V. Michel, B. Thirion, O. Grisel, M. Blondel, P. Prettenhofer, R. Weiss, V. Dubourg, et al. “Scikit-learn: Machine learning in Python”. In: *the Journal of machine Learning research* 12 (2011), pp. 2825–2830 (cit. on p. 150).
- [Pla73] J. Plateau. *Statique expérimentale et théorique des liquides soumis aux seules forces moléculaires*. Vol. 2. Gauthier-Villars, 1873 (cit. on p. 11).
- [PMO15] F. Piscaglia, A. Montorfano, and A. Onorati. “A scale adaptive filtering technique for turbulence modeling of unsteady flows in IC engines”. In: *SAE International Journal of Engines* 8.2 (2015), pp. 426–436 (cit. on p. 9).
- [Pop00] S.B. Pope. *Turbulent flows*. Cambridge university press, 2000 (cit. on pp. 21, 22, 23, 24, 114, 119).
- [Pop18] S. Popinet. “Numerical models of surface tension”. In: *Annual Review of Fluid Mechanics* 50 (2018), pp. 49–75 (cit. on p. 25).
- [Pop88] S.B. Pope. “The evolution of surfaces in turbulence”. In: *International journal of engineering science* 26.5 (1988), pp. 445–469 (cit. on p. 26).
- [Pro56] Y.V. Prokhorov. “Convergence of random processes and limit theorems in probability theory”. In: *Theory of Probability & Its Applications* 1.2 (1956), pp. 157–214 (cit. on p. 50).
- [Pug18] S. Puggelli. “Towards a unified approach for Large Eddy Simulation of turbulent spray flames”. PhD thesis. Normandie Université, 2018 (cit. on pp. 24, 25, 26, 132).
- [PZ99] S. Popinet and S. Zaleski. “A front-tracking algorithm for accurate representation of surface tension”. In: *International Journal for Numerical Methods in Fluids* 30.6 (1999), pp. 775–793 (cit. on p. 31).
- [QA13] L. Quartapelle and F. Auteri. *Fluidodinamica comprimibile*. Casa editrice ambrosiana, 2013 (cit. on p. 99).
- [QQ09] A. Quarteroni and S. Quarteroni. *Numerical models for differential problems*. Vol. 2. Springer, 2009 (cit. on pp. 36, 40).
- [Rem+19] A. Remigi, R. Di Battista, F-X Demoulin, B. Duret, M. Massot, T. Ménard, and H. Deneuille. “Exploring different approaches for the simulation of multi-scale atomization process”. In: *10th International Conference of Multiphase Flow*. Rio de Janeiro, Brazil, May 2019 (cit. on pp. 7, 35).
- [Rey83] O. Reynolds. “An experimental investigation of the circumstances which determine whether the motion of water shall be direct or sinuous, and of the law of resistance in parallel channels.” In: *Proceedings of the royal society of London* 35.224-226 (1883), pp. 84–99 (cit. on p. 22).
- [Ric07] L.F. Richardson. *Weather prediction by numerical process*. Cambridge university press, 2007 (cit. on p. 22).
- [RL80] N. K. Rizk and A. H. Lefebvre. “The Influence of Liquid Film Thickness on Airblast Atomization”. In: *Journal of Engineering for Power* 102.3 (July 1980), pp. 706–710 (cit. on pp. 46, 105).



- [RL85] N.K Rizk and A.H Lefebvre. "Internal flow characteristics of simplex swirl atomizers". In: *Journal of Propulsion and Power* 1.3 (1985), pp. 193–199 (cit. on pp. 97, 98, 99, 101, 102).
- [RL87] N.K Rizk and A.H Lefebvre. "Prediction of velocity coefficient and spray cone angle for simplex swirl atomizers". In: *International Journal of Turbo and Jet Engines* 4.1-2 (1987), pp. 65–74 (cit. on pp. 97, 100).
- [RN01] J-H Rhim and S-Y No. "Breakup length of conical emulsion sheet discharged by pressure-swirl atomizer". In: *International journal of automotive technology* 2.3 (2001), pp. 103–107 (cit. on pp. 7, 105, 113).
- [RP02] M. Rumpf and T. Preusser. "A level set method for anisotropic geometric diffusion in 3D image processing". In: *SIAM Journal on Applied Mathematics* 62.5 (2002), pp. 1772–1793 (cit. on p. 170).
- [Rud98] M. Rudman. "A volume-tracking method for incompressible multifluid flows with large density variations". In: *International Journal for numerical methods in fluids* 28.2 (1998), pp. 357–378 (cit. on p. 37).
- [Rus02] H. Rusche. "Computational Fluid Dynamics of Dispersed Two-Phase Flows at High Phase Fractions". London: Imperial College, Dec. 2002 (cit. on pp. 19, 33, 36, 41, 148).
- [SA99] R. Saurel and R. Abgrall. "A multiphase Godunov method for compressible multifluid and multiphase flows". In: *Journal of Computational Physics* 150.2 (1999), pp. 425–467 (cit. on pp. 20, 38).
- [Sag06] P. Sagaut. *Large eddy simulation for incompressible flows: an introduction*. Springer Science & Business Media, 2006 (cit. on p. 22).
- [Sav33] F. Savart. "Mémoire sur le choc d'une veine liquide lancée contre un plan circulaire". In: *Ann. chim* 54.56 (1833), p. 1833 (cit. on p. 46).
- [SB13] R. Stickles and J. Barrett. "TAPS II Combustor Final Report". In: *CLEEN Program. General Electric, Washington, DC* (2013) (cit. on p. 5).
- [SC95] U. Shavit and N. Chigier. "Fractal dimensions of liquid jet interface under breakup". In: *Atomization and Sprays* 5.6 (1995) (cit. on p. 46).
- [Sch74] H. Schlichting. *Boundary-layer theory*. Springer, 1974 (cit. on p. 48).
- [Sen+99] P.K Senecal, D.P Schmidt, I. Nouar, C.J Rutland, Rolf D. Reitz, and M.L Corradini. "Modeling high-speed viscous liquid sheet atomization". In: *International Journal of Multiphase Flow* 25.6-7 (1999), pp. 1073–1097 (cit. on p. 6).
- [SF99] M. Sussman and E. Fatemi. "An efficient, interface-preserving level set redistancing algorithm and its application to interfacial incompressible fluid flow". In: *SIAM Journal on scientific computing* 20.4 (1999), pp. 1165–1191 (cit. on p. 19).
- [SGD18] Maciej Skarysz, Andrew Garmory, and Mehriar Dianat. "An iterative interface reconstruction method for PLIC in general convex grids as part of a Coupled Level Set Volume of Fluid solver". In: *Journal of Computational Physics* 368 (2018), pp. 254–276 (cit. on p. 19).
- [SGR03] R. Saurel, S. Gavrilyuk, and F. Renaud. "A multiphase model with internal degrees of freedom : application to shock-bubble interaction". In: *Journal of Fluid Mechanics* 495 (2003), pp. 283–321 (cit. on pp. 39, 40).

- [SHT16] S. Sahu, Y. Hardalupas, and A.M.K.P Taylor. “Droplet–turbulence interaction in a confined polydispersed spray: effect of turbulence on droplet dispersion”. In: *Journal of Fluid Mechanics* 794 (2016), pp. 267–309 (cit. on p. 7).
- [Shu98] C-W Shu. “Essentially non-oscillatory and weighted essentially non-oscillatory schemes for hyperbolic conservation laws”. In: *Advanced numerical approximation of nonlinear hyperbolic equations*. Springer, 1998, pp. 325–432 (cit. on p. 36).
- [Siv+15] D. Sivakumar, S.K Vankeswaram, R. Sakthikumar, and B.N Raghunandan. “Analysis on the atomization characteristics of aviation biofuel discharging from simplex swirl atomizer”. In: *International Journal of Multiphase Flow* 72 (2015), pp. 88–96 (cit. on p. 7).
- [SL86] M. Suyari and A.H Lefebvre. “Film thickness measurements in a simplex swirl atomizer”. In: *Journal of Propulsion and Power* 2.6 (1986), pp. 528–533 (cit. on pp. 7, 97, 103).
- [Sma63] J. Smagorinsky. “General circulation experiments with the primitive equations: I. The basic experiment”. In: *Monthly weather review* 91.3 (1963), pp. 99–164 (cit. on pp. 24, 43, 122).
- [SP00] M. Sussman and E.G. Puckett. “A coupled level set and volume-of-fluid method for computing 3D and axisymmetric incompressible two-phase flows”. In: *Journal of computational physics* 162.2 (2000), pp. 301–337 (cit. on p. 19).
- [SP18] R. Saurel and C. Pantano. “Diffuse-Interface Capturing Methods for Compressible Two-Phase Flows”. In: *Annual Review of Fluid Mechanics* 50.1 (2018), pp. 105–130 (cit. on pp. 8, 11, 20, 33, 38, 147).
- [Squ53] H.B Squire. “Investigation of the instability of a moving liquid film”. In: *British Journal of Applied Physics* 4.6 (1953), p. 167 (cit. on p. 46).
- [SS03] J.A Sethian and P. Smereka. “Level set methods for fluid interfaces”. In: *Annual review of fluid mechanics* 35.1 (2003), pp. 341–372 (cit. on p. 19).
- [SS90] B.E Stapper and G.S Samuelsen. “An experimental study of the breakup of a two-dimensional liquid sheet in the presence of co-flow air shear”. In: *28th Aerospace Sciences Meeting*. 1990, p. 461 (cit. on p. 46).
- [SSO94] M. Sussman, P. Smereka, and S. Osher. “A level set approach for computing solutions to incompressible two-phase flow”. In: *Journal of Computational Physics* 114.1 (1994), pp. 146–159 (cit. on p. 19).
- [SSS92] B.E Stapper, W.A Sowa, and G.S Samuelsen. “An experimental study of the effects of liquid properties on the breakup of a two-dimensional liquid sheet”. In: *Journal of engineering for gas turbines and power* 114.1 (1992), pp. 39–45 (cit. on p. 46).
- [SU10] J. Shinjo and A. Umemura. “Simulation of liquid jet primary breakup: Dynamics of ligament and droplet formation”. In: *International Journal of Multiphase Flow* 36.7 (2010), pp. 513–532 (cit. on pp. 29, 52).
- [Sus+07] M. Sussman, K. M Smith, M.Y Hussaini, M. Ohta, and R Zhi-Wei. “A sharp interface method for incompressible two-phase flows”. In: *Journal of computational physics* 221.2 (2007), pp. 469–505 (cit. on p. 37).
- [SV94] S.G Saddoughi and S.V Veeravalli. “Local isotropy in turbulent boundary layers at high Reynolds number”. In: *Journal of Fluid Mechanics* 268 (1994), pp. 333–372 (cit. on p. 22).

- [Syr+17] A. Syrakos, S. Varchanis, Y. Dimakopoulos, A. Goulas, and J. Tsamopoulos. “A critical analysis of some popular methods for the discretisation of the gradient operator in finite volume methods”. In: *Physics of Fluids* 29.12 (2017), p. 127103 (cit. on p. 123).
- [Tav+15] M. Tavares, S. Vincent, M. Ould-Rouiss, and J-L Estivalezes. “A priori study for the modeling of LES subgrid scale terms in resolved scale multiphase flows”. In: *Turbulence and Interactions*. Springer. 2015, pp. 249–254 (cit. on p. 25).
- [Tay48] G.I Taylor. “The mechanics of swirl atomizers”. In: *Seventh International Congress of Applied Mechanics*. Vol. 2. 1948, pp. 280–285 (cit. on p. 97).
- [Tay50] G.I Taylor. “The boundary layer in the converging nozzle of a swirl atomizer”. In: *The Quarterly Journal of Mechanics and Applied Mathematics* 3.2 (1950), pp. 129–139 (cit. on pp. 7, 97).
- [Tay59a] G.I Taylor. “The dynamics of thin-sheets of fluid. I. water bells”. In: *Proceedings of the Royal Society of London. Series A. Mathematical and Physical Sciences* 253.1274 (1959), pp. 289–295 (cit. on p. 46).
- [Tay59b] G.I Taylor. “The dynamics of thin sheets of fluid II. Waves on fluid sheets”. In: *Proceedings of the Royal Society of London. Series A. Mathematical and Physical Sciences* 253.1274 (1959), pp. 296–312 (cit. on p. 46).
- [TB00] D.J Torres and J.U Brackbill. “The point-set method: front-tracking without connectivity”. In: *Journal of Computational Physics* 165.2 (2000), pp. 620–644 (cit. on p. 31).
- [Tho71] W. Thomson. “XLVI. Hydrokinetic solutions and observations”. In: *The London, Edinburgh, and Dublin Philosophical Magazine and Journal of Science* 42.281 (1871), pp. 362–377 (cit. on p. 105).
- [Try+01] G. Tryggvason, B. Bunner, A. Esmaeeli, D. Juric, N. Al-Rawahi, W. Tauber, J. Han, S. Nas, and Y-J Jan. “A front-tracking method for the computations of multiphase flow”. In: *Journal of Computational Physics* 169.2 (2001), pp. 708–759 (cit. on p. 18).
- [TSZ11] Gretar Tryggvason, R Scardovelli, and Stéphane Zaleski. *Direct Numerical Simulations of Gas-Liquid Multiphase Flow*. Jan. 2011 (cit. on pp. 8, 13).
- [TY07] C. Tropea and A.L Yarin. *Springer handbook of experimental fluid mechanics*. Springer Science & Business Media, 2007 (cit. on pp. 97, 108).
- [Vau15] Geoffroy Vaudor. “Atomisation assistée par un cisaillement de l’écoulement gazeux Développement et validation”. PhD thesis. University of Normandie, Apr. 2015 (cit. on p. 36).
- [Vau+17] G. Vaudor, T. Ménard, W. Aniszewski, M. Doring, and A. Berlemont. “A consistent mass and momentum flux computation method for two phase flows. Application to atomization process”. In: *Computers & Fluids* 152 (2017), pp. 204–216 (cit. on pp. 35, 37).
- [VB99] Ariane Vallet and Roland Borghi. “Modélisation eulerienne de l’atomisation d’un jet liquide”. In: *Comptes Rendus de l’Académie des Sciences* 327.10 (1999), pp. 1015–1020 (cit. on pp. 24, 25, 26, 27, 33, 43, 116, 132, 147).
- [VC02] E. Villermaux and C. Clanet. “Life of a flapping liquid sheet”. In: *Journal of Fluid Mechanics* 462 (2002), pp. 341–363 (cit. on p. 46).

- [Vee+93] S.V Veeravalli, S.G Saddoughi, A.A Praskovsky, and P. Bradshaw. "A Note on Local Isotropy in High-Reynolds-Number Turbulence". In: *New Approaches and Concepts in Turbulence*. Springer, 1993, pp. 377–383 (cit. on p. 22).
- [Vin+16] R. Vinuesa, C. Prus, P. Schlatter, and H.M Nagib. "Convergence of numerical simulations of turbulent wall-bounded flows and mean cross-flow structure of rectangular ducts". In: *Meccanica* 51.12 (2016), pp. 3025–3042 (cit. on p. 50).
- [Vin+18] S. Vincent, M. Tavares, S. Fleau, S. Mimouni, M. Ould-Rouiss, and J-L Estivalèzes. "A priori filtering and LES modeling of turbulent two-phase flows application to phase separation". In: *Computers & Fluids* 176 (2018), pp. 245–259 (cit. on pp. 9, 24, 25).
- [VL74] B. Van Leer. "Towards the ultimate conservative difference scheme. II. Monotonicity and conservation combined in a second-order scheme". In: *Journal of computational physics* 14.4 (1974), pp. 361–370 (cit. on p. 123).
- [Waa94] J.D Van der Waals. "Thermodynamische Theorie der Kapillarität unter Voraussetzung stetiger Dichteänderung". In: *Zeitschrift für Physikalische Chemie* 13.1 (1894), pp. 657–725 (cit. on p. 17).
- [Wal93] P. Walzel. "Liquid atomization". In: *International Chemical Engineering* 33.1 (1993) (cit. on p. 6).
- [Wel] H. Weller. *A new approach to vof-based interface capturing methods for incompressible and compressible flow*. Tech. rep. OpenCFD Ltd., Report TR/HGW/04 (cit. on pp. 19, 35).
- [Wil58] F.A Williams. "Spray combustion and atomization". In: *The Physics of Fluids* 1.6 (1958), pp. 541–545 (cit. on pp. 21, 33).
- [WW13] K.E Wardle and H.G Weller. "Hybrid multiphase CFD solver for coupled dispersed/segregated flows in liquid-liquid extraction". In: *International Journal of Chemical Engineering* 2013 (2013) (cit. on pp. 19, 41).
- [XSC11] J-F Xie, S. S Sazhin, and B-Y Cao. "Molecular dynamics study of the processes in the vicinity of the n-dodecane vapour/liquid interface". In: *Physics of Fluids* 23.11 (2011), p. 112104 (cit. on pp. 8, 14).
- [Yan+14] H. Yanagihara, I. Stanković, A. Blomgren F.and Rosén, and I. Sakata. "A molecular dynamics simulation investigation of fuel droplet in evolving ambient conditions". In: *Combustion and flame* 161.2 (2014), pp. 541–550 (cit. on p. 13).
- [Zal79] S.T Zalesak. "Fully multidimensional flux-corrected transport algorithms for fluids". In: *Journal of computational physics* 31.3 (1979), pp. 335–362 (cit. on p. 42).
- [ZED18] D. Zuzio, J-L Estivalèzes, and B. DiPierro. "An improved multiscale Eulerian–Lagrangian method for simulation of atomization process". In: *Computers & Fluids* 176 (2018), pp. 285–301 (cit. on p. 28).
- [Zha96] J. Zhang. "Acceleration of five-point red-black Gauss-Seidel in multigrid for Poisson equation". In: *Applied Mathematics and Computation* 80.1 (1996), pp. 73–93 (cit. on p. 37).
- [Zou+20] Z. Zou, E. Audit, N. Grenier, and C. Tenaud. "An accurate sharp interface method for two-phase compressible flows at low-Mach regime". In: *Flow, Turbulence and Combustion* 105.4 (2020), pp. 1413–1444 (cit. on p. 33).

- [ZSH16] A. Zandian, W.A Sirignano, and F. Hussain. “Three-dimensional liquid sheet breakup: vorticity dynamics”. In: *54th AIAA aerospace sciences meeting*. 2016, p. 1593 (cit. on p. 46).
- [ZSH17a] A. Zandian, W. Sirignano, and F. Hussain. “Mechanisms of Liquid Stream Breakup: Vorticity and Time and Length Scales”. In: *ILASS Europe. 28th european conference on Liquid Atomization and Spray Systems*. Editorial Universitat Politècnica de València. 2017, pp. 362–367 (cit. on p. 46).
- [ZSH17b] A. Zandian, W.A. Sirignano, and F. Hussain. “Planar liquid jet: Early deformation and atomization cascades”. In: *Physics of Fluids* 29.6 (2017), p. 062109 (cit. on p. 46).
- [ZSH18] A. Zandian, W. A Sirignano, and F. Hussain. “Understanding liquid-jet atomization cascades via vortex dynamics”. In: *Journal of Fluid Mechanics* 843 (2018), pp. 293–354 (cit. on p. 46).

# Appendices



# Chap. A | Computation of Gaussian curvature through an analytical method

## A.1 Introduction

One of the most advanced method to compute the curvature can be found in [Kin+03], where the authors reconstruct it starting from an implicit formulation. The proposed approach (already implemented in the DNS code *ARCHER* [MTB07]) is hereafter implemented in the multi purpose C++ library *OpenFoam*, with the objective to use it coupled with different Level-Set reconstruction algorithms ([DB21]).

## A.2 Theoretical framework

The *curvature* of a surface is defined by the relationship between positional changes in the neighborhood of a point placed on the surface and the change in the surface normal. Given a level-set  $\Phi(\mathbf{x})$ , we consider that the value of the level-set is positive inside the object, negative outside. Hence, we define the normal unit vector:

$$\mathbf{n} = -\frac{\nabla\Phi}{|\nabla\Phi|} \quad (\text{A.1})$$

The curvature information is contained in the 3x3 matrix  $\nabla\mathbf{n}^T$ . Considering the Hessian matrix:

$$\mathbf{H} = \begin{bmatrix} \frac{\partial^2\Phi}{\partial x^2} & \frac{\partial^2\Phi}{\partial x\partial y} & \frac{\partial^2\Phi}{\partial x\partial z} \\ \frac{\partial^2\Phi}{\partial x\partial y} & \frac{\partial^2\Phi}{\partial y^2} & \frac{\partial^2\Phi}{\partial y\partial z} \\ \frac{\partial^2\Phi}{\partial x\partial z} & \frac{\partial^2\Phi}{\partial y\partial z} & \frac{\partial^2\Phi}{\partial z^2} \end{bmatrix} \quad (\text{A.2})$$

The projection matrix, defined as  $\mathbf{P} = \mathbf{I} - \mathbf{nn}^T$ , projects the matrix on the tangent plane to the surface described by the function  $\Phi(\mathbf{x}) = 0$ . As described in [Kin+03] and in [MH92] it is possible to write the relationship:

$$\nabla\mathbf{n}^T = -\frac{1}{|\nabla\Phi|}(\mathbf{P}\mathbf{H}) \quad (\text{A.3})$$

The Hessian matrix describes how the gradient changes around the neighborhood of the points placed on an iso-surface of the function  $\Phi(\mathbf{x})$  [MT03]. In order to describe the curvature we are interested only in changes of direction of the gradient. Hence we project  $\mathbf{H}$  on the tangent plane, as in eq. (A.3). The restriction of the Hessian to the tangent plane is a symmetric



matrix and it is possible to find an orthonormal basis  $\{\mathbf{p}_1, \mathbf{p}_2, \mathbf{n}\}$  able to diagonalize the matrix. In this basis we will obtain:

$$\nabla \mathbf{n}^T = \begin{bmatrix} k_1 & 0 & \sigma_1 \\ 0 & k_2 & \sigma_2 \\ 0 & 0 & 0 \end{bmatrix} \quad (\text{A.4})$$

$\mathbf{p}_1$  and  $\mathbf{p}_2$  are the two eigenvectors associated to the principal curvatures, with eigenvalues  $k_1$  and  $k_2$ . The other two values  $\sigma_1$  and  $\sigma_2$  describe how the normal tilts. This aspect is called *flowline curvature*. Further details can be found in [Kin+03]. In this case the goal is to isolate  $k_1$  and  $k_2$ , and as proposed by [RP02], we multiply  $\nabla \mathbf{n}^T$  by the projection matrix  $\mathbf{P}$ , obtaining the *Geometry tensor*:

$$\mathbf{G} = \nabla \mathbf{n}^T \mathbf{P} \quad (\text{A.5})$$

The algorithm to compute the two Gaussian curvature can be summarized in the following steps:

- a. Compute the normal  $\mathbf{n}$  and the projection matrix  $\mathbf{P}$ .
- b. Compute the Hessian  $\mathbf{H}$  and the geometric tensor  $\mathbf{G}$ .
- c. Analytically compute  $k_1$  and  $k_2$ . Defining as  $T$  the trace of  $\mathbf{G}$  and  $F$  the Euclidean norm of  $\mathbf{G}$  the two eigenvalues (and hence the two curvatures) of the geometric vector can be computed as:

$$k_1 = \frac{T + \sqrt{2F^2 - T^2}}{2} \quad (\text{A.6})$$

$$k_2 = \frac{T - \sqrt{2F^2 - T^2}}{2} \quad (\text{A.7})$$

from this it is possible to define the two Gaussian principal curvatures as follows:

$$H = \frac{k_1 + k_2}{2} \quad (\text{A.8})$$

$$G = k_1 \cdot k_2 \quad (\text{A.9})$$

### A.3 Validation

For the validation of the algorithm inside OpenFOAM, we take the distance function of objects with known geometrical properties and we evaluate the difference in the distribution of the two *L1 relative error* for the mean  $H$  and Gauss  $G$  curvature with increasing domain refinement.

#### A.3.1 Sphere

We start considering a sphere. The distance function of a sphere is:

$$\Phi(\mathbf{x}) = -\sqrt{(x - x_C)^2 + (y - y_C)^2 + (z - z_C)^2} + R \quad (\text{A.10})$$

where  $(x_C, y_C, z_C)$  are the coordinates of the center of the sphere and  $R$  its radius. In the case of a sphere the curvature is an analytical function of the radius.

$$G_{an} = \frac{1}{R^2} \quad (\text{A.11})$$

$$H_{an} = \frac{1}{R} \quad (\text{A.12})$$

In our test case we consider a sphere of radius  $R = 5e - 5[m]$  in a cubic domain of  $L = 1.8e - 4[m]$  (fig. A.1). We define the distance function as in the definition given in eq. (A.10) and we vary the number of elements inside a drop diameter from 30 to 90 elements. We define the *L1 relative error* for  $H$  and  $G$  as follow:

$$errH(el) = \sum_0^{n.el} \frac{H - H_{an}}{H_{an}} \quad (\text{A.13})$$

$$errG(el) = \sum_0^{n.el} \frac{G - G_{an}}{G_{an}} \quad (\text{A.14})$$

The results of the error are reported in fig. A.2. The algorithm is capable of approximating with a reasonable accuracy the value of the curvatures up to a certain level of refinement. The relevant result is that, even if the level of refinement is still not sufficient (algorithms like the one presented in [DB21] have been tested on  $10^4$  number of points) the error is limited.



Figure A.1 – Domain of computation for the test of the curvature algorithm on a sphere. On the left the 0 iso-surface of the level-set function, on the right a slice of the field with the shadow of the level-set distance function 0 iso-surface.

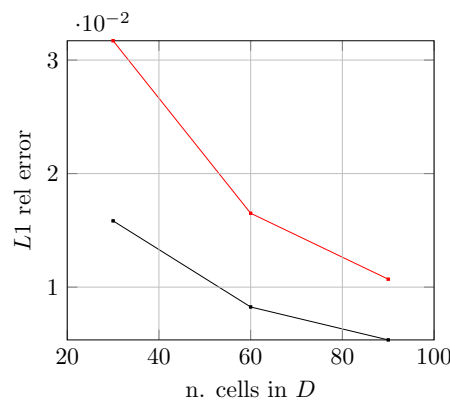


Figure A.2 – Relative error trend for the two Gaussian curvature on the surface of the sphere ( —  $H$ , —  $G$ ). The *L1 relative error* has been computed with the formulation in eq. (A.14) and eq. (A.13).

### A.3.2 Ellipsis

The distance function of an ellipsis is:

$$\Phi(\mathbf{x}) = -\sqrt{(x - x_C)^2/a^2 + (y - y_C)^2/b^2 + (z - z_C)^2/c^2} + 1 \quad (\text{A.15})$$

where  $(x_C, y_C, z_C)$  are the coordinates of the center of the ellipsis and  $(a, b, c)$  are the value of the semi-axis. The curvature is an analytical function of the semi-axis ([Bek17]).

$$G_{an} = \frac{1}{\left[abc\left(\frac{x^2}{a^4} + \frac{y^2}{b^4} + \frac{z^2}{c^4}\right)\right]^2} \quad (\text{A.16})$$

$$H_{an} = \frac{x^2 + y^2 + z^2 - a^2 - b^2 - c^2}{2(abc)^2 \left[\left(\frac{x^2}{a^4} + \frac{y^2}{b^4} + \frac{z^2}{c^4}\right)\right]^{3/2}} \quad (\text{A.17})$$

In our test case we consider an ellipsis with semi-axis  $a, b, c = 1e - 5, 2e - 5, 3e - 5[m]$  in a cubic domain of  $L = 1.8e - 4[m]$  we define the distance function as in the definition given in eq. (A.15) and we vary the number of elements in the domain, considering the unitary length-scale of  $1e - 4[m]$  from 30 to 90 elements. We compute the  $L1$  relative errors as defined in eq. (A.13) and eq. (A.14). The results of the errors are reported in fig. A.4. We observe the results found on the sphere are confirmed.

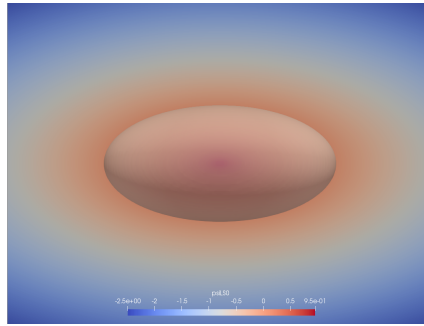


Figure A.3 – Slice of the domain for the ellipsis test case with distance function iso-contour and shaded 0 iso-surface.

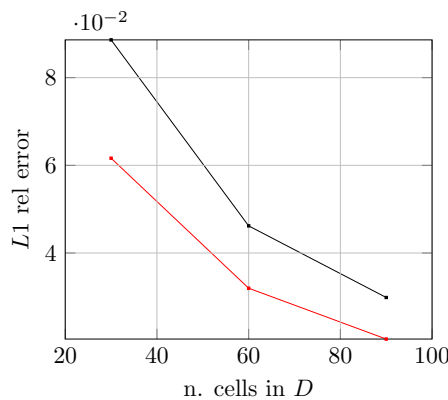


Figure A.4 – Relative error changing for the two Gaussian curvature on the surface of the ellipsis ( —  $H$ , —  $G$ ). The  $L1$  relative error has been computed with the formulation in eq. (A.14) and eq. (A.13).

## Chap. B | $IRQ_{\Sigma}$ parametric study

In the last years, different works studied the influence of the sensibility and the tune of the  $IRQ$  parameters. In [Can] and [Can19] the sensibility of the parameter  $IRQ_K$  has been studied, by setting the value of  $IRQ_{K,lim} = 2$  as the most suitable to determine if the interface is well resolved or not well resolved. In [Ane+19a] and [Ahm19] the  $IRQ_K$  criteria has been applied together with the  $IRQ_{\Sigma}$  criteria, even if in the conclusion and perspective, the suggestion of the author was to go more in-depth in the  $IRQ$  computation, and to understand better the problematic. No details about the threshold used has been given. In the present manuscript we go more in deep in the problem, trying to optimize the  $IRQ_{\Sigma}$  sensor on the two numerical domain presented.

It is possible to state that when  $\Sigma = 2\Sigma_{min}$ , physically it could mean that two interfaces are present in the same cells and hence we are going through a breakup. It means that the breakup is not well captured and as a consequence it is suggested to set our  $IRQ$  value to  $IRQ_{\Sigma,lim} > 0.5$ . Starting from this point, in order to set-up the  $IRQ_{\Sigma,lim}$  value, we evaluate the surface field of  $IRQ_{\Sigma}$  on a clipped field of  $\alpha_l \in [0.1, 1]$  (fig. B.1). At the interface  $IRQ_{\Sigma}$  assumes value that are between  $IRQ_{\Sigma} = 0.5$  and  $IRQ_{\Sigma} = 0.8$ . Thus we test different limits in this range, to understand which is the most suitable value of  $IRQ_{\Sigma,lim}$  for the academical test case (and as a consequence for the industrial configuration) studied in the manuscript. The field of  $C_{\alpha}$  for 4 different value of  $IRQ_{\Sigma,lim}$  is showed in fig. B.2 and fig. B.3. As it is possible to observe in fig. B.3b, for  $IRQ_{\Sigma,lim} = 0.75$ , the sharpening flux starts not to act properly on the big structure of the flow. On the contrary in fig. B.2a and fig. B.2b we observe that for the respective  $IRQ_{\Sigma,lim}$  the sharpening term seems activated also for some small structures of the flow that are not well resolved. For this reason, the choice has been to set the  $IRQ_{\Sigma,lim} = 0.65$ . This value conserves the sharpening flux activated for large structures of the flow and ignores the not resolved structures, as it is expected to be for the *ICMelsa* model.

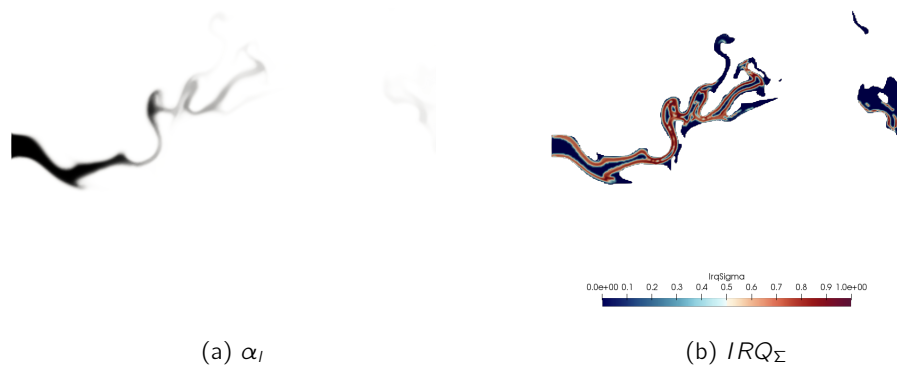



Figure B.1 – On the left: liquid volume fraction surface plot of a snapshot of the box configuration defined along the thesis.  $\alpha_l = 0$    $1$ . On the right:  $IRQ_{\Sigma}$  surface plot, on the clipped field of liquid volume fraction  $\alpha_l \in [0.1, 1]$ .

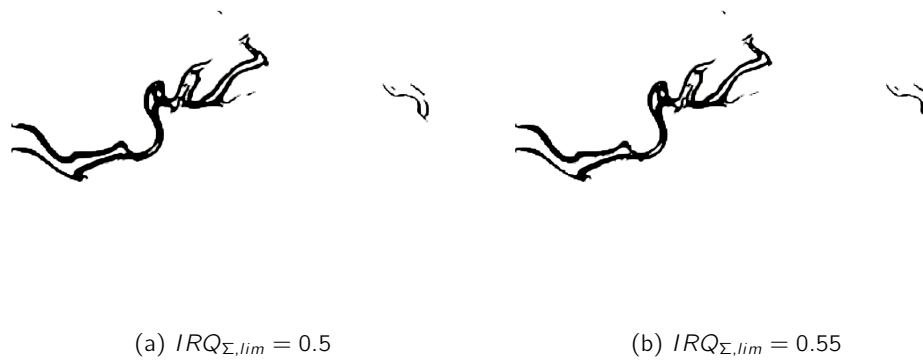


Figure B.2 – The  $C_{\alpha}$  field with varying  $IRQ$  limit  $IRQ_{\Sigma,lim}$ . In black  $C_{\alpha} = 1$ , in white  $C_{\alpha} = 0$ . On the left:  $IRQ_{\Sigma,lim} = 0.5$ . On the right:  $IRQ_{\Sigma,lim} = 0.55$ . For the  $\alpha_l$  field, refer to fig. B.1a.

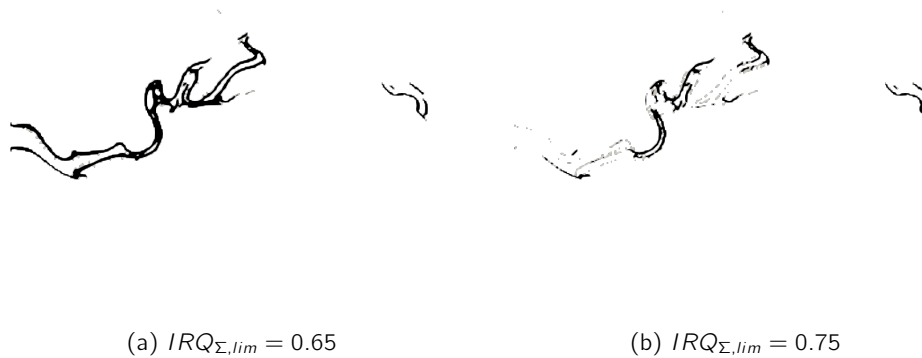


Figure B.3 – The  $C_\alpha$  field with varying  $IRQ$  limit  $IRQ_{\Sigma,lim}$ . In black  $C_\alpha = 1$ , in white  $C_\alpha = 0$ . On the left:  $IRQ_{\Sigma,lim} = 0.65$ . On the right:  $IRQ_{\Sigma,lim} = 0.75$ . For the  $\alpha_l$  field, refer to fig. B.1a.



## Chap. C | Weak ergodicity

In order to prove the *weak ergodicity* of the signal, we have to compute the statistics on two uncorrelated part of the signal and verify that the results are similar. Thus we have to chose two uncorrelated part of the signal, and hence a *correlation time*. We consider the temporal history of the *ARCHER* level-set signal, took at the location of  $(L_x/6, L_y/2, L_z/2)$ . First we do a moving average to watch how it evolves with a varying average window.

$${}^t\bar{\alpha}(t) = \frac{1}{\Delta t} \int_{t_0}^{t_0+\Delta t} \alpha(t) dt \quad (C.1)$$

Where  $\Delta t = t - t_0$  and  $t_0 = 3.8[ms]$ . The values of  $t_0$  has been chosen in accordance with the manuscript to cut the flow settling transitory. We can see that for  $t = 10[ms]$  the average

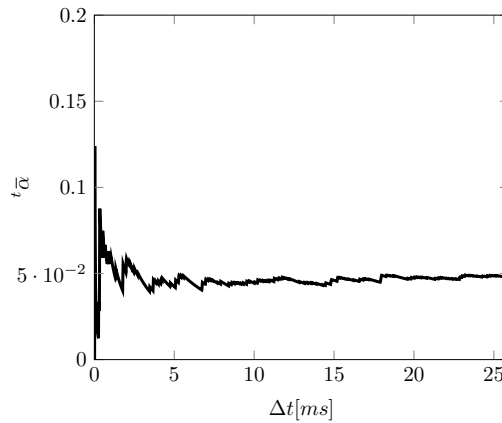


Figure C.1 – Moving average  ${}^t\bar{\alpha}$  taking as a phase marker the level-set distance function.  $t$  is the dimension of the averaging window starting from  $t_0 = 3.8[ms]$ .

stabilizes. Hence we chose  $t = 10[ms]$  as a correlation time and we compute the average on two different time windows, with different  $t_0$ :

- A: window positioned at  $[10[ms] - 20[ms]]$  with  $t_0 = 10[ms]$ ;
- B: window positioned at  $[20[ms] - 30[ms]]$  with  $t_0 = 20[ms]$ ;

For the window A, the average results to be  ${}^t\bar{\alpha}_A = 0.047$ , while for the window B results to be  ${}^t\bar{\alpha}_B = 0.049$ . The small residual gives proof of *weak ergodicity* of the signal. To further verify it, it is possible to draw the correlation function for the entire interval  $[3.8[ms], 30[ms]]$  and for the two different time window A and B with the respective starting time at the lower limit of the time window.

$$r(\Delta t) = \frac{{}^t\overline{\alpha(t)\alpha(t+\Delta t)}}{{}^t\overline{\alpha^2}} \quad (C.2)$$

In fig. C.2 are represented the autocorrelation for the complete signal, and in fig. C.4 and fig. C.3 the autocorrelation function for the two different time window. Over imposing the



two time windows autocorrelation it is possible to see that the frequency and topology is recovered and hence we can, another time, state the weak ergodicity of the process. As it is possible to see, as far as the process is unsteady, we recognize small and large fluctuations. It can be interesting to study these fluctuations in order to give a spectral characterization of the process. We have to remember that the process is strongly dependent on the location of the domain in which we consider the probe and on the type of the inclusions, hence small and big frequencies are expected to change in changing the location of the probe.

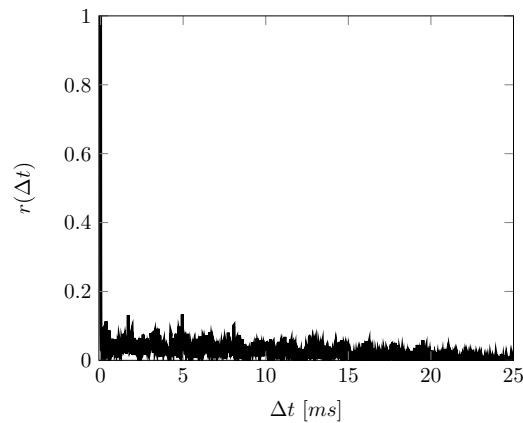


Figure C.2 – Autocorrelation function for the time interval  $[3.8[ms], 30[ms]]$  with  $t_0 = 3.8[ms]$ .

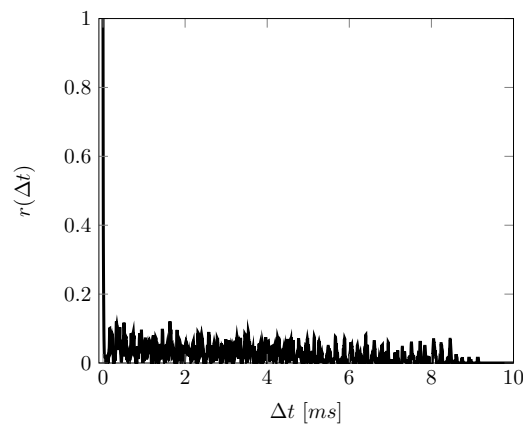


Figure C.3 – Autocorrelation function for the time window A. Time interval  $[10[ms], 20[ms]]$ ,  $t_0 = 10[ms]$ .

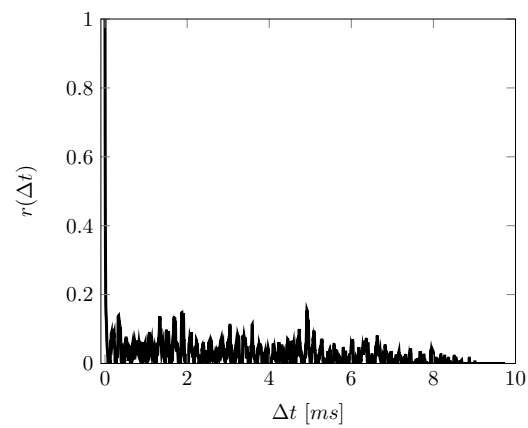


Figure C.4 – Autocorrelation function for the time window B. Time interval  $[20[ms], 30[ms]]$ ,  $t_0 = 20[ms]$ .



# Chap. D | Other phase analysis results

## D.1 Turbulent liquid flux

The turbulent liquid flux term  $\overline{v'\alpha'_l}$  identify the dispersion of the liquid due to the action of the velocity field. Analysing the flux  $\overline{v\alpha_l}$  it is possible to decompose it following the Reynolds formalism in:

$$\overline{v\alpha_l} = \overline{v^t\alpha_l} + \overline{v'\alpha'_l} \quad (D.1)$$

Observing fig. D.1 we identify the vector field of  $\overline{v\alpha_l}$  and  $\overline{v^t\alpha_l}$  overimposed to the contour of of averaged liquid volume fraction  $\overline{\alpha_l}$  for the *ARCHER* simulation. We observe how, in a context of time averaged quantities and hence Reynolds decomposition, it is of fundamental importance the *turbulent liquid flux* modeling  $\overline{v'\alpha'_l}$ . Hence it is important to look at that term for the different solution deployed to model (or to not model) this term.

We can observe in fig. D.1 that the predominant term is the  $z^*$  component of the *turbulent liquid flux* and hence  $\overline{v'_z\alpha'_l}$ .

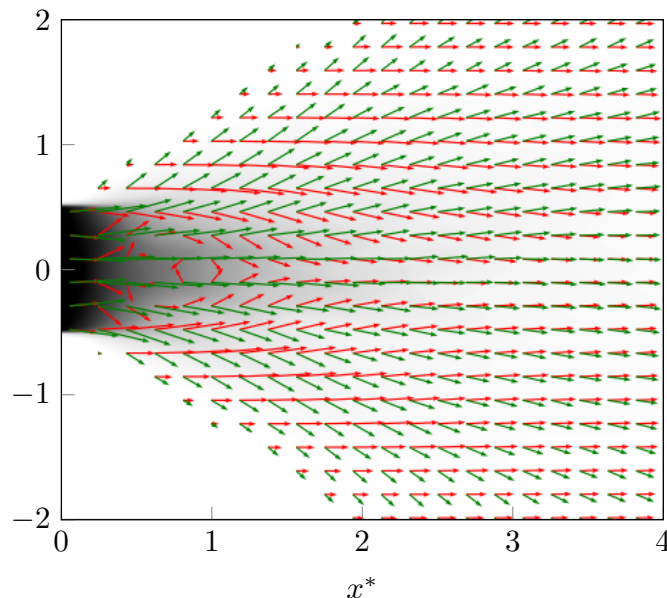


Figure D.1 – Liquid volume fraction contour with over imposed the liquid volume fraction dispersion. In red the scaled  $\overline{v\alpha_l}$  and in green the scaled  $\overline{v'\alpha'_l}$ .

Figure D.2 and fig. D.3 presents the turbulent liquid flux in  $z^*$  direction  $\overline{v'_z\alpha'_l}$  at  $y^* = 0$  plane. For all the models the shape of the contour is the same. Furthermore it is possible to see a slight magnitude difference among the *sharp interface* approaches and the *diffuse interface*

approaches. Looking at this term we would attend to see a huge difference among the case in which the turbulent liquid flux is modelled (*ELSA* and *ICMelsa*) and the case in which it is not (*CEDRE*, *ARCHER*, *InterFoam*). This difference is not noticed. This is probably due to the high resolution of the meshes used. It is enough to resolve well the liquid dispersion also without the turbulent liquid flux model. Figure D.4 shows the profiles of turbulent liquid flux in  $z^*$  direction at  $x^* = 1, 2, 3$  location. The profiles nearly over impose and no differences among them is noticed.

These results are confirmed by the results of the axial turbulent liquid flux. Surface plots and profiles are reported in fig. D.5, fig. D.6, fig. D.7.

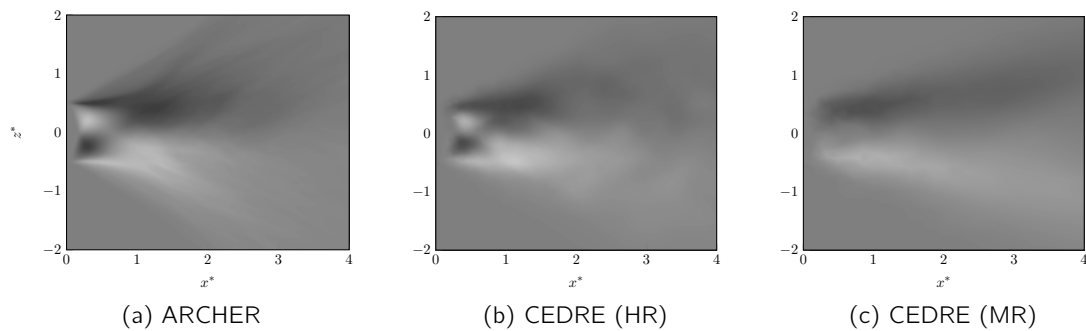


Figure D.2 –  $z^*$  component of the turbulent liquid flux  $\overline{v'_z \alpha'_l} = -1.5 \text{ } \blacksquare \text{ } 1.5 [m/s]$  at the  $y^* = 0$  plane.

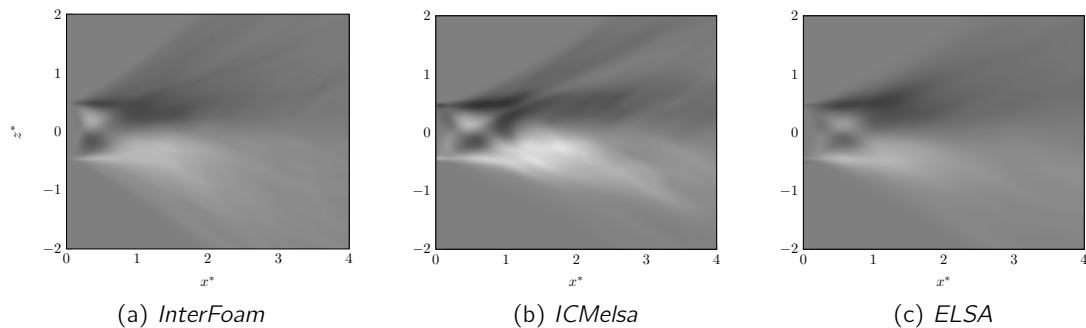


Figure D.3 –  $z^*$  component of the turbulent liquid flux  $\overline{v'_z \alpha'_l} = -1.5 [m/s] \text{ } \blacksquare \text{ } 1.5 [m/s]$  at the  $y^* = 0$  plane.

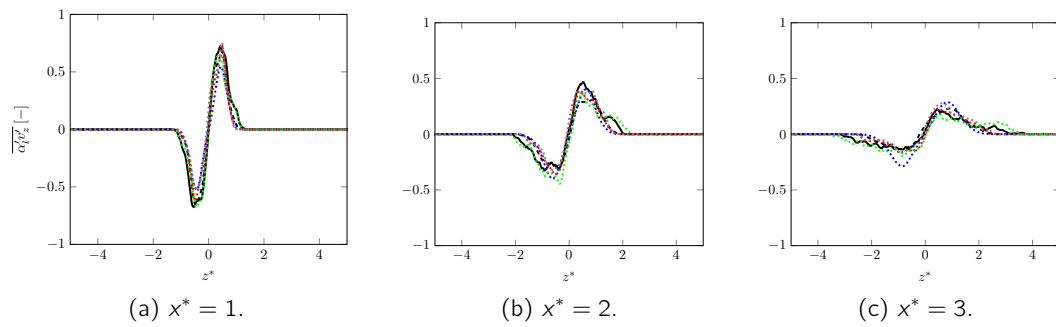


Figure D.4 –  $z^*$  component of the turbulent liquid flux  $\overline{v'_z \alpha'_l}$  along  $x^* = 1, 2, 3$ . — ARCHER, ..... CEDRE (HR), ..... CEDRE (MR), ..... InterFoam, ..... ELSA, ..... ICMelsa .

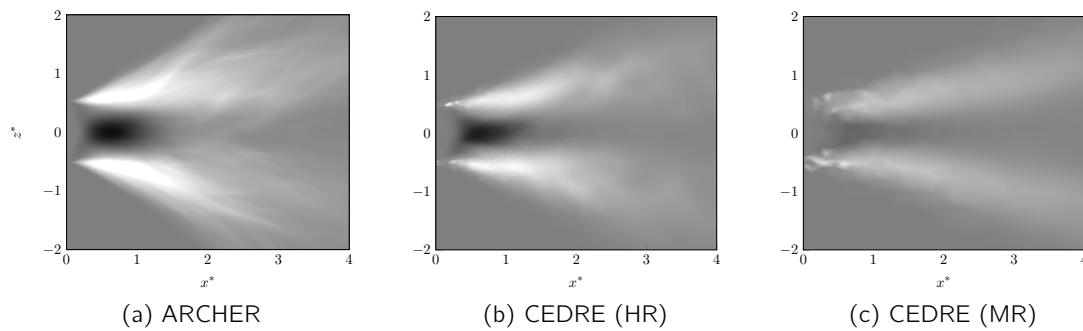


Figure D.5 – Streamwise turbulent liquid flux  $\overline{v'_x \alpha'_l} = -2 \text{ [m/s]} \text{ --- } 2 \text{ [m/s]}$  at the  $y^* = 0$  plane.

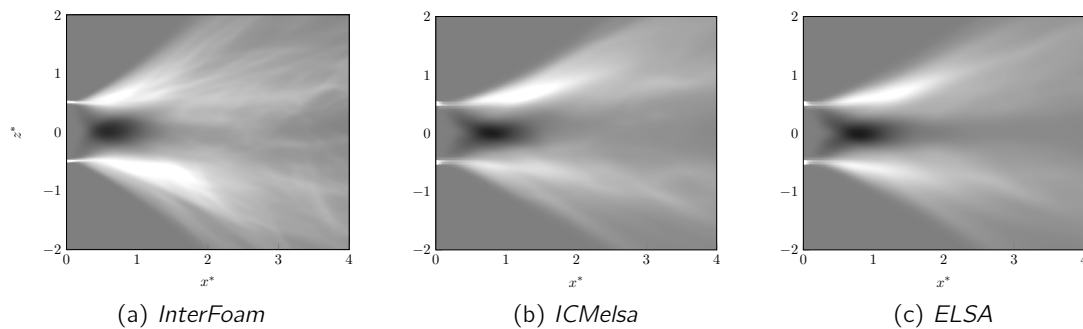


Figure D.6 – Streamwise turbulent liquid flux  $\overline{v'_x \alpha'_l} = -2 \text{ [m/s]} \text{ --- } 2 \text{ [m/s]}$  at the  $y^* = 0$  plane.

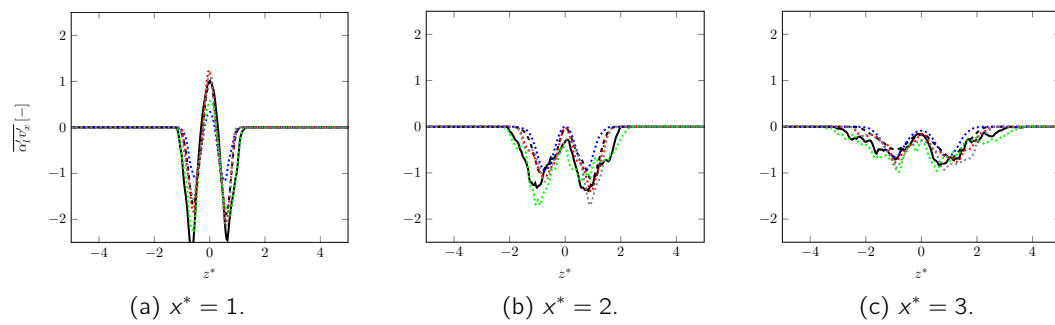


Figure D.7 – Streamwise turbulent liquid flux  $\overline{v'_l \alpha'_l}$  along fig. 3.14 and fig. 3.15 dashed lines. — ARCHER, ..... CEDRE (HR), ..... CEDRE (MR), ..... *InterFoam*, ..... *ELSA*, ..... *ICMelsa*.